



University of
Strathclyde
Glasgow

The impact of single-point mutations and IgG
subclass on the developability of high
concentration monoclonal antibody
formulations

Thesis presented by

Georgina Armstrong

Supervised by Dr William J Lewis and Dr Zahra Rattray

In fulfilment of the requirement for the degree of

Doctor of Philosophy

2024

BioPharm Process Research, Drug Substance Development

GlaxoSmithKline

Gunnel Woods Road, Stevenage, UK

Strathclyde Institute of Pharmacy and Biomedical Science

University of Strathclyde

Glasgow, UK

This thesis is the result of the author's original research. It has been composed by the author and has not been previously submitted for examination which has led to the award of a degree.

The copyright of this thesis belongs to GSK in accordance with the author's contract of employment with GSK under the terms of the United Kingdom Copyright Acts. Due acknowledgement must always be made of the use of any material contained in, or derived from, this thesis.

Signed:

A handwritten signature in black ink, appearing to read 'G. Armstrong', with a large, stylized initial 'G' and a long, sweeping flourish extending to the right.

Date:

28th August 2024

Acknowledgements

I would like to express immense gratitude to my academic supervisor Dr Zahra Rattray whose expertise in analytical characterisation of pharmaceuticals has been invaluable. I deeply appreciate all the support and encouragement she has given me in growing my confidence as a research scientist over the past three years. I would also like to thank my industrial supervisor and line manager Dr William Lewis at GSK for offering me the opportunity to carry out a doctorate at work and his support through this programme.

At GSK, I would like to acknowledge the downstream team in the Biopharm Process Research department for their continual check-ins with me and support. I'd also like to thank the various members of the wider department and Analytical Development who have helped with technical training, including Joanne Williams, Dr Holly Corrigan and Dr Robyn Emmins for DNA transfections, cell line guidance and subculture technique, and Dr Shradha Dattani, Dr Emily Hetherington, Ricky Casey, Dr Nicola Ford and Selina Rawal for support on analytical techniques. I would like to thank Vidhi Shah in the large molecule Discovery team for running of AC-SINS assays. For their guidance on *in silico* modelling, I would like to express gratitude to Dr Alan Lewis as well as experts from the Chemical Computing Group. I'd also like to extend a big thank you to Dr Aisling Roche, whose insightful discussions on mAb viscosity have been so helpful in validating just how complex viscosity is to study. I would like to acknowledge the GSK-Strathclyde collaborative programme directors and coordinators, Professor Billy Kerr, Dr Harry Kelly, Dr Laura Patterson and Laura West for this opportunity to carry out a doctorate at work.

It has been a pleasure to also get to know members into the Rattray Translational Pharmaceuticals lab group and have such productive conversations about our research projects. A big thank you also to my cohort Larissa, Lindsey and Claire, and other cohorts of PhD candidates at GSK for our regular tea breaks and support.

Finally, to my friends and my family who have put up with me droning on about viscosity for the past three years. Thank you immensely to Hum, to my sister Hannah and most of all to my Dad for your continued support, tracking me down all the way Boston to see me present, and your persistent encouragement. I dedicate this thesis to my Dad and also to my much missed Mum- thank you, I want to always make you proud.

Preface to Journal Format Thesis

This thesis is presented in journal format, containing four manuscripts with individual methodology, results, discussion and conclusions.

Contributions included in the thesis

All following publications had permission from respective journals for use in in thesis/dissertation works.

<https://www.elsevier.com/about/policies-and-standards/copyright>

<https://pubs.acs.org/pb-assets/acspubs/Migrated/dissertation-1632927826810.pdf>

Publications

Armstrong, G. B. *et al.* A framework for the biophysical screening of antibody mutations targeting solvent-accessible hydrophobic and electrostatic patches for enhanced viscosity profiles. *Computational and Structural Biotechnology Journal* **23**, 2345–2357 (2024). <https://doi.org/10.1016/j.csbj.2024.05.041>

Armstrong, G.B. *et al.* A first insight into the developability of an IgG3: A combined computational and experimental approach. *ACS Pharmacology and Translational Science*. (2024) <https://doi.org/10.1021/acscptsci.4c00271>

Pre-Prints

Armstrong, G. B., Roche, A., Lewis, W. & Rattray, Z. Reconciling predicted and measured viscosity parameters in high concentration antibody solutions. *ChemRxiv* (2024). doi:10.26434/chemrxiv-2024-vk935. *This content is a preprint and has not been peer-reviewed.*

Conference presentations

Sequence engineering of monoclonal antibodies to reduce the viscosity of high concentration formulations. **22nd November 2022, JPAG Pharmaceutical Analysis Research Awards and Careers Fair 2022, London, UK**

Sequence engineering to improve the syringeability of high concentration monoclonal antibody formulations. **16th August 2023, 15th Annual BioProcessing Summit 2023, Boston, US**

Sequence engineering to reduce the viscosity of high concentration mAb formulations. **11th October 2023, BioProNet 2023, GSK, Stevenage, UK**

Sequence engineering to improve the syringeability of high-concentration monoclonal antibody formulations. **6th September 2023, APS PharmSci 2023, Reading, UK**

The impact of single-point mutations and subclass on the viscosity of high concentration monoclonal antibody formulations **6th September 2024, APS PharmSci, Huddersfield, UK**

Conference posters

Sequence engineering of monoclonal antibodies to reduce the viscosity of high concentration formulations: an *in silico* approach to viscosity predictions for IgG Fvs. **19th October 2022. 10th Year MIBio 2022 Stability of Biopharmaceuticals, Cambridge, UK**

Enhancing viscosity control in antibody formulations: A framework for the biophysical screening of mutations targeting solvent-accessible hydrophobic and electrostatic patches. **17th April 2024, Spring SciX, University of Strathclyde, Glasgow, UK**

List of Abbreviations

[η]	Intrinsic viscosity
AC-SINS	Affinity chromatography self interaction nano-spectroscopy
Ag	Antigen
aSEC	Analytical Size Exclusion Chromatography
BCR	B-Cell Receptor
CDRs	Complementarity-Determining Regions
CEX	Cation Exchange Chromatography
CHO	Chinese Hamster Ovary
cIEF	Capillary Isoelectric Focussing
Cmv	Cytomegalovirus
CQA	Critical quality attribute
DLS	Dynamic Light Scattering
DSF	Differential Scanning Fluorimetry
ELISA	Enzyme-linked immunosorbent assay
Fab	Fragment antigen-binding region
Fv	Variable fragment
Fc	Frgament crystalisable/ constant region
GS	Glutamine Synthetase
HCP	Host cell protein
HMwS	High molecular weight species
i.v.	Intravenous
Ig	Immunoglobulin
k_a	Association rate
k_D	Self-interaction or diffusion-interaction parameter
k_d	Dissociation rate
KD	Equilibrium constant or affinity
k_H	Huggins coefficient
k_k	Kraemer coefficient
(HP)LC	(High performance) Liquid chromatography
LMwS	Low molecular weight species
mAb	Monoclonal Antibody
MS	Mass Spectrometry
PTM	Post translational modification
RSA	Reversible self-association
s.c.	Subcutaneous
scFv	Single-chained Fv
SPR	Surface Plasmon Resonance
T_{agg}	Temperature at aggregation onset
TFF	Tangential Flow Filtration

T_m	Unfolding/ melting temperature
UF/DF	Ultra-filtration/ Diafiltration
VH	Variable domain of heavy chain
VL	Variable domain of light chain
ζ	Zeta potential

Table of Contents

Acknowledgements.....	3
Preface to Journal Format Thesis	4
List of Abbreviations.....	6
Table of Contents.....	8
List of figures	13
List of tables	16
Abstract	18
1. Introduction.....	20
1.1. The growth of therapeutic monoclonal antibodies (mAbs).....	20
1.2. Discovery and development pipelines for therapeutic mAbs	20
1.2.1 Early-phase discovery	20
1.2.2 Early-phase upstream development	24
1.2.3 Early-phase downstream development.....	25
1.2.4 Developability of mAbs	26
1.3. Subcutaneous administration of biologics	44
1.4. Mitigating high viscosity risks.....	47
1.4.1 Device design.....	47
1.4.2 Formulation optimisation.....	47
1.4.3 Sequence engineering.....	48
1.5. Aims and Objectives.....	55
2. Surface patch directed design and biophysical analysis of viscosity-reducing single point mutations in high-concentration monoclonal antibody formulations.....	57
2.1. Abstract	57
2.2. Introduction.....	57
2.3. Aims	59

2.4.	Materials.....	60
2.5.	Methods.....	62
2.5.1	Computational methods.....	62
2.5.2	Protein Expression and Purification.	64
2.5.3	Biophysical analysis of the anti-IL-8 mAb panel.....	65
2.6.	Results	71
2.6.1	Generation of the anti-IL-8 mutant panel.....	71
2.6.2	Biophysical Parameters of the Expressed Mutant Panel.....	76
2.7.	Discussion	87
2.8.	Conclusions.....	92
3.	Assessing the manufacturability and critical quality attribute profiles of anti-IL-8 mutant variants	93
3.1.	Abstract	93
3.2.	Introduction.....	93
3.3.	Aims	94
3.4.	Materials.....	94
3.5.	Methods.....	94
3.5.1	Computational methods.....	94
3.5.2	Protein expression and purification.....	95
3.5.3	Biophysical characterisation	97
3.6.	Results	98
3.6.1	Cell growth, viability and anti-IL-8 mAb expression.....	98
3.6.2	Downstream purification polishing steps.....	101
3.6.3	Theoretical gel point, opacity and liquid-liquid phase separation of anti-IL-8 mutants.....	102
3.6.4	Post-translational modifications of the anti-IL-8 mutants.....	104
3.7.	Discussion	106

3.8.	Conclusions.....	110
4.	A first insight into the developability of IgG3: A combined computational and experimental approach	111
4.1.	Abstract.....	111
4.2.	Introduction.....	111
4.3.	Aims	114
4.4.	Materials.....	114
4.5.	Methods.....	114
4.5.1	Computational methods.....	114
4.5.2	Generation and biophysical analysis of anti-IL-8 IgG1 and IgG3.....	116
4.6.	Results	122
4.6.1	Patch analysis and homology constructs of anti-IL-8 IgG1 and IgG3 122	
4.6.2	Biophysical Parameters of anti-IL-8 IgG1 and IgG3	123
4.7.	Discussion	134
4.8.	Conclusions.....	138
5.	Reconciling predicted and measured viscosity parameters for high concentration monoclonal antibody formulations.....	140
5.1.	Abstract	140
5.2.	Introduction.....	140
5.3.	Aims	142
5.4.	Materials.....	142
5.5.	Methods.....	142
5.5.1	Computational methods.....	142
5.5.2	Protein expression and purification.....	145
5.5.3	Viscosity measurement.....	145
5.6.	Results	151

5.6.1	Viscosity profile fitting for the anti-IL-8 mAb mutant panel.....	151
5.6.2	Intrinsic viscosity, pair-wise interactions and hydrodynamic properties of the anti-IL-8 mAb mutant panel.....	157
5.6.3	Computational viscosity predictions of the anti-IL-8 mAb mutant panel 162	
5.6.4	Machine learning for viscosity prediction.....	167
5.6.5	Predictive modelling of the anti-IL-8 molecule panel	168
5.7.	Discussion	171
5.8.	Conclusion.....	176
6.	General discussion, conclusions and future work	178
6.1.	Thesis summary	178
6.2.	Future work	180
6.3.	Conclusion.....	182
7.	Appendix 1	183
7.1.	Computational design of anti-IL8 mutants.....	183
7.2.	Biophysical Characterisation of anti-IL8 mutant panel.....	198
7.3.	Molecular dynamics- an alternative mutagenesis strategy	204
8.	Appendix 2	210
8.1.	Free kappa light chain abundance	210
8.2.	Clearance of free kappa light chain via cation exchange chromatography 212	
8.3.	Gel point calculation for anti-IL-8 molecule panel.....	215
8.4.	Opacity/turbidity observed during concentration of anti-IL-8 molecules..	216
9.	Appendix 3	217
9.1.	Homology modelling of IgG3.....	217
9.2.	Biophysical Characterisation.....	224
9.2.1	Analysis of identity by mass spectrometry	224

9.2.2	Scattering intensity profiles from nano-differential scanning fluorimetry (nano-DSF) of anti-IL-8 IgG1 and IgG3.....	225
9.2.3	Diffusion coefficients from dynamic light scattering (DLS) for anti-IL-8 IgG1 and IgG3.....	226
9.2.4	Intrinsic viscosity and the Huggins coefficient for anti-IL-8 IgG1 and IgG3	226
10.	Appendix 4.....	228
10.1.	Molecular descriptors relevant to viscosity modelling	228
10.2.	Viscosity model fit parameters.....	229
10.3.	Determination of the Huggins and Kraemer Parameters	230
10.4.	Shape factors of anti-IL-8 molecule panel	237
10.5.	Cross-coreating hydrodynamic parameters to experimental viscosity	238
10.6.	Predicting viscosity from molecular descriptors	239
	Bibliography.....	248

List of figures

Figure 1.1 <i>In vitro</i> antibody discovery platform historical timeline. Created in BioRender.com	21
Figure 1.2 Generic affinity screening cycle in phage display	22
Figure 1.3 Summary illustration for single B-cell cloning techniques	23
Figure 1.4 Early-phase upstream process workflow from DNA transfection to bioreactor production process	25
Figure 1.5 Downstream process workflow in early phase development for mAb drug substances	26
Figure 1.6 Critical Quality Attributes screened to profile mAb developability	27
Figure 1.7 Three-dimensional structure of IgG1 (PDB ID 1IGY)	28
Figure 1.8 Depiction of principles of the Stokes-Einstein equation describing the forces present on a colloidal hard sphere under laminar flow	36
Figure 1.9 Different types of viscosity arise from rheology method used	39
Figure 1.10 Primary, secondary, and tertiary electroviscous effects and surface-charge driven pair wise interactions	42
Figure 2.1 Homology models of anti-IL-8	72
Figure 2.2 Patch analysis of mutant candidates	74
Figure 2.3 Negative and positive patch disrupting mutants show a strong correlation between predicted and measured pI	78
Figure 2.4 Hydrophobic Interaction Chromatography (HIC) of WT and mutant anti-IL-8 panel and correlation with predicted hydrophobicity molecular descriptors	80
Figure 2.5 WT and mutant propensity for self-association measured with AC-SINS and self-interaction parameter (k_D), categorised by mutation location, and mutation strategy	82
Figure 2.6 Anti-IL-8 mutant panel viscosity correlation heatmap	84
Figure 2.7 Ranking matrices for the anti-IL-8 mutant panel	91
Figure 3.1 Process unit operations for expression and purification of anti-IL-8 mAb molecules	95
Figure 3.2 Viable cell count, cell viability and mAb titre over 15 day fed-batch production process	100
Figure 3.3 Use of difference in predicted net charge of full IgG to kLC in determining exclusive monomer binding and elution at specific pH	101
Figure 3.4 Gelation concentrations (C_{gel}) estimated from extrapolating flux through small-scale tangential flow filters during UFDF	103
Figure 3.5 Reversible temperature-dependent phase separation with the K42E mutant	104
Figure 4.1 Homology constructs of the full IgG1 and IgG3 molecules. a, the full IgG1 structure	123
Figure 4.2 Reduced stability after freeze-thaw cycling and at 25 °C over 57 days for IgG3 compared to IgG1	125
Figure 4.3 IgG3 shows reduced conformational stability compared to IgG1 at high concentrations from nano-DSF unfolding temperatures	126
Figure 4.4 Different surface potential profiles were obtained for anti-IL-8 IgG1 and IgG3 predictions, which yielded comparable measured isoelectric points	127
Figure 4.5 Comparing charge differences to <i>in silico</i> charge descriptors for anti-IL-8 IgG1 (grey) and IgG3 (red)	128
Figure 4.6 IgG3 exhibits a lower degree of hydrophobicity in comparison to IgG1, contradicting computed solvent accessible hydrophobic area data	130
Figure 4.7 Colloidal interaction data from dynamic light scattering (DLS) measurements and Affinity-Chromatography Self-Interaction Nanospectroscopy (AC-SINS) for anti-IL-8 IgG1 and IgG3	131

Figure 4.8 IgG3 demonstrated higher apparent viscosity (η) than IgG1 at high concentrations.	133
Figure 5.1 Anti-IL-8 IgG framework mutant concentration-viscosity profiles fitted with four models.....	153
Figure 5.2 Anti-IL-8 CDR mutant concentration-viscosity profiles were fitted with four models.	154
Figure 5.3 Negative correlation between average intrinsic viscosity and Huggins and Kraemer coefficients, but no correlation with anti-IL-8 mAb charge.	158
Figure 5.4 Hydrodynamic diameter from intrinsic viscosity versus dynamic light scattering and effective volume fraction of anti-IL-8 molecules.	160
Figure 5.5 Theoretical viscosities for anti-IL-8 molecules derived from Generalised Stokes Einstein equation.....	162
Figure 5.6 Predicted viscosity (η) scores from three regression models.	164
Figure 5.7 Experimental parameters and sequence-based molecular descriptors, categorised according to Kingsbury <i>et al.</i> ¹⁷³ for anti-IL-8 IgGs, categorised by mutation strategy.	166
Figure 5.8 Lai ¹⁵¹ decision tree classed all anti-IL-8 mAb molecules to have high viscosity at 150 mg/mL.	167
Figure 5.9 Negative patch targeting mutants predicted to have lower viscosity using the Makowski decision tree. ¹⁵³	168
Figure 5.10 Viscosity regression model from an anti-IL-8 mAb panel lacked predictive ability with in-house test molecules.	170
Figure 7.1 The Therapeutic Antibody Profiler (TAP) tool computed four structural attributes for anti-IL-8 candidate mutants.....	194
Figure 7.2 Two-dimensional patch maps of expressed mutants Fv homology constructs. .	195
Figure 7.3 Peptide map coverage for D70N light chain. Possible modification site at N70 flagged (light green).	199
Figure 7.4 Hydrophobic interaction chromatography chromatograms for anti-IL-8 mutants.	200
Figure 7.5 Thermal unfolding profiles for all anti-IL-8 mutant panel and wild-type.	202
Figure 7.6 Diffusion coefficients for each expressed anti-IL-8 mutant and WT over a dilute concentration range (1-20 mg/mL), fitted with linear regression.....	203
Figure 7.7 Number of arginine contacts summed per residue for the light chain Fv (A) and heavy chain Fv (B), ordered by residue number.	205
Figure 7.8 Summed interaction energies for each residue of the light chain Fv (A) and heavy chain Fv (B).	206
Figure 7.9 Average interaction energies per interaction type for all contacts assessed in the trajectory (variable and constant regions considered).	207
Figure 7.10 Mean hydrodynamic diameters (Z-ave) and polydispersity indices for anti-IL-8 WT and mutant panel.	208
Figure 7.11 The second virial coefficient, B_{22} (mL/nmol/g ²) for anti-IL-8 molecules.	209
Figure 8.1 A high abundance of free kappa light chain (kLC) was observed in the Protein L eluates of anti-IL-8 molecules.	211
Figure 8.2: Mean % low molecular weight species from protein L eluates per anti-IL8 IgG1 molecule.	214
Figure 8.3 Gel points for anti-IL-8 mAb molecules were calculated from logarithmic extrapolation of flux during the first concentration phase (UF1) in small-scale TFF. Retentate concentrations were estimated from retentate vessel weight changes during UF1. Linear extrapolation of concentrations were used to calculate the concentration at which the flux reached zero.	215
Figure 8.4: Opacity observed during TFF for all anti-IL-8 molecules.....	216
Figure 9.1 Mean scattering intensity for anti-IL-8 IgG1 (black) and IgG3 (red) differential scanning fluorimetry experiments.	225

Figure 9.2 Diffusion coefficients measured from dynamic light scattering (DLS) experiments.	226
Figure 9.3 a, Relative (η_{rel}) and b, reduced (η_{red}) viscosity for anti-IL-8 IgG1 (grey) and IgG3 (red) over concentration (g/mL) in the dilute regime.	227
Figure 10.1 Individual linear regression plots of reduced viscosity (η_{sp}/c) versus concentration profiles used to derive the Huggins coefficient for the anti-IL-8 panel.	230
Figure 10.2 Individual linear regression plots of natural log of relative viscosity (η_{rel}/C) versus concentration profiles used to derive the Kraemer coefficient for the anti-IL-8 panel.	231
Figure 10.3 Reduced viscosity (η_{red}) (cP) over concentration (mg/mL) plots for anti-IL-8 mutants with highest concentration data points removed.	232
Figure 10.4 Individual second order polynomial (quadratic) plots of relative viscosity versus concentration profiles used to derive $[\eta]_v$ for the anti-IL-8 mutant panel.	233
Figure 10.5 Correlation between intrinsic viscosities derived from linear regression ($[\eta]_{avg}$) and polynomial non-linear fitting ($[\eta]_v$).	234
Figure 10.6 Correlations of intrinsic viscosity from HYDROPRO program to experimental intrinsic viscosity ($[\eta]_{avg}$).	236
Figure 10.7 Poor correlations were observed between the Ross-Minton fit derived intrinsic viscosity versus the average intrinsic viscosity ($[\eta]_{avg}$).	236
Figure 10.8 Shape factors of the anti-IL-8 mAb panel.	237
Figure 10.9 a, Correlations and b, variable importance plot (VIP) of averaged knee of viscosity profiles for anti-IL-8 panel to computational molecular descriptors.	246

List of tables

Table 1.1 Notable literature on sequence engineering studies to modify viscosity of high concentration mAb formulations.	49
Table 2 Materials for anti-IL-8 mAb expression, purification and analysis	60
Table 3.1 Liability antibody profiler (LAP) tool was used to predict PTMs for anti-IL-8 mutant Fv sequences.	105
Table 4.1 Antigen (IL-8) binding kinetics for IgG1 and IgG3 assessed <i>via</i> SPR.	124
Table 4.2 Intrinsic viscosity and Huggins coefficient for anti-IL-8 IgG1 and IgG3.	134
Table 5.1 Viscosity model equations used in this work.	146
Table 5.2 Interpolated/extrapolated viscosity values at 180 mg/mL.	156
Table 6.1 Alternative residues to mutate proposed from molecular dynamics of anti-IL8 IgG1 wild-type.	182
Table 7.1 Top-scoring residues contributing to hydrophobic (res_hyd), positive (res_pos) and negative (res_neg) patches.	183
Table 7.2 Patch numbers and corresponding area coverage for candidate mutant Fv homology constructs.	185
Table 7.3 Physicochemical descriptors computed for WT and mutant homology models that have been used in previous studies to predict viscosity.	187
Table 7.4 Charge-based physicochemical descriptors computed for each anti-IL-8 mutant Fv homology construct.	190
Table 7.5 Hydrophobicity-based physicochemical molecular descriptors and TANGO aggregation propensity scores of anti-IL-8 mutant variants. Dipole and ionic to hydrophobicity ratios are also reported.	192
Table 7.6 Quantitation of specific modified patch areas and energy changes for expressed mutants Fv homology constructs.	196
Table 7.7 Top and bottom scoring anti-IL-8 mutants progressed to experimental characterisation based on min-max normalisation.	197
Table 7.8 Verification of anti-IL-8 WT and mutant variant identity by peptide fragmentations.	198
Table 7.9 Monomeric purity of all anti-IL-8 molecules (N=3).	199
Table 7.10 Biacore analysis of binding kinetics. Wild-type and mutant anti-IL-8 binding to an IL-8 antigen was assessed with SPR.	201
Table 7.11 Details for segments specified in molecular dynamics simulation set-up.	204
Table 8.1 Cation exchange chromatography in bind-elute mode was deployed, screening at multiple pH conditions, for clearance of free kappa light chain (kLC).	212
Table 9.1 IgG3 hinge was designed based off copied sequence of mouse IgG2A hinge (pdb 1IGT).	217
Table 9.2 Hinge homology models for anti-IL-8 IgG3.	218
Table 9.3 Additional patch and physicochemical descriptors applied to anti-IL-8 IgG1 and IgG3 homology constructs.	221
Table 9.4 Analysis of positive, negative and hydrophobic surface patches for anti-IL-8 IgG1 and IgG3 homology constructs.	222
Table 9.5 Analysis of positive, negative and hydrophobic surface patches for the hinge regions of anti-IL-8 IgG1 and IgG3 homology constructs.	222
Table 9.6 Sequence and structure based descriptors computed for anti-IL-8 IgG1 and IgG3 homology constructs.	223
Table 9.7 Verification of anti-IL-8 IgG1 and IgG3 identity by peptide fragmentations.	224
Table 10.1 In silico molecular descriptors for anti-IL-8 molecules computed from Fv homology constructs.	228
Table 10.2 Parameters derived from four viscosity model fits applied to concentration-viscosity profiles for mutant variants and WT molecule.	229

Table 10.3 Mean intrinsic viscosity, $[\eta]_{\text{avg}}$, k_{exp} , Huggins and Kraemer coefficients determined for anti-IL-8 mAbs.....	235
Table 10.4 Cross-correlation matrix for hydrodynamic parameters and high concentration viscosity (η) for anti-IL-8 mAb panel.	238
Table 10.5 Ranking of anti-IL-8 molecules, in increasing viscosity order, according to Li, Sharma and Tomar predictions against experimental viscosity fitted across four models at 150 and 180 mg/mL.	239
Table 10.6 Viscosity values from Ross-Minton fitting at 120 , 150 and 180 mg/mL with high-concentration and ultra-high-concentration data.	240
Table 10.7 Confusion matrix demonstrating number of molecules with predicted low or high viscosity from use of ensemble charge (ens_charge).	241
Table 10.8 Confusion matrices of viscosity classification of anti-IL-8 molecules from Lai <i>et al.</i> decision tree ¹⁵¹ versus experimental viscosity data.	242
Table 10.9 Confusion matrix of viscosity classification of anti-IL-8 molecules from Makowski <i>et al.</i> decision tree ¹⁵³ versus experimental viscosity data.	244
Table 10.10 Molecular descriptors from four in-house proprietary mAbs were used to test regression model developed from anti-IL-8 panel.	247

Abstract

The developability of therapeutic monoclonal antibodies (mAbs) is a growing field of research poised to increase the probability of successful clinical translation for early-phase mAb candidates. Developability assessments typically entail high-throughput, low volume biophysical assays with parallel *in silico* sequence and structure based predictions to scope manufacturing, safety and efficacy risks. These include colloidal and conformational stability, and solution viscosity, which impact formulation shelf-life, immunogenicity, and manufacturability risks. High viscosity presents challenges with increased filtration pressure and reduced recovery during processing steps, with implications for vial filling during manufacture, and injection failure during administration. The latter is a growing concern with the move to patient self-administration using subcutaneous devices for improved patient autonomy and adherence. The dose volume limitations in autoinjector device design and high dosing requirements for mAb potency further complicates viscosity associated risks in mAb solutions.

In this thesis, the impact of single-point mutations introduced in IgG1 variable regions, and different mAb subclasses on viscosity and other biophysical developability properties was investigated.

Chapter 2 investigated the use of computational molecular descriptors derived from homology constructs to engineer mutants and the role of solvent accessible surface potential in promoting mAb self-interactions was assessed. Mutations with significant reductions in hydrophobicity resulted in lower solution viscosity, and a lack of correlation with *in silico* descriptors demonstrate the need for case-by-case evaluation of mAbs.

Whilst many studies explore the design of mutants to enhance viscosity, few demonstrate the impacts of these mutations on manufacturing process and critical quality attributes. Chapter 3 explored the manufacturability of the single-point Fv mutants, assessing upstream and downstream process observations as well as phase behaviour and process-related impurities. Significant modifications on mAb expression, required chromatography conditions, phase stability and post-translational modifications were observed and were mutation site-specific.

Chapter 4 presented an insight into the reduced developability of an IgG3 relative to IgG1, with comparisons to *in silico* descriptors. This chapter targeted the knowledge gap in understanding the biophysical behaviour of the IgG3 subclass which holds unique therapeutic potential. The results in this chapter also demonstrate the impact of the constant domain sequence and structure on interactions governing viscosity. Overall IgG3 showed reduced developability, with increased viscosity, compared to the Fv-matched IgG1 ortholog assessed.

Finally, the use of viscosity models in fitting and predicting formulation behaviour was evaluated in chapter 5. This chapter expanded upon interpretation limits of viscosity with regards to model-fit equation used and the concentration-dependence of viscosity, highlighting changes in contributing underlying mechanisms with increased molecular crowding. While low-concentration hydrodynamic parameters provided insights into such mechanisms, they poorly correlated with ultra-high concentration viscosity. Furthermore, the lack of generalisability of predictive models explored in this chapter highlights the necessity for machine-learning modelling to incorporate larger, diverse datasets for robust and accurate viscosity predictions of high concentration mAb formulations.

Overall, this thesis has provided a framework for the combined computational and experimental assessment of the biophysical behaviour of mAbs in high concentration formulations. Mutants designed from targeting computed surface patches were ineffective in reducing viscosity in the dose relevant concentration regime, so future works include combining mutations, exploring mechanistic contributions to viscosity further and use of machine-learning models for directed mutagenesis.

1. Introduction

1.1. The growth of therapeutic monoclonal antibodies (mAbs)

Therapeutic monoclonal antibodies (mAbs) have consistently dominated the biopharmaceutical market for > 30 years¹, with 165 mAbs approved or under regulatory evaluation in 2024.² The benefits of increased specificity to key biological targets in chronic diseases- such as cancer and respiratory conditions- combined with reduced adverse effects in comparison to small molecule therapies, has propelled the development of novel mAbs. Furthermore, the urgency for safe and effective immune-targeting treatments during the COVID-19 pandemic, further accelerated development timelines from DNA transfection to Investigational New Drug (IND) filing.³ Technologies enabling accelerated process development have spanned early-phase discovery with molecular design, lead optimisation and high-throughput 'developability' screening, through to pre-clinical development with cell line, upstream and downstream process improvements.

1.2. Discovery and development pipelines for therapeutic mAbs

1.2.1 Early-phase discovery

The discovery pipeline for mAbs has evolved considerably over the past 50 years (Figure 1.1).

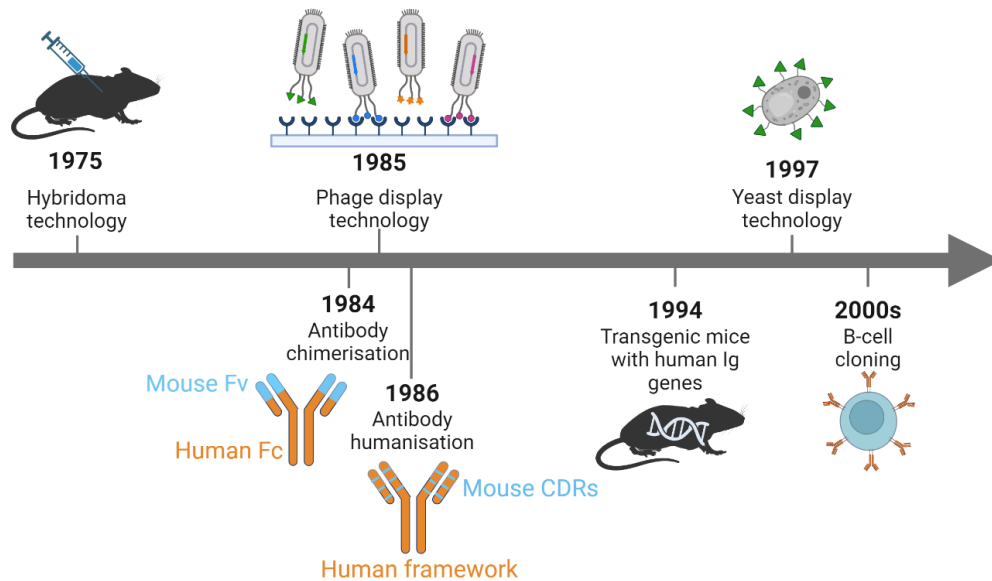


Figure 1.1 *In vitro* antibody discovery platform historical timeline.

Created in BioRender.com

Traditional techniques include immunising mice with target antigens to produce B cells, which are then extracted and fused with immortal myeloma cells to create antibody-producing **hybridoma cells**. Due to the human anti-mouse (HAMA) responses, **chimeric** mAbs were developed, whereby the variable region of the mouse antibody is combined with the constant region of a human antibody. This recombinant technology was expanded with humanised antibodies by transplanting the mouse Complementarity-Determining Regions (CDRs) into human framework variable regions, with affinity-preserving mutations. Subsequently, **transgenic mice** emerged as an approach to produce partially or fully human antibodies with the benefits of *in vivo* somatic hypermutation and antigen selection in the germinal centre (affinity maturation) and no requirement for humanisation.⁴

Phage display technology was also developed where synthetic human antibody variable region genes were extracted from human B cells, amplified, and incorporated into a filamentous bacteriophage that displays the expressed single chain variable fragment (scFv). These are amplified in *E. coli* and the bacteriophages are screened for their affinity to a target antigen, ranking the effect of their phenotypic differences. Large libraries of bacteriophages are screened in iterative antigen selection cycles (biopanning) to identify antibodies with a strong affinity for the target and potential biological activity (**Figure 1.2**).⁵

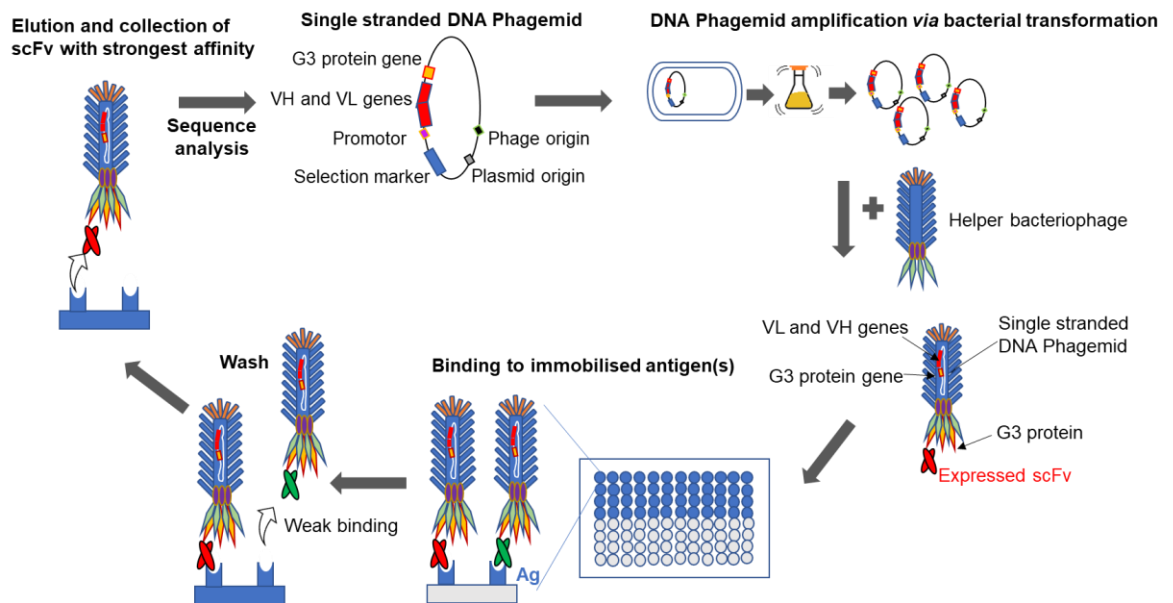


Figure 1.2 Generic affinity screening cycle in phage display.

Single strand DNA phagemids are transformed into bacterial cells, amplified, and helper bacteriophages are introduced.

Unlike bacteriophage libraries, **yeast display** systems offer the advantage of expressing proteins with post-translational modifications (PTMs) such as glycosylation, deamidation and oxidation, which are more representative of *in vivo* antibody expression, impacting antibody stability and function.⁶ Variant triaging is performed with magnetic-activated cell sorting, or staining yeast cells with fluorescent-labelled antigen for fluorescence-activated cell sorting (FACS) based on relative binding affinity.⁷ This expression platform has been used in directed evolution to achieve femtomolar affinity.⁷

Finally, **single B cell cloning** has become a popular mAb discovery platform (**Figure 1.3**). This involves sorting of B cells from peripheral blood mononuclear cell (PBMC) human samples using flow cytometry or microfluidics-based techniques.⁸ B cell mRNA is extracted, amplified and sequenced *via* gene-specific single cell Polymerase Chain Reaction (PCR). The sequence is then inserted into a vector, expressed, and assessed for functional activity.⁹ This technique eliminates HAMA response risks that are still observed even with humanized antibodies¹⁰, and has the advantage of *in vivo* affinity maturation with increased target specificity and reduced off-target binding to host cell proteins.⁸

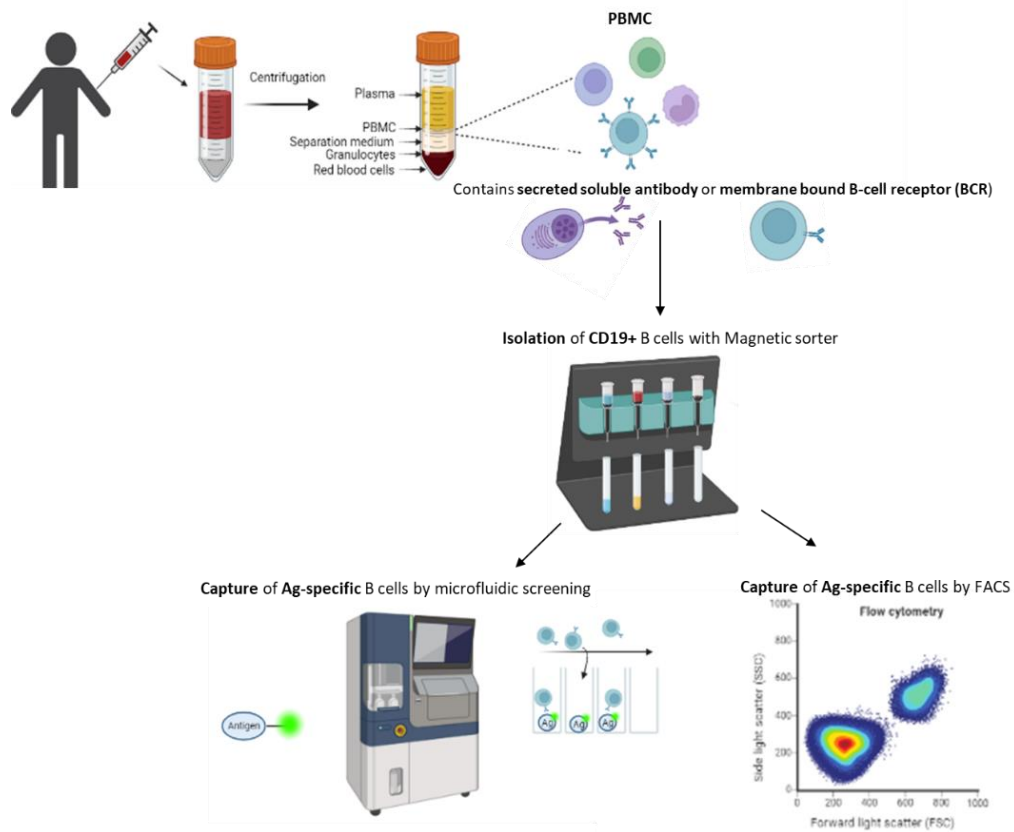


Figure 1.3 Summary illustration for single B-cell cloning techniques.

Created with Biorender.com

Surface-displayed antibodies commonly undergo **directed evolution** (guided affinity maturation), with the goal of increasing affinity, avidity and fragment crystallizable region (Fc) functionality.¹¹ The increased diversity of variants resulting from guided affinity maturation (up to 10^{14} clones compared with a maximum of 10^{11} clones from natural maturation)¹² add to synthetic genetic libraries, to maximise the probability of identifying enhanced antibody sequences with desired selectivity, potency and with unique paratopes against novel epitopes. However, the deviation in sequence homology from such guided maturation to the native sequence has resulted in a developability gap, necessitating the conservation of residues that are critical to structural integrity and physicochemical stability.¹³ This has driven research into next-generation sequencing, epitope mapping and *in silico* mutagenesis with affinity and developability predictions.^{13–15}

1.2.2 Early-phase upstream development

For manufacturing purposes, recombinant mAbs are typically expressed by **transfecting mammalian cell lines**, such as human embryonic kidney 293T (HEK-293T) or Chinese hamster ovary (CHO) cells, with antibody genes from naïve or synthetic libraries, and a selection marker (**Figure 1.4**).¹⁶ Post-translational processing in the mammalian platform result in natively glycosylated antibodies with reduced misfolding risks.¹⁷ Successfully transfected polyclonal cells are monitored for their titre, growth rate and resultant cell lines are sorted to ensure monoclonality. Monoclonal cells are scaled up and transferred to upstream process development. The generational stability of these cell lines and product quality are evaluated, with promising cultures inoculated for production processes in either shake flasks or bioreactors.^{18,19} Various parameters such as basal media, amino acid feed content and regimen, temperature, pH and dissolved oxygen, mixing and shear stress are monitored to understand their impact on antibody product quality, and process efficiency.

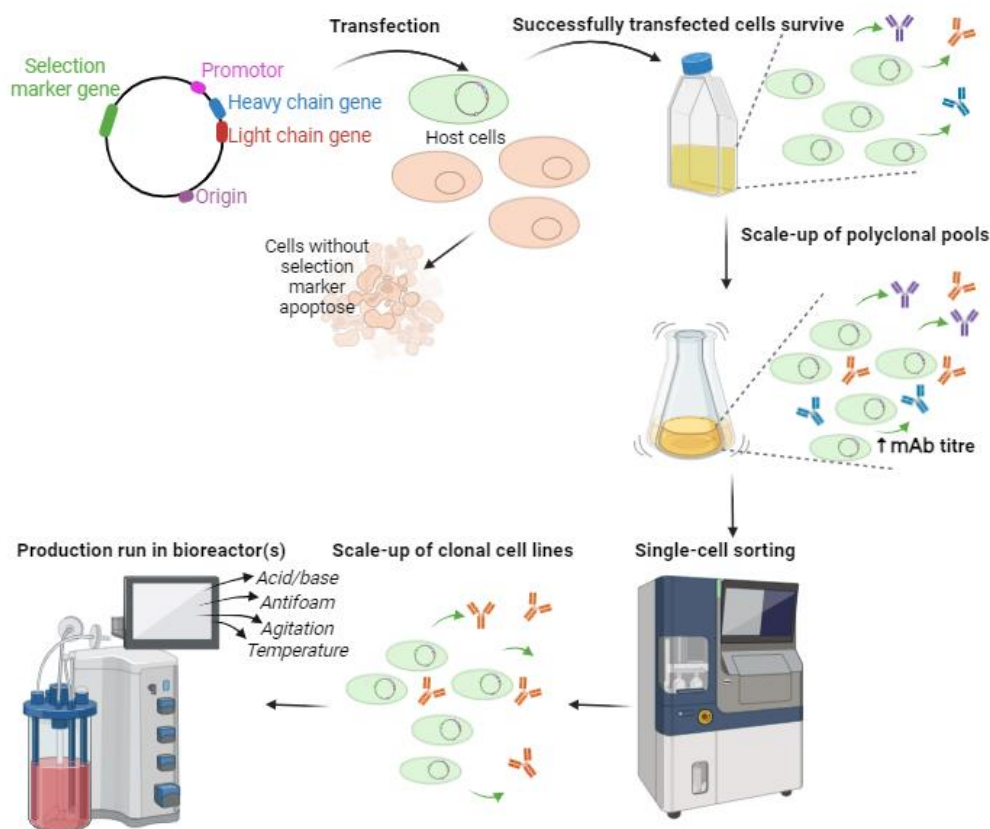


Figure 1.4 Early-phase upstream process workflow from DNA transfection to bioreactor production process.

Created with Biorender.com

1.2.3 Early-phase downstream development

Antibodies are harvested from culture expression medium and transferred for subsequent downstream process development. Here, the aim is to develop a robust and scalable purification process for clinical manufacturing.²⁰ Typically, antibodies are captured with an affinity chromatography technique²¹, which is followed by virus inactivation²² and polishing chromatography.^{23,24} The purified mAb is nanofiltered,^{21,25} concentrated and dialysed into formulation buffer *via* tangential flow filtration (TFF) or ultrafiltration/diafiltration (UF/DF).^{24,26}

Analytical techniques such as small-scale size exclusion chromatography (SEC),^{27,28} enzyme-linked immunosorbent assay (ELISA),^{29,30} capillary isoelectric focussing (cIEF)³¹, mass spectrometry (MS),³² and surface plasmon resonance (SPR)³³ are used to assess purity, host cell protein content, charge heterogeneity, N-glycan profiles, and antigen affinity, respectively. Product-specific method development and

complementary analytics are used to elucidate specific impurities to direct removal techniques (**Figure 1.5**).

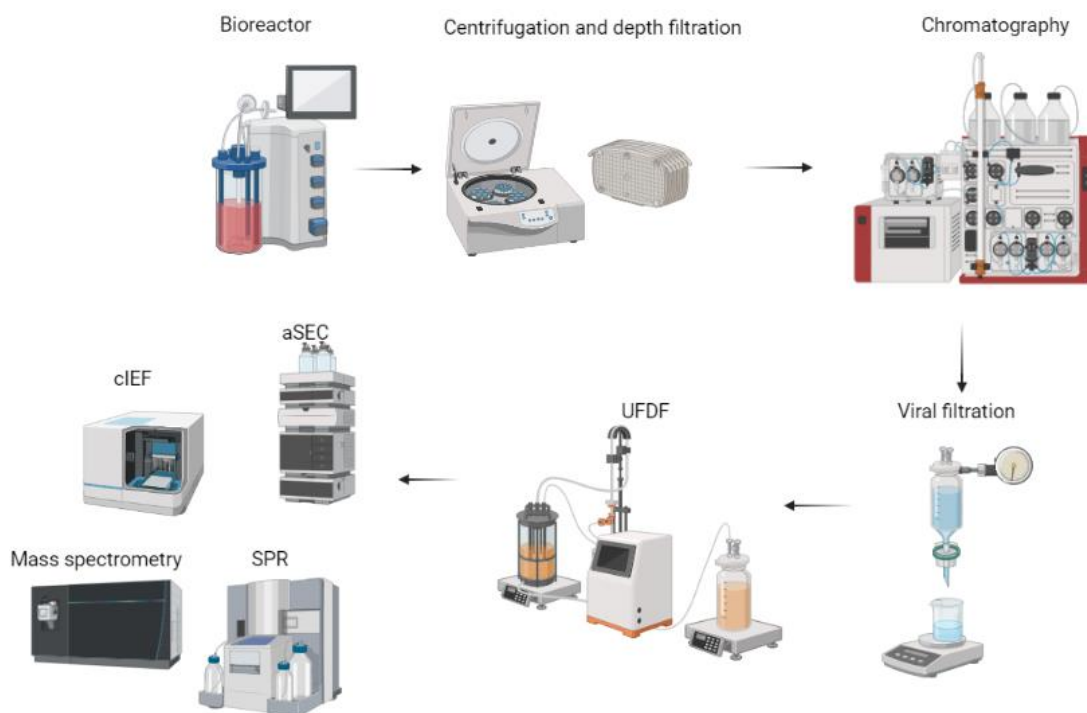


Figure 1.5 Downstream process workflow in early phase development for mAb drug substances.

Created with Biorender.com

1.2.4 Developability of mAbs

The term ‘developability’ refers to the probability of successful progression of a mAb from early-phase development through to clinical use.^{34,35} This involves assessing intrinsically linked critical quality attributes (CQAs) such as conformational and colloidal stability, post-translational modification/ chemical liabilities, immunogenicity, biological activity/functionality and manufacturability (**Figure 1.6**). Various analytics and *in silico* tools are used to aid mAb quality, safety and efficacy predictions.

This thesis focusses primarily on viscosity as one developability parameter, which is inherently related to other CQAs which are described briefly in this chapter.

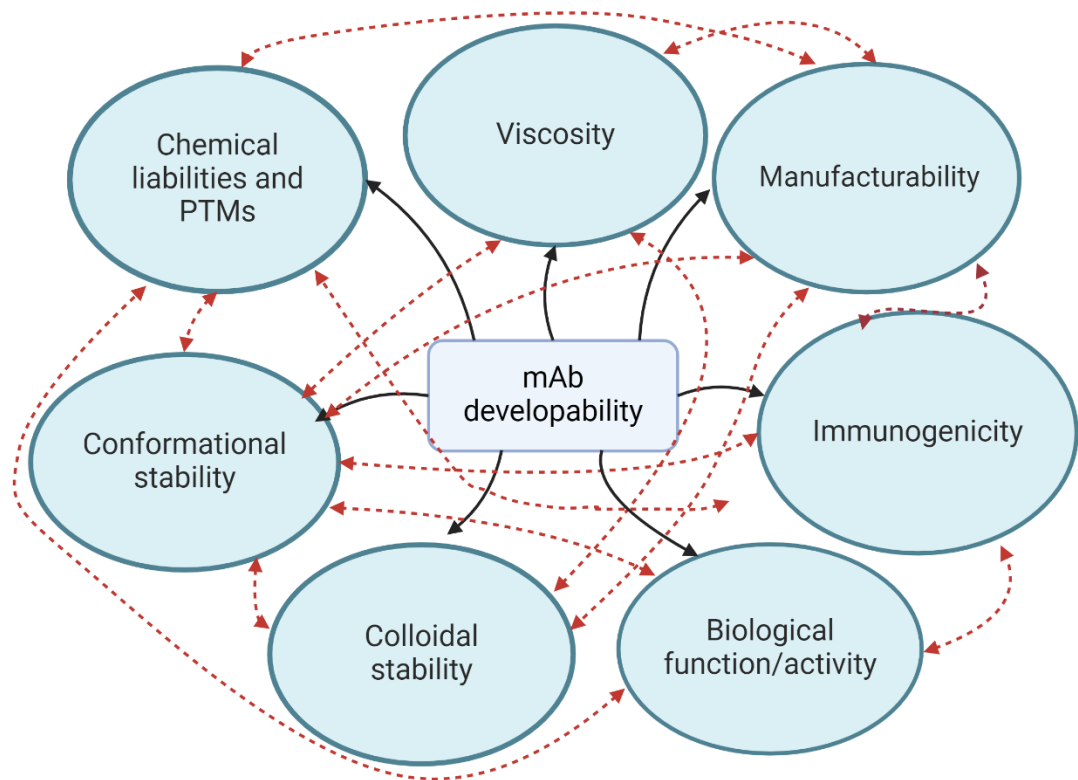


Figure 1.6 Critical Quality Attributes screened to profile mAb developability.

Red dotted arrows represent correlations and dependencies between CQAs. *Created with Biorender.com*

Antibody structure and function

Developability characterisation of mAbs relies on knowledge of sequence, structure and function to understand inherent molecular properties and the influence of manufacturing process on the integrity of mAbs. Antibodies are large (150 kDa) glycosylated macromolecules produced in the adaptive immune response by B-cells upon activation by T-helper cells in response to an antigen.^{36,37} They are typically described as ‘Y-shaped’ molecules with the variable fragment region (Fv) on the head of the antibody, which recognises and binds a specific antigen epitope. This binding can invoke an immunomodulatory response depending on the target antigen (e.g. inhibition of downstream signalling by targeting against cytokines for autoimmune conditions, or binding and inhibiting immune checkpoints that are upregulated in cancers to increase T-cell activation to tumours). The fragment crystallisable region,

or constant region, (Fc) on the tail of the antibody interacts with Fc receptors and other proteins to perform effector functions, such as antibody-dependent cellular cytotoxicity (ADCC), antibody-dependent cellular phagocytosis (ADCP) and complement-dependent cytotoxicity (CDC) (**Figure 1.7**).^{38,39}

There are five antibody isotypes; IgM, IgE, IgD, IgA and IgG in descending order of molecular weight (IgM forms a pentamer ~970 kDa),⁴⁰ which have different effector functions. Furthermore, IgG antibodies, the most abundant isotype in serum,⁴¹ are further categorised by subclass and allotype with IgG1, IgG2, IgG3 and IgG4 commonly used as therapeutic mAb scaffolds, possessing either kappa and lambda light chains. Despite 90% sequence homology, IgG subclasses have diversity in their structure and function, and *in vivo* stability.⁴² The choice of IgG subclass as well as molecular format for therapeutic mAb development depends on the clinical indication (pro-inflammatory or anti-inflammatory), target accessibility, desired plasma half-life and delivery strategy.^{42,43}

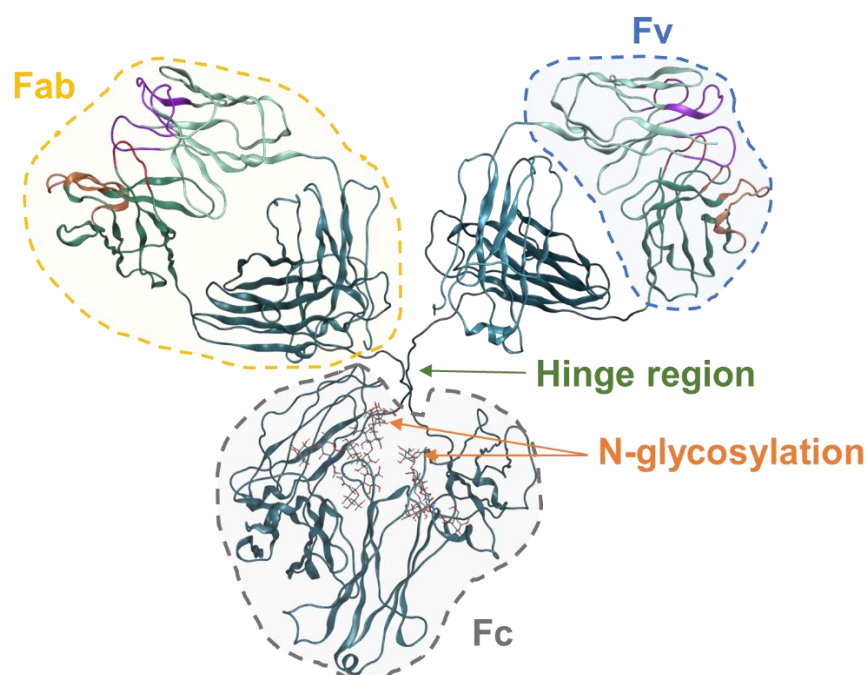


Figure 1.7 Three-dimensional structure of IgG1 (PDB ID 1IGY).

Constant region (teal), variable heavy chain (dark green) variable light chain (light green), heavy chain CDRs (red/orange) and light chain CDRs (purple). *Structure visualised and*

exported from Molecular Operating Environment software version 2020.0901 (Chemical Computing Group, Montreal, Canada).

Conformational stability

Unfolding propensity and structural stability of IgGs can be characterised by differential scanning calorimetry (DSC) and differential scanning fluorimetry (DSF) where unfolding temperatures from thermal denaturation are determined.⁴⁴ DSC provides apparent enthalpies for each unfolding temperature allowing for domain assignment in accordance with the energy required for the unfolding event to occur (endothermic process). For example, Fab unfolding results in the largest unfolding energy peak in comparison to constant heavy chain 2 and 3 (CH2 and CH3) domain unfolding.⁴⁵ Alternatively, DSF can use intrinsic fluorescence from tryptophan, tyrosine and phenylalanine amino acid residues. As with DSC, a thermal profile is acquired, highlighting temperatures at which unfolding events occur. However, the emergence of capillary based nano-DSF meets high-throughput requirements in early-phase discovery campaigns.⁴⁶ Alternatively, SYPRO Orange dye can also be used with DSF to mark hydrophobic regions, which are exposed during unfolding events.⁴⁷ Both DSF and DSC can assess reversibility of unfolding, providing mechanistic insights into phase behaviour/particulate formation or aggregation kinetics.^{48,49}

Opalescence from particulate formation and liquid-liquid phase separation (LLPS) are correlated with unfolding propensity with mAb aggregation.⁵⁰ Dynamic light-scattering (DLS), nephelometry and particle tracking analysis are often used for particle quantitation and sizing.^{51–53}

Hydrogen/deuterium exchange mass spectrometry (HDX-MS) is another technique used to define the dynamic higher-order structure of mAbs, with amide hydrogens being substituted with deuterium atoms. HDX-MS is used for identifying different protein states⁵⁴, epitope mapping⁵⁵ and is commonly paired with static but full-atomistic resolution techniques such as X-ray crystallography, cryo-transmission electron microscopy,⁵⁶ and nuclear magnetic resonance (NMR)⁵⁷. The apparent trade-off between the high structural resolution of these techniques *versus* the low throughput nature with protein-dependent method development requirements and cost is prohibitive to their routine use in early-phase mAb development.⁵⁸

Forced degradation studies are performed to assess the formation of high-molecular weight species (HMwS) amongst different mAb formulation compositions and temperature hold conditions. Analytical size-exclusion chromatography (aSEC) is used to quantify soluble aggregation and there are various modelling efforts to predict long term stability for shelf-life approximation.^{59–61}

Furthermore, *in silico* structural modelling has garnered attention with the emergence of molecular dynamics simulations on assumed homology antibody structures to decipher conformational flexibility, self-association and solute interactions. Different scales have been explored with either all-atom simulation or a coarse-grained modelling, where beads are assigned to antibody domains to reduce complexity and computational expense.^{62–66}

Molecular drivers for loss of higher order protein structure are often interrelated with hydrodynamic and colloidal properties of the molecule, such as self-association propensity and surface charge and hydrophobicity anisotropy.

Colloidal stability

For decades proteins have been modelled based on colloidal assumptions; *i.e.*, as charged-hard spheres that are heterogenous in solution, and exhibiting the Tyndall effect (light scattering from particles) and Brownian motion (random diffusion of particles in suspension).⁶⁷ The Derjaguin-Landau-Verwey-Overbeek (DLVO) theory describes the colloidal stability between charged particles, which is expressed as the sum of attractive van der Waals plus the electrostatic repulsion from the electric double layer (EDL).⁶⁸ The EDL consists of two layers of counterions surrounding the charged particle; the Stern layer (the more condensed inner layer of ordered ions) and the diffuse layer (the larger and less ordered layer of ions).⁶⁹

The charge present at the 'slipping plane', the interface between the Stern and diffuse layers, is the zeta potential (ζ) and is frequently characterised to understand local surface charge of molecules *via* electrophoretic light scattering (ELS).⁷⁰ A more positive ζ is hypothesised to indicate more inter-particle repulsion and therefore increased colloidal stability.^{71,72} Furthermore, the isoelectric point (pI) of a mAb can be derived from screening the sample across a pH range of the dispersant buffer to identify where electrophoretic mobility is zero in the presence of an applied electrical field.⁷³ Discrepancies in pI characterised by ELS and alternative characterisation methods, such as capillary isoelectric focussing (cIEF) and cation exchange

chromatography (CEX), have been previously observed due to hypothesised preferential anion binding to the protein surface in ζ measurements.⁷⁴

ζ (V) is given by the Henry equation:⁷⁵

$$\zeta = \frac{3\eta\mu_p}{2\epsilon f(ka)}$$

1.1

Where η is dynamic viscosity of the solvent (Pa-s), μ_p electrophoretic mobility ($\mu\text{m}\cdot\text{cm}/\text{V}\cdot\text{s}$) measured from the frequency or Doppler shifts of the laser beam in accordance with changes in particle velocities, ϵ dielectric constant of dispersant (F/m), $f(ka)$ Henry's function which accounts for the impact of the EDL on flow towards electrodes (approximately 1.1 for mAbs⁷⁴).

Static light scattering (SLS) and dynamic light scattering (DLS) techniques can elucidate hydrodynamic properties such as molecular size, shape and sample polydispersity. Average hydrodynamic diameters (z-average values) are typically 10 nm⁷⁶ and systems are categorised as monodisperse if the polydispersity index (PDI) is <0.2.⁷⁷ Presence of HMwS such as multimers can be detected with an increase in the cumulant z-average and PDI.⁷⁸ Use of DLS to characterise absolute molecular size of mAbs is not recommended if the sample is not monodisperse as z-average values are skewed with intensity-weighted distributions.⁷⁹

Frequently, the second osmotic virial coefficient, B_{22} , and the self-interaction parameter, k_D , are used as surrogate measures of protein-protein interactions, with B_{22} indicating deviation from thermodynamic ideality, and k_D indicative of hydrodynamic contributions with the inclusion of frictional drag of the particle (Equation 1.2). Negative values for B_{22} and values of less than -15mL/g for k_D suggest attractive forces, with positive values indicating repulsive forces between particles.⁸⁰ These are calculated from the linear regression in Debye plots or diffusion coefficients over concentration range tested for B_{22} and k_D respectively, with recommendations of a maximum 20 mg/mL concentration.^{81,82} At higher mAb concentrations and in the presence of macromolecular crowding, higher order interactions occur, resulting in non-linear plots.⁸³

Whilst B_{22} and k_D are routinely correlated with self-association propensity⁸⁴⁻⁸⁷ weak correlations have been observed at high mAb concentrations and in the final drug product formulation.⁸⁸⁻⁹⁰

The relationship between k_D (mL/g) and B_{22} (mol mL/g²) can be represented as: ⁹¹

$$k_D = 2M_w B_{22} - kf - v$$

1.2

Where M_w is the protein molecular weight (g/mol), kf is the first-order concentration coefficient from the virial expansion of the frictional coefficient, v the partial specific volume of the solute (cm³/g). kf can be interchanged with k_s , the sedimentation coefficient (S), which can be derived from analytical ultra-centrifugation (AUC).⁹²

k_D and ζ have been used as complementary analytics to conformational stability studies, which have previously shown correlations to aggregation propensity.^{93,94} However, the reliance on these theoretical models with colloidal model assumptions of shape and charge has raised criticism of their isolated use in the biophysical characterisation of mAbs. Light scattering techniques do not account for mAb heterogeneous charge distributions, which means the degree of frequency shifts detected is dependent on the orientation of the molecules in solution.

There is a general consensus that aggregation arises from both conformational and colloidal instability and k_D and ζ are insufficient to comprehensively probe stability, particularly when exceeding ionic or concentration limits.^{74,95} Increasing molecular crowding at high concentrations, beyond thermodynamic idealities, can promote higher order interactions (self-association, aggregation or clustering) which in turn can affect both the calculated surface charge and diffusivity.⁹⁶

The use of orthogonal colloidal techniques such as sedimentation velocity analytical ultracentrifugation⁸⁷, affinity chromatography self-interaction nano-spectroscopy (AC-SINS)⁹⁷, charge stabilised nano-spectroscopy (CS-SINS)⁹⁸, and *in silico* predictions from molecular structure size and predicted charge⁹⁹ are commonplace in the developability screening of mAbs to increase model predictive power.

Post-translational modifications and process-related impurities

The choice of mAb expression platform has a significant impact on the number and type of post-translational modifications (PTMs). Eukaryotic hosts can generate PTMs that naturally occur in human cells, resulting in mAb micro-heterogeneity (> 400 variants).^{100,101} Native Fc-glycosylation is seen to not only be a necessity for conformational stability¹⁰² but also plays a crucial role in ADCP and CDC mAb potency¹⁰³ and *in vivo* half-life¹⁰⁴. Truncated glycoforms at the asparagine 297 in the

CH2 domain have more closed conformations resulting in reduced Fc gamma receptor (FcγR) binding form which would otherwise activate effector functions.¹⁰⁵ Furthermore, glycoforms with increased mannose content (yeast post-translational processing) are correlated with a reduction in plasma half-life.¹⁰⁴ Some specific glycoforms have also been correlated to immunogenicity risks.¹⁰⁶ Glycan and PTM heterogeneity can arise from both enzymatic (e.g. proteases like glycosidase and sialidase secreted from CHO cells) and chemical degradation (e.g. oxidation, deamidation and isomerisation).¹⁰⁷

Experimental analysis of PTMs primarily hinges on mass spectrometry (MS) techniques which have high specificity and sensitivity.¹⁰⁸ However, lack of throughput and requirement for specialised expertise with MS has expedited the development of computational tools to predict sequence motifs derived from PTM databases.¹⁰⁰ These predictive tools primarily use machine-learning methods to score liabilities from either or both sequence and structure based information. Many tools have aimed to incorporate data on all PTMs to get a holistic PTM risk profile for mAb developability for example, PTMProber,¹⁰⁹ PTMScape,¹¹⁰ MIND-S,¹¹¹ MusiteDeep,¹¹² and LAP.¹¹³

Beyond PTMs, host cell proteins (HCPs), resulting from co-purification with the mAb during downstream processing induce enzymatic degradation, are also correlated with increased aggregation and immunogenicity (e.g. phospholipase B-like 2, annexin A5 and pyruvate kinase).^{114,115} Immunogenicity is characterised with *in vitro* immune cell assays (e.g. MHC associated peptide proteomics), or more immune-relevant animal models.^{116,117} Assessment of such process-related impurities and immunogenicity is beyond the scope of this thesis, but is important to highlight as developability CQAs.

Manufacturability

The feasibility of manufacturing a mAb at scale is intrinsically linked with developability parameters such as phase behaviour and thermal stability, which require rigorous assessment under industrially relevant conditions. pH and temperature hold conditions between unit operations, materials used, molecular interfacial stability, and shear stress from filtration and chromatography can define the manufacturability of a mAb. Furthermore, there are ongoing efforts to maximise upstream and downstream process efficiency in early phase development, focussing on improving viable cell densities, mAb expression titres, yield and product quality.

^{118–121} The optimised processes are then transferred for toxicology studies for late phase development before first-in-human trials.

Conformational and chemical stability assessment of process intermediates from unprocessed bulk culture to affinity eluate through to final drug substance enable thresholds to be set for in-process hold times.¹²²

Moreover, non-specific interfacial adsorption of mAb molecules onto process materials (e.g., silicone oil- prefilled syringes) or at the air/water interface (resulting in high surface tension) have been extensively studied with molecular dynamics simulations.^{123–126} Addition of surfactants (e.g., polysorbate 80)^{124,125} or salts to disrupt electrostatic interactions⁵⁰ are used as mitigation strategies.

Mechanical shear stress during processing and shipping induces aggregation. Notably, this is observed with high agitation rates in bioreactors¹²⁷, and during tangential flow filtration (TFF)¹²⁸ (both frequently expose mAbs to air interfaces, encouraging adsorption).

mAb manufacturability also hinges on its viscosity, which can lead to high transmembrane pressures, reduction in flux and reduced recoveries during filtration processes.^{129,130}

Viscosity

Viscosity is the resistance of a fluid to flow or hydrodynamic forces, and mathematically with Newton's law of viscosity:^{131–133}

$$\eta = \frac{\tau}{\dot{\gamma}}$$

1.3

Where τ the shear stress (Pa) and $\dot{\gamma}$ the shear rate (s^{-1}).

The shear stress is defined as shear force over the shear area it is applied:

$$\tau = \frac{F}{A}$$

1.4

Where F is the shear force (N) and A the shear area (m^2)

The shear rate is the velocity over the distance travelled:

$$\dot{\gamma} = \frac{v}{h}$$

1.5

Where v is the velocity (m/s) and h is the shear gap (m).

Modelling viscosity

An understanding of mAb solution viscosity propagated from colloidal principles. Stokes' law (Equation 1.6) expresses how dynamic viscosity relates to frictional or drag force of a homogenous solution of spherical particles under laminar flow, when the Reynolds number is low (Equation 1.7).¹³⁴

$$F_D = 6\pi\eta Rv$$

1.6

Where F_D is the force of drag (N), R the sphere radius (m), and v the velocity (m^s).

$$Re = \rho \frac{vl}{\eta}$$

1.7

Where Re is the Reynolds number (dimensionless), ρ the density of the fluid (kg/m³), l the length along which the fluid is flowing (m).

Stokes' law was subsequently combined with the Einstein equation for Brownian motion (**Equation 1.8**) to result in the Generalised Stokes-Einstein (GSE) equation (**Figure 1.8**).

$$D_0 = kT/f$$

1.8

Where D_0 is the diffusion coefficient (m²/s), k the Boltzmann constant, T the absolute temperature (K) and f the frictional coefficient of the particle which is replaced by the Stokes equation for drag force.

Stokes-Einstein equation

$$D_0 = kT / 6\pi R\eta v$$

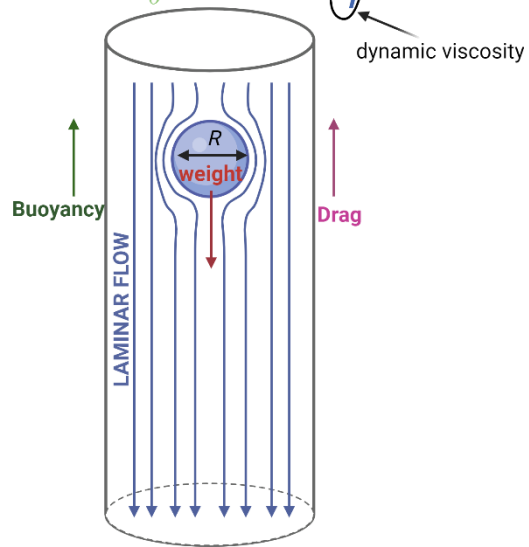


Figure 1.8 Depiction of principles of the Stokes-Einstein equation describing the forces present on a colloidal hard sphere under laminar flow.

Einstein also defined the volume fraction occupied by a hard sphere in dilute colloidal suspensions (**Equation 1.9**)¹³⁵:

$$\eta = \eta_0 \left\{ 1 + \frac{5v}{2V} + O\left(\frac{v}{V}\right)^2 \right\}$$

1.9

Where η_0 the apparent viscosity of the solution (buffer only) (cP), O the terms of the order $(v/V)^n$, v the volume occupied by hard spheres in volume, V , of suspension (nm^3).

Jeffrey *et al.*¹³⁶ further developed this colloidal model to describe ellipsoids, rotating in a viscous liquid (**Equation 1.10**) :

$$\frac{\eta}{\eta_0} - 1 = f \frac{v}{V}$$

1.10

Where f is the frictional coefficient dependent on the ellipsoid dimensions, v is the volume occupied by ellipsoids in volume, V of suspension (nm^3).

The addition of zeta potential (ζ) into viscosity models, where the mobility or velocity of the colloid is impacted by the charge of the colloid and the electric double-layer that surrounds it, was first explained by Smoluchowski *et al.*¹³⁷ (**Equation 1.11**).¹³⁸

$$\eta = \eta_0 \left[1 + \frac{5v}{2V} \left\{ 1 + \frac{1}{\sigma \eta_0 r^2} \left(\frac{\zeta \varepsilon}{2\pi} \right)^2 \right\} \right]$$

1.11

Where σ is electrolyte conductivity, r the particle radius and ε the dielectric constant of the dispersion medium.

The impact of the EDL on viscosity is described later with reference to mechanistic contributions to viscosity.

The *crowding effect* of particles with increasing concentration was a concept used to explain viscosity, which was first introduced by Mooney¹³⁹ (**Equation 1.12**):¹⁴⁰

$$\eta_r = \exp(2.5\phi/(1 - k\phi))$$

1.12

Where k is the self-crowding factor and ϕ the volume fraction of suspended spheres.

The subsequent Krieger-Dougherty model¹⁴¹ described more concentrated solutions with the addition of ϕ_m as the maximum solid fraction suspended whilst under flow, or packing factor (**Equation 1.13**):⁷⁴

$$\frac{\eta}{\eta_0} = \left(1 - \frac{\phi}{\phi_m}\right)^{-[\eta]_{\phi}\phi_m}$$

1.13

Where ϕ is volume fraction of suspended particles and ϕ_m the packing factor, which is 0.64 for spheres. $[\eta]_{\phi}$ is intrinsic viscosity of the solution in terms of volume fraction, which is 2.5 for spheres.

Semi-empirical models for viscosity continued to develop in the 1970s where Ross and Minton¹⁴² identified the limits of previous colloidal models (assuming sphericity of molecules and not relating the exponential dependence of viscosity on the concentration of solute).¹⁴³ Their studies were modelled from haemoglobin (globular proteins) and a fixed buffer viscosity of 0.7 cP at 37°C to mimic physiological temperature (**Equation 1.14**).¹⁴⁴

$$\eta = \eta_0 \exp\left(\frac{[\eta]c}{1 - \left(\frac{k}{v}\right) [\eta]c}\right)$$

1.14

Where c is concentration (mg/mL) and k is the self-crowding based on the Mooney equation and v is the Simha shape factor which is 2.5 for spheres (volume fraction).

These models have formed the basis of our current understanding of protein rheology. For viscosity modelling of mAbs, the Ross-Minton model is widely adopted to fit viscosity-concentration profiles with the parameterisation of the terms k/v and $[\eta]$.^{89,145,146} Often these parameters are not constrained and therefore cannot be deconvoluted into size contributions of intrinsic viscosity $[\eta]$ or shape or crowding contributions from k and v . Moreover, unconstrained parameters can promote overfitting to viscosity data, which is observed with case by case variation of parameters, limiting the predictive use of the model.

Alternative exponential models are used to fit viscosity data with varying complexities. Simple exponential growth equations are used in some cases for ease of data processing¹⁴⁷, while more mechanistic modelling approaches, such as the Schwenger

model have been implemented.¹⁶⁴ Furthermore, polymer-based entanglement models have been examined to understand clustering at high mAb concentrations.^{149,150} The overall lack of generalisability of these empirical models has initiated growth in machine-learning based predictive modelling, using large mAb viscosity datasets in combination with sequence and structure based *in silico* molecular descriptors.^{151–153}

Measuring viscosity

The interpretation of viscosity data is not only impacted by the fit model, but also the method used to measure mAb viscosity. Different types of viscosity are reported in accordance with measurement technique (**Figure 1.9**).

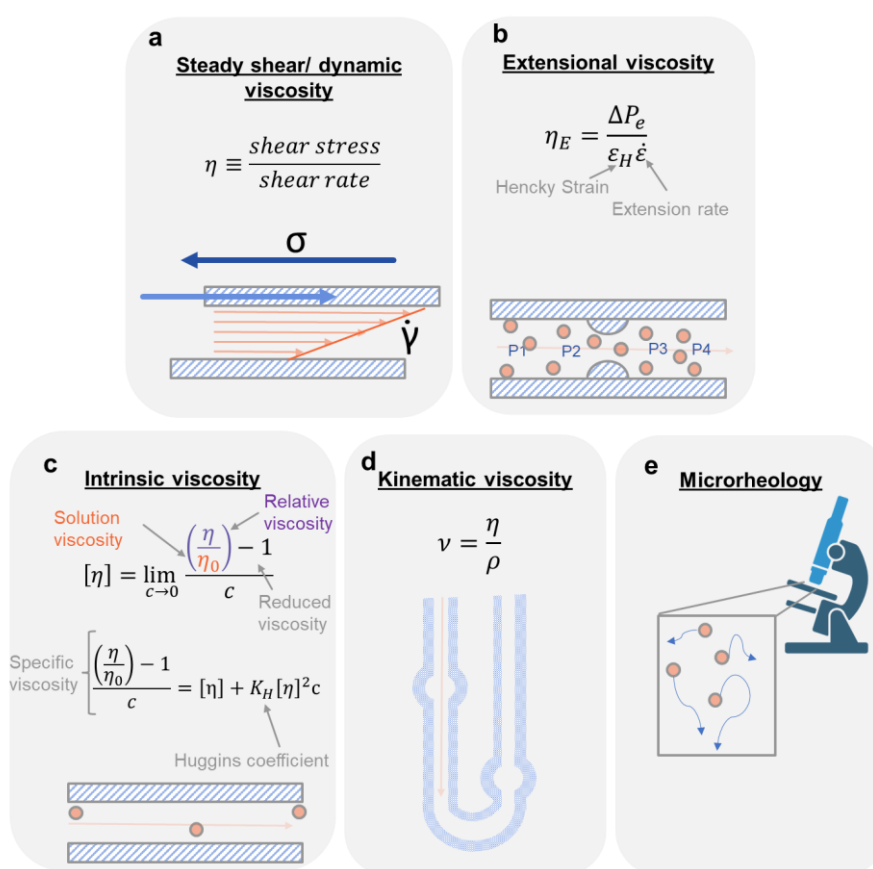


Figure 1.9 Different types of viscosity arise from rheology method used.

a, Newton's Law. **b**, Extensional viscosity based on changes in dimensions of a flow channel. **c**, Intrinsic viscosity. **d**, Kinematic viscosity. **e**, Microrheology. Diagrams were adapted from Rheosense (USA) blogs and webinars and some icons were created with Biorender.com.

Dynamic viscosity describes the shear-resistance to flow (**Figure 1.9a**). These measurements are performed on microfluidic instruments in which flow-rate is

adjusted through a channel with fixed and constant dimensions. Shear sweep experiments are used for mAbs exhibiting concentration-dependent non-Newtonian behaviour^{44,154,155} (*i.e.* shear thinning- viscosity of the molecule decreases under shear stress).¹⁵⁶ Moreover, solutions with aggregate structures and protein clusters have been seen to deviate from Newtonian behaviour with shear thinning observations.^{89,157} Temperature sweep experiments are routinely performed as the molecule viscosity is inversely correlated to temperature, explained with reduced Brownian motion (lower Boltzmann coefficient numerator in **Equation 1.8**).¹⁵⁸

Extensional viscosity (**Figure 1.9b**), η_E , is calculated with change in the cross-sectional area of the flow field (hyperbolic contraction of a flow channel). The Hencky strain, ϵ_H , explains the strain within the contracted space, which is calculated from pressure difference measured pre-contraction and pressure post-contraction (ΔPe). The extensional rate ($\dot{\epsilon}$) is calculated from volumetric flow rate, accounting for changes in channel dimensions.¹⁵⁹ Typically, extensional viscosity is more difficult to measure and thus less commonly adopted. The viscosity values are much higher than dynamic viscosity, cautioning against cross-comparison if different viscometry methods are used.^{159,160}

Intrinsic viscosity (**Figure 1.9c**), $[\eta]$, describes the contribution of molecules to solution viscosity and is indicative of the hydrodynamic size and shape contributions to flow resistance at dilute concentrations. Intrinsic viscosity is derived from linear regression of the reduced viscosity-concentration and has been correlated to high concentration mAb viscosity.^{90,161}

Kinematic viscosity (**Figure 1.9d**), ν , is the ratio between dynamic viscosity and the density of the molecule and is usually reported from gravitational viscometry, such as falling sphere or cylinder viscometers or gravimetric capillaries.^{162,163}

The emergence of microrheology (**Figure 1.9e**) where either passive molecule movement or movement under a magnetic force field is traced, has led to developments in particle tracking and imaging algorithms. This technique commonly uses either high-resolution microscopic techniques, DLS or diffusion wave spectroscopy (DWS) and offers the advantage of low sample consumption and non-disruptive analysis of shear sensitive materials.¹⁶⁴ Microrheology has recently been used to probe interfacial stability of mAbs with tensiometry techniques.^{165,166}

Contributions to viscosity

Electroviscous effects

The electroviscous effect explains the colloidal contributions of excluded volume effects and pair-wise interactions of mAb molecules to solution viscosity (**Figure 1.10**).^{74,167,168}

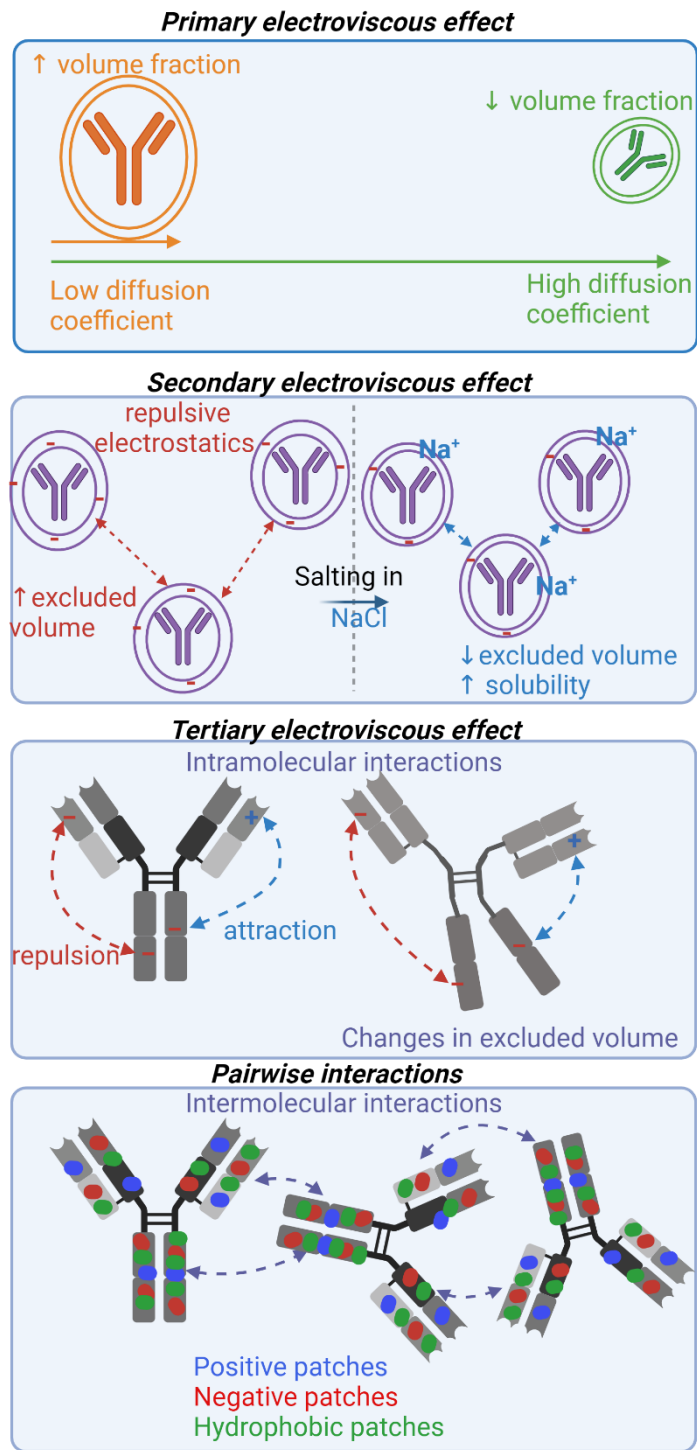


Figure 1.10 Primary, secondary, and tertiary electroviscous effects and surface-charge driven pair wise interactions.

The electroviscous effect is defined on the primary, secondary and tertiary scales. The primary electroviscous effect describes the influence of hydrodynamic size and

hydrodynamic volume of a single molecule on drag force in Stokes' Law (**Equation 1.6**), which reduces Brownian motion for larger molecules.^{168,169}

The secondary electroviscous effect introduces another molecule(s) into the system and describes the repulsive forces in the diffuse layer acting between molecules increasing the resistance of motion within the fluid. Long range electrostatic repulsion dominates over short-range attractive van der Waals forces, which results in large interparticle distances. The 'salting in' phenomenon demonstrates the reduction in repulsive forces with the introduction of anions, reducing the EDL thickness and excluded volume effects and thereby viscosity.^{91,168,170}

Finally, the tertiary electroviscous effect accounts for surface charges on the molecule and begins to describe intramolecular interactions between domains of the protein. Repulsive and attractive forces affect the dynamic positioning of these domains which can in turn affect the excluded volume fraction in solution.^{91,168}

The Huggins and Kraemer coefficients are derived from the intrinsic viscosity measurements and are used to understand the contributions of pairwise interactions to solution viscosity. These pairwise interactions can result from molecular-dependent surface potential anisotropy (positive, negative and hydrophobic surface patch mosaics) across various antibody domains (Fc-Fv, Fab-Fc, Fv-Fv) and different types of interactions (non-covalent, hydrophobic π - π , cation- π , dipole-dipole, charge-dipole, dispersion)^{90,171} Moreover proximity energies are assigned per interaction type to understand the activation energy barriers for the interaction to occur and pair-interaction potentials.¹⁷²

Reversible self-association

DLS and self-interaction nanospectroscopy techniques can help determine self-association propensity in protein solutions. k_D and AC-SINS red shift have been correlated with viscosity mAb solutions^{83,97,98,173,174} and self-association propensity increases with increased protein concentrations.¹⁷⁵ However these low concentration techniques have limited predictive ability for high (>100 mg/mL) and ultra-high (>150 mg/mL) concentration viscosities as they do not account for the complexity of short-range attractions in highly crowded structures. Molecular crowding (*i.e.*, where the distance between molecules is the same order of magnitude as the size of the molecules)¹⁷² results in reversible cluster formation.⁷⁴

The reversibility of self-interactions has been studied with salts, excipients and formulation buffer pH as well as exclusive antibody Fab fragments to examine domain dependent interactions,^{175,176} concluding that both hydrophobic and electrostatic forces drive self-association.^{177,178} Self-interactions are often considered the first stage of mAb aggregation where the native structure of the mAb is retained.

Non-native aggregation

Protein aggregation has been extensively studied primarily due to its links to neurodegenerative disorders such as Alzheimer's and Parkinson's diseases.¹⁷⁹ Research has spanned from mechanistic understanding (colloidal, conformational and chemical stability) through to process optimisation and formulation design to mitigate for and model aggregation risk.

A critical protein concentration exists where the aggregated state is more thermodynamically favourable than the native monomer. This aggregated state can be native oligomer which may retain protein functionality or a partially unfolded oligomer that may have increased exposure of hydrophobic residues driving irreversible nucleation.¹⁸⁰ Intermolecular forces governing self-assembly are attributed to sequences of non-covalent interactions, which are also seen in protein folding.¹⁸¹

Information on stretches of hydrophobic residues- aggregation hot-spots- has led to the design of *in silico* tools for predicting aggregation.¹⁸² These can be sequence (AGGRESCAN¹⁸³, Waltz¹⁸⁴, TANGO¹⁸⁵) or structure-based predictive tools (Aggscore¹⁸⁶, SAP¹⁸⁷, CamSol¹⁸⁸).

There is an apparent overlap in concentration-dependent self-association mechanisms promoting increased viscosity and aggregation risk. The correlation between aggregation and viscosity has been explained from the increase in size of aggregate species and resultant excluded volume effects.^{189,190}

1.3. Subcutaneous administration of biologics

Traditionally, therapeutic mAbs have been formulated for intravenous (*i.v.*) infusion, offering rapid action onset and complete bioavailability ($F=1$) with direct injection of the drug product into the bloodstream.¹⁹¹ Infusions typically require a healthcare professional for initial dilution of the mAb product into an infusion solution, for

catheterisation of the patient and to ensure the full dose is administered at a controlled rate.^{192,193}

Despite more variability in bioavailability and pharmacokinetics^{194,195}, the subcutaneous (s.c.) route of administration is preferred over the intravenous (i.v.) route in patient preference studies, and for time and resource savings.¹⁹⁶ Dosing *via* the s.c. route involves an injection into the fatty tissue under the skin delivered with pre-filled syringes or autoinjector devices for ease of self-administration.¹⁹⁷

The s.c. route may reduce the number of clinic visits or the length of stays in hospitals, while also reducing infection risk and the frequency of dosing, improving patient adherence. Cost-saving benefits are associated with the s.c. route, with less healthcare professional time needed for administration and fewer consumables associated with *i.v.* treatment.^{192,198,199} Furthermore, injection site infection risk decreases with s.c. injection and is likely to be less severe types of infections, such as cellulitis. There are several clinical studies comparing the traditional *i.v.* route to the s.c. route, showing non-inferior efficacy and cost reduction for healthcare providers.^{214–216}

mAbs typically have low potency and need to be administered at concentrations >150 mg/mL to deliver dose-relevant levels of mAb within the therapeutic window.¹²⁹

The industry standard platform s.c. autoinjector device has a volume capacity of approximately 1 mL. As the dose unit concentration increases, the risk of high mAb viscosity increases resulting in manufacturability issues. Beyond filtration issues, higher viscosity of mAb formulations can lead to nozzle-clogging for vial filling, reducing consistency in dose volume accuracy, and issues with *injectability*. Increases in autoinjector injection times and the potential for mechanical failure from needle blockages.²⁰⁵ Furthermore, a greater force is required for injecting the entire mAb dose, increasing shear stress (τ) on the product:

$$\tau = \frac{F}{CSA}$$

1.15

Where F is force applied (Newtons), and CSA the cross-sectional area over which the force is applied (accounting for the syringe barrel, transition region between barrel and needle, and the needle)(m²).

Various device designs have been explored for the administration of therapeutic mAbs with a variety of indications. Approximately 60 autoinjectors are approved in the EU with indications for rheumatoid arthritis, multiple sclerosis and Crohn's Disease.²⁰⁶ Autoinjector devices can be customised to suit the end-user with respect to dexterity, visual or audio impediments and mental health issues, including needle phobia. Human factor studies evaluate the ease of device handling for users with varying levels of training, and user feedback is incorporated into device design.²⁰⁷

Beyond 'usability' adjustments based on the target demographic, device design also considers needle dimensions, dosing regimen (volume capacity), viscosity of the formulation and injection force, injection force (spring material or compressed air), maximum target injection time and safety measures.^{208,209}

Injectability can be screened with extrusion force experiments and modelling. The injection force can be calculated from the viscosity, needle, and syringe barrel dimensions:

$$F = 32 * \eta * l * \left(\frac{D^2}{d^4}\right) * \left(\frac{V}{T}\right)$$

1.16

Where F is the force for injection (N), l needle length (mm), d the inner needle diameter (mm), D the inner barrel diameter (mm), V the volume to extrude (mm³) and T the expected estimated time through the needle (s).

Generally, a viscosity ≥ 20 cP is considered an injectability risk.⁹⁵ The increased injection force required delivering a full dose may cause device failure as the wall stress on the barrel exceeds the tensile strength of its material.²⁰⁹ The resistance from plunger friction and skin contribute to this increased pressure and device failure can be defined as under-delivery of the full dose, breakage of the device (posing safety issues), or malfunction with a temperamental spring force, leading to underdosing.²¹⁰

1.4. Mitigating high viscosity risks

Considering manufacturability, product quality and injectability risks of highly viscous mAb formulations, a variety of mitigation strategies have been investigated to improve the likelihood of mAb translation to the clinic.

1.4.1 Device design

A significant body of research exists on adjusting autoinjector design to accommodate larger dose volumes or increased force from highly viscous products. Firstly, size adjustments on the syringe barrel and needle gauge can increase the volume capacity (> 1-2 mL), reducing the requirement for as high of mAb concentrations and thereby reducing viscosity risks. Current high-volume, low-concentration devices are wearable injectors or syringe-driven infusion pumps, but there are ongoing efforts to translate this research to autoinjectors.^{205,211} Furthermore, actuation of highly viscous mAbs requires high spring strengths, which has led to research on spring design and material.^{212,213} The increased delivery times and needle gauge required to accommodate large volumes has been correlated with increase injection-site pain, which may affect patient adherence.²⁰⁵

Modelling parameters such as air gap within the syringe, spring force and elasticity, volume, frictional force (including viscosity terms) and needle dimensions are used to optimise design.^{197,214}

1.4.2 Formulation optimisation

Hyaluronidase is used in subcutaneous drug products in combination with device adjustments. For example, daratumumab for multiple myeloma is formulated with hyaluronidase to allow for an injection dose up to 15 mL (120 mg/mL). Hyaluronidase is a permeation enhancer, which increases the absorption of drugs in the s.c. matrix.²¹⁵ However, formulations containing hyaluronidase require an increased needle gauge, screening of product compatibility, increasing development time and the risk of tissue damage and/or infusion site erythema.²⁰⁵ Therefore, alternative viscosity reducing formulation adjustments have been investigated.

Formulation pH significantly impacts mAb physicochemical stability. Promotion of electrostatic interactions at $\text{pH} < \text{pI}$ increases reversible self-association risks correlated with viscosity. Moreover, slightly more acidic pH buffers promote PTMs such as isomerisation.²¹⁶ Formulation pH needs to be distanced away from the mAb

pI to reduce attractive van der Waals intermolecular interactions but at very high pH can cause disulfide bond degradation.²⁰⁵ Most mAbs are formulated at pH 5.8 (± 0.6) where they have a net positive charge with long-range repulsions.¹⁴⁴

Most formulations are histidine-based, which like L-arginine (a common excipient), is known to bind mAb hydrophobic regions to reduce aggregation risk.^{217–219} Sugars and polyols are also used as excipients to increase the conformational stability of the protein with preferential exclusion of the sugar molecule to surround the protein²²⁰

Significant variation in mAb viscosity control exists in the formulation optimisation space with some reports showing significant improvements on both colloidal and conformational stability,²²¹ while others reporting reduced viscosity at the detriment of conformational stability.²²² This is unsurprising considering mAb-mAb diversity in biophysical behaviour with different developability baselines. Furthermore, buffer incompatibilities and the significant time and resource requirements to derisk formulations has driven research on sequence engineering as an alternative mitigation strategy to high viscosity mAb formulations.

1.4.3 Sequence engineering

Sequence engineering offers viscosity mitigation risks during the early discovery and molecular design stage. Several reports have designed mutant molecules with the aim to disrupt regions that are hypothesised to contribute to viscosity. These are summarised in **Table 1.1**.

Table 1.1 Notable literature on sequence engineering studies to modify viscosity of high concentration mAb formulations.

Abbreviations WT= wild-type molecule, Fv= variable region, FWRH= heavy chain framework region, CH1= heavy chain constant region 1, CL= light chain constant region, VH= heavy chain variable region, RSA= reversible self-association, Ag= antigen, PBS= phosphate buffered saline, SASA= solvent-accessible surface area, SAP= spatial aggregation propensity, A= alanine, R= arginine, D= aspartic acid, N= asparagine, C= cysteine, E= glutamic acid, Q= glutamine, H= histidine, L= leucine, K= lysine, M= methionine, P= proline, S= serine, T= threonine, W= tryptophan, Y= tyrosine, V= valine.

Reference	Rationale and mutant design	Viscosity method	Conclusions
Yadav <i>et al.</i> ²²³	Based on previous work performed to decipher interactions and mAb domains responsible for high mAb viscosity ^{224,145,225} , charge-swap mutations were introduced into the CDRs and flanking residues of two mAbs which had the same framework sequences. These were in either VL, VH or both. An aglycosylated mAb was also tested.	All mAbs prepared >100 mg/mL, ranging up to ~260 mg/mL for less viscous mAbs in histidine-based formulation buffer. Cone and plate rheometer shear rate sweeps performed at 25 °C and data at 1,000 1/s shear rate reported (Viscosity measurements N=2).	Glycosylation did not affect viscosity (not solvent accessible). Mutants with increase in charge (favouring intermolecular repulsions) showed reduced viscosity to WT. Hypothesis that mutant with same charge to WT had decreased viscosity due to a knock out of dipole potential from histidyl residue. Subsequent work supported findings with dipole moment experiments ²²⁶ , and correlations to k_D and B_{22} ⁷⁵ .
Bethea <i>et al.</i> ²²⁷	Previous structural studies to improve an anti-IL13 IgG1 solubility identified aggregation hotspots in FWRH aromatic residues. ²²⁸ Combinations of FWRH mutants tested, as well as WT Fab, and CH1 and CL mutants (hypothesised to reduce electrostatic Fab-Fab interactions from proximity analysis in crystal structure). Isotype switch to IgG4 also assessed.	MAbs prepared up to respective maximum solubility (100 mg/mL) in PBS. Microfluidic viscometer (no shear rate stated) at 25 °C (Viscosity measurements N=2/3).	Viscosity concluded to be driven by compact Fab-Fab clustering and aggregation. Combinations of FWRH mutants saw much lower viscosity over single-point FWRH mutant. Charge CH1 and CL mutants showed only slight viscosity reductions retaining RSA propensity.
Nichols <i>et al.</i> ¹⁷⁸	Aimed to decouple hydrophobic versus electrostatic contributions with single-point FWRL mutants of a highly viscous, phase separating WT model identified from works by Li <i>et al.</i> ¹⁶¹ Mutant designed was based off aggregation propensity predictions (TANGO/PAGE) and surface patch analysis from Fv homology constructs.	All mAbs prepared up to 50-130 mg/mL in histidine-based formulation buffer. Cone and plate rheometry, fixed shear rate 900 1/s at 25 °C (Viscosity measurements N=2).	Hydrophobic patch/ APR- disrupting V to K mutant showed reduced viscosity. Charge neutralisation mutants (E to Y) showed improved viscosity over charge reversal (E to K). Solubility improvements aligned with reduced viscosity. However, viscosity data was limited from material constraints.

Chow <i>et al.</i> ²²⁹	CDR-driven RSA investigated of a IgG4 Fab fragment WT which demonstrated high viscosity and phase separation. Residues involved in Fab-Fab interactions of crystal structure were substituted by all possible residues and screened to ensure Ag binding was retained, resulting in four CDR mutants. Surface potential was mapped per mutant.	Mabs were concentrated to 130 mg/mL in 'low ionic strength' buffers. A microfluidic viscometer was used at 682 1/s fixed shear rates with a 10, 15, 20 and 25 °C temperature sweep (Viscosity measurements N=2).	Hypothesised that surface charge imbalance contributes to viscosity. Significant viscosity reductions with NàE and RàG (positive-patch disrupting) mutants whereas FàH (hydrophobicity reduction) showed no reduction compared to WT. Reduction in computed dipole moments correlated with reduced viscosity. B22 values did not align to viscosity results.
Geoghegan <i>et al.</i> ²³⁰	The correlation between RSA and high concentration viscosity was explored. Mutants of RSA-prone IgG1 designed from combination of HDX-MS and from Fv homology constructs to compute solvent accessible surface area. Histidine (CDRH) and hydrophobic-patch contributing residues mutated in(W, Y and L in CDRH, FWRL and CDRL respectively). Mutants with significantly reduced RSA risks were selected for viscosity analysis.	mAb samples prepared to 70 mg/mL in PBS. Cone and plate rheometer was used with a fixed shear rate of 1000 1/s at 4 °C (Viscosity measurements N=6).	Removing exposed hydrophobic residues and altering buried hydrophobic residues at VH/VL interface improves solution behaviour. However, CDRH mutants had reduced affinity. This study did not assess viscosity for other mutants with no/less significant RSA reductions.
Shan <i>et al.</i> ²³¹	Assessment of both electrostatic and hydrophobic contributions to RSA of an IgG1 WT. Similarly to Geoghegan <i>et al.</i> ²³⁰ , HDX-MS used to identify RSA hotspots to focus mutagenesis. 12 residues contributing to significant surface patches modelled on the WT full IgG homology construct were identified (two CDRL1, three CDRH3, 7 CH3 in Fc).	Viscosity was not examined but RSA and solubility assessed.	Positively charged residues were identified to be in juxtaposition to hydrophobic. Reduction in RSA dependent on position and size of side chain. Hydrophobicity targeting mutants had more dominant role in RSA reduction.
Tilegenova <i>et al.</i> ²³²	Previous work on IgG1 found positive or negative residues had little impact on viscosity as Fabs still had large number of positively charged residues. ²²¹ Hypothesised that viscosity is predominantly driven by hydrophobic interactions from aromatic CDR residues which can be disrupted from L-arginine excipients. MD simulations of IgG1 Fv and IgG4 Fv in a system solvated with free arginine were used to identify residues to mutate for enhancing IgG1/IgG4 bispecific	All mAb fragments/full IgG were prepared in histidine-based formulation buffer up to 150 mg/mL. A cone and plate rheometer was used at 23°C with shear rate sweeps tested and data at 1000 1/s reported (Viscosity measurements N=2).	Aromatic CDR residues had the largest contact frequency with free solvated arginine. Seven out of 12 mutants had reduced viscosity and two out the seven had retained binding affinity. Weak intermolecular interactions between Fabs proposed involving both cationic and aromatic residues. Consistent reductions in viscosity from Y/W to L (when leucine is hydrophobic) suggested importance of aromatic rings in π-π interactions for high viscosity.

	mAb viscosity. R/K/D/E to Q and Y/W to L/Q substitutions were made.		
Apgar <i>et al.</i> ²³³	Premise of short-range negative charge patch interactions in the Fv with positive patches leading to RSAs at high concentrations. This suggests Fv charge plays a larger role in viscosity than hydrophobicity. A highly viscous IgG1 WT was mutated to reduce net negative charge of the Fv (both CDRs and FWRs) in two rounds with ~20 variants with combined mutants per round. These were designed with the rules of 1) assessing change in stability and binding ($\Delta\Delta G < 1.0$ kcal/mol), 2) E to G and D to N, 3) neutral CDR residue to R/K/H, 4) FWR mutant was likely to be positive in human germlines, 5) Improvement in viscosity scores from two predictive models. Round two was designed based on promising round 1 mutants with the same initial stability rule and the similar neutral to R/K/H and D/E to N/Q strategies with viscosity scoring.	mAbs were prepared in histidine-based formulation buffer between 25-160 mg/mL. A cone and plate rheometer was used with 150 rpm speed and at 25 °C (Viscosity measurements N=10).	Positive charge repulsions and location of mutants play a significant role in RSA propensity. A reduction in viscosity from WT seen in the first round with VL mutant N to K which was improved further with combined VH E to Q and Q to K mutations. Additional S to K and D to N mutations in second round to the lowest viscosity mutant confirmed interruptions of specific negative patch reduced viscosity significantly compared to WT. Extrapolated data for WT viscosity was fitted from Ross-Minton equation used to compare against mutants. However, mutant with best viscosity reduction had 3-fold loss in binding.
Makowski <i>et al.</i> ²³⁴	Development of antibody yeast-display library framework with selections not just by affinity but also colloidal stability (RSA propensity) using quantum-dot antibody conjugates. Variants of bococizumab were examined and a logistic regression model trained deep sequencing data was used to classify binding and RSA propensity.	Viscosity was not specifically assessed, but RSA propensity as well as non-specific interactions and other biophysical properties.	High affinity variants possess positively charged Fvs and high RSA. Variants which introduced negatively charged residues just outside of the paratope had reduced RSA and retained binding for bococizumab. Fvs variants had low RSA and very rarely high affinity. Variants with reduced self-association were also correlated with reduced non-specific binding with this mAb.
Dai <i>et al.</i> ²³⁵	Following on from Tilegenova <i>et al.</i> ²³² , both negatively charged patches and hydrophobic patches were determined as viscosity risk factors and viscosity was driven by Fab-Fab interactions. Crystallographic Fab-Fab (IgG1)	mAbs were prepared in histidine-based formulation buffer to 180 mg/mL. A cone and plate rheometer assessed samples at a fixed shear rate of 1000 1/s at 25 °C (Viscosity measurements N=30).	Most significant viscosity reducing variants had a SASA of $>50\text{\AA}^2$ and high SAP score (>2.3). High viscosity was independent of presence of Fc region.

	<p>contacts were assessed, and surface properties computed (SAP, patch analysis). Hydrophobic patches targeted (high SAP scores) and residues interacting with FWR and at VL/VH interface were excluded. W/Y to A strategy was adopted in both VL and VH. Additive effects were tested with combined mutations. Mutants with reductions in viscosity were selected for further mutations with all amino acids except C,G,P,M (conformational risks).</p>		<p>Salt addition to mAb increased viscosity, suggesting predominantly hydrophobic interactions govern viscosity with this mAb (arginine reduced viscosity). However, not all W/Y to A mutants had reduced viscosity and high solvent accessibility was necessary. Strong correlations were observed between kD and viscosity. Replacing aromatic to positive was particularly effective at reducing viscosity (introducing repulsion).</p>
<p>Heisler <i>et al.</i>²³⁶</p>	<p>Fc contributions to viscosity are largely unknown. Common Fc mutations were explored off an IgG1 omalizumab and trastuzumab scaffolds.</p>	<p>mAbs were prepared up to 180 mg/mL in histidine-based formulation buffer. Cone and plate rheometry was used at a fixed shear rate of 1000 1/s at 25 °C. For the initial screening experiments viscosity measurements N=1; for further investigations of variants viscosity measurements N=2-5.</p>	<p>Half-life extending YTE mutation showed significant reduction in viscosity for omalizumab but not trastuzumab. This was hypothesised to be from reducing positive charge from negatively charged E residue. Half-life extending LS mutation showed increase in viscosity for omalizumab (no difference with trastuzumab). Differences in spatial orientation of the mutations between the mAbs was proposed to understand why the same mutation impacts viscosity to different extents.</p>

The progression of directed mutagenesis to reduce high concentration mAb viscosity led to concurrent efforts to develop models predicting the viscosity from sequence and structure based molecular descriptors.

Empirical regression models have been developed using *in silico* molecular descriptors derived from sequence or computed structure. Li *et al.* computed electrostatic and hydrophobic physicochemical descriptors for 11 proprietary mAbs of different subclasses which showed distinct differences in viscosity at 150 mg/mL.¹⁶¹ They found computed structure-based pI and sequence-based aggregation propensity were highly correlated with their dataset and formed a regression model (R^2 0.93, RMSE 0.00123, p value 1.91×10^{-5}). Subsequently, Sharma *et al.* performed similar regression analysis on a set of 14 IgG1 molecules and observed correlations of sequence-based Fv charge, Fv charge asymmetry between heavy and light chain and to the lesser extent hydrophobic index descriptors to viscosity at 180 mg/mL.²³⁷ Tomar *et al.* also developed a regression model from a dataset of 16 mAbs and their respective viscosities at 150 mg/mL.²³⁸ They found the combinations of VH,VL and hinge charge as well as solvent accessible hydrophobic surface area to best describe the rate of increase in the logarithm of relative viscosity. This model performed well after leave-one-out cross validation ($R= 0.8$), however this model was trained from mAbs with no developability flags so the generality to other datasets is cautioned. The predictive ability of these regression models is limited by the relatively small datasets that they are trained on as well as not being recommended for use with molecules in different formulations.

Considering these limitations, guidelines and generalised developability scoring tools were developed from larger datasets. The spatial charge map (SCM) was developed to describe the magnitude of electronegative patches and scores of >1200-2000 were seen to indicate high viscosity risks for the mAbs studied.²³⁹ Later, a convolutional neural network was trained on computed SCM scores for >6500 Fv regions which showed reasonable model performance ($R= 0.9$) and suggested a threshold score of 1000 for high viscosity flags.²⁴⁰ The Therapeutic Antibody Profiler (TAP) was built using 137 clinical stage mAbs as developable models and assessed CDR length, CDR canonical forms and hydrophobicity and charge patch vicinity to CDRs from homology models.²⁴¹ Kingsbury *et al.* did not find TAP to discern between well and poorly-behaved mAbs of the 59 they studied.¹⁷⁴ Instead, thresholds were set on three experimental (k_D , ζ and pI) and three molecular descriptors (hydrophobic index, Fv

charge asymmetry and Fab-Fc charge asymmetry). A subsequent study defined a cut-off of +2 for the ensemble charge descriptor which was highly correlated with concentration at 20cP in a dataset of 38 IgG1 variants.²⁴² Ahmed *et al.* also identified non-redundant molecular descriptors based on 77 commercial mAbs (buried surface area between heavy and light chain, ratio of charged to hydrophobic patches, structure-based predicted pI, ratio of dipole to hydrophobic moments and hydrophobic imbalance).²⁴³

Numerous research efforts have focussed on machine-learning (ML) algorithms to guide developability. Lai *et al.* generated a decision tree trained from 27 commercial mAbs with diverse viscosities at 150 mg/mL.¹⁵¹ A high viscosity index parameter was introduced on the basis that highly viscous mAbs have predominantly hydrophilic Fvs (less hydrophobic). This, along with net charge was able to categorise high *versus* low viscosity mAbs, tested with Apgar variants²³³. The flexibility in the thresholds set as well as the cutoff points need to be adjusted for mAb formulated in different buffers and to account for experimental uncertainties. The decision tree was further tested with 20 pre-clinical mAbs which showed a lack of generalisability.¹⁷³ Therefore, both an alternative logistical regression model and decision tree model (one or two feature constraints) were assessed to incorporate both clinical and commercial datasets, but cautioned that more data is needed to validate these models. Rai *et al.* similarly highlighted the discrepancy of viscosity distributions between preclinical and commercial mAb datasets.²⁴⁴ They used both (58 mAbs in total) to develop a convolutional neural network assessing surface potential. Hydrophobicity surface potential was assessed, but the generalisability of the model was significantly improved with use of electrostatic surface potential. The development of an alternative decision tree model by Makowski and coworkers used 79 mAbs with similar properties to clinical stage IgG1s.²⁴⁹ They identified structure based Fv pI, largest Fv hydrophobic patch and number of Fv negative patches to be highly correlated to viscosity. Comparisons with their dataset showed this model outperformed preceding Sharma²³⁷ scores and the Lai¹⁵¹ decision tree model but the authors caution that retraining may be required if alternative formulation buffer conditions are used in viscosity measurements. Estes *et al.* also generated a ML-derived viscosity tool from 30 sequence-based molecular descriptors of proprietary mAbs through a random forest algorithm.²⁴⁵ Whilst this tool proved valuable in

informing rational design of variants with enhanced viscosity, no details were disclosed in order to reproduce or test the predictive power with other datasets.

General consensus amongst viscosity-predictive models is that predictive accuracy is dependent on 1) sufficiently large datasets with diversity in both preclinical and approved and in different formulations, 2) the difficulties in accessibility of large preclinical mAb datasets, 3) challenges in inferring ML-models with version dependencies and license accessibility.

Viscosity modelling efforts not only flag developability risks but can also help elucidate mechanistic contributions to high viscosity in high concentration mAb formulations promoting rational mutagenesis to mitigate such risks.

1.5. Aims and Objectives

The sequence, structural and functional diversity of mAbs in early-phase development has incited the advancement of analytical and *in silico* tools to predict and derisk developability. High viscosity of high concentration mAb formulations is one of the major obstacles in manufacturing feasibility and subcutaneous injectability and relates to inherent conformational and colloidal molecular stability. One of the aims of this thesis is to identify the impact of engineering single-point mutations of an IgG1 molecule targeting surface potential disruptions (electrostatic or hydrophobic) on viscosity and other biophysical developability parameters (**Chapter 2**), including manufacturability observations (**Chapter 3**). Moreover, this thesis aims to explore the developability of an IgG3 molecule compared to an Fv-matched IgG1 molecule using the same *in silico* and experimental framework as mutant panel (**Chapter 4**). Finally, viscosity modelling and viscosity predictions are explored to understand the limits of generalisability from empirical model fits and predictions (**Chapter 5**). The objectives per chapter are detailed as follows.

Chapter 2 focusses on the rational design and developability profiling of eight anti-IL-8 IgG1 mutants that are hypothesised to have altered viscosity profiles. Both sequence and structure based molecular descriptors are explored in the directed mutagenesis targeting hydrophobic, negative or positive surface exposed patches. Viscosity improvements are hypothesised for hydrophobic and negative patch disrupting mutants and increased viscosity is hypothesised for positive patch disrupting mutants. Electrostatic, hydrophobic and colloidal properties are also explored in this chapter to identify the extent of changes to the biophysical behaviour

from single-point mutations. These properties, along with *in silico* molecular properties are also used to identify correlations to viscosity to better comprehend underlying mechanistic contributions to viscosity. This research chapter addresses whether single point Fv mutations are sufficient to reduce viscosity and discusses if engineered viscosity alterations are dependent on site (CDR versus framework) and strategy implemented (hydrophobic *versus* electrostatic). Furthermore, correlations of both biophysical parameters and sequence and structure *in silico* parameters to viscosity are investigated.

Beyond electrostatic, hydrophobic and colloidal properties, the manufacturability of the anti-IL-8 mutant panel is explored in **Chapter 3**. The objectives of this chapter are to understand what implications single-point mutations have on upstream and downstream processability and if viscosity risks can be predicted from the extrapolation of flux during filtration processes. This chapter also assesses if the phase behaviour of the mutant panel aligns with biophysical and viscosity observations and also discusses the impact of single-point mutations on process-related critical quality attributes such as post-translational modification liabilities.

Additionally, the IgG3 subclass was assessed in **Chapter 4** with the same *in silico* and biophysical framework to give a first time insight into the developability of this subclass against its Fv-match IgG1 ortholog. The objectives of this chapter are to compare the developability of the IgG3 molecule to the IgG1 with regards to electrostatic, hydrophobic, colloidal properties as well as viscosity. Similar to Chapter 2, an evaluation of correlations between the viscosity of IgG3 to *in silico* and biophysical parameters is made to aid viscosity predictions.

Viscosity modelling strategies were assessed with the anti-IL-8 mutant panel in **Chapter 5**. The implications of viscosity model fit selection and concentration-regime is studied, including assessment of low-concentration hydrodynamic parameters in viscosity predictions. This chapter also evaluates the accuracy of a selection of empirical and ML-derived viscosity predictive models with the anti-IL-8 mutant panel.

Finally, **Chapter 6** summarises the key findings of this thesis with emphasis on future directions.

2. Surface patch directed design and biophysical analysis of viscosity-reducing single point mutations in high-concentration monoclonal antibody formulations.

This chapter contains the published material from the Computational and Structural Biotechnology Journal with permissions; Armstrong G.B, Shah V., Sanches P., Patel M., Casey R., Jamieson C., Burley G.A, Lewis W., Rattray Z. “A Framework for the Biophysical Screening of Antibody Mutations Targeting Solvent-Accessible Hydrophobic and Electrostatic Patches for Enhanced Viscosity Profiles.” *CSBJ* (2024) <https://doi.org/10.1016/j.csbj.2024.05.041>.

GB Armstrong- the author of this thesis- contributed to the cell line generation, and performed all mutant expression, biophysical analytics (except from LC-MS and AC-SINS assays) and *in silico* homology modelling reported in this chapter.

2.1. Abstract

This chapter describes the design of single-point mutations in the Fv of an anti-IL-8 IgG1 to target electrostatic or hydrophobic solvent-accessible surface patches hypothesised to alter viscosity profiles. A biophysical characterisation framework was developed here, and viscosity was measured up to 120 mg/mL. Correlations between *in silico* descriptors and biophysical parameters are also discussed. Viscosity reduction with this mutant panel is dependent on reducing net hydrophobicity and a decrease in net charge is correlated with increased viscosity. No single molecular descriptor can predict viscosity and machine learning directed mutagenesis is a prominent alternative research direction.

2.2. Introduction

Therapeutic monoclonal antibodies (mAbs) have emerged as indispensable tools in the treatment of chronic diseases such as diabetes, cancer, and autoimmune disorders.⁴ Empowering patients with self-administration regimens, subcutaneous injection is the route of administration of choice for the delivery of these life-changing therapies, necessitating formulation design strategies to accommodate small injection volumes.²⁴⁶ However, this pursuit of patient convenience presents a formidable

challenge: how to achieve high mAb formulation concentrations (>100 mg/mL) at low dose volumes (0.5-1 mL) without facing developability challenges, a term which refers to the likelihood of a mAb molecule to become a suitable candidate in the context of manufacturability, safety, and efficacy at a reasonable cost and timeframe.²¹⁵ Developability challenges in the context of mAbs include a high risk of aggregation and elevated solution viscosity at dose-relevant concentrations, which have implications for quality, safety and efficacy throughout the mAb product lifecycle.³⁴

The viscosity of mAb formulations, a critical parameter governing dosing and delivery efficacy, is intricately linked to protein-protein interactions arising from the mAb amino acid sequence and formulation excipient composition.^{247,248}

High concentration mAb formulations exacerbate these interactions, leading to increased aggregation risk and elevated formulation viscosity (>30 centipoise).²⁴⁹ High mAb formulation concentrations result in an exponential increase in protein-protein interactions leading to a higher aggregation risk. The diffusion interaction parameter (k_D) is used to measure protein-protein interactions and colloid stability, with high viscosity mAbs generally exhibiting large negative k_D values (attractive).^{174,250,251}

In this pursuit, various strategies have been employed to modulate protein-protein interactions and mitigate mAb solution viscosity. These strategies have ranged from the alteration of electrostatic properties by changing formulation buffer pH and salt composition, to employing viscosity reducing excipients (e.g., amino acids) to increase the solubility of partially folded and unfolded states.^{219,252,253} Furthermore, advancements in sequence-based engineering offer a promising avenue for targeting solvent-accessible electrostatic patches on the mAb surface, with the potential to revolutionize the mAb design landscape.

In the emerging era of precision medicine, the integration of high throughput *in silico* predictions and molecular triaging approaches holds immense potential in streamlining early-stage discovery campaigns.^{146,147,173} By elucidating the intricate relationship between mAb molecular descriptors and developability risks, these cutting-edge approaches empower researchers to more expediently identify candidate mAbs with superior physicochemical properties, paving the way for more agile drug development pipelines with less attrition.²⁵⁴

Current landscape analyses and models defining optimal developability for mAbs are based on clinically approved drug products with optimal characteristics. However, amidst these advancements, it is imperative to broaden our focus beyond clinically approved mAbs and encompass those with unknown or sub-optimal developability characteristics. In doing so, we expand our understanding of how to navigate high formulation concentration solution viscosity more effectively, ultimately enhancing the success rate of mAb drug development endeavors.¹⁷⁴

In this work, computational molecular descriptors were harnessed as a guiding tool for the design and triage of a mutant mAb panel altering solvent-accessible hydrophobic and electrostatic surface patch area coverage. Through a combined computational and experimental pipeline, the relationship between single-point mutations and the biophysical properties of a model antibody, anti-IL-8 mAb was examined. The site-specific and strategy-dependent impact of mutations based on surface patch composition was demonstrated, offering an insight into downstream effects of molecular alterations. Significant alterations in surface potential from single-point mutations in the variable region and favourable developability characteristics were observed for hydrophobic or negative patch-disrupting mutants. Furthermore, correlations between hydrophobicity-based molecular descriptors and colloidal parameters in predicting hydrophobicity-driven self-associations were found, impacting solution viscosity at high mAb concentrations.

2.3. Aims

The goal of this chapter is to describe the use computational molecular descriptors as a triaging tool for the design of a mutant panel targeting hydrophobic and electrostatic surface patches and measure the mutant mAb panel physicochemical parameters and viscosity profiles at high concentration using an analytical pipeline. The experimental findings from the biophysical and physicochemical analyses of the anti-IL-8 mutant panel targeting electrostatic and hydrophobic interactions are reported and correlated to their viscosity-concentration profiles.

2.4. Materials

Table 2.1 Materials for anti-IL-8 mAb expression, purification and analysis

Material	Catalogue number	Manufacturer
mAb expression		
pD2500 Stable Vector with Leap-In Transposase® compatibility and CMV promoter with glutamine synthetase and heavy and light chain gene insertions	Custom	ATUM, USA
Chinese Hamster Ovary K1 GS Knock Out cell line	N/A	GSK, United Kingdom
Defined cell culture media (In-house proprietary composition)	N/A	GSK, United Kingdom
200mM L-Glutamine	25030081	Gibco, Thermo Fisher, USA
Amaxa 4D Nucleofector kit	V4XP-3024	Lonza, United Kingdom
VI-CELL XR Quad Pack Reagent Kit	383722	Beckman Coulter, USA
TrypLE™ Express Enzyme (1X), phenol red	12-605-010	Gibco, Thermo Fisher, USA
Octet® ProL Biosensors	18-5085	Sartorius, Germany
IgG Bio HT, NH3 Bio HT, Glutamate V2 Bio HT, LDH Bio HT, Lactate Bio HT, Glutamine V2 Bio HT, Glucose Bio HT Kits for the CEDEX instrument	06608540001, 06608515001, 07395566001, 06608493001, 06608485001, 07395612001, 06608418001	Roche, Switzerland
D-(+)-Glucose	G7021	Sigma-Aldrich, Germany
Proprietary amino acid feed media	N/A	GSK, United Kingdom
mAb purification		
Clarisolve® 60 µm Lab Scale Depth Filters, 0.027 m ²	CS60HX02H1	Millipore, Sigma-Aldrich, Germany
Posidyne membrane in Kleenpak capsule filters	KA2NFZP2	Cytiva, Danaher, USA
Capto L resin	17547803	Cytiva, Danaher, USA
Capto SP ImpRes resin	17546803	Cytiva, Danaher, USA
In-house Tris-Acetate buffer, pH 6.5-7.5	N/A	GSK, United Kingdom
Sodium hydroxide pellets	10743591	Acros Organics, Belgium
Trizma® base	T6066	Sigma-Aldrich, Germany
Hydrochloric acid, 37% v/v	20255.368	VWR, Avantor, USA
Sodium acetate trihydrate	3461-01	Avantor, JT Baker, Fisher Scientific, USA
Sodium chloride	64060500	Merck, Sigma-Aldrich, Germany
Ambr CF Filter 30,000 MWC0 HY	3MA1445910	Sartorius, Germany
In-house histidine formulation buffer, containing trehalose and arginine, pH 6	N/A	GSK, United Kingdom
Acetic acid	695092	Sigma-Aldrich, Germany
Sodium Octanoate	C5038	Sigma-Aldrich, Germany

Sodium phosphate	342483	Sigma-Aldrich, Germany
Millipore® Steriflip® Vacuum Tube Top Filter	SCGP00525	Millipore, Sigma-Aldrich, Germany
Biophysical characterisation		
Urea 8M	97063-804	VWR, Avantor, USA
Pharmolytes pH 3-10 and pH 8-10.5	17045601 and 17045501	Cytiva, Danaher, USA
pI markers 4.65, 6.61, 8.18, 9.46, 9.77	102223, 102409, 102408, 102349, 102219	Bio-Teche, Proteinsimple, USA
iCE System Suitability Kit	102093	Bio-Teche, Proteinsimple, USA
Methyl cellulose 0.5% w/v and 1% w/v	102505 and 101876	Bio-Teche, Proteinsimple, USA
iCE Electrolyte Kit	102506	Bio-Teche, Proteinsimple, USA
Recombinant IL-8/CXCL8 Protein (carrier free)	208-IL-050/CF	R&D Systems, USA
Tween 20	P1379-1L	Sigma-Aldrich, Germany
Dulbecco's phosphate buffered saline (DPBS)	11593377	Gibco, Thermo Fisher, USA
Biacore CM3 dextran chip	BR100536	Cytiva, Danaher, USA
Amine Coupling Kit	BR100050	Cytiva, Danaher, USA
Glycine	G2879	Sigma-Aldrich, Germany
Guanidine hydrochloride 6M	SRE0066	Sigma-Aldrich, Germany
20 nm gold nanoparticles	15705	Ted Pella Inc., USA
Poly(ethylene glycol) methyl ether thiol (2000 Da)	729140	Sigma-Aldrich, Germany
Goat anti-human Fc and whole goat IgG (polyclonal)	109-005-098, 109-005-088	Jackson ImmunoResearch, USA
Millex-GP Syringe Filter Unit, 0.22 µm, PES	SLGPR33RS	Millipore, Sigma-Aldrich, Germany
Methanol	20846.292	VWR, Avantor, USA
Folded Capillary Zeta Cell	DTS1070	Malvern Panalytical, UK
Ammonium sulfate	7783-20-2	Avantor, JT Baker, Fisher Scientific, USA
Potassium phosphate tribasic	P5629	Merck, Sigma-Aldrich, Germany
PolyLC PolyPROPUL 4.6 x 100 mm column	104PR0215	PolyLC inc., USA
TSKgel Super SW3000, 4.6 x 300 mm column	18675	TOSOH BioScience, USA
Sodium phosphate	342483	Sigma-Aldrich, Germany
Trypsin	V5111	Promega, USA
Chymotrypsin	V1062	Promega, USA
Dithiothreitol (DTT) 1M	P2325	Thermo Fisher Scientific, USA
ACQUITY UPLC PEPTIDE CSH C18 column	186006938	Waters, USA
0.1% v/v Formic Acid	10429474	Thermo Fisher Scientific, USA
Acetonitrile	15329865	Thermo Fisher Scientific, USA
Calcium chloride dihydrate	21102	Sigma-Aldrich, Germany
Trizma® base	T6066	Sigma-Aldrich, Germany

Prometheus NT.Plex nanoDSF Grade Standard Capillaries	PR-AC002	NanoTemper Technologies, Germany
Unchained Labs Stunner plates	MSPP701-2022	VWR, Avantor, USA
Unchained Labs Lunatic plates	MSPP701-2001	VWR, Avantor, USA
NIST mAb	RM 8671	National Institute of Standards and Technology, MD, USA

2.5. Methods

2.5.1 Computational methods

In silico homology modelling and antibody molecular descriptor calculations were performed in the Molecular Operating Environment (MOE) software, version 2020.0901 (Chemical Computing Group, Montreal, Canada).

Homology modelling of IgG1 wild-type

Full sequences of the heavy and light chains of an immunoglobulin G1 (IgG1) wild-type (WT) molecule were inputted as FASTA format into the MOE sequence editor and annotated with a Kabat numbering scheme. The Antibody modeller in MOE (version 2020.0901) was used to search for similar sequences with solved antibody structures as a template for homology constructs. The variable fragment (Fv) of anti-IL-8 mAb is published as PDB ID: 5OB5 (fAb complex with GroBeta). Fv fragments and full IgG structures were modelled by selecting 'variable domain' and 'immunoglobulin' model types, respectively. The immunoglobulin model type uses the 1IGY PDB structure as a template to model the Fc region. A refinement gradient limit value of 1 was applied, and C-termini were capped with neutral residues, and superimposed to confirm alignment of structures. Partial charges were added to all atoms, and energy minimization performed using the AMBER10:EHT default forcefield. The Protein Silo (PSILO) database was used to locate sites of hydrogen bonding and other potential interactions with the GroBeta ligand in complex with the Fv.

Patch analysis and identification of the mutant panel.

The protein patch tool in MOE was applied to the wild-type Fv homology construct to identify electrostatic and hydrophobic surface patches contributing to protein-protein interactions (PPIs). To aid visualisation of smaller surface patches, parameter thresholds were adjusted from the default values to a hydrophobic cut-off of ≥ 0.09

kcal/mol, a hydrophobic min area of $\geq 30 \text{ \AA}^2$, a charge cut-off of $\geq 30 \text{ kcal/mol/C}$, a charge min area of $\geq 30 \text{ \AA}^2$, and a probe sphere radius of 1.8 \AA . The residue contribution to surface patches was analyzed using the Protein Properties tool, selecting the 'res_hyd', 'res_pos' and 'res_neg' descriptors. The top scoring residues were then selected as candidate residues for mutations, excluding terminal residues (**Appendix 1 Table 7.1**). Any residues previously observed in the PSILO database to directly interact with the GroBeta ligand (CXCR2), were eliminated from the list of top-scoring residues. The substitution strategy was informed from prior work using computational approaches to introduce viscosity-reducing mutations.^{229,232,233} Three approaches were implemented to alter surface area coverage of charge distribution profiles, by **i**) targeting aromatic hydrophobic residues and their substitution to leucine or glutamine (L or Q),²³² and **ii**) substituting positively-charged residues (e.g., N or R) to glutamic acid or glycine (E or G),²²⁹ and **iii**) substituting negatively-charged glutamic acid or aspartic acid (E or D) to positive residues (e.g. Q or N).²³³ The Residue Scan tool in MOE was used to introduce point mutations in the WT anti-IL-8 Fv IgG1 sequence to generate mutant variant models. Patch analysis was performed in the same manner for each of the mutant variant models (**Appendix 1 Table 7.2**).

Computational prediction of physicochemical descriptors.

Various physicochemical descriptors (**Appendix 1 Table 7.3**) were computed for each Fv model using the Protein Properties tool in MOE. A NaCl concentration of 0.1 M was used in all simulations to mimic the ionic strength of the histidine formulation buffer (pH 6). Hydrophobic imbalance and buried surface area, Fv_chml values were generated through the BioMOE (version 2021-11-18, Chemical Computing Group, Montreal, Canada) module for which the models had been protonated to pH 6 using the QuickPrep tool.

TANGO aggregation propensity (<http://tango.crg.es/tango.jsp>).^{255,256}

The TANGO aggregation propensity tool was used to predict the sequence-based propensity for beta-sheet formation for all mutant sequences in this work.

Ranking of mutant variants

Candidate anti-IL-8 mutant variants were ranked using a min-max normalisation method to triage mutants for expression in CHO cells and comprehensive downstream analysis of the expressed mutant panel. Physicochemical descriptors were selected based on previously-established correlations with viscosity, and

weighted evenly. The physicochemical descriptors used were hydrophobic index, TANGO aggregation propensity, the normalised hydrophobic score (proportion of exposed hydrophobic areas (Res_hyd) to the total exposed surface area (Res_ASA), zeta potential, buried surface area between heavy and light chains (BSA) and the ensemble charge (ens_charge). Descriptor values were normalised between 0-1 (**Equation 2.1**).

$$NDV = \frac{x - x_{min}}{(x_{max} - x_{min})}$$

2.1

Where *NDV* is the normalised descriptor value for the individual mutant, *x* is the actual descriptor value for the individual mutant, and x_{min} and x_{max} are the actual minimum and maximum values found in the mutant panel for that descriptor.

A normalised score was calculated by summing each normalised descriptor value for descriptors correlating positively with elevated viscosity (**Equation 2.2**) or by summing 1- normalised descriptor value for descriptors correlating negatively with elevated viscosity (**Equation 2.3**). Therefore, a lower normalised score overall represented a reduced hypothetical viscosity.

$$Normalised\ score = SUM(NDV_{HI} + NDV_{TANGO} + NDV_{Tomar} + NDV_{Sharma} + NDV_{Normalised\ hydrophobic\ score})$$

2.2

$$Normalised\ score = SUM((1 - NDV_{zeta}) + (1 - NDV_{BSA}) + (1 - NDV_{ens_charge}))$$

2.3

DeepSCM (<https://github.com/Lailabcode/DeepSCM>).²⁵⁷ The spatial charge map is a scoring system used to rank antibodies exhibiting elevated viscosity at high solution concentrations in a crowded system, by calculating the charge of side chain atoms of exposed residues of a homology Fv model over molecular dynamics simulations.^{240,257} For this work, the anti-IL-8 IgG Fv sequences were inputted as separate heavy and light chain FASTA files and the code was ran in a terminal.

2.5.2 Protein Expression and Purification.

Chinese Hamster Ovary (CHO) K1 GS-KO (glutamine-synthetase-knockout) cells were used for expression of the anti-IL-8 mAb panel. Sequences for anti-IL-8 mAb

variants underwent codon optimisation and plasmid generation by Atum Biosciences (Newark, California, USA). The heavy and light chain genes were inserted into Leap-in Transposase® pD2500 vectors with the CMV promoter including glutamine synthetase (for selection) and heavy and light chain insertions were nucleofected into CHO cells. Cells were maintained under selection conditions as stable pooled cultures. A fed-batch production process (in up to 4 x 2.8L shake flasks per molecule) was employed over 15 days, with glucose and supplementary amino acid feeds added at various intervals. Expression media were harvested, and the supernatant clarified by centrifugation at 4 °C (4,000 g for 20 minutes) and depth-filtered, resulting in ~5.5L of unprocessed bulk per molecule. Protein L chromatography on an ÄKTA Avant 150 system (Cytiva, Danaher, USA) was used for purification, followed by a cation exchange polishing step to achieve ≥95% monomeric purity. The purified mAbs were concentrated, diafiltered and buffer exchanged into formulation buffer containing histidine, trehalose, and arginine (pH 6) to a final concentration of ≥100 mg/mL using the Ambr® Crossflow system (Sartorius, Germany). All mutants showed full solubility at 25 °C with no liquid-liquid phase separation observations.

2.5.3 Biophysical analysis of the anti-IL-8 mAb panel

Analysis of Monomeric Purity by Analytical Size Exclusion Chromatography (aSEC).

Samples were injected onto a TSKgel Super SW3000, 4.6 x 300 mm (TOSOH Bioscience, United States) column on an Agilent 1260 series HPLC, with 0.1M sodium phosphate containing 400 mM NaCl (pH 6.8) as the mobile phase. All samples were analysed at 5 mg/mL at a 0.2 mL/min flow rate and detected at 280 nm. The OpenLab CDS Data Analysis software (version 2.6, Agilent, California, US) was used to process and integrate the chromatograms. Areas under the chromatographic peaks were integrated to quantify the monomeric mAb, and high and low molecular weight species. The target monomeric purity of ≥95% was met by all WT and mutant anti-IL-8 molecules and aSEC was used to monitor physicochemical stability, by monitoring changes in chromatogram peak retention times and profiles for each molecule. Analysis of the expressed anti-IL-8 mutants showed retention times comparable to the anti-IL-8 WT IgG1 (~27.5 minutes), except for the D70N mutant, which had a consistent reduced retention time of ~26.6 minutes suggesting a slight increase in molecular size.

Analysis of identity by mass spectrometry.

The sequence and composition of the anti-IL-8 panel was verified using peptide fingerprinting mass spectrometry. 250µg of each sample was denatured with guanidine buffer (6M, pH 7.5), reduced with dithiothreitol (DTT 1M) and incubated for 20 minutes at ambient temperature. All samples were alkylated with 1M sodium iodoacetate and incubated for a further 30 minutes at ambient temperature and protected from light. A further reduction step was performed in DTT (1M), and the samples were desalted using Micro Bio-Spin 6 size exclusion columns (Bio-Rad, CA, USA). Samples were enzyme-digested with either trypsin or chymotrypsin (both sequencing-grade, Promega, WI, USA) at a 1:20 (w/w) ratio of trypsin or chymotrypsin: mAb in a digestion buffer containing 50 mM Tris, 1 mM calcium chloride dihydrate (pH 7.5). Samples were incubated at 37 °C under agitation for two hours, prior to liquid chromatography-mass spectrometry (LC-MS) analysis with an Orbitrap Exploris™ 240 Mass Spectrometer (Thermo Fisher Scientific, MA, USA), controlled by Xcalibur software (version 4.4.16.14, Thermo Fisher Scientific, MA, USA). An ACQUITY UPLC PEPTIDE CSH C18 (Waters, US) 1.7 µm, 2.1 mm x 150 mm column was used for separating digested peptides with a column temperature of 40 °C. Mobile phase A was 0.1% v/v Formic Acid LC-MS grade (Thermo Fisher Scientific, MA, USA) in LC-MS grade water and B was 0.1% v/v Formic Acid in Acetonitrile LC-MS grade (Thermo Fisher Scientific, MA, USA). Step wise gradients were applied with 5-40 %B (over 80 min), 40-100 %B (5 min), plateau of 100 %B (5 min), and a return to 5 %B (10 min). The flow rate was set at 200 µL/min and monitored at 214 nm by UV detection.

The Orbitrap Exploris 240 MS system was operated in the positive ion mode. Tandem MS/MS analyses were performed for the identification of peptide in data dependent mode. Full MS scan data acquired within a 200-2000 m/z scan range, 60,000 resolution over 100ms injection time, followed by 5 sequential MS/MS scan with orbitrap resolution target of 15000. A minimum intensity threshold was set to 1000 with a custom dynamic exclusion filter applied. Charge states were filtered to include charges of 2-8 and the number of dependent scans was set to 5. A 2 m/z isolation window was applied for the ddMS scan with HCD collision energies set to 20, 25 and 30% over 200 ms injection time. MS2 data acquired in profile mode. The MS2 AGC target was set at 100% whereas full scan AGC target was set at 300%. Byos software (version 5.0-88 (2022.12), Protein Metrics, CA, USA) was used to processing of

peptide fragments using the following parameters: Precursor Mass Tolerance set at 20 ppm, Fragment Mass Tolerance 1 and 2 set at 20 ppm, Cleavage Site(s) set as RK (trypsin) and WFLY (chymotrypsin), Missed Cleavages set at 2, Cleavage Side set as C-terminal and Fragmentation type set as QTOF/HCD. The post translation modifications (PTMs) screened for were methylation, oxidation, deamidation, pyroglutamate formation and N-glycosylation (glycosylation consistent at N299 in Fc across anti-IL-8 mAb panel).

Hydrophobic interaction chromatography.

Hydrophobicity of the mutant panel was assessed *via* hydrophobic interaction chromatography (HIC) with UV detection. A PolyLC PolyPROPUL 4.6 x 100 mm column was used on an Agilent 1260 series HPLC (Agilent, California, US). The mobile phase A consisted of high salt 1.3 M ammonium sulfate in a 50 mM potassium phosphate buffer (pH 7) with stepwise gradient segments, introducing a mobile phase B which consisted of 20% acetonitrile in 50mM potassium phosphate buffer (pH 7). All samples were analysed at 1 mg/mL (5 μ L injection) at 0.7 mL/min and detected at 214 and 280 nm.

Electrophoretic light scattering.

A Malvern Zetasizer (Malvern Panalytical, Malvern, UK) equipped with a 633 nm laser was used to measure zeta potential by electrophoretic light scattering. Default settings were an equilibration time of 120s, automatic attenuation and 10-100 measurement runs. A 60s pause was added between measurements and three technical replicate measurements were run. WT and mutant anti-IL-8 molecules were prepared at 5 mg/mL in formulation buffer and filtered prior to analysis. The corresponding refractive index for anti-IL-8 (protein) and the buffer (dispersant) were set at 1.59 and 1.33, respectively, with viscosity set at 1.26 mPa.s.

Binding analysis.

A Biacore 8K+ surface plasmon resonance (SPR) (Cytiva, Danaher, USA) was used to compare the association and dissociation rates, and affinity for IL-8 carrier-free antigen (R&D systems, USA) between the WT and mutant panel. IL-8 (0.5 μ g/mL) was immobilised onto one flow cell of a Biacore CM3 dextran chip (Cytiva, Danaher, USA). Ten start-up cycles were followed by ten antibody injections at a flow rate of 30 μ L/min and measurement temperature of 25 °C, and with a 240 second contact time, and following injection, dissociation was tracked over 900 seconds. All

antibodies (0.31-20 µg/mL) were formulated in phosphate-buffered saline containing 0.05% v/v Tween™ 20, with the same running buffer composition. Surfaces were regenerated between measurements using 10 mM glycine (pH 1.5) and 3 M guanidine. Sensograms were reference subtracted and fitted using a 1:1 Langmuir binding model in the Biacore Insight Evaluation software (version 4.0.8.20368, Cytiva, Danaher, USA).

To determine the apparent dissociation (k_a) and dissociation rate constants (k_d). The $\frac{k_d}{k_a}$ ratio was used to determine the equilibrium dissociation constant (K_D).

Diffusion self-interaction parameter.

A Stunner instrument (Unchained Labs, CA, USA) dynamic light scattering (DLS) setup was used to measure hydrodynamic size, polydispersity, and the diffusion coefficient for each antibody. Data were analysed using the Lunatic & Stunner Client software (version 8.1.0.254). The measurement temperature was set as 25 °C and five, 10-second measurements were acquired with a corresponding 1% extinction coefficient of 1.55AU*L/(g*cm) for all samples. Custom dispersant settings were applied (viscosity 1.26 cP and refractive index 1.33 at 20 °C) and all mAbs were prepared in formulation buffer (1-20 mg/mL) for WT and mutant variants. The Lunatic and Stunner software (v8.1.0.244) were used for data export, and the corresponding diffusion coefficients were measured at five concentrations to determine the interaction parameter (k_D) using linear regression plots.

$$D_{app} = D_0(1 + k_D c)$$

2.4

Where D_{app} refers to the apparent diffusion coefficient, D_0 the self-diffusion coefficient at infinite dilution, and k_D the interaction parameter.

Dynamic light scattering measurements were used to interpret the second virial coefficients (B_{22}) of each anti-IL-8 molecule:

$$\frac{Kc}{R} = \frac{1}{MwP_0} + 2B_{22}c$$

2.5

Where K is the optical constant, c is the concentration (g/mL), R is the Rayleigh ratio of scattered light to incident light, M_w is the molecular weight of the protein (g/mol), P_θ is the angular scattering dependence (assumed equal to 1).

Kc/R values per molecule were exported from the Stunner analysis software (v8.1.0.244, Unchained Labs, CA, US) and plotted over the concentration range tested (1-20 mg/mL). The slope of the linear regression was divided by 2 to generate B_{22} values.

Analysis of the anti-IL-8 charge distribution profile.

The charge distribution profile was measured using the iCE3 capillary isoelectric focusing instrument equipped with a PrinCE autosampler (Protein Simple, USA). A broad range of pI markers (pI 3.85-8.77) were used to capture all main isoforms and impurity isoforms for each sample (Bio-Tech, Protein Simple, USA). To minimise self-association, 2M urea and ampholytes (Bio-Tech, Protein Simple, USA) in the pH 3-10 and 8-10.5 ranges were used at a 1:1 ratio in the buffer mix. All samples were diluted to 1 mg/mL in deionised water prior to a final dilution to 0.4 mg/mL in analyte buffer. The iCE3 instrument was set to the following parameters: a pre-focus voltage of 1500 V; a 10-12-minute focus voltage of 3000 V; an autosampler and transfer capillary temperature of 15 °C; UV detection at 280 nm; a sample injection pressure of 2000 mbar; a pre-focus time of 1 min; and a focus time of 10-12 min. All data were imported to the Empower 3 software (v4, Waters, US) for data analysis.

Analysis of anti-IL-8 self-interaction.

Affinity-Capture Self-Interaction Nanoparticle Spectroscopy (AC-SINS) was used to estimate the propensity of self-association for the anti-IL-8 panel. Goat anti-human Fc and whole goat IgG antibodies (Jackson ImmunoResearch, PA, USA) were prepared in 20 mM acetate buffer (pH 4.3). The antibodies were each diluted to achieve a final concentration of 320 µg anti-Fc IgG and 80 µg goat whole IgG and mixed with 20 nM colloidal gold nanoparticle suspension (Ted Pella Inc., CA, USA, concentration 7.0×10^{11} particles /mL). The mixture was incubated for 90 minutes at ambient temperature, and 10 µM PEG2000 solution (Sigma-Aldrich, MO, USA) was added at a final 1% v/v concentration and incubated for 90 minutes followed by centrifugation at 13000 x g for six minutes. WT and mutant anti-IL-8 test samples were prepared at 50 µg/mL in phosphate buffered saline (Gibco, Thermo Fisher Scientific, MA, USA). Aliquots (99 µL) of each sample were added to wells of a 96-

well plate, with 11 μL of gold nanoparticle suspension added to each well, resulting in a final solution concentration of 50 $\mu\text{g}/\text{mL}$ test mAb, 10x bead:anti-Fc conjugate and 0.02 mg/mL PEG2000. All samples were mixed, incubated for 90 minutes and gently centrifuged to remove air bubbles. Following incubation, the absorbance spectra (450-650 nm) of the antibody-gold conjugates were measured using a Pherastar FSX (BMG Labtech Ltd., Germany) plate reader. The spectra were analysed with MARS software (v3.32, BMG Labtech Ltd., Germany), applying smoothing to the best fit curves and the difference in plasmon wavelengths for each sample was calculated. Experimental cutoffs included a <535 nm wavelength for negative controls (*i.e.*, buffer) to ensure nanoparticle aggregation, and a red shift of >10 nm was flagged as a mAb candidate being at a higher risk of self-association.

Analysis of unfolding temperatures.

Thermal differential scanning fluorimetry (DSF) measurements were performed using a Prometheus NT.48 (NanoTemper Technologies, Germany) equipped with back-reflection technology for the high-throughput analysis of unfolding temperature (T_m), calculated from the intrinsic fluorescence intensity ratio of tyrosine and tryptophan (350/330 nm) as a function of temperature.²⁵⁸ For each experiment, 20 μL of a 150 mg/mL sample was analysed. Prior to each experiment, the excitation power was set to achieve $\geq 5,000$ counts in the discovery scan. Corresponding profiles were analysed in the Prometheus NT.48 software and the first derivative calculated. A temperature ramp of $2^\circ\text{C}/\text{minute}$ from 20-95 $^\circ\text{C}$ was performed for each set of capillaries. Drop lines were assessed and corrected, to determine the first derivative peaks, marking the unfolding temperatures of antibody domains (T_{m1} to T_{m3}) and the unfolding onset (T_{onset}). The first derivative peak of the scattering profile marked the aggregation temperature (T_{agg}) values.

Viscosity measurement.

Viscosity curves were generated for the WT and mutant panel using the VROC Initium (Rheosense, United States), with an optimised protocol to measure viscosity samples using the 'Auto' shear rate function as well as at fixed shear rates of 100-2000 s^{-1} . The viscosity of all samples was measured at different concentrations to obtain viscosity-concentration profiles for each wild-type and mutant IgG molecule. Resulting data were filtered using the following inclusion criteria; no priming segments were included, the percent full scale was in the 5-95% range, the R^2 fit of the pressure

sensor position was ≥ 0.998 , and transient curves reached steady plateaus with no drift. Exponential-growth decay fits were applied to each viscosity-concentration curve.

Developability rankings

All biophysical data and *in silico* descriptors were normalised from 0-1 with min-max normalisation as per **Equation 2.1**. Sums of these scores per molecule were used to rank developability.

Statistical approaches.

GraphPad Prism (v5.04) was used for plotting scatter plots and bar graphs, and ANOVA statistical analysis to determine significant differences in experimental data. JMP Pro (v16.0.0, 2021) was used for the multivariate analyses of computational and experimental data to establish existing correlations.

2.6. Results

2.6.1 Generation of the anti-IL-8 mutant panel

Using homology models of anti-IL-8 mAb, the impact of targeting solvent-accessible hydrophobic and charged patches on solution viscosity was examined at high mAb concentration.^{229,232,233} Patch analysis of an anti-IL-8 mAb wild-type (WT) IgG1 homology model identified residues contributing to positive, negative, and hydrophobic patches as potential candidates for mutation. Computation of mutant physicochemical molecular descriptors and patch analysis were subsequently performed.

Homology modelling and patch analysis of WT anti-IL-8

Homology models of the full anti-IL-8 mAb structure and the variable fragment (Fv) of WT anti-IL-8 mAb were constructed in the MOE molecular modelling suite.²⁵⁹ Since the fragment antigen-binding region (Fab) crystal structure (PDB 5OB5) matched the framework and complementarity determining regions (CDRs) perfectly, patch analysis was conducted on resulting structures (**Figure 2.1a**). The surface potential mapped onto the anti-IL-8 mAb surface (**Figure 2.1b**), shows negative, positive, and hydrophobic patch distributions.

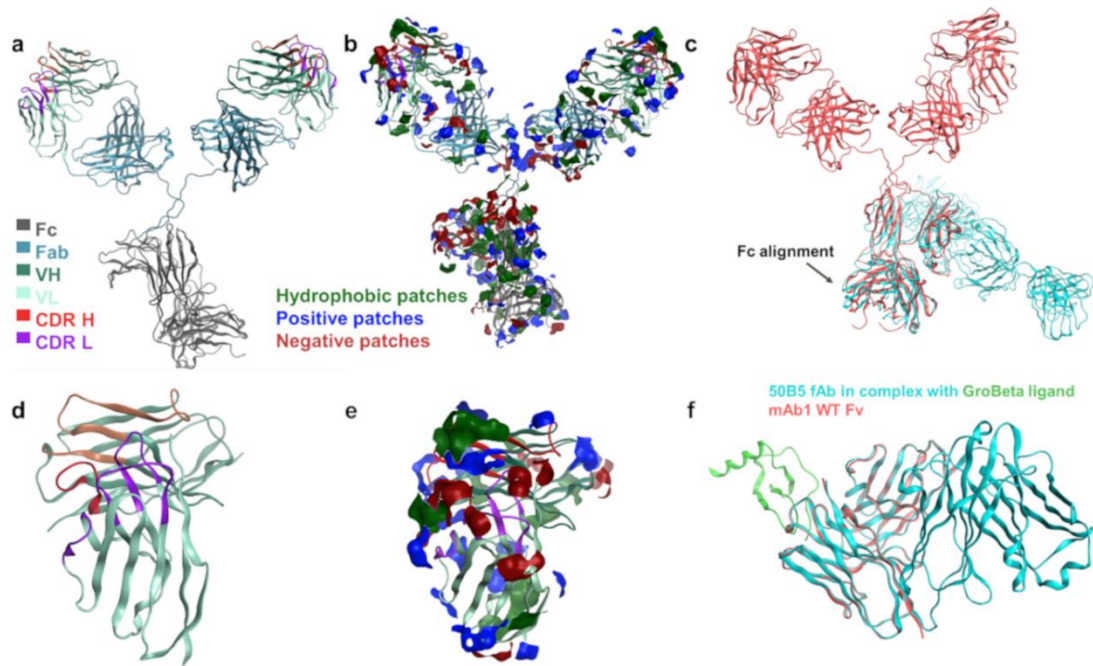


Figure 2.1 Homology models of anti-IL-8.

a, the full IgG structure was modelled using the PDB 5OB5 template for the Fab region and IgG model in the MOE platform. The Fc (grey), constant light chain 1 and heavy chain 1 (blue), variable heavy chain (dark green) variable light chain (light green), heavy chain CDRs (red) and light chain CDRs (purple) with Kabat annotation. **b**, the hydrophobic (green), positive (blue), and negative (red) patches applied onto the full IgG1 homology model to show exposed surface non-polar and charged regions. **c**, superimposition and alignment of the anti-IL-8 WT full IgG homology model (pink) onto the template 1IGY PDB IgG1 structure (blue) to model Fc structure. **d**, modelling of the Fv region. **e**, patch analysis of the Fv to aid identification of candidate sites for single-point mutation. **f**, alignment of the WT Fv homology construct (pink) onto the template 5OB5 PDB fAb structure (blue) in complex with the GroBeta ligand (green).

Overall, the largest contribution to the surface potential of WT anti-IL-8 mAb IgG (**Figure 2.1b**) was from hydrophobic (3,790 Å²), positive (2,940 Å²) and negative (2,250 Å²) patches, with a net charge of +22.68 C (pH 6). A similar trend was seen with the anti-IL-8 Fv (**Figure 2.1d and e**), with surface area coverage of 520, 160, and 50 Å² for hydrophobic, positive and negative patches, respectively, and a net charge of +0.05 C (pH 6). Mutant residues in the anti-IL-8 framework and CDRs significantly disrupting hydrophobic, positive, and negative patches were identified (**Appendix 1 Table 7.1**), which can potentially influence protein-protein interactions and self-association.

Patch analysis of anti-IL-8 mutants

The effects of single point mutations on anti-IL-8 charge and hydrophobic patch distributions, was examined by introducing Fv point mutations. Employing strategies targeting positive, hydrophobic, and negative patches, changes in electrostatic surface potential following framework region and CDR mutations were observed (**Figure 2.2**).^{229,232,233} The anti-IL-8 Fv carries a net positive charge (+0.05 C, pH 6.0), with heterogeneous surface charge distribution, resulting in asymmetry between heavy and light chain net charges (3.93 C and -1.23 C, respectively). Patch analysis of the WT Fv revealed significant hydrophobicity (520 Å², 38% of Fv patches) with prevalent surface coverage by positive patches (blue) (39% of Fv patches) (**Appendix 1 Table 7.2**).

Residues with the highest contributions to positive (blue), negative (red), and hydrophobic (green) patches were identified from patch analysis of the anti-IL-8 WT Fv homology model. Key residues for sequence-based modification included those contributing to positive (blue) (e.g., K42, K23, R18, K13, R85 and R70 for the framework region, and R53 and K63 for CDRs), negative (red) (e.g., D70, E10, E87, D17 for the framework region, and E30A, D56, Q27 and D28 for CDRs) and hydrophobic (green) (e.g., F83, L110, V11, V5 for the framework region, and W32, Y99, F57 and Y55 for CDRs, **Appendix 1 Table 7.1** and **Table 7.2**) patches.

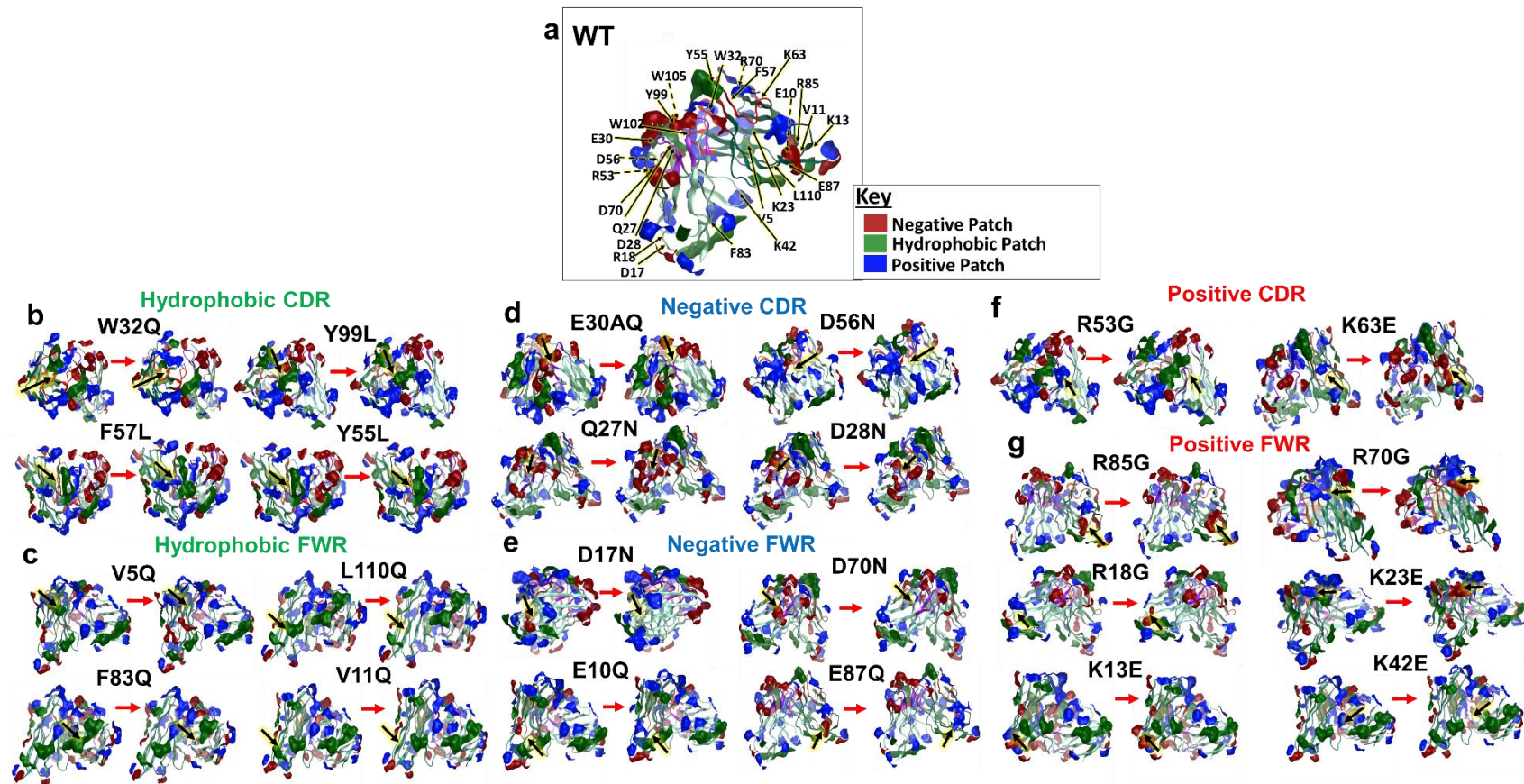


Figure 2.2 Patch analysis of mutant candidates.

a, WT and mutant Fv homology models disrupting **b**, **c**, hydrophobic patches (green), **d**, **e**, negative patches (red), and **f**, **g**, positive patches (blue). VL (light green), VH (dark green), heavy chain CDRs (red), and light chain CDRs (purple). The WT (left) and corresponding mutant (right) are represented for each molecule. Arrows show the location of the single point mutation. Dashed lines: residues behind the field of view.

Global patch analysis of anti-IL-8 Fv mutants (**Figure 2.2**) revealed that RàG and KàE mutants (positive patch-targeting²²⁹) exhibited reduced positive patch coverage, while V/W/L/FàQ and F/YàL mutants (hydrophobic patch-targeting²³²) showed reduced hydrophobic patch area coverage. DàN and EàQ mutants (negative patch-targeting²³³) displayed a reduction in negative patch area coverage. However, these mutations did not exclusively impact the targeted patch, with depletion and enhancement of neighbouring patches being observed. This is exemplified by changes in proportional patch percentages (**Appendix 1 Table 7.2**); for example, R53G (positive patch targeting) reduced patch_pos% from 39% to 36%, but saw an increase in patch_hyd% from 38% to 41%.

Next, physicochemical molecular descriptors for all candidate mutant Fv homology structures were computed, some of which have shown prior positive or negative correlations with viscosity (**Appendix 1 Table 7.3**).^{237,238} Charge-based mutant Fvs resulted in changes in predicted net charge, ensemble charge (*ens_charge*), zeta potential, isoelectric point (*pl_seq* and *pl_3D*), and light and heavy chain charge imbalance (*Fv_chml*) (**Appendix 1 Table 7.4**). Significant differences in hydrophobicity descriptors were observed with mutants targeting hydrophobic patches (**Appendix 1 Table 7.5**).²³² The therapeutic antibody profiler (TAP)^{241,260} was used to predict developability risk for each candidate mutant (**Appendix 1 Figure 7.1**). All mutants were amber-flagged for hydrophobic patches near CDRs, red-flagged for a positive patch targeting mutant (K42E) and a hydrophobic patch targeting mutant (W102Q). Charge symmetry was also evaluated, with three positive patch-targeting mutants (K42E, R18G and R53G) being amber flagged. From TAP analyses, the W102Q, R18G, R53G and K42E mutants were identified as the '*least developable*' candidates.

Light chain-heavy chain charge separation

Shifts in charge distribution profiles were observed as reflected in *Fv_chml* and *FvCSP* descriptors, which indicate charge imbalances between heavy (VH net charge) and light chains (VL net charge). In all cases, VL net charge was negative (-1.23 C for the anti-IL-8 WT) and VH net charge was positive (+3.93 C for the anti-IL-8 WT). Since *FvCSP* is a product of VH and VL charges, a larger difference was seen with negatively charged VL mutants. For example, with VL and VH charges at -1 C and -4 C, respectively, a 1 C drop in VL net charge reduced *FvCSP* from -4 to -8 C.

A 1 C reduction in VH net charge reduced *FvCSP* from -4 C to -3 C. When net charges of either VL or VH chain were 0, *FvCSP* was 0, potentially misinterpreted as no existing charge differences between chains.²⁴² This highlights the importance of *Fv_chml* descriptors, which subtract VL charge from VH charge.

Mutants targeting negative patches in VL,²³³ resulted in a ≤ 0.91 C charge increase, with a similar increase seen for VH mutants. For nearly all VL DàN mutants, an increased *FvCSP* and reduced *Fv_chml* was observed, suggesting enhanced charge symmetry between VH and VL chains. However, VH EàQ mutants showed a reduction in *FvCSP* and increased *Fv_chml*, indicating increased charge imbalance, absent in Q27N.

Conversely, mutants targeting positive patches²²⁹ exhibited increased VL negative charge (K42E: -1.9 C), resulting in more negative *FvCSP* and increased *Fv_chml* descriptors. VH mutants had reduced VH charge, approaching VL charge (~ 3 C), leading to increased *FvCSP* and decreased *Fv_chml*, reflecting reduced charge imbalance between VL and VH. Mutants primarily targeting hydrophobic patches²³² resulted in *FvCSP* and *Fv_chml* comparable to anti-IL-8 WT. These data emphasise that single-point mutations in VL versus VH depend on parent WT mAb initial charge symmetry and must be evaluated on a case-by-case basis.

Triage of candidate mutants

The anti-IL-8 mutant panel was ranked using a summed normalised score, guiding our selection of mutants for expression and physicochemical measurements (**Appendix 1 Table 7.7**). Two hydrophobic-targeting mutants, four negative patch-targeting mutants, and two positive patch-targeting mutants were selected for expression and subsequent formulation at high concentration (>200 mg/mL). The W32Q mutant, disrupting hydrophobic patches, was expected to significantly reduce viscosity relative to anti-IL-8 WT, while mutants disrupting positive patches (R53G and K42E) would likely show increased viscosity at high concentrations.

2.6.2 Biophysical Parameters of the Expressed Mutant Panel

The goal of this chapter was to establish a comprehensive measurement pipeline for the expressed anti-IL-8 mutant panel, correlating these observations with predicted physicochemical descriptors and viscosity-related parameters to understand factors underlying elevated viscosity in high-concentration antibody formulations. The

sequence identity and post-translational modifications of WT and anti-IL-8 mutants were confirmed *via* mass spectrometry-based peptide mapping (**Appendix 1 Table 7.8**). Additionally, all mutants met the monomeric purity threshold by aSEC ($\geq 95\%$,) (**Appendix 1 Table 7.9**). Apart from W32Q (CDRH2 mutant), mutants retained antigen binding affinity and kinetics equivalent to WT anti-IL-8 (**Appendix 1 Table 7.10**). Next, the mutants were analysed for their hydrophobic, colloidal, electrostatic, and conformational properties.

Electrostatic properties of the anti-IL-8 mutant panel and the correlation between predicted and experimental parameters.

Therapeutic antibodies are typically formulated at high concentrations in the pH 5.2-6.3 range, where the constant regions exhibit a positive net charge, driving repulsive interactions. Variations in charges within the variable region can influence viscosity at high concentrations.^{161,237}

Two strategies were employed to generate mutants, targeting positive and negative patches. Therefore, the electrostatic properties of the mutant anti-IL-8 panel were measured and correlated with their viscosity-concentration profiles. Predicted net charge, isoelectric point (pI), and zeta-potential based on anti-IL-8 Fv (**Appendix 1 Table 7.4**) were compared with experimental measurements (**Figure 2.3**).

Spatial charge distributions of mutants were visualised with two-dimensional maps (**Appendix 1 Figure 7.2 and Table 7.6**) to track changes resulting from single point mutations. For example, the D17N mutation led to the loss of a 30 Å² negative patch and a similarly sized hydrophobic patch, with adjacent positive patch surface distributions shifting (WT 2D map numbers 9 and 18 to D17N 2D map numbers 10 and 6). Changes in measured isoelectric point (pI) were observed, with increased charge for negative patch disrupting mutants, decreased charge for positive patch disrupting mutants, and no significant changes for hydrophobic patch disrupting mutants (**Figure 2.3e**). Most anti-IL-8 mutants displayed a negative zeta potential (**Figure 2.3f**), except for W32Q and D56N, which had a positive zeta potential. D17N and R53G showed significant increases in zeta potential, while K42E (a positive patch-disrupting mutant) exhibited a reduced zeta potential relative to the WT.

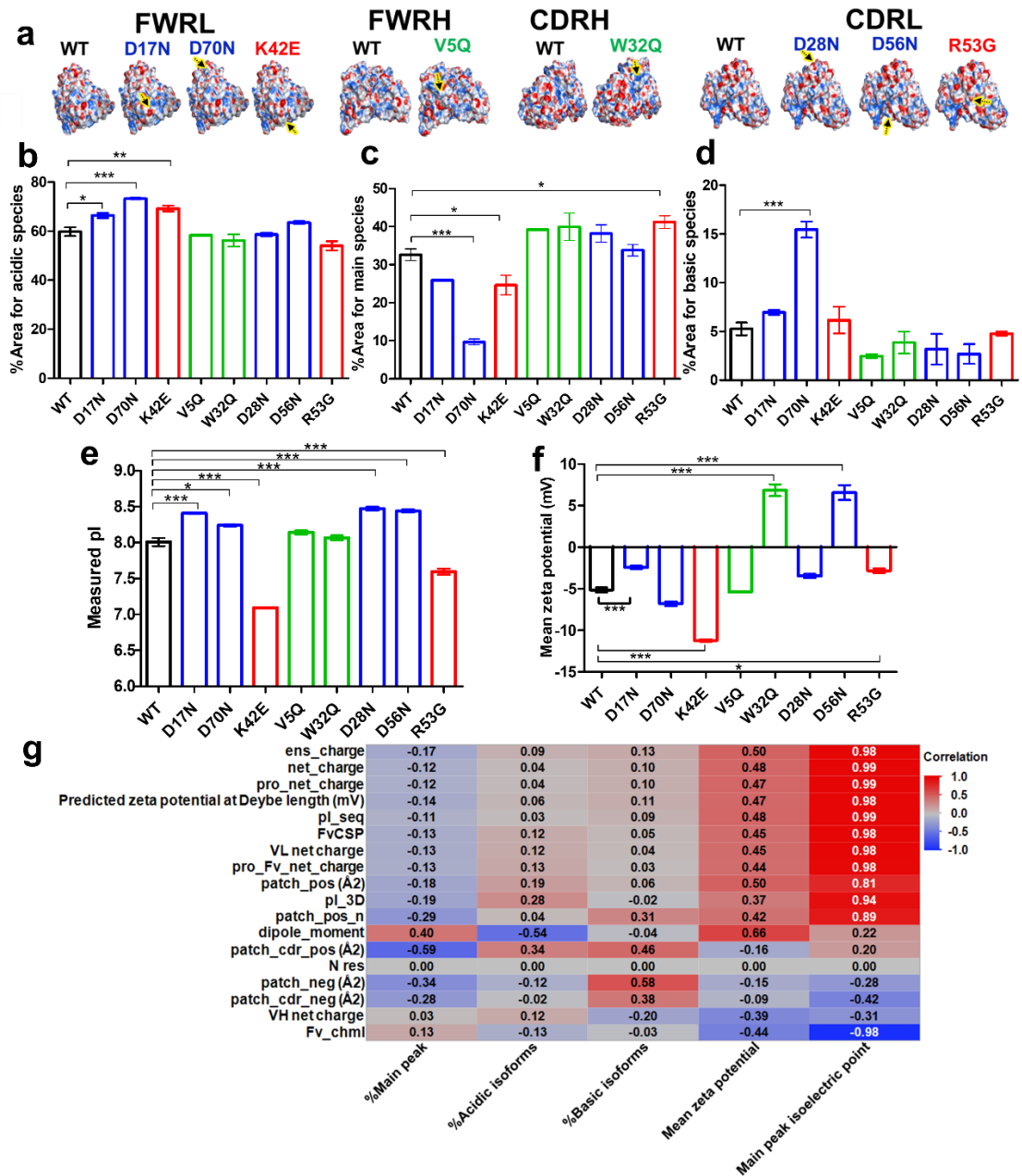


Figure 2.3 Negative and positive patch disrupting mutants show a strong correlation between predicted and measured pI.

a, Poisson-Boltzmann surfaces mapped onto all Fv models, demonstrating the impact of single-point mutations on electrostatic distributions marked by an arrow. **b-f**, Charge-based profiling of the mutant panel with cIEF. Error bars represent standard deviation (N=2) **g**, correlation analyses of *in silico* and experimentally derived charge based parameters. A one-way ANOVA with Dunnett's comparison test was used to compare mutants with the WT. *** denotes a P<0.001, ** P<0.01, * P<0.1. Non-significant differences are not represented. R

values were computed from the linear regression of *in silico* molecular descriptors and experimental values.

Experimental charge data were correlated with predicted *in silico* zeta potential and pI descriptors using linear regression (**Figure 2.3g**). While no correlation was found between the predicted and experimental zeta potential (Pearson correlation coefficient, $R = 0.47$), a strong positive correlation was observed for sequence- and structure-based pI descriptors and measured pI ($R = 0.99$ and 0.94 , respectively).

Hydrophobicity of the mutant anti-IL-8 panel and correlations between predicted and measured parameters.

Hydrophobic interactions drive protein-protein interactions and self-association at high formulation concentrations, potentially leading to elevated viscosity. Therefore, alterations in hydrophobic surface area coverage were explored as a strategy to reduce viscosity, correlating predicted hydrophobicity descriptors with experimental measures.²³²

Using Hydrophobic Interaction Chromatography (HIC), changes in hydrophobicity were investigated for the mutant panel. A reduction in hydrophobicity was predicted for mutants targeting hydrophobic patches, and smaller changes for those targeting charged patches (**Figure 2.4** and **Appendix 1 Table 7.5**). A shorter retention time was observed for W32Q, consistent with predicted reduction in hydrophobicity. Unexpectedly, D70N also showed reduced retention time compared to WT, contrary to predictions. Interestingly, V5Q, predicted to have reduced hydrophobicity, exhibited longer retention time. However, this contradicted predictions, possibly due to differences in targeted hydrophobic patch sizes. Mutants in the CDRL region (D28N, D56N and R53G) showed longer retention times, correlating with spatial hydrophobicity profiles (**Appendix 1 Figure 7.2** and **Table 7.6**). Using correlation analysis, a strong correlation ($R = 0.87$) was seen between normalised hydrophobicity score and summed residue contributions to hydrophobic patch area (*res_hyd*), offering insights into ranking the hydrophobicity of anti-IL-8 mutants.

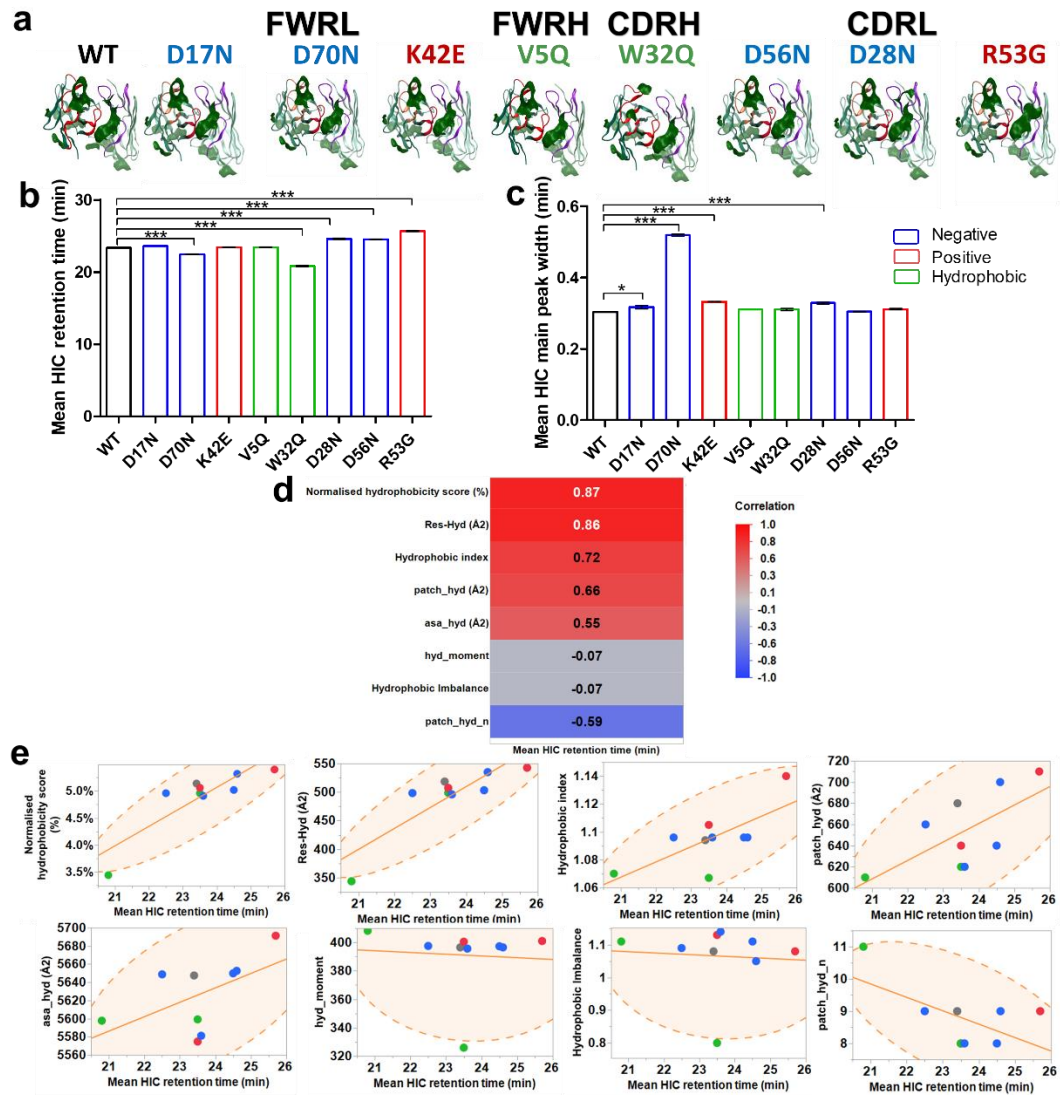


Figure 2.4 Hydrophobic Interaction Chromatography (HIC) of WT and mutant anti-IL-8 panel and correlation with predicted hydrophobicity molecular descriptors.

a, Protein patch surface maps depicted for all mutants, filtered for hydrophobic patches (green). **b**, HIC retention time and **c**, corresponding HIC peak widths for the anti-IL-8 mutants. Error bars represent standard deviation (N=2). A one-way ANOVA with Dunnett's comparison test was used relative to WT (***) denotes a $P < 0.001$, * $P < 0.1$). Non-significant differences are not represented. **d**, correlation analysis between *in silico* hydrophobicity descriptors and experimental retention time for anti-IL-8 mutants. **e**, scatterplots showing linear correlations for anti-IL-8 mutants with $P = 0.95$ bivariate density ellipses. All antibodies

are colour-coded according to mutants targeting positive (red), negative (blue), and hydrophobic (green) patches.

Conformational Stability of the Mutant Anti-IL-8 Panel

Intrinsic fluorescence differential scanning fluorimetry (DSF) was used to measure the effects of single-point mutations on anti-IL-8 mAb conformational stability. First derivative 350/330 nm ratio traces and scattering traces were used to calculate the unfolding onset temperature (T_{onset}), melting temperatures, and the temperature of aggregation onset (T_{agg}). Overall, mutants showed comparable thermal stability, except for W32Q and R53G (**Appendix 1 Figure 7.5**). W32Q (hydrophobic patch-targeting) exhibited decreased T_{onset} , T_{agg} and T_{m1} , suggesting reduced thermal stability. This reduction may stem from the disruption of a large hydrophobic patch (150 Å²), critical for stabilising the CDRH2 domain secondary/tertiary structure. R53G (positive patch-disrupting mutant), also showed reduced thermal stability (decreased T_{onset}).

Propensity for interactions promoting self-association.

AC-SINS and high throughput diffusion self-interaction parameters (k_{D}) were used to determine diffusion coefficients (**Appendix 1 Figure 7.6**) as surrogate measures of propensity for protein-protein interactions (**Figure 2.5**).

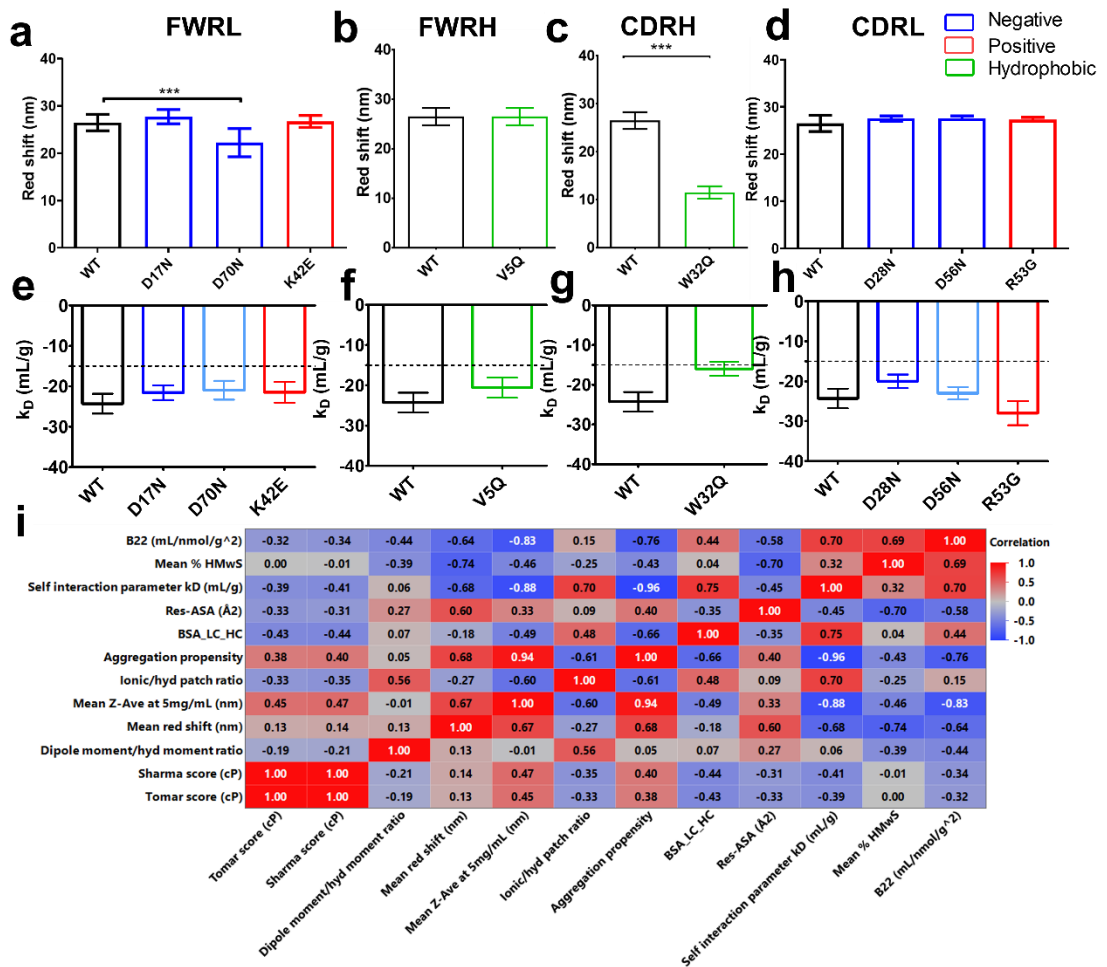


Figure 2.5 WT and mutant propensity for self-association measured with AC-SINS and self-interaction parameter (k_D), categorised by mutation location, and mutation strategy.

All antibodies are colour-coded according to mutants targeting positive (red), negative (blue), and hydrophobic (green) patches. **a-d**, corresponding AC-SINS data (N=4) **e-h**, the self-interaction parameter calculated from analysis of diffusion coefficients measured by DLS (1-30 mg/mL). Error bars represent standard deviation (N=2). A dotted line at -15 mL/g represents an arbitrary threshold for k_D . A one-way ANOVA with Dunnett's comparison test to WT (***) denotes a $P < 0.001$, ** $P < 0.01$. Non-significant differences are not represented. **i**, correlation heatmap.

AC-SINS detects self-association by red shifts in UV-Vis spectra (**Figure 2.5**), indicating increased particle size. Compared to the anti-IL-8 WT, D70N and W32Q mutants showed reduced red shift in absorbance measurements (**Figure 2.5a, c**), suggesting decreased self-association propensity.

The k_D parameter, indicative of protein-protein interaction risk, was comparable to WT for all mutants except W32Q, which, although not statistically significant, had a notably higher k_D (>-15 mL/g), signifying reduced short-range attractive self-interactions.²⁶¹ (**Figure 2.5g**). This was consistent with a less negative second virial coefficient (B_{22}) for W32Q (**Appendix 1, Figure 7.11**) Overall, both AC-SINS and k_D data suggest reduced aggregation risk for W32Q.

TANGO aggregation propensity scores, serving as *in silico* predictors of aggregation, negatively correlated with k_D , soluble aggregates (high molecular weight species, %HMwS) and hydrodynamic diameter (Z-Ave) (**Figure 2.5i**), indicating solvent exposure plays a key role in driving mAb self-association.²³⁵

Viscosity-concentration profiles of anti-IL-8 mutants.

The viscosity of the anti-IL-8 panel was analysed at various concentrations using microfluidic rheometry and compared to the WT molecule. Newtonian behaviour was observed across shear sweep experiments, so average apparent viscosities were determined with exponential growth fits (**Figure 2.6**). Among the mutants, D70N (negative patch-disrupting FWRL) and W32Q (hydrophobic patch-disrupting CDRH), showed reduced viscosity compared to WT.

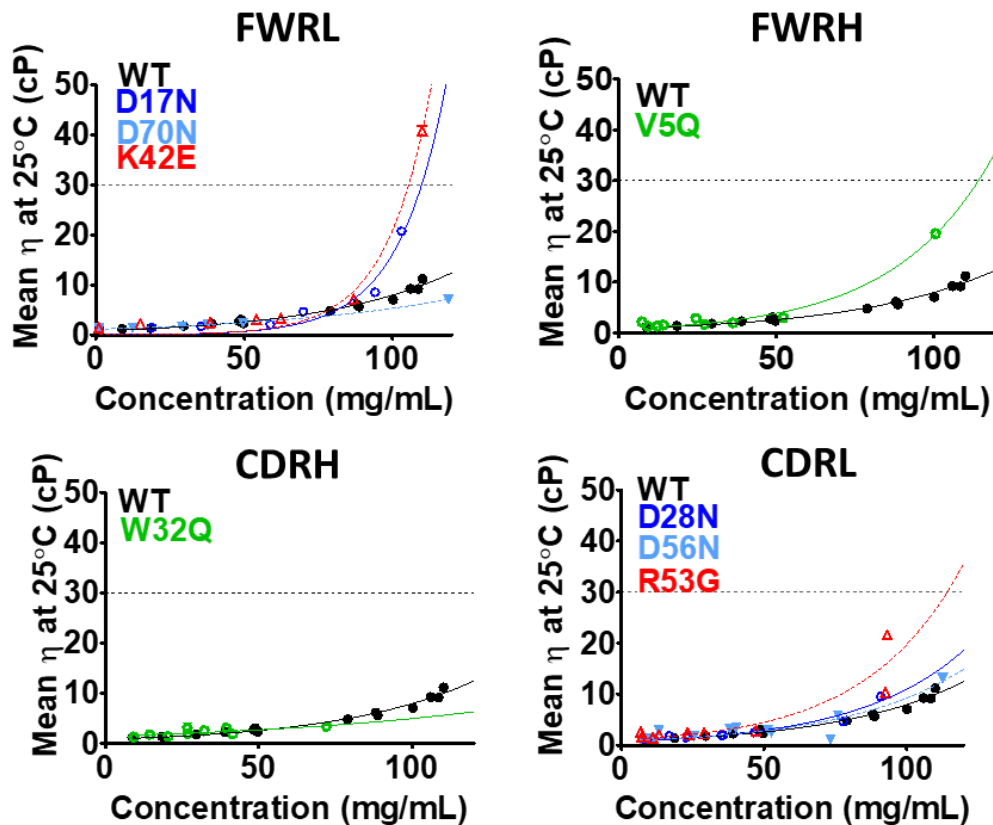


Figure 2.6 Mean apparent viscosity-concentration profiles measured at 25 °C for all anti-IL-8 variants (<120 mg/mL).

Dotted grey line at 30cP represents 'acceptable viscosity'. All measurement data were fitted to exponential growth equations through a least squares fitting method. Error bars represent standard deviation (N=2).

Correlating in silico descriptors with biophysical characterisations

All molecular descriptors used for designing anti-IL-8 mutants were correlated with their biophysical characteristics (**Figure 2.7**). For charge-based *in silico* descriptors, the strongest correlations were observed with mean *experimental pI* (**Figure 2.3**). Weak negative correlations were noted between *net charge* and *pI_seq* and the *mean apparent viscosity* (R= -0.6). A strong negative correlation was found between *patch_cdr_pos area* and the *mean hydrodynamic diameter* (R= -0.85).

Regarding hydrophobicity-based descriptors, strong correlations were observed with *HIC retention time* (**Figure 2.4**), affinity (KD), AC-SINS red shift and the self-association parameter k_D . Some strong correlations were also noted between *res_hyd* (R=0.89), *normalised hydrophobicity scores* (R=0.88), and *hydrophobic*

patch counts (Fv and near CDRs) ($R=-0.94$ and -0.79 , respectively) with the T_{m1} *unfolding temperatures*, suggesting the influence of exposed hydrophobic patches on conformational stability of the mutants. The number of hydrophobic patches near CDRs was correlated with the *temperature of aggregation onset* (T_{agg}). Additionally, a correlation was observed between the *number of hydrophobic patches* and the *% high molecular weight species* from the aSEC analysis ($R=0.86$), aligning with hypotheses on the impact of hydrophobic interactions in the mechanism for aggregation.^{262,263} Strong correlations were observed with TANGO aggregation propensity scores to hydrodynamic diameter ($R=0.94$), HIC retention time ($R=0.83$) and k_D ($R=-0.8$). Finally, strong negative correlations were seen with Tomar and Sharma viscosity models, and experimental pls (-0.98), which is expected as these models are primarily based on charge-related parameters.

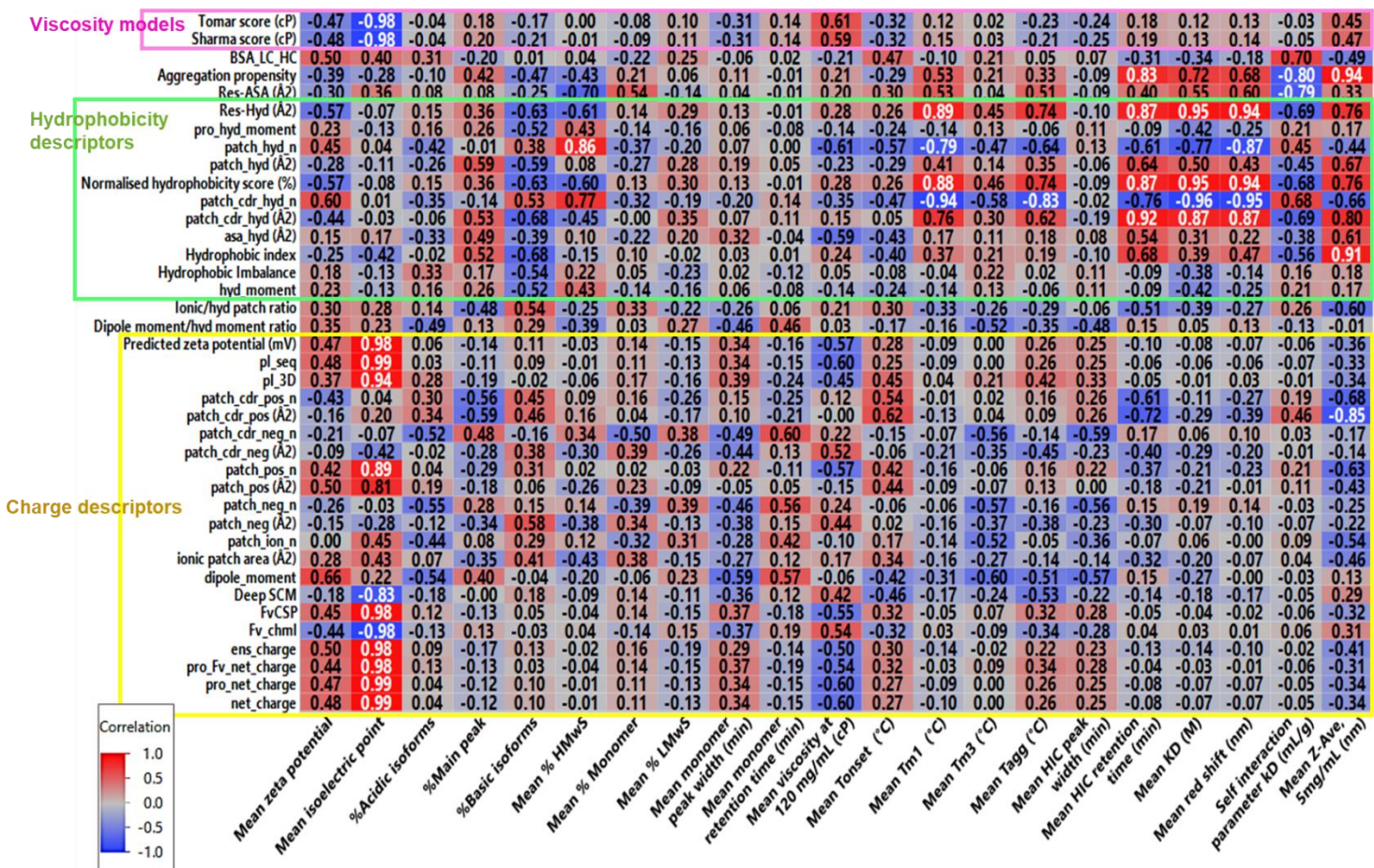


Figure 2.7 Correlation heat map between *in silico* descriptors to experimental parameters for anti-IL-8 mAb panel.

Correlation heat map values are reported with strong correlations ($R > \pm 0.8$) in white font.

2.7. Discussion

In this chapter a combination of computational and experimental approaches were used to assess how single-point mutations affect surface exposed electrostatic parameters, hydrophobicity, colloidal, and viscosity behaviour at high formulation concentration in an anti-IL-8 model antibody. Three sequence-structure based strategies were implemented to design mutants based on targeting charged (positive and negative) and hydrophobic patches, so that their effectiveness in predicting developability risks could be compared.^{257,264} Controlling protein-protein interactions known to govern elevated solution viscosity at high formulation concentrations was a particular focus of these efforts.

In silico predictions of anti-IL-8 physicochemical descriptors revealed notable changes in surface-exposed charged and hydrophobic patches. While mutations in the CDR have previously been associated with reduced mAb viscosity and antigen affinity loss, we expanded our screening to include mutants in the anti-IL-8 heavy and light chain framework regions (**Appendix 1 Table 7.10**)^{178,251} Except for W32Q (a CDRH mutation), seven mutants (87.5%) maintained binding affinities for IL-8 equivalent to the WT anti-IL-8 mAb (3.9 nM). W32Q, however, exhibited a five-fold reduction in hydrophobic patch area coverage, suggesting a critical role for tryptophan in antigen binding. This observation aligns with prior studies, where substituting the tryptophan with non-polar and polar amino acids retained binding affinity for phenylalanine mutants, emphasising the importance of the aromatic ring in antigen binding.²⁶⁵

The monomeric purity and aggregation status were acceptable for all anti-IL-8 mAb mutants and equivalent to the WT. Overall, point mutations in the anti-IL-8 mAb positive and negative patches significantly altered surface potential, inferred colloidal stability, charge heterogeneity and net charge (**Figure 2.3**).

Charge-disrupting mutants do not mitigate for elevated viscosity at high-concentration

Adjusting the electrostatic surface potential of mAbs is routinely explored during formulation development, focusing on buffer composition, which alters the excluded volume of the protein in solution (the secondary electroviscous effect).^{266,267} Chow *et al.*²²⁹ demonstrated viscosity reductions in an IgG4 Fab fragment by reducing charge imbalance across the Fv (R→G and K→E mutants), indicating the impact of positive

patch disruption on protein-protein interactions. Conversely, Apgar *et al.*²³³ observed viscosity reduction in mAbs by reducing negative charge, as evidenced by viscosity reduction for D→E to N→Q mutants.²⁵⁷

In the context of this chapter, the anti-IL-8 WT Fv homology construct exhibited a high proportion of positive patches, indicating a potentially high baseline electrostatic potential with developability risks. Various *in silico* molecular descriptors (**Appendix 1 Table 7.3**) were examined to assess developability risks arising from anti-IL-8 electrostatic properties. Negative patch-disrupting mutants were found to reduce charge imbalance,²³⁷ increase net charge,²⁶⁸ and ensemble charges,²⁴² which have previously been correlated with viscosity reduction. These mutants also exhibited higher pIs, potentially enhancing anti-IL-8 colloidal stability. Conversely, positive patch-disrupting mutants showed reduced ensemble charges and significantly decreased pIs, suggesting diminished colloidal stability.

Contrary to the predicted net charges and surface charges, zeta potential values for most anti-IL-8 mAb mutants (except W32Q and D56N which had positive zeta potentials) revealed predominantly negative zeta potential values at pH 6.0, consistent with a net negative surface charge observed in the WT anti-IL-8 mAb. The discrepancies between computed predicted charges (+22.68 C for WT Fv at pH 6) and the negative measured zeta potentials can be attributed to multiple factors. One is a lack of accurate modelling of buffer components, affecting surface bound ions. Another is not accounting for other potential species in the system, such as aggregates or fragments carrying different surface charges. Furthermore, charge computations did not account for multiple molecules in the system and thereby neglected electrostatic effects from protein-protein interactions. These factors may also explain the lack of correlation to isoelectric points, which were measured at a much lower concentration (0.4 mg/mL versus 5 mg/mL for cIEF and zeta potential, respectively). The positive patch disrupting mutant, R53G, had more positive zeta potential but the second-lowest pI value in the mutant panel. Potential clustering of this mutant even at 5 mg/mL could be increasing the surface charge in this instance. Conversely, the K42E mutant exhibited a significantly lower zeta potential compared to the WT, supporting the notion that mutants disrupting positive patches tend to have more negative zeta potentials.

Therapeutic antibody profiler (TAP) predictions provide charge-based metrics for the anti-IL-8 mAb mutants, with flags indicating charge symmetry primarily in R53G and K42E positive patch targeting mutants (**Appendix 1 Figure 7.1**). However, all TAP scores for both positive and negative disrupting mutants fell within an ‘acceptable’ range, suggesting limited discriminatory power of TAP. This lack of differentiation in TAP scores has been noted in previous studies, highlighting potential limitations in its applicability for comprehensive mAb characterization.¹⁷⁴

Mutants targeting hydrophobic patches exhibit altered viscosity

Research strategies have explored strategies beyond neutralising charged patches to reduce hydrophobic interactions, for mitigating high concentration mAb stability and viscosity risks.²³² Hydrophobicity-based descriptors were computed for correlation with viscosity and developability, and compared with HIC retention times (**Figure 2.4**). Our analyses revealed a reduced hydrophobicity for W32Q, consistent with a predicted decrease in solvent-accessible hydrophobic patch area. However, smaller changes in hydrophobic patch area coverage were undetectable *via* HIC. Mutants with the lowest HIC retention times demonstrated lower solution viscosities (**Figure 2.6**), indicating a significant role for hydrophobic interactions in driving self-association. Strong correlations were observed between hydrophobic-based *in silico* descriptors and the observed HIC retention times for the anti-IL-8 mAb mutant panel, highlighting the predictive power of these descriptors in understanding viscosity behaviour.

Various research efforts have explored colloidal self-interaction as part of early mAb developability assessments.³⁵ The B_{22} or A_2 second virial coefficient and the self-interaction parameter, k_D , are key metrics capturing the thermodynamic effects of self-associating mAbs at dilute mAb concentrations.⁷⁹ Negative values for B_{22} and k_D indicate attractive protein-protein interactions, associated with decreased formulation stability and increased solution viscosity at high concentrations.^{83,229,269} In this study, all anti-IL-8 mAb mutants exhibited negative k_D values, with the W32Q mutant showing a less negative k_D , aligning with its reduced hydrophobicity. The AC-SINS assay further supported reduced self-association propensity for W32Q, consistent with the measured k_D (**Figure 2.5**). Trends were observed between colloidal parameters measured at lower anti-IL-8 mAb concentrations and viscosity-

concentration profiles (<120mg/mL), indicating reduced self-association propensities and viscosities for D70N and W32Q.

Most mutants showed similar unfolding temperatures to the WT, except for W32Q, suggesting a critical role for tryptophan in maintaining a large hydrophobic patch in the CDRH2, which impart stability which is lost upon mutation (**Appendix 1 Figure 7.5**). This reduced thermal stability also aligns with the observed reduction in antigen binding for W32Q.

Overall trends for each anti-IL-8 molecule in relation to *in silico* physicochemical descriptors and experimental parameters correlated with developability. Kingsbury *et al.*¹⁷⁴ correlated multiple *in silico* parameters with opalescence and viscosity for a dataset of 59 commercial mAbs and observed significant clustering with measured pI, effective charge and charge imbalances related to solution behaviour. Overall, the WT and anti-IL-8 rankings across *in silico* and experimental molecular descriptors from this chapter are summarised in **Figure 2.8**. Overall normalised experimental and computational developability scores (**Figure 2.8c**) demonstrated positive patch disrupting mutants to have consistently poorer developability. Ranking with all *in silico* molecular descriptors resulted in negative patch disrupting mutants as the highest developability, aligning with the experimental developability scores. However, ranking with descriptors previously selected to triage mutants showed the hydrophobic patch disrupting mutant W32Q as the highest scoring mAb with exclusion of more charge-based parameters.

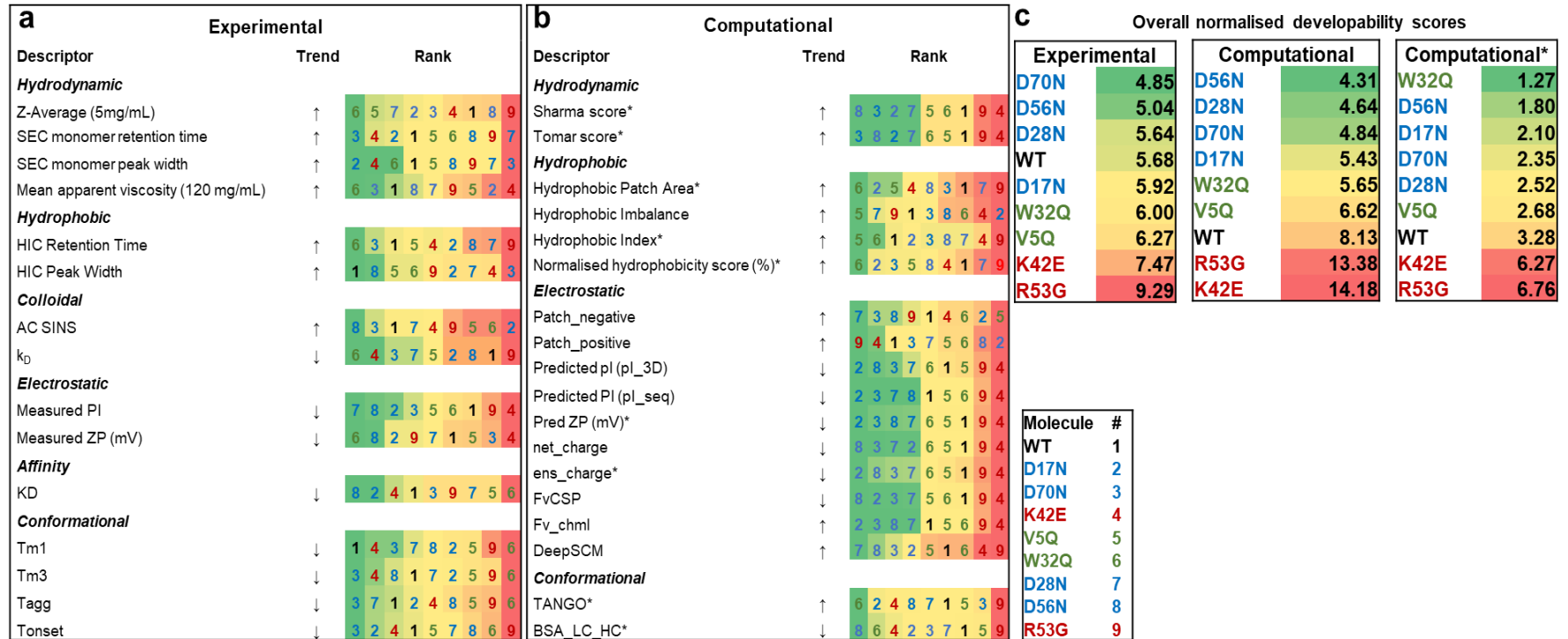


Figure 2.8 Ranking matrices for the anti-IL-8 mutant panel.

A colour-coded from min-max ranking in order of decreasing developability and categorised by **a**, experimental parameters and **b**, computed descriptors. **c**, Overall normalised scores (min-max normalisation) are shown. Two computational developability scores are reported to demonstrate ranking differences with use of all parameters *versus* selected parameters used originally to triaged mutants (*).

This is the first study that enables comparison of predictive and empirical approaches to understand the role of electrostatic and hydrophobic patch targeting in altering viscosity in the same mAb molecule. While these findings offer valuable insight into these strategies, there are associated limitations. Unlike previous reports,¹⁴⁷ specific trends in viscosity reduction based on mutation site (CDR versus FWR) in the anti-IL-8 mAb scaffold were not observed. Given the variability in charge and non-polar patch distribution among individual mAbs, generalised approaches to reduce molecular interactions driving self-associations may not be suitable and require a systematic design-build-test-learn approach. While single-point mutations were explored in this chapter, sequence engineering may require multiple mutation sites for improved developability. Previous studies have shown enhanced viscosity reduction through combined substitutions in both VH and VL regions.²⁷⁰ The computational simulations in this work focused on Fv models and did not consider the influence of hinge and constant domains on biophysical characteristics such as charge and hydrophobicity. Also, additional investigations are required to ascertain the impacts of non-CDR mutations on downstream biological properties of mutant mAbs (e.g., immunogenicity, half-life).

2.8. Conclusions

Early-stage assessment of pharmaceutical candidates is crucial for guiding decisions on clinical translation. Various industry-wide criteria are used to triage lead biomolecules, and the use of data-driven sequence-engineering strategies to optimise lead candidates represents a growing field. This chapter shows that trends observed from molecular descriptors to biophysical properties have a strong dependence on the mutation strategy employed. Mutations with significant reductions in hydrophobic patches significantly improved mAb solution viscosity, suggesting the predictive power of hydrophobic-based descriptors. However, mutations altering electrostatic patch coverage alone were insufficient to impact viscosity, irrespective of mutation site. Integrating deep learning approaches holds promise for deeper mechanistic insights into mAb developability, yet challenges such as wider data availability in the pre-competitive research landscape remain. This chapter highlights the importance of considering both sequence-based and structural alterations in optimising mAb developability characteristics.

3. Assessing the manufacturability and critical quality attribute profiles of anti-IL-8 mutant variants

3.1. Abstract

This chapter expands further on the developability for the anti-IL-8 mutant panel assessed in chapter 2 to highlight the impact of single-point mutations on upstream and downstream processability, phase behaviour and process-related impurities. This chapter uniquely describes trends between the biophysical molecular properties of a mAb to cell growth, expression, filtration flux, solubility, and post translational modifications. Here, trends biophysical properties of the anti-IL-8 mAb panel are correlated with their cell growth, expression, filtration flux, solubility, and post translational modifications. Significant trends in increased relative free light chain expression with heavy chain mutants were observed and a requirement for adjusted operation pH for cation exchange polishing steps with charge-altering variants was detected. Moreover, trends between phase stability and high concentration viscosity were observed. Finally, unique correlations between increased glycosylation and biophysical behaviour were investigated. Further in-depth characterisation and modelling to decipher the impact of sequence on expression system metabolism, solubility limits and alternative gelation models, as well as quantitation of other host-cell residual impurities is recommended for future works.

3.2. Introduction

A prerequisite for progression of therapeutic monoclonal antibody (mAb) candidates to toxicology studies and clinical manufacture, is upstream and downstream process de-risking during early-phase development. Process parameters, such as cell line viability, protein expression, type and number of purification steps and process-related impurities quantitation, help determine the feasibility of manufacturing the drug product robustly at scale whilst meeting Quality Target Product Profiles (QTPP).^{271,272} The importance of achieving high titre mAb expression, with high product quality to reduce requirement for multi-step chromatography purification, has driven the evolution of cell line development^{120,273,274}, production process optimisation^{119,275}, chromatography mode and resin diversity and selection^{20,276,277}, and reliable and high sensitivity in-process characterisation analytics^{278,279}. As more

complex biopharmaceutical modalities, such as multi-specific molecules and bioconjugates emerge, the quality by design (QbD) approach^{280,281} and moreover quality by molecular design²⁸², becomes imperative to mitigate downstream inefficiencies that would arise from molecules with poor manufacturability. Therefore, a surge of modelling initiatives, from digital twins^{283,284} to mechanistic modelling,^{285–287} has been seen in early-phase development. Recently, the incorporation of predicted physicochemical molecular properties to elucidate binding mechanisms in chromatography separation processes have been reported²⁸⁸, but there still remains a knowledge gap on translating inherent molecular properties to processability.

Here, the processing data for the anti-IL-8 mutant molecule panel generated in chapter 2 was evaluated to determine the impact of single-point Fv mutations on upstream and downstream processability and process-related impurity profiles. Single-point mutations had site-specific process and CQA implications including free light chain abundance, required pH for separation of charged species, phase separation and glycosylation risk.

3.3. Aims

The purpose of this chapter is to describe the process-related observations and manufacturability risks of the anti-IL-8 mutant panel, beyond the biophysical assessment described in chapter 2. Upstream and downstream observations are reported as well as an exploration of critical quality attributes such as opacity, phase separation and post-translational modifications.

3.4. Materials

Materials for mAb expression, purification and analysis are detailed in **Chapter 2, Table 2.1**.

3.5. Methods

3.5.1 Computational methods

Charge predictions

Homology models of kappa light chain fragments were generated from previously modelled Fv regions of the anti-IL-8 mutants panel in chapter 2 using Molecular Operating Environment (MOE) software, version 2020.0901 (Chemical Computing

Group, Montreal, Canada). The Protein Properties tool in MOE was used to compute predicted net charge and sequence and structure based isoelectric points.

Liability Antibody Profiler (LAP). <https://lap.naturalantibody.com/>

The Liability Antibody Profiler (LAP) was used to predict post-translational modifications of the anti-IL-8 mutant panel with Fv sequence input.¹¹³

3.5.2 Protein expression and purification

The upstream and downstream processing steps for the anti-IL-8 mutant panel are summarised in **Figure 3.1**.

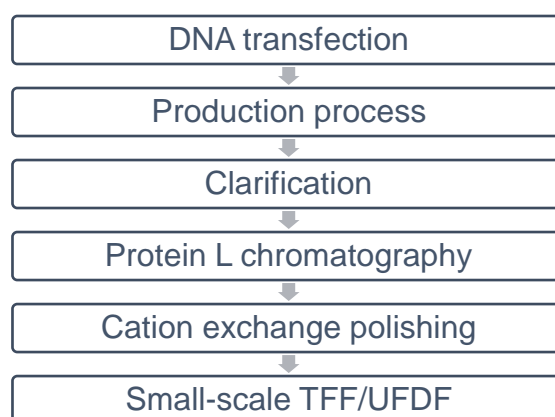


Figure 3.1 Process unit operations for expression and purification of anti-IL-8 mAb molecules.

DNA transfection

Sequences for the anti-IL-8 mAb panel were submitted for codon optimisation and plasmid generation by ATUM Biosciences (Newark, CA, USA). Sequences were confirmed with the MegAlign Pro tool (DNASar, WI, USA) before progressing to gene synthesis, with insertion of both heavy and light chain genes into Leap-in Transposon® pD2500 vectors with a cytomegalovirus (CMV) promoters. These plasmids contained glutamine synthetase (GS) genes to allow for the selection of cells integrating this DNA into their chromosomes.

Chinese Hamster Ovary (CHO) K1 GS-KO (GS knockout) host cells were grown in a commercial cell culture media supplemented with 8 mM glutamine. CHO cells were subcultured for a maximum of 10 passages before seeding (1×10^6 cells /mL) 24 hours prior to transfection. 12.5 μ g of each DNA plasmid was nucleofected into 5 x

10⁶ host CHO cells with 3 µg of Transposase mRNA (Atum Biosciences, CA, USA) using the Amaxa 4D Nucleofector kit (Lonza, UK).

Cell culture media without glutamine supplementation was used to maintain and scale up CHO cells expressing the anti-IL-8 mAbs to sufficient volumes for inoculating 1.6-2.8L shake flasks.

Upstream production process

Increased titres for the anti-IL-8 mAb panel were achieved by a 15-day production process. Glucose and supplementary amino acid feeds were supplemented on days 3, 6, 8, 10 and 13. Cell growth was monitored *via* a trypsinizing assay, using the Vi-CELL XR Cell Analyzer (Beckman Coulter, United States). Converse to the amino acid feeds, glucose feeding was cell-specific and so glucose was monitored, along with glutamine, ammonium, lactate, and other metabolite levels with the Cedex Bio HT Analyzer (Roche, Switzerland). This immunoturbidity assay was also used to measure the IgG titre in each supernatant. Cultures were harvested and clarified *via* centrifugation (4 °C, 4,000 g for 20 minutes) and two-stage depth filtration step on either day 15 or when the viability dropped to ≤50 %.

Downstream processing

Protein L chromatography on an ÄKTA Avant 150 system (Cytiva, Danaher, USA) was used for the first capture step of the anti-IL-8 panel. Free kappa light chain co-eluted in Protein L purification was removed through cation exchange chromatography in the bind-elute mode. Exclusive monomer binding at either pH 5.0, 5.5, 6.0 or 6.5 was targeted and a 0-100% w/v 500 mM NaCl salt gradient step was performed to elute the monomer and achieve ≥95% purity.

Purified mAbs were concentrated initially to ≥70 mg/mL (ultrafiltration step 1 (UF1)), and then diafiltered and buffer exchanged into formulation buffer containing histidine, trehalose, and arginine (pH 6.0) using the Ambr® Crossflow system (Sartorius, Germany). A second concentration step (UF2) was performed to concentrate to ≥150 mg/mL, which was either continued on the Ambr® Crossflow, or transferred to the Big Tuna instrument (Unchained Labs, CA, USA) if the retentate volume was estimated to be lower than the hold-up volume of the Ambr® Crossflow system (<5 mL). Gel points (C_{gel}) were computed from logarithmic extrapolation of flux over UF1 to identify the time at which flux reaches zero (T_{gel}). Linear extrapolation of concentration data across the whole TFF process (both UF1 and UF2) was used to estimate the

concentration at T_{gel} for each molecule. These estimates derived from input mass and retentate volume (density set to 1 for all molecules) and UF2 data were required as the initial stages of UF1 appeared to have no change in concentration as the 100 mL volume-limited retentate vessel was topped up to concentrate the material.

3.5.3 Biophysical characterisation

Analytical size-exclusion chromatography

Monomer and free kappa light chain (kLC) fragment abundance was quantified with analytical size exclusion chromatography with the same method as previously described in chapter 2.

Charge distribution determination

Experimental isoelectric points (pIs) and charge distribution profiles of the anti-IL-8 mAb panel were obtained previously from capillary isoelectric focussing (cIEF) experiments in chapter 2. In brief, samples were assessed on the iCE3 instrument (Protein Simple, USA). Samples were prepared in a buffer containing broad range pI markers, 2M urea to reduce self-association, and a 1:1 ratio of ampholytes in pH 3-10 and 8-10.5 ranges. Charge isoforms and pIs were determined from integration of electropherograms in Empower 3 software (v4, Waters, US).

Differential scanning fluorimetry

Intrinsic fluorescence measurements were performed in chapter 2 *via* nano-differential scanning fluorimetry to obtain unfolding/aggregation temperatures. Briefly, Prometheus NT.48 (NanoTemper Technologies, Germany) was used to calculate 350/330 nm intensity ratio of each 20 μ L mAb sample loaded onto capillaries in duplicate at 150 mg/mL. Excitation power was set to obtain $\geq 5,000$ counts. Prometheus NT.48 software was used to analyse thermal profiles.

Viscosity measurements

Viscosity measurements were performed previously in chapter 2 for mAb up to 120 mg/mL using the VROC Initium (Rheosense, United States) across a range of shear rates (100-2000 1/s). Non-newtonian behaviour was observed for all mAbs and

exponential-growth fits were applied to each viscosity-concentration curve. Mean apparent viscosity reported are from extrapolation of exponential fits to 120 mg/mL.

Peptide mapping (LC-MS) for PTM identification

Sequence verification was performed for all anti-IL-8 mAbs *via* liquid chromatography-mass spectrometry in chapter 2 with screening for methylation, oxidation, deamidation, pyroglutamate formation and N-glycosylation (glycosylation consistent at N299 in Fc across anti-IL-8 mAb panel). Briefly, samples were denatured with guanidine, reduced with DTT, alkylated with iodoacetate and desalted with size exclusion microcentrifugation. Trypsin or chymotrypsin were used for mAb digestion (1:20 enzyme to mAb) and an ACQUITY UPLC PEPTIDE CSH C18 column was used for chromatographic separation before MS/MS analysis for peptide identification on the Orbitrap Exploris 240 MS system (positive ion mode). Byos software (version 5.0-88 (2022.12), Protein Metrics, CA, USA) was used to processing of peptide fragments.

Diffusion self-interaction parameter determination (k_D)

Self-interaction parameter (k_D) was determined from dynamic light scattering as described in chapter 2. Briefly, samples were prepared in a histidine-based formulation buffer (pH 6) at 0.5-20 mg/mL and the Stunner instrument (Unchained Labs, CA, USA) was used to measure diffusion coefficients. These were plotted against concentration and linear regression was performed to derive k_D according to **Equation 2.4**.

Statistical approaches

GraphPad Prism (v5.04) and JMP 17 (v17.2.0) were used for plotting scatter plots and bar graphs and to determine correlations.

3.6. Results

3.6.1 Cell growth, viability and anti-IL-8 mAb expression

Cell growth, viability and expression for each anti-IL-8 mutant molecule was monitored across the 15-day production process (Figure 3.2). In total, three batches of wild-type molecule (WT) were manufactured. The first two batches were used for

analytical method development and as a comparator to the cell growth and expression of framework L mutants (**Figure 3.2a-c**). Viable cell count and viability for FWRL mutants were comparable to WT with slightly increased mAb titre. Both WT batches had a reduced cell viability of $\leq 50\%$ on day 13 and were harvested earlier than FWRL mutants. A third batch of WT molecule was grown at the same time as the remaining mutants generated (**Figure 3.2d-f**). Overall, heavy chain mutants showed reduced cell growth and mAb expression compared to WT, particularly the CDRH2 mutant, W32Q.

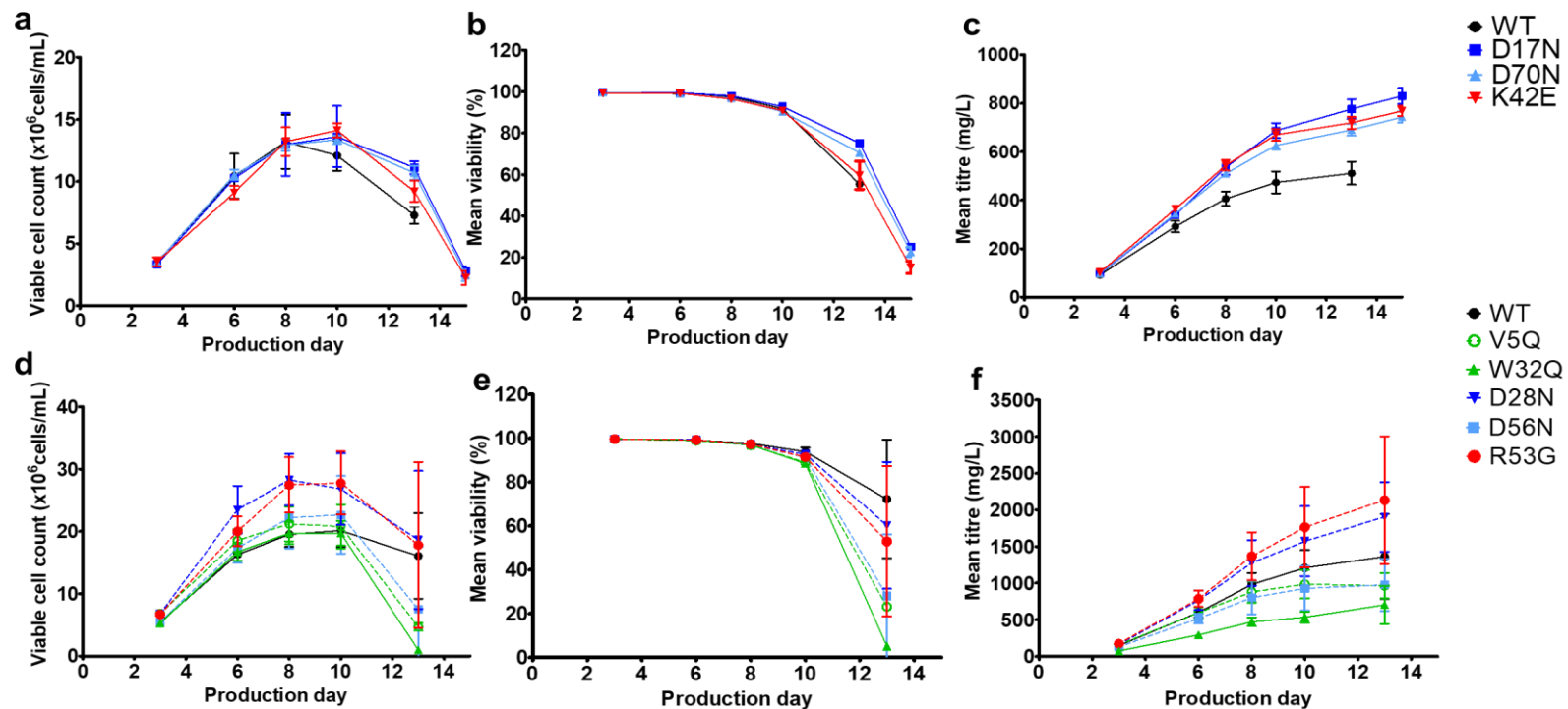


Figure 3.2 Viable cell count, cell viability and mAb titre over 15 day fed-batch production process.

Cultures were harvested if cell viability <50% on day 13. a-c, the first batch generated were of framework L mutants. Wild-type (WT) data is averaged across two batches prior to this. d-f, a second batch with the framework H (V5Q), CDRH (W32Q) and CDRL (D28N, D56N, R53G) mutants alongside another WT batch was grown. Heavy chain mutants targeting hydrophobic patches (green), particularly W32Q, had a greater drop in viability and lower expression compared to mutants targeting negative (blue) or positive (red) patches. Error bars represent standard deviations (N=4).

3.6.2 Downstream purification polishing steps

To achieve acceptable monomeric purity (>95%), a polishing chromatography step was used to process all anti-IL-8 molecule Protein L eluates, separating co-eluted free kappa light chain (kLC) (**Appendix 2 Figure 8.1**). Cation exchange (CEX) chromatography in bind-elute mode was applied to separate the predicted negatively charged kLC from the positively charged monomer (**Appendix 2 Table 8.1**). Multiple pH conditions were screened to identify pH required for exclusive monomer binding (**Appendix 2 Table 8.1**). The disruption of charged patches resulted in mutants targeting positive patches and negative patches to have decreased and increased isoelectric points, respectively (**Figure 2.3**). For sufficient separation of kLC, the CEX elution buffer pH was ~0.5 pH units lower for positive patch disrupting mutants compared to the pH for negative patch disrupting mutants and WT (**Appendix 2, Table 8.1**); for example in scaled down screening experiments (4.67 mL column), R53G required elution at pH 5 (monomer yield at 44%), whereas D17N had sufficient kLC separation at pH 5.5 (monomer yield 50%). Finally, a pH at which there is a predicted difference in charge of ~26.05 C between the full IgG monomer and kLC was found to provide reasonable reduction of % monomer in the flow-through (<10%) (**Figure 3.3a**), as well as sufficient monomer yield in the eluate (>31%) (**Figure 3.3b**).

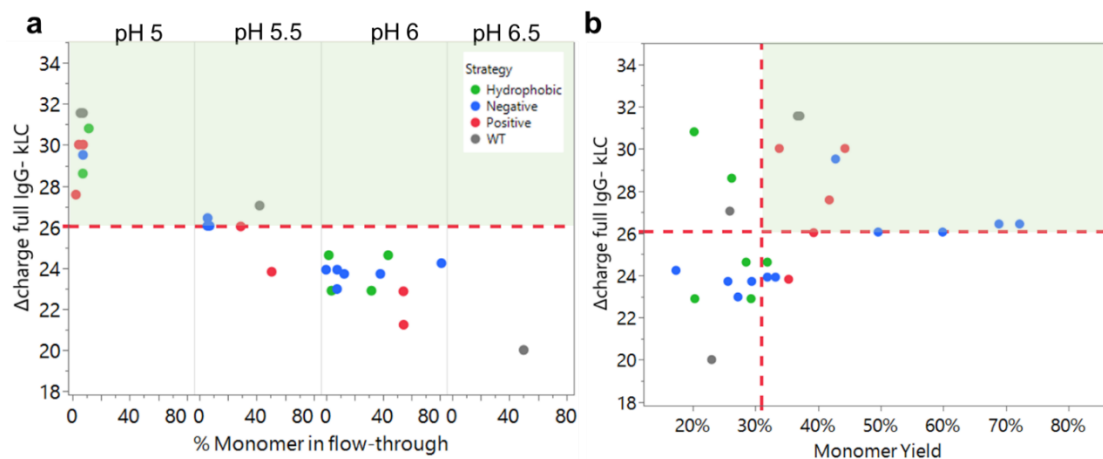


Figure 3.3 Use of difference in predicted net charge of full IgG to kLC in determining exclusive monomer binding and elution at specific pH.

Analytical size-exclusion chromatography to determine monomeric purity in flow-through for the anti-IL-8 mutant molecules and WT. a, %monomer in pooled flow-through per pH was reported against predicted charge difference. b, monomer yield was reported against predicted charge difference. A horizontal red dotted line represents a charge difference cut-off at 26.05 C, above which molecules are seen to have sufficiently minimal monomer in

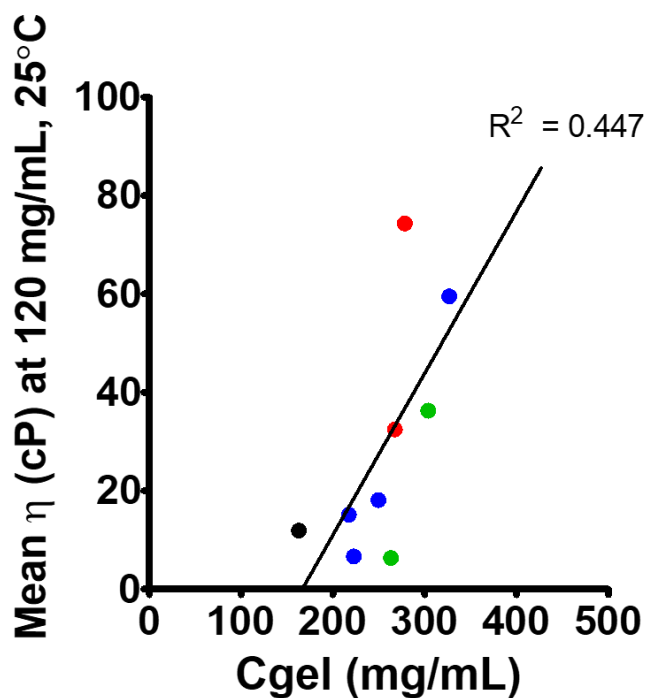
flow-through (exclusive monomer binding), and reasonable monomer yield (>31%, red vertical dotted line).

3.6.3 Theoretical gel point, opacity and liquid-liquid phase separation of anti-IL-8 mutants

Tangential flow-filtration (TFF), or ultra-filtration diafiltration (UFDF), is a routine unit operation in downstream processing to concentrate and diafilter mAb drug substance into the final formulation buffer at a target concentration.^{289,290}

Both the mechanical stress from retentate agitation, wall shear stress, and concentration polarisation on TFF membranes promote aggregation events and viscosity increases giving rise to opacity.^{291–293} Moreover, molecules with higher inherent viscosity risks may have reduced filterability during concentration steps. Severe flux decay and membrane adsorption and fouling can lead to prolonged processing and product losses, highlighting the need for optimising transmembrane pressure (TMP) and cross-flow rates on a case-by-case basis.²⁹²

In this chapter, all molecules were processed with equivalent UFDF parameters to identify the relation between differences in flux and viscosity. The concentration at which gelation (C_{gel}) occurs was calculated for each anti-IL-8 molecule from logarithmic extrapolation of flux during small-scale UFDF to find the time at which the flux reached zero (T_{gel}) and infer the estimated concentration at T_{gel} from the retentate vessel weight (**Figure 3.4** and **Appendix 2 Figure 8.3**). No trends were observed between C_{gel} and viscosity, suggesting limitations to the extrapolations of flux and potential errors in estimated projected concentrations.



Molecule	C _{gel} (mg/mL)	Mean apparent viscosity (120 mg/mL)
WT	162.82	11.911
D17N	326.63	59.52
D70N	222.68	6.66
K42E	278.4	74.30
V5Q	303.85	36.29
W32Q	263.1	6.33
D28N	249.56	18.12
D56N	217.31	15.14
R53G	267.48	32.46

Figure 3.4 Gelation concentrations (C_{gel}) estimated from extrapolating flux through small-scale tangential flow filters during UFDF.

Opacity was observed in the retentate vessels during TFF for all anti-IL-8 molecules (**Appendix 2 Figure 8.4**), which was eliminated during sterile filtration. Interestingly, no significant mAb loss was observed from removal of particulates. Except for K42E, all anti-IL-8 molecules were physically stable with no phase-separation observed in the concentration range studied. Temperature-dependent phase separation was observed with K42E, which was the mutant with the highest apparent viscosity at 120 mg/mL (**Figure 3.5**).

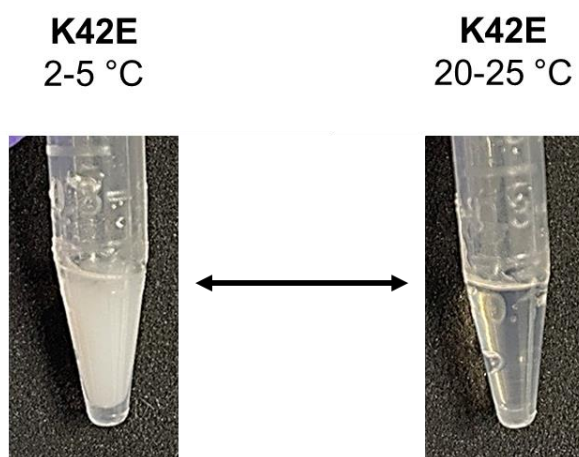


Figure 3.5 Reversible temperature-dependent phase separation with the K42E mutant. A sedimented solid-like white precipitate was observed at 2-5 °C which reversed at ambient temperature.

3.6.4 Post-translational modifications of the anti-IL-8 mutants

Post-translational modifications (PTMs) of mAbs *in vivo* give rise to sequence and structural heterogeneity.¹⁰¹ *In silico* sequence-based PTM liabilities are typically assessed during early-phase developability screening.

Here, predicted PTMs for all mutants were assessed *via* Liability Antibody Profiler (LAP)¹¹³ (**Table 3.1**) and validated experimentally with LC-MS (**Appendix 1 Table 7.8** and **Figure 7.3**). Interestingly, the D70N mutant showed high predicted N-linked glycosylation risk, which aligned with the hypothetical increased abundance of glycoforms driving experimental differences observed with decreased SEC retention time (partially increased hydrodynamic size)²⁹⁴ (**Appendix 1 Table 7.9**), peak broadening on the HIC column (polydiversity)²⁹⁵ (**Figure 2.4** and **Appendix 1 Figure 7.4**), and increased acidic species (increased sialylation)²⁹⁶ (**Chapter 2 Figure 2.3**). No changes in thermal stability were observed for D70N (**Appendix 1 Figure 7.5**), nor were there significant differences in antigen affinity compared to the other anti-IL-8 mutant molecules (**Table 7.10**).

Table 3.1 Liability antibody profiler (LAP) tool was used to predict PTMs for anti-IL-8 mutant Fv sequences.

Abbreviations: LC: light chain, HC: heavy chain

Molecule	LC		HC	
WT	None		Deamidation (low)	T30A
			Deamidation (low)	N30B
			Trp (W) oxidation (medium)	W32
			Trp (W) oxidation (medium)	W102B
D17N	None		Deamidation (low)	T30A
			Deamidation (low)	N30B
			Trp (W) oxidation (medium)	W32
			Trp (W) oxidation (medium)	W102B
D70N	N-linked glycosylation (high)	N70	Deamidation (low)	T30A
		Y71	Deamidation (low)	N30B
		T72	Trp (W) oxidation (medium)	W32
			Trp (W) oxidation (medium)	W102B
K42E	None		Deamidation (low)	T30A
			Deamidation (low)	N30B
			Trp (W) oxidation (medium)	W32
			Trp (W) oxidation (medium)	W102B
V5Q	None		Deamidation (low)	T30A
			Deamidation (low)	N30B
			Trp (W) oxidation (medium)	W32
			Trp (W) oxidation (medium)	W102B
W32Q	None		Deamidation (low)	T30A
			Deamidation (low)	N30B
			Trp (W) oxidation (medium)	W102B
D28N	None		Deamidation (low)	T30A
			Deamidation (low)	N30B
			Trp (W) oxidation (medium)	W32
			Trp (W) oxidation (medium)	W102B
D56N	None		Deamidation (low)	T30A
			Deamidation (low)	N30B
			Trp (W) oxidation (medium)	W32
			Trp (W) oxidation (medium)	W102B
R53G	None		Deamidation (low)	T30A
			Deamidation (low)	N30B
			Trp (W) oxidation (medium)	W32
			Trp (W) oxidation (medium)	W102B

3.7. Discussion

Critical Quality Attributes (CQAs) of mAbs include purity, charge heterogeneity, physicochemical integrity and stability, biological specificity and activity, and pharmacokinetic/pharmacodynamic profiles (bioavailability and clearance assessment). These are routinely screened to evaluate quality, safety, efficacy and establish potential chemistry manufacturing and control (CMC) challenges in developing a novel mAb product.^{297,298} This chapter reports the process implications observed from single-point Fv mutants, drawing correlations between *in silico* descriptors and biophysical assessments in chapter 2.

Heavy chain mutants demonstrate reduced cell growth and monomer expression.

Contributions to understanding factors influencing cell growth, viability and mAb expression typically focus on vector optimisation, gene transfer technology, cell line-to-cell line comparisons, media and feed composition and incubation conditions.^{299–302} There is a knowledge gap on the influence of the transfected molecular sequence on CHO cell gene integration, metabolism and subsequent protein translation.

In this chapter, host cell line, vector backbone, transfection parameters, culture conditions and production feeding for the anti-IL-8 mutant panel were maintained consistent, aiming to decouple the impact of these parameters on cell growth and expression^{303,304} from the molecular sequence. Cell viability, growth and expression were monitored for all anti-IL-8 molecules throughout the production process (**Figure 3.2**), which showed reduced expression for heavy chain (and incidentally hydrophobic-patch disrupting) mutants, V5Q and particularly W32Q. An increased proportional expression of free kappa light chain was also observed for V5Q and W32Q in comparison to the other mutants (**Appendix 2 Table 8.1** and **Figure 8.2**). Since expression was quantified with an immunoturbidity assay using an Fc-specific antiserum,³⁰⁵ light chain fragment was not detected. Drivers for increased light chain fragmentation can be explained by two hypotheses: Reduced transfection efficiency of heavy chain resulting from single-point mutations, particularly in the case of W32Q where the mutation site is in a hydrophobic rich CDRH2, reducing downstream protein synthesis and folding of the heavy chain polypeptide in the endoplasmic reticulum. The optimisation of heavy to light chain ratios to improve transfection efficiencies has previously been investigated³⁰⁶, particularly with relation to bispecific mAb

expression.³⁰⁷ However, no reports to-date have correlated heavy chain sequence to transfection efficiency. Alternatively, mutations could disrupt or reduce protein folding stability and heavy chain assembly with the light chain, due to the location of V5Q and W32Q mutation sites, which are near the N-terminus of the VH chain. This hypothesis correlates with the reduced conformational stability observed from differential scanning fluorimetry thermal profiling for W32Q (**Appendix 1 Figure 7.5c**), where the unfolding temperature (T_{onset}) was ~ 2 °C lower than the T_{onset} for the WT mAb (**Appendix 1 Figure 7.5e**). The thermal profile shifted to the left for V5Q compared to WT, indicating slightly reduced thermal stability (**Appendix 1 Figure 7.5b**), although this was not significant upon examination of mean unfolding temperatures (**Appendix 1 Figure 7.5e**). Cell lines used to express the anti-IL-8 panel were from polyclonal pools with heterogenous metabolic profiles and expression efficiencies, hence why large standard deviations were observed between shake flasks.

Positive patch-disrupting mutants require a lower pH in cation exchange chromatography

Mapping sequence and structure molecular descriptors to downstream process development remains underreported but holds promise in optimising resin selection and chromatography runs for mAb purification. Hess *et al.* screened 64 IgG-like molecules and observed clustering for the pH required for elution from mixed mode resins in accordance with subclass and format.³⁰⁸ They constructed a regression model comprising of six *in silico* Fv-based molecular descriptors to predict elution pH, concluding dependence on both electrostatic and hydrophobic properties of both CDRs and framework regions. Although this study focussed on monomeric purity, it provided insights into mechanisms of monomer binding and subsequent elution to multimodal matrices, applying *in silico* descriptors for predicting downstream process parameters.

In this chapter, trends were observed between the predicted charge of the molecule with pH required to remove free light chain in cation exchange chromatography (CEX) (**Figure 3.3**). K42E and R53G were designed disrupt positive patches in Chapter 2 which increased their viscosity and reduced overall developability (**Figure 2.6** and **Figure 2.8**). This change in charge was validated using cIEF experiments, which showed lower isoelectric points for the main species (**Figure 2.3**). Both K42E and

R53G required the lowest CEX operating pH (pH 5) for separation of kLC in the flow-through and exclusive monomer binding (**Figure 3.3a**), driven by the necessity for a distinct difference in charge between kLC and monomer. Predicted net charges for kLC and full IgG were computed (**Appendix 1 Table 8.1**) to determine a threshold of charge difference for sufficient separation and a value of ≥ -26.05 C was determined. Whilst this requires future validation with a larger dataset with more charge variants, these findings propose the potential for generating decision tree frameworks based on charge or hydrophobicity predictions and mapping design space thresholds to accelerate downstream process development.

Lack of translatability of gel points from small-scale tangential flow filtration flux and viscosity

A key manufacturability risk posed by high concentration, high viscosity mAb formulations is reduced filtration ability in multiple unit operations, including tangential flow-filtration for concentration and diafiltration of the bulk drug substance.

Gel polarisation theory was originally proposed to describe the rate of flux decay on a membrane as proportional to the negative natural log of bulk concentration and proportional to a mass transfer coefficient that incorporates solute diffusivity.³⁰⁹ With diffusivity significantly reduced under high viscosity conditions, a correlation with gel point (C_{gel}) was hypothesised, *i.e.* the concentration where there is an assumed zero flux, and viscosities of the anti-IL-8 mutant panel ≤ 120 mg/mL.

No strong correlation was observed between C_{gel} and viscosity ($R^2 = 0.45$) (**Figure 3.4**), which was attributed to a lack of accuracy from the extrapolation of both flux and estimated concentration (based of retentate vessel weight and does not account for hold-up volumes of the TFF system) (**Appendix 2, Figure 3.4**). Moreover, final retentate concentrations, particularly for the WT, often exceeded the C_{gel} . Accurate estimation of C_{gel} could prove useful in the context of needle-clogging events in subcutaneous autoinjector devices, correlating with extrusion force, and define injectability risks for each mAb and formulation. Alternative C_{gel} points could be derived from polymer gelation models, which overlap with rheology models describing the complexity of multi-step aggregation, cluster and network formation.^{310–312}

Correlation with high concentration viscosity and phase stability

Opacity and liquid-liquid phase separation (LLPS) of mAb formulations are key developability parameters, correlated with conformational stability, aggregation

propensity and viscosity.^{313,44,180} Previous formulation development efforts have aimed to reduce LLPS with pH titration and the introduction of various excipients (e.g., arginine, glutamate).^{314,44,315}

In this chapter, visual observations of opacity and LLPS are reported for all anti-IL-8 mutants. Correlations of opacity and phase separation between self-interaction propensity have previously been proposed.⁵² Kingsbury *et al.*¹⁷⁴ found the self-interaction parameter, k_D , as a strong predictor of solution behaviour, coupling together opacity with viscosity of 59 manufacturable mAbs. Here, all anti-IL-8 molecules had negative k_D values (**Figure 2.5**), aligning with the opacity observations during the first concentration step (UF1) of the TFF process (**Appendix 2 Figure 8.4**). Moreover, the positive-patch disrupting mutant, K42E, demonstrated reversible temperature phase separation (**Figure 3.5**), which correlated with higher viscosity at 120 mg/mL for K42E compared to WT (**Figure 2.6**). However, elevated viscosity was also observed for other mutants in the ≤ 120 mg/mL concentration regime, but none of these molecules demonstrated LLPS, including R53G which had the most negative k_D . This emphasises the requirement for case-by-case evaluation of solution parameters and the potential lack of resolution of predictors when dealing with datasets containing 'non-developable' molecules.

Biophysical impact of post-translational modifications

Post-translational modifications (PTMs, glycosylation, methionine oxidation isomerisation and deamidation) and process-related impurities (including host-cell protein and residual host DNA) are routinely screened during early-phase development to characterise product quality and determine immunogenicity risks.³¹⁶ This screening incorporates not only experimental validation with mass spectrometry and ELISA techniques for PTMs and HCP respectively, and *in silico* liability screening. A variety of sequence-based PTM computational tools have been developed, with evolution into machine-learning based algorithms.^{152,317}

For simplicity, the Liability Antibody Profiler tool was used to screen the anti-IL-8 molecules, relying on identification of liable residue motifs.¹¹³ All molecules showed comparable PTM risk profiles, except for D70N which had high N-glycosylation flags at the mutation position (**Table 3.1**). Due to poor fragmentation on mass spectrometry analysis, this modification was not confirmed, but flagged as a potential modification site (**Appendix 1 Figure 7.3**). Biophysical characterisation of D70N in Chapter 2

presented unique observations for D70N with peak broadening observed on both SEC (**Appendix 1 Table 7.9**) and HIC columns (**Figure 2.4** and **Appendix 1 Figure 7.4**), which aligns with the potential presence of different glycoforms known to impact peak shape.³¹⁸ Moreover, the increased acidic isoforms and relatively smaller increase in isoelectric point compared to D17N (a framework light chain mutant) supports the hypothesis of bound positively charged glycans (e.g., sialic acid modification).³¹⁹ Interestingly, D70N showed no distinct differences in CHO cell expression titres and growth despite the presence of N-glycosylation, demonstrating minimal inhibitory impact on cell-signalling pathways.³²⁰

3.8. Conclusions

This work highlights the significant impact of single-point Fv mutations on both process parameters and process-related observations and impurities. Site-dependent reduction in heavy chain expression with increased light chain fragment presence was observed from heavy chain mutants, aligning to the conformational stability data presented in chapter 2. Beyond upstream process implications, charge-altering single point mutations necessitated pH adjustment for monomer purification *via* cation exchange chromatography in the downstream process development phase. Correlations between viscosity, measured in chapter 2, to gelation theory, extrapolated from small-scale TFF, and to phase-separation proved inconsistent and unpredictable. Finally, *in silico* and experimental PTM screening provided increased understanding of biophysical phenomena from chapter 2. This study supplements developability screening in chapter 2 with further understanding of the process-implications of single-point mutants. Future confirmation of these conclusions is required with larger datasets and more in-depth analytical characterisation. For example, to test the hypothesis of heavy *versus* light chain transfection efficiency differences, co-expression of fluorescent protein-encoding gene could be used. Furthermore, opacity observations could be quantified with nephelometric turbidity measurements. Finally, host-cell related impurities from the upstream process, such as host-cell proteins (HCP) or residual DNA, require quantitation and characterisation to better elucidate immunogenicity risks additional to the PTMs identified.

4. A first insight into the developability of IgG3: A combined computational and experimental approach

The contents of this chapter contains material from published work, reprinted with permissions from Armstrong, G. B., Lewis A., Shah V., Taylor P., Jamieson C., Burley G.A., Lewis W., Rattray Z. "A First Insight into the Developability of an Immunoglobulin G3: A Combined Computational and Experimental Approach." *ACS Pharmacology & Translational Science* (2024). <https://doi.org/10.1021/acsptsci.4c00271>. Copyright 2024 American Chemical Society.

GB Armstrong- author of this thesis- performed all experimental (except from LC-MS and AC-SINS assays) and *in silico* modelling on the reported for anti-IL-8 IgG3 and IgG1 molecules.

4.1. Abstract

This chapter describes the molecular descriptors and biophysical parameters of an anti-IL-8 IgG3, to understand the developability of this subclass comparing to an Fv-matched IgG1 molecule. While poorer conformational and colloidal stability, and elevated solution viscosity is observed for IgG3, future efforts controlling surface potential through sequence-engineering of solvent-accessible patches can be used to improve biophysical parameters that dictate mAb developability.

4.2. Introduction

Antibody-based therapies possessing high specificity and superior efficacy have gained tremendous traction and growth in the biopharmaceuticals sector. Antibodies exert their pharmacological activity *via* a range of biological mechanisms- including and not limited to- direct blockade or activation of cell signal transduction pathways; Fc-mediated functions (antibody-dependent cell-mediated cytotoxicity,³²¹ complement-dependent cytotoxicity, antibody-dependent cell phagocytosis); and immune activation. The molecular diversity of monoclonal antibody isotypes and subclasses can be harnessed to achieve different mechanisms of action in combating disease. Immunoglobulin G (IgG), the most abundant antibody isotype, can be further

categorized as IgG1, IgG2, IgG3, and IgG4 subclasses in descending order of their prevalence in human serum.³²²

IgG subclasses are >90% conserved at the amino acid level, each possessing a unique profile in terms of their hinge region length, number of inter-chain disulfide bonds and Fc-effector functionality.³²² The molecular diversity of IgG subclasses and their involvement in mediating responses to different immunologic stimuli reflects the differing functional roles of IgG subclasses, and affording their application in targeting a diverse antigen landscape. There is growing recognition in recent years that the biomolecular properties of the different IgG subclasses can be harnessed to engineer novel therapeutic antibodies with improved developability characteristics, particularly in the context of targeting otherwise inaccessible biological targets.³²³

Of the four IgG subclasses, IgG3 has the highest binding affinity for FcγRs, but is not routinely explored for therapeutic indications due to its suboptimal physicochemical stability profile and immunogenicity risk. However, the flexibility of the IgG3 hinge region confers the flexibility for this subclass of antibody to interact more effectively with target antigens that are expressed at lower abundance.³²⁴ Despite the challenges with IgG3 immunostimulatory behaviour, there is growing interest in their use as Fc-mediated immunotherapies.³²⁵ While both IgG1 and IgG3 play key roles in mediating immune responses, their structural differences lead to variations in their interactions with FcγRs and subsequent immune effector functions. IgG1 and IgG3 interact differently with most immune receptors (FcγR), triggering various immune effector mechanisms such as phagocytosis or antibody-dependent-cell-mediated cytotoxicity, which can offer therapeutic potential in immunooncology applications.

IgG1 and IgG3 differ mostly based on the composition of their hinge region, which alters the extent of their ability to activate the immune system. IgG1 mAbs contain two inter-chain disulphide bonds in the hinge region, while IgG3 mAbs have 11 inter-chain disulphides. These structural differences influence their effector functions, with the IgG3 longer hinge length contributing to a combined greater accessibility to antigens and Fcγ receptors, resulting in more potent opsonic activity.

Beyond differences in their biological properties, each IgG subclass is associated with developability challenges, in the context of resistance to fragmentation, aggregation

propensity, and elevation solution viscosity at high concentration. Though IgG1 mAbs exhibit superior stability under different pH conditions and in response to mechanical stress, they are more prone to fragmentation. However, IgG2 mAbs by comparison are less prone to fragmentation, but are more susceptible to aggregation.³²³

While IgG3 as a subclass has diverse functional roles in immunity, there remains a distinct lack of clinically-approved IgG3-based mAb therapies, as well as a significant lack of IgG3 candidates under pre-clinical evaluation. The lack of IgG3 adoption in pharma pipelines has been attributed as a historical artifact to its developability relative to the IgG subclass; namely the lack of protein A binding hampering downstream processing efforts,^{326,327} lack of *in vivo* stability resulting from proteolytic susceptibility, short plasma half-life necessitating a higher dosing frequency to achieve therapeutically-relevant levels,³²⁸ and immunogenicity concerns.^{329,330} However, with recent biotechnological advances in antibody sequence-based engineering, formulation strategies, and advancements in downstream processing these challenges can be circumvented. Consequently, by virtue of historical challenges there is a significant paucity of data on IgG3 molecular descriptors and biophysical properties under mAb formulation conditions.

The focus of this chapter is to address the gap in our knowledge of IgG3 developability characteristics, arising from sequence and structural differences to the IgG1 subclass by directly comparing the computational molecular descriptors of an anti-IL-8 IgG1 and IgG3 pair, both possessing identical variable domains. A comprehensive framework was implemented for the computational prediction of their sequence and structural molecular descriptors, correlating these with measured experimental parameters evaluating their self-association behaviour and solution viscosity at high formulation concentration (>100 mg/mL).

Anti-IL-8 IgG3 showed an increase in accessible hydrophobic and ionic patch areas, which was reflected in changes in charge and increased self-association propensity compared to anti-IL-8 IgG1. Interestingly, converse to predictions, a reduction in net hydrophobicity was observed for IgG3. Anti-IL-8 IgG3 demonstrated reduced physical stability and elevated solution viscosity at high concentrations, resulting in overall poorer developability characteristics compared to IgG1.

The ability to implement predictive models that can inform developability risks (self-association, viscosity), can underpin sequence-engineering efforts during early discovery stages to optimise for biological activity and developability characteristics. Most computational prediction and biophysical efforts to-date have focused on IgG1 mAbs; therefore, there is a critical need to develop predictive models contributing to fundamental knowledge on IgG2-4 subclass physicochemical properties that can shed light on their downstream developability characteristics.

4.3. Aims

This chapter aims to reconcile the *in silico* molecular descriptors and experimental physicochemical properties of an IgG3 compared to IgG1 in the context of determining its developability. Similarly to chapter 2, full IgG homology constructs and biophysical characterisation were used to assess charge, hydrophobicity, conformational stability, colloidal parameters, and viscosity of the two subclasses of anti-IL-8.

4.4. Materials

Materials for mAb expression, purification and analysis are detailed in **chapter 2, Table 2.1**.

4.5. Methods

4.5.1 Computational methods

In silico homology modelling and antibody molecular descriptor calculations were performed in the Molecular Operating Environment (MOE) software, version 2020.0901 (Chemical Computing Group, Montreal, Canada).

Homology modelling of anti-IL-8 IgG1 and IgG3

For both IgG1 and IgG3 molecules, full sequences of the heavy and light chains were inputted as the FASTA format into MOE (sequence editor) and annotated with a Kabat numbering scheme, with identical variable chain sequences. Constant chains were selected from the IMGT Repertoire database (<https://www.imgt.org/IMGRepertoire/>), with accession numbers J00228 (IGHG1*01) and M12958 (IGHG3*01) for IgG1 and IgG3, respectively.

For the IgG1 molecule, the Antibody modeller in MOE (version 2020.0901) was used and the full IgG construct was built as described in chapter 2.

For the IgG3, a different approach of independently modelling each antibody component was required due the absence of resolved IgG3 structures arising from the long hinge length. A new template hinge was generated independently using a mouse IgG2A (pdb:1IGT) as the second and fifth C-C disulfide bridges were in the same positions to the IgG3 hinge sequence. The alignment to the IgG2A hinge sequence is shown in **Appendix 3 Table 9.1**. This sequence was copied a further three times to generate the four modules of the hinge. The Homology modeller in MOE (version 2020.0901) was used to generate 10 refined homology models for the hinge. The quality assessment parameters for each resulting model are reported in **Appendix 3 Table 9.2** and each parameter was normalised to rank the geometric quality per model:

$$NDV = \frac{x - x_{\min}}{(x_{\max} - x_{\min})}$$

4.1

Where *NDV* is the normalised value for all geometric quality scores, except from the packing score, which was computed using **Equation 4.2**.

$$NDV_{packing\ score} = 1 - \frac{x - x_{\min}}{(x_{\max} - x_{\min})}$$

4.2

The lowest heavy atom root mean square deviation to the average position of intermediate models and lowest normalised score model were selected. A human Fc (pdb: 6D58) was imported for the Fc fragment, and the fragment antigen-binding regions (Fabs) were modelled *via* the Antibody modeller tool in MOE (version 2020.0901) from the anti-IL-8 IgG3 Fab sequence, with Fab selected as the model type. A 100% match to PDB ID 5OB5 was found as the variable sequence was the same between IgG1 and IgG3, with only a five-residue sequence difference in the constant regions of the Fab. All components were then joined manually and the joins energy minimised.

Patch analysis of anti-IL-8 IgG1 and IgG3 homology constructs

As described in chapter 2, the protein patch tool in MOE was applied to each homology construct to identify electrostatic and hydrophobic surface patches. To aid visualisation of smaller surface patches, the following parameter thresholds were used: hydrophobic cut-off: ≥ 0.09 kcal/mol, hydrophobic min area: ≥ 30 Å², charge cut-off: ≥ 30 kcal/mol/C, charge min area: ≥ 30 Å², probe sphere radius: 1.8 Å.

Predicted physicochemical descriptors

Similarly to chapter 2, a range of molecular descriptors (**Appendix 1 Table 7.3**) were computed but using each full IgG1 and IgG3 model instead of Fv only models. Descriptors that were based on Fv only models were excluded from this analysis *i.e.*, Fv_chml, Pro_Fv_net_charge, Pro_net_charge, Ens_charge, Fv charge symmetry (FvSCP). Further descriptors of the hinge and buried surface area were included (**Appendix 3 Table 9.3**).

4.5.2 Generation and biophysical analysis of anti-IL-8 IgG1 and IgG3

IgG1 and IgG3 Expression and Downstream Purification.

The same expression platform and downstream processing pipeline as the anti-IL-8 mutants in chapter 2 was used for the generation of high concentration IgG1 and IgG3 material. Briefly, heavy and light chain sequences were codon optimised and inserted into plasmids with CMV promoters by Atum Biosciences (Newark, CA,US). Plasmids were transfected *via* nucleofection with Leap-in Transposase® mRNA into Chinese Hamster Ovary (CHO) cells and kept under selection conditions (no glutamine supplement) to generate stable pools. A fed-batch production process for 15 days with nutrient/glucose feeds every two or three days was deployed to increase expression of anti-IL-8 IgG1 and IgG3. Cell culture bulks were fully clarified and then purified with an initial Protein L capture step followed by cation exchange polishing. Purified IgG1 and IgG3 were then concentrated, diafiltered and exchanged into formulation buffer containing histidine, trehalose, and arginine (pH 6) to a final target concentration of ≥ 150 mg/mL.

Analysis of identity of anti-IL-8 IgG1 and IgG3

Peptide mapping was used to verify the full sequence identity of IgG1 and IgG3. The method reported in chapter 2 was used, with only trypsin digest being used. In summary, 250 µg of each molecule was denatured, reduced and alkylated. Further reduction and desalting to exchange samples into the digestion buffer followed, with trypsin digest (sequencing-grade, Promega, WI, USA) at a 1:20 (w/w) ratio after 2 hours of incubation. Liquid chromatography-mass spectrometry (LC-MS) was performed using an Orbitrap Exploris™ 240 Mass Spectrometer (Thermo Fisher Scientific, MA, USA), controlled by Xcalibur software (version 4.4.16.14, Thermo Fisher Scientific, MA, USA). A ACQUITY UPLC PEPTIDE CSH C18 (Waters, US) column was used for peptide separation, with 214 nm absorbance detection. Separation of digested peptides was achieved by a method comprising of step wise gradients of buffer B, containing acetonitrile. The MS system was operated in positive ion mode, with a 200-2000 m/z scan range and a final resolution target of 15,000. Filtering criteria included charge states of 2-8 and minimum of 5 scans. Byos software (version 5.0-88 (2022.12), Protein Metrics, CA, USA) was used to process peptide fragments with precursor Mass Tolerance set at 20 ppm, fragment mass tolerance 1 and 2 set at 20 ppm and cleavage sites set as arginine and lysine. The post translation modifications (PTMs) screened for were methylation, glycosylation, oxidation, deamidation and pyroglutamate formation.

Analysis of purity of anti-IL-8 IgG1 and IgG3

Analytical size-exclusion chromatography (aSEC) with UV-detection was deployed for monomeric purity assessment of anti-IL-8 IgG1 and IgG3. A TSKgel Super SW3000, 4.6 x 300 mm (TOSOH Bioscience, United States) column was used with Agilent 1260 series HPLC (CA, US). Samples were prepared in water at 5 mg/mL and ran at 0.2mL/min with a mobile phase containing 400 mM NaCl (pH 6.8). Chromatogram processing and integration was performed in The OpenLab CDS Data Analysis software (version 2.6, Agilent, California, US). The target monomeric purity of ≥95% was met by both anti-IL-8 IgG1 and IgG3 molecules and aSEC was used to monitor physicochemical stability, by monitoring changes in the chromatogram.

Antigen affinity of anti-IL-8 IgG1 and IgG3

Surface plasmon resonance (SPR) was used with a Biacore 8K+ system (Cytiva, Danaher, USA) to measure the on and off rates (k_a and k_d respectively) to calculate the equilibrium dissociation constant (K_D) with the k_d/k_a ratio. A 0.31-20 $\mu\text{g/mL}$ concentration series for IgG1 and IgG3 was prepared in phosphate buffered saline containing 0.05% v/v Tween™ 20 (PBS-T). 0.5 $\mu\text{g/mL}$ IL-8 carrier-free antigen (R&D systems, USA) was immobilised onto one flow cell of a Biacore CM3 dextran chip (Cytiva, Danaher, USA). Ten antibody injections followed ten start-up (PBS-T only) cycles, at 30 $\mu\text{L/min}$ and measurement temperature of 25 °C, and with a 240 second contact time. A 900 seconds dissociation time was set and 10 mM glycine (pH 1.5) followed with 3 M guanidine regenerated the chip surface for the next injection. A 1:1 Langmuir binding model in the Biacore Insight Evaluation software (version 4.0.8.20368, Cytiva, Danaher, USA) was applied to the sensorgrams after reference subtraction.

Hydrophobic Interaction Chromatography of IgG1 and IgG3

The hydrophobicity of IgG1 and IgG3 was assessed using hydrophobic interaction chromatography (HIC) on an Agilent 1260 series HPLC (Agilent, California, US), coupled with UV detection (214 and 280 nm). A PolyLC PolyPROPUL 4.6 x 100 mm column was used on to resolve each sample. To achieve separation based on net hydrophobicity, step-wise gradients of mobile phase B (low salt, with 50 mM ammonium sulfate) followed equilibration with mobile phase A (high salt, 1.3 M ammonium sulfate). IgG1 and IgG3 samples were analysed at 1 mg/mL (5 μL injection volume) and a 0.7 mL/min flow rate.

Capillary Isoelectric Focusing (cIEF) of anti-IL-8 IgG1 and IgG3

Charge distribution profiles of anti-IL-8 IgG1 and IgG3 were assessed *via* capillary isoelectric focussing using an iCE3 instrument (Protein Simple, US). A range of pI markers (pI 3.85-8.77, Bio-Tec, Protein Simple, USA) were used to capture all acidic and basic isoforms for both molecules. To help prevent aggregation, 2M urea was added to the 1:1 ampholyte mixture (pH 3-10 and pH 8-10.5). The method entailed a pre-focus voltage of 1,500 V; an autosampler/transfer capillary temperature of 15 °C; a 10-12-minute focus voltage of 3,000 V; UV detection at 280 nm; a sample injection pressure of 2,000 mbar; a pre-focus time of 1 min; and a focus time of 10-

12 minutes. The Empower 3 software (v4, Waters, US) was used for data analysis of peaks.

Zeta potential of anti-IL-8 IgG1 and IgG3

A Malvern Zetasizer (Malvern Panalytical, Malvern, UK) with a 633 nm laser was used to measure the zeta potential of the IgG1 and IgG3 pair by electrophoretic light scattering. Each sample (refractive index 1.59) was prepared to 5 mg/mL in formulation buffer (pH 6, refractive index 1.33, viscosity at 1.26 cP) and a method was set up with equilibration time of 120s, automatic attenuation and up to 100 runs per sample. A 60s pause was also set between sample runs (a minimum of three technical replicates performed).

Analysis of anti-IL-8 IgG1 and IgG3 self-interaction

Similarly to the anti-IL-8 mutant panel in chapter 2, self-association propensity of anti-IL-8 IgG1 and IgG3 was measured with Affinity-Capture Self-Interaction Nanoparticle Spectroscopy (AC-SINS). Goat anti-human Fc and whole goat antibodies (Jackson ImmunoResearch, PA, USA) were prepared in 20 mM acetate buffer (pH 4.3) then mixed and incubated with 20 nm gold particles (Ted Pella Inc., CA, USA, concentration 7.0×10^{11} particles /mL). Test samples were prepared at 50 µg/mL in phosphate buffered saline (PBS) and 99 µL was added to 11 µL of nanoparticles in a 96 well plate, resulting in a final solution concentration of 50 µg/mL test mAb, 10x bead:anti-Fc conjugate and 0.02 mg/mL PEG2000. Plates were agitated, incubated for 2 h 30 min and gently centrifuged to remove air bubbles. Absorbances were then read using the Pherastar FSX (BMG Labtech Ltd., Germany) plate reader, and spectra were analysed with MARS software (v3.32, BMG Labtech Ltd., Germany). Differences in plasmon wavelengths for each sample was calculated from smoothed best fit curves. Experimental cutoffs included a <535 nm wavelength for negative controls (*i.e.*, PBS buffer).

Diffusion self-interaction parameter for anti-IL-8 IgG1 and IgG3

A Stunner (Unchained Labs, CA, USA) was used to measure hydrodynamic size, polydispersity, and diffusion coefficient for both molecules. The self-interaction parameter, k_D , was computed according to **Equation 2.4**. Exponential fits for diffusion coefficients over the test concentration range were used to calculate theoretical viscosities, adapted from the Generalised Stokes Einstein equation:

$$\eta = \frac{k_B T}{3d_H D \pi}$$

4.3

Where η is the theoretical dynamic viscosity (cP), $k_B T$ the Boltzmann constant at 298K, d_H the Z-ave diameter (m) and D the diffusion coefficient (m/s).

Analysis of unfolding temperatures for anti-IL-8 IgG1 and IgG3

Differential scanning fluorimetry was performed on IgG1 and IgG3 anti-IL-8 molecules using a Prometheus NT.48 setup (NanoTemper Technologies, Germany) with back-reflection technology. The intrinsic fluorescence from unfolding events exposing tyrosine and tryptophan residues were monitored *via* the 350/330 nm intensity ratio.³³¹ A temperature ramp of 2°C/minute from 20-95 °C was performed. Both samples were assessed at concentrations ~150 mg/mL and unfolding temperatures of antibody domains (T_{m1} , T_{m2} and T_{m3}) were detected from first-derivative peaks of the 350/330 nm fluorescence intensity ratio. The first derivative peak of the scattering profile marked the aggregation temperature (T_{agg}) values.

Measurement of Solution Viscosity

Viscosity curves were obtained using a VROC Initium (Rheosense, United States). The measurement protocol was optimised using the 'Auto' shear rate function, with fixed shear rates in the 100-2000 s⁻¹ per concentration tested. Data were filtered to only include transient curves with steady plateaus with no drift and pressure over sensor position linear fits of $R^2 \geq 0.998$.

Various models were used to fit the viscosity data. Firstly, the exponential-growth equation was applied:

$$\eta = Y_0 e^{kc}$$

4.4

Where η is the dynamic viscosity (cP), Y_0 the intercept, k the rate constant, and c the concentration of antibody (mg/mL).

Another model, developed by Tomar *et al.*^{144,238} was deployed for fitting the viscosity data:

$$\ln \frac{\eta}{\eta_0} = \ln A + Bc$$

4.5

Where η is the dynamic viscosity (cP), η_0 the buffer viscosity (cP) set at 1.13, c the concentration (mg/mL), and $\ln A$ the intercept of the slope B , when $\ln \frac{\eta}{\eta_0}$ is plotted against concentration.

Finally, a modified Ross-Minton model was used to fit the viscosity-concentration profiles:

$$\eta = \eta_0 e^{\left(\frac{[\eta]c}{1 - \left(\frac{k}{v}\right)[\eta]c} \right)}$$

4.6

Where k the crowding factor, v the Simha shape parameter. The $[\eta]$, k and v parameters were estimated using the generalised reduced gradient (GRG) non-linear solver function to determine the local optimum reducing the sum of squared errors.

For intrinsic viscosity $[\eta]$ measurements, multiple priming segments were set up followed by 10 replicates at the maximum shear rate of 23,080 s⁻¹. Formulation buffer and anti-IL-8 formulations in the 5-50 mg/mL concentration range were measured to determine the relative viscosities (η_{rel}) from which the specific (η_{sp}) and reduced viscosities (η_{red}) could be calculated (**Appendix 3 Equation 9.1 and 9.2**). The intrinsic viscosity was calculated from the linear regression of η_{red} over the sample concentration range tested, from which the Huggins coefficient was derived (**Equation 4.7**).

$$k_H = \frac{\eta_{red} - [\eta]c}{[\eta]^2 c}$$

4.7

Where k_H is the Huggins Coefficient, η_{red} the reduced viscosity (cP) which is η_{sp}/c , $[\eta]$ the intrinsic viscosity (cP) and c the sample concentration (mg/mL).

The uncertainty of k_H (σk_H) was calculated from the propagation of error equation:

$$\sigma k_H = k_H * \sqrt{\left(\frac{\sigma[\eta]^2}{[\eta]^2}\right)^2 + \left(\frac{\sigma x}{x}\right)^2 - 2 \frac{\sigma[\eta]^2 * \sigma x}{[\eta] * x}}$$

4.8

Where $[\eta]^2$ the squared intrinsic viscosity, $\sigma[\eta]^2$ the error of squared intrinsic viscosity, x the slope determined from the linear regression of η_{red} versus concentration, and σx error of the slope.

Statistical Analysis.

JMP Pro (v16.0.0, 2021) was used for multivariate analysis of computational predictions and measurement data to determine correlations between molecular descriptors and experimental parameters. We used GraphPad Prism (v5.04) for constructing graphs and performing unpaired t-test statistical analysis.

4.6. Results

4.6.1 Patch analysis and homology constructs of anti-IL-8 IgG1 and IgG3

Solvent-accessible charge and hydrophobicity distribution profiles mAb self-association propensity that can promote aggregation.^{178,235,270} Disruption of hydrophobic patches has been previously correlated with reduced viscosity,^{230,232} driven by reduced native and non-native aggregation events.²³¹ Furthermore, charge asymmetry between heavy and light chains has been correlated to increased self-association propensity, with increased electrostatic interactions.^{233,241,270} Therefore, the hydrophobic and electrostatic surface patch distribution profile of the anti-IL-8 IgG1 and IgG3 pair was assessed using full IgG homology constructs (Figure 4.1). Since the variable regions for both molecules were similar, any differences occurring in the surface potential distributions were attributed to differences in the constant region (Fc) between the molecules. Overall, with both IgG1 and IgG3 molecules we see a high proportion of hydrophobic patches (42% and 37%, respectively), with distinct differences in electrostatic patch (*i.e.*, positive and negative patch) distributions deriving predominantly from the increased residue exposure of the larger Fc domain of IgG3 (**Appendix 3 Table 9.4**). The lowest energy conformation for the 62-residue IgG3 hinge region homology model was chosen (**Appendix 3 Table 9.2**), contributing to 11% and 9% of the overall negative patch and positive residue

contributions, respectively in comparison to the 4% and 1% contributions from the IgG1 hinge (**Appendix 3 Table 9.5**). The modelled IgG3 hinge also demonstrated a high hydrophobic contribution to total hydrophobic residue contributions (9%, versus 1% from the IgG1 hinge).

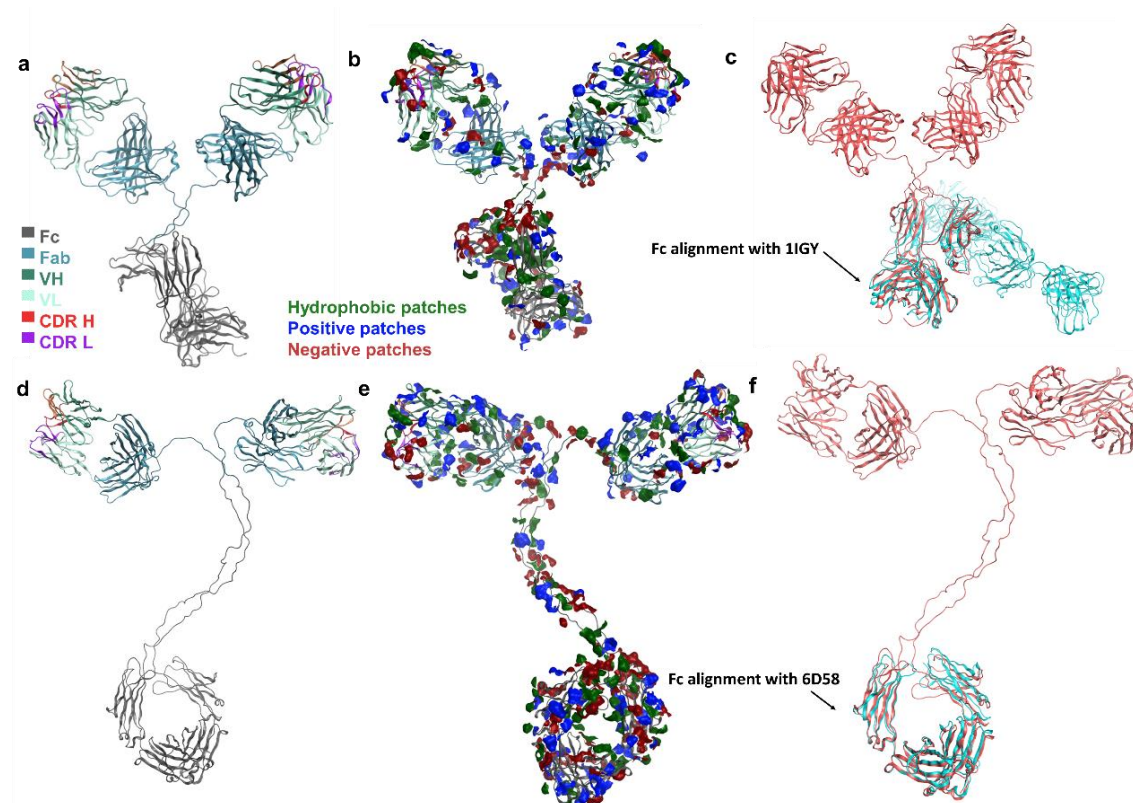


Figure 4.1 Homology constructs of the full IgG1 and IgG3 molecules.

The Fc (grey), constant light chain 1 and heavy chain 1 (blue), variable heavy chain (dark green) variable light chain (light green), heavy chain CDRs (red) and light chain CDRs (purple). **a**, Full IgG1 structure, **d**, full IgG3 structure, **b** and **e** patch analysis of IgG1 and IgG3 homology constructs, and **c** and **f**, Fc templates for IgG1 and IgG3.

As expected, due to the increased molecular size, IgG3 presented with a greater total solvent-accessible exposed area than IgG1 (Res_ASA of 40,569 Å² and 33,365 Å², respectively). However, this assumed structure may not accurately represent the surface patch exposure of IgG3 due to hinge flexibility, affecting domain angles.

4.6.2 Biophysical Parameters of anti-IL-8 IgG1 and IgG3

Confirmation of identity and purity of anti-IL-8 IgG1 and IgG3. To compare the biophysical properties of IgG3 to IgG1, a combined comprehensive pipeline

consisting of computationally predicted molecular descriptors and experimental biophysical analyses was used. We analysed the correlations between *in silico* and experimental charge, including hydrophobicity and colloidal parameters, and viscosity predictions and measurements. Both IgG1 and IgG3 sequence identities were confirmed with LC-MS peptide mapping (**Appendix 3 Table 9.7**).

Antigen binding affinity of anti-IL-8 IgG1 and IgG3

The antigen affinity for the anti-IL-8 IgG1 and IgG3 antibody pair was assessed *via* surface plasmon resonance (SPR). Both molecules showed affinity (K_D) for the IL-8 antigen with comparable association (k_a) and dissociation (k_d) rates (within the same order of magnitude). This demonstrated that the sequence and structural differences of the IgG3 constant domain had little influence on the Fv affinity for the target antigen.

Table 4.1 Antigen (IL-8) binding kinetics for IgG1 and IgG3 assessed *via* SPR.

Corresponding (mean \pm standard deviation) binding on-rate (k_a), binding off-rate (k_d) and the equilibrium dissociation constant (K_D), the maximum response (R_{max}) and goodness of fit (Chi-squared) of the 1:1 binding model. (N=3)

Molecule	1:1 binding kinetics				Kinetics (χ^2)
	$k_a \times 10^5$ ($M^{-1}s^{-1}$)	$k_d \times 10^{-4}$ (s^{-1})	K_D (nM)	R_{max} (RU)	χ^2
IgG1	3.84 (± 0.12)	10.27 (± 0.98)	2.67 (± 0.16)	15.57 (± 0.38)	1.57 (± 0.62)
IgG3	2.41 (± 0.18)	9.17 (± 0.05)	3.82 (± 0.26)	14.63 (± 0.15)	1.69 (± 0.27)

Reduced physical stability of anti-IL-8 IgG3 compared to IgG1

To be therapeutically viable, mAb formulations must have a solution phase stability of up to two years at refrigerated temperature and hours-several days under ambient storage conditions. A short-term stability study (up to 57 days) was conducted to assess relative changes in anti-IL-8 IgG monomeric purity from day 0 under refrigerated and ambient storage conditions and through three freeze-thaw cycles (**Figure 4.2**). Both mAbs were within specification at day zero (>95% monomeric purity). IgG3 showed a significant reduction in monomer purity from day 0 (surpassing the 2% high molecular weight species threshold) when held at 25 °C by day 7, which

could be attributed to increased soluble aggregation. This increased aggregation was exacerbated after freeze-thaw cycling, particularly when held at 25 °C.

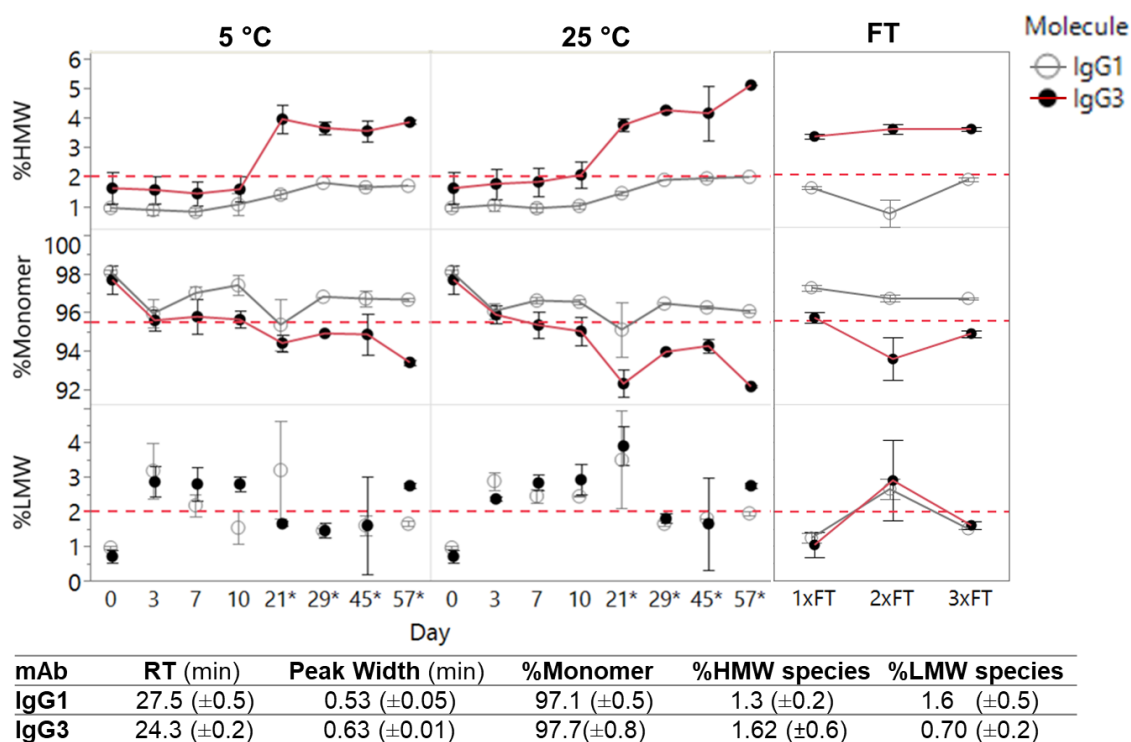
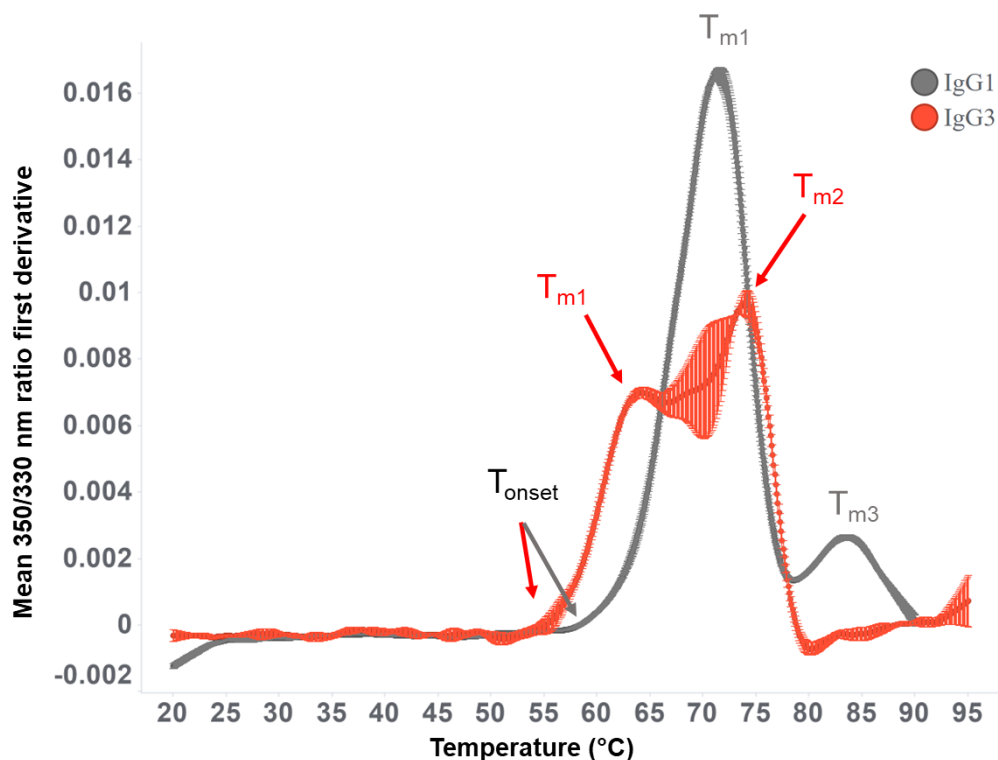


Figure 4.2 Reduced stability after freeze-thaw cycling and at 25 °C over 57 days for IgG3 compared to IgG1.

aSEC was used to monitor the monomeric purity of mAb 1 IgG1 and IgG3 over 57 days at 5 °C and 25 °C. Freeze-thaw stability was also assessed through three cycles. *aSEC data from day 21 to 57 was after one freeze-thaw cycle. Red dotted lines represent thresholds flag-ging changes in physical stability of mAbs. Corresponding monomeric purity and aggregate content as analysed by aSEC on day 0 for both molecules (bottom). Error bars represent standard deviations per sample, N=2. *Abbreviations: HMwS: high molecular weight species, LMwS: low molecular weight species, FT: freeze-thaw.*

Differential scanning fluorimetry (DSF) was used to assess unfolding temperatures to distinguish conformational stability for the anti-IL-8 IgG1 and IgG3 pair (Figure 4.3). A lower temperature for the unfolding onset (T_{onset}) and first unfolding event (T_{m1}) were detected for IgG3, as well as significant changes in thermal profile. Interestingly, no significant differences were detected for the temperature of aggregation onset (T_{agg}) with IgG3 showing distinctly different scattering intensity profiles compared to IgG1 (**Appendix 3 Figure 9.1**), potentially indicating a range of different aggregate confirmation states for IgG3, leading to variable back-reflection.



Molecule	T_{onset} (°C)	T_{m1} (°C)	T_{m2} (°C)	T_{m3} (°C)	T_{agg} (°C)
IgG1	62.85 (± 0.34)	71.28 (± 0.17)	ND	83.71 (± 0.08)	71.31 (± 2.40)
IgG3	54.86 (± 1.04)	64.13 (± 0.03)	73.20 (± 0.56)	ND	73.36 (± 1.35)

Figure 4.3 IgG3 shows reduced conformational stability compared to IgG1 at high concentrations from nano-DSF unfolding temperatures.

Thermal unfolding profiles for anti-IL-8 IgG1 (grey) and IgG3 (red). The mean first derivative values from the 350/330 nm ratio over a 20-95 °C range. Error bars represent standard deviation. N=3.

Anti-IL-8 IgG3 has a positive charge under formulation conditions

Next, the predicted differences in electrostatic patch distribution profiles translated to measured charge parameters for anti-IL-8 IgG1 and IgG3 molecules (**Figure 4.4** and **Figure 4.5**) were investigated. Comparable isoelectric points (pIs) (**Figure 4.4d**) were measured for IgG1 and IgG3; however, charge heterogeneity differences were observed with an increased proportion of acidic isoforms for IgG3 (**Figure 4.4a**), accompanied with an increased proportion of predicted negatively-charged patches in the constant domain. IgG1 and IgG3 showed significant differences in the mean measured zeta potential in formulation buffer at pH 6.0 (**Figure 4.4e**). IgG3 had a positive zeta potential, whereas, IgG1 had a negative zeta potential.

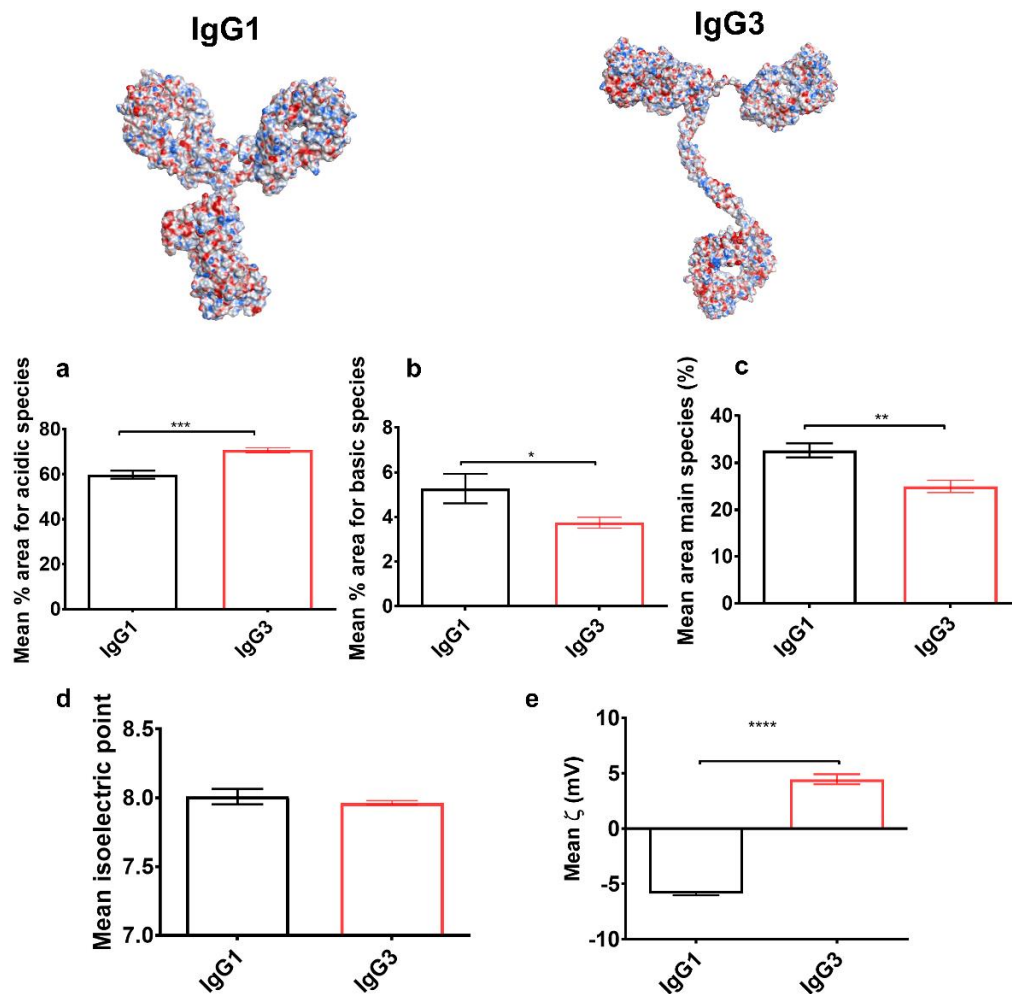


Figure 4.4 Different surface potential profiles were obtained for anti-IL-8 IgG1 and IgG3 predictions, which yielded comparable measured isoelectric points.

Poisson-Boltzmann surface electrostatics were mapped onto homology constructs of anti-IL-8 IgG1 and IgG3, indicating regions of negative and positive charge density. Charge heterogeneity assessed via capillary isoelectric focussing (cIEF), **a**, acidic isoforms **b**, basic isoforms, **c**, main species, **d**, mean isoelectric point (pI), and **e**, mean zeta potential at 5mg/mL at pH 6 (formulation buffer). Unpaired t-test **** denotes a $P < 0.0001$, *** $P < 0.001$, ** $P < 0.01$, * $P < 0.1$). Error bars represent standard deviation, $N=3$.

The sequence and structure-based theoretical pIs predicted for IgG3 were slightly lower than those for IgG1, but the structure based pI (pI_3D) directly correlated with experimental pI (**Figure 4.5a**). There was no significant correlation observed between the predicted and measured zeta potential (**Figure 4.5b**). The slight reduction observed in measured isoelectric point and increased measured zeta potential for IgG3 correlated with increased ionic patch area descriptors and reduced net charge (**Figure 4.5c**).

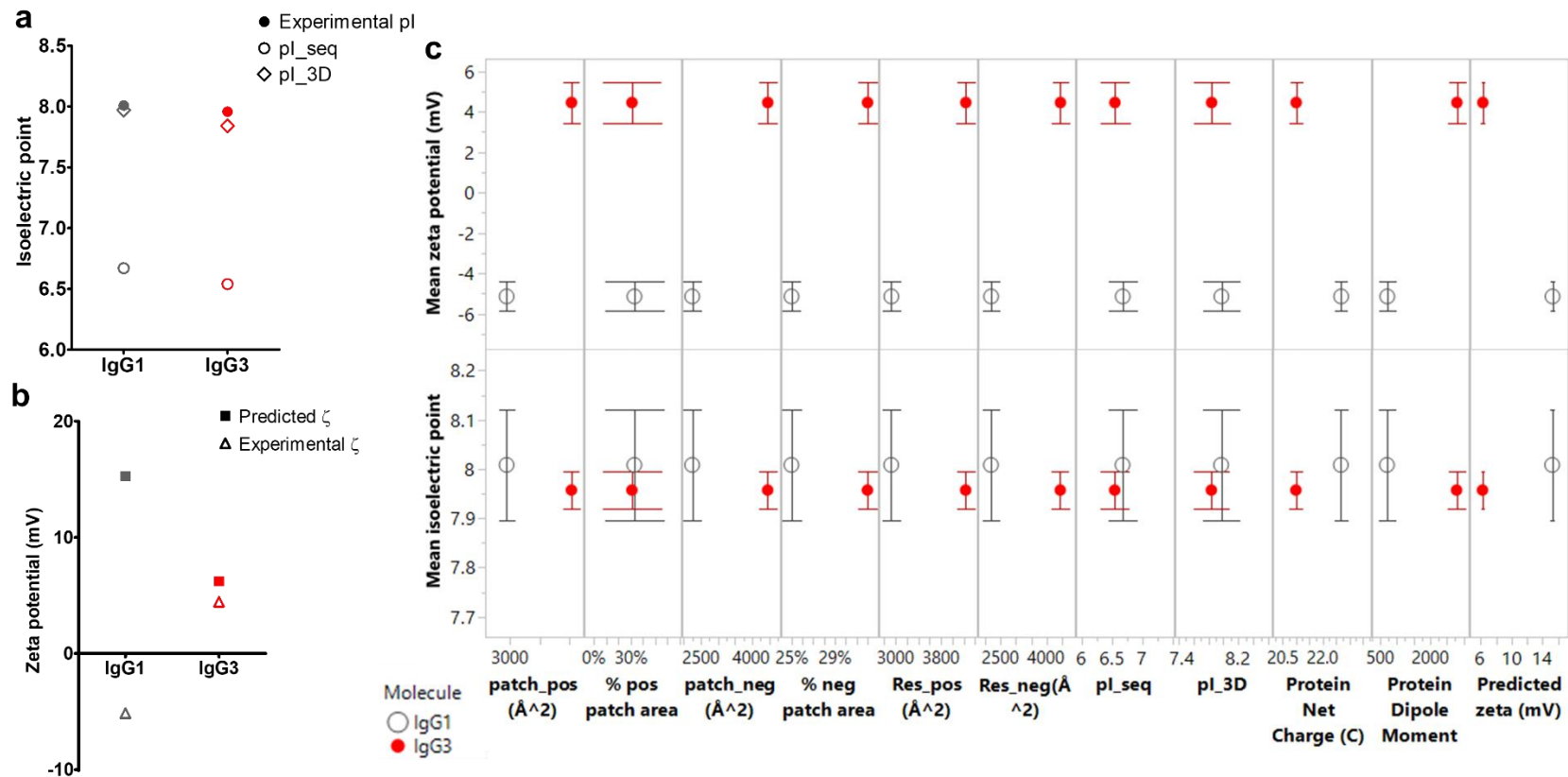


Figure 4.5 Comparing charge differences to *in silico* charge descriptors for anti-IL-8 IgG1 (grey) and IgG3 (red).

a, The theoretical sequence-based pI was significantly lower than the experimentally measured pI. **b**, Predicted zeta potential (computed at pH 6.0, 0.1 M NaCl) showed poor correlation with measured zeta potential values (at 5mg/mL). **c**, Pair-wise comparisons between charge based in silico descriptors and experimental pI and zeta potential values. Error bars represent standard deviation of experimental data.

Anti-IL-8 IgG3 exhibits a lower degree of hydrophobicity compared to IgG1

The hydrophobicity of anti-IL-8 IgG1 and IgG3 was assessed *via* hydrophobic interaction chromatography (HIC) (**Figure 4.6**). A significantly lower on-column retention time (RT) was observed for IgG3 in comparison to IgG1 (**Figure 4.6a**), disagreeing with most hydrophobic-based *in silico* descriptors showing higher predicted hydrophobicity for IgG3 compared to IgG1 (with the exception of a slightly lower hydrophobic index and proportional percentage hydrophobic patch area) (**Figure 4.6c**). IgG3 also presented with increased peak broadening on the HIC column (**Figure 4.6b**), suggesting a potential increased population of different hydrophobic conformations.

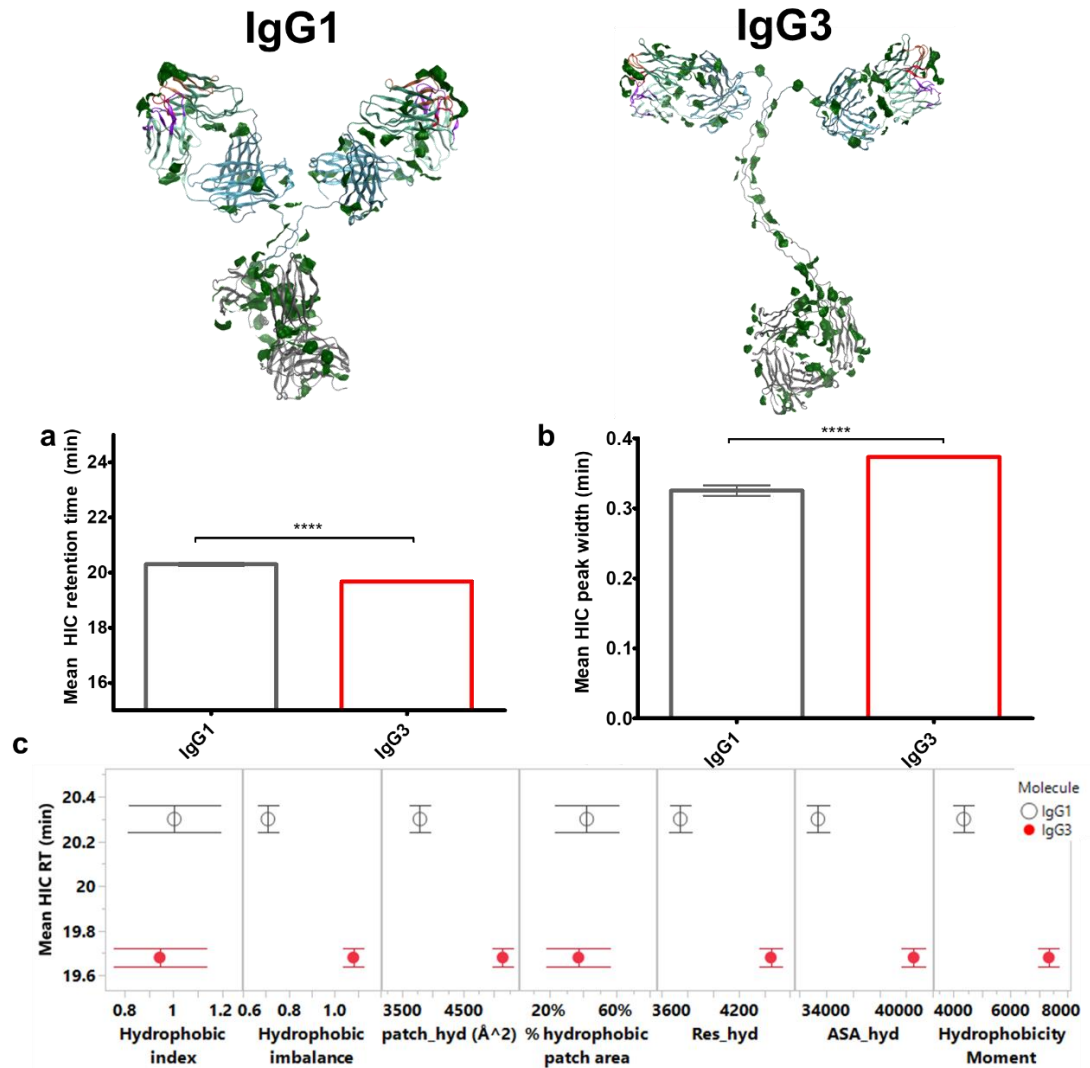


Figure 4.6 IgG3 exhibits a lower degree of hydrophobicity in comparison to IgG1, contradicting computed solvent accessible hydrophobic area data.

Protein patch surface maps for anti-IL-8 IgG1 and IgG3, filtered for hydrophobic patches (green). **a**, Retention time and, **b**, peak width on the HIC column between IgG1 and IgG3 are compared. **c**, Pair-wise scatter plot comparisons between *in silico* descriptors and HIC retention time (RT). Unpaired t-test **** denotes a $P < 0.0001$. Error bars represent standard deviation, $N=2$. Non-significant differences are not represented.

Colloidal parameters of anti-IL-8 IgG1 and IgG3

Parameters obtained from light scattering measurements have routinely been used as an indicator of solution-phase interactions occurring between mAb molecules. Using dynamic light scattering, the concentration-dependent diffusion coefficient for

anti-IL-8 IgG1 and IgG3 was measured. Affinity-Chromatography Self-Interaction Nanospectroscopy (AC-SINS) was also used as an orthogonal approach to measure the comparative self-association behaviour of IgG1 and IgG3 (**Figure 4.7**). As expected, IgG3 measurements showed a larger hydrodynamic diameter (Z_{ave}) in comparison to IgG1, with a steady concentration-dependent increase over the 1-20 mg/mL test concentration range (**Figure 4.7a**), which corresponded to slower diffusion coefficients (**Appendix 3 Figure 9.2**). The measured self-interaction parameter, k_D , for both molecules was negative and below the -15 mL/g threshold set, suggesting predominant attractive forces. However, k_D was significantly more negative for IgG3 anti-IL-8 compared to IgG1, indicative of increased self-association propensity. Conversely, IgG3 showed a comparable red shift from the AC-SINS assay, not aligning to the increased self-association propensity suggested from DLS data.

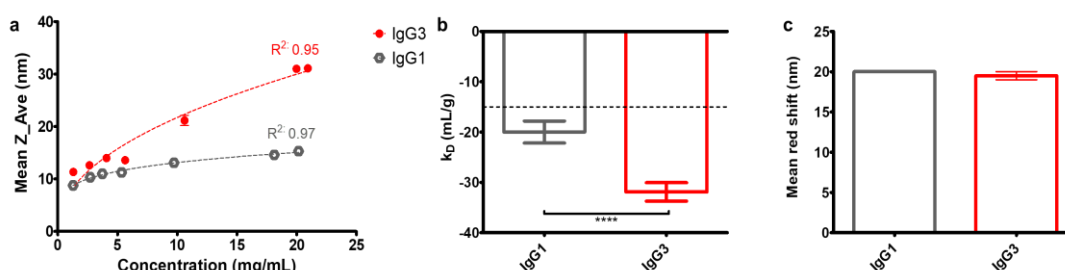


Figure 4.7 Colloidal interaction data from dynamic light scattering (DLS) measurements and Affinity-Chromatography Self-Interaction Nanospectroscopy (AC-SINS) for anti-IL-8 IgG1 and IgG3.

a, Concentration-dependent measured z-average hydrodynamic diameter. Logarithmic fits of $10^{0.2 \log(\text{concentration}) + 0.92}$ and $10^{0.46 \log(\text{concentration}) + 0.87}$ were applied to IgG1 and IgG3, respectively. Goodness of fit R^2 values are reported. **b**, self-interaction parameter (k_D) for IgG3. A dotted line at -15 mL/g represents a threshold for k_D . **c**, Mean red shift in absorbance spectra from AC-SINS (N=2). Unpaired t-tests were performed to determine significant differences between means (**** denotes a $P < 0.0001$). Error bars represent standard deviation. N=3.

Viscosity predictions and analysis for anti-IL-8 IgG1 and IgG3

The Generalised Stokes Einstein viscosity (**Equation 4.3**) was calculated using DLS-derived diffusion coefficients (**Appendix 3 Figure 9.2**) and hydrodynamic diameters (**Figure 4.7a**). The resulting theoretical viscosities (**Figure 4.8a**) were log-transformed and showed a distinct increased viscosity for IgG3 at formulation concentrations ≥ 50 mg/mL in comparison to IgG1. Overestimation of the IgG3

viscosity and underestimation of IgG1 viscosity at 180 mg/mL (3,430 cP and 52 cP, respectively) is reflective of the derivation of data measured in the 1-20 mg/mL concentration regime, and the assumptions of using exponential fits for the diffusion coefficients and logarithmic fits for the Z-average values.

Therefore, the apparent viscosities of IgG1 and IgG3 were also measured at concentrations up to 150 mg/mL (**Figure 4.8b-d**). An elevated apparent viscosity was observed for IgG3 compared to IgG1, in agreement with predicted theoretical viscosity and colloidal measurements.

To-date various models have been applied to modelling mAb viscosity-concentration profiles. To compare the predictive power of different viscosity models, three different viscosity-concentration curves fits were used, including an exponential growth model (**Equation 4.4**), a Tomar model (**Equation 4.5**), and a modified Ross-Minton model (**Equation 4.6**). The exponential growth fit (**Figure 4.8b**) had a similar knee of the curve and gradient to the Ross-Minton fit (**Figure 4.8d**), resulting in similar viscosity interpolations at 180 mg/mL of 81.22 cP and 84 cP for IgG1, and 151.76 cP and 161.72 cP for IgG3, respectively. The Tomar model fit (**Figure 4.8c**) exhibited a shifted the knee of the curve and steeper gradient compared to two previous models, resulting in higher interpolated viscosity predictions at 180 mg/mL (85.16 cP for IgG1 and 290.54 cP for IgG3).

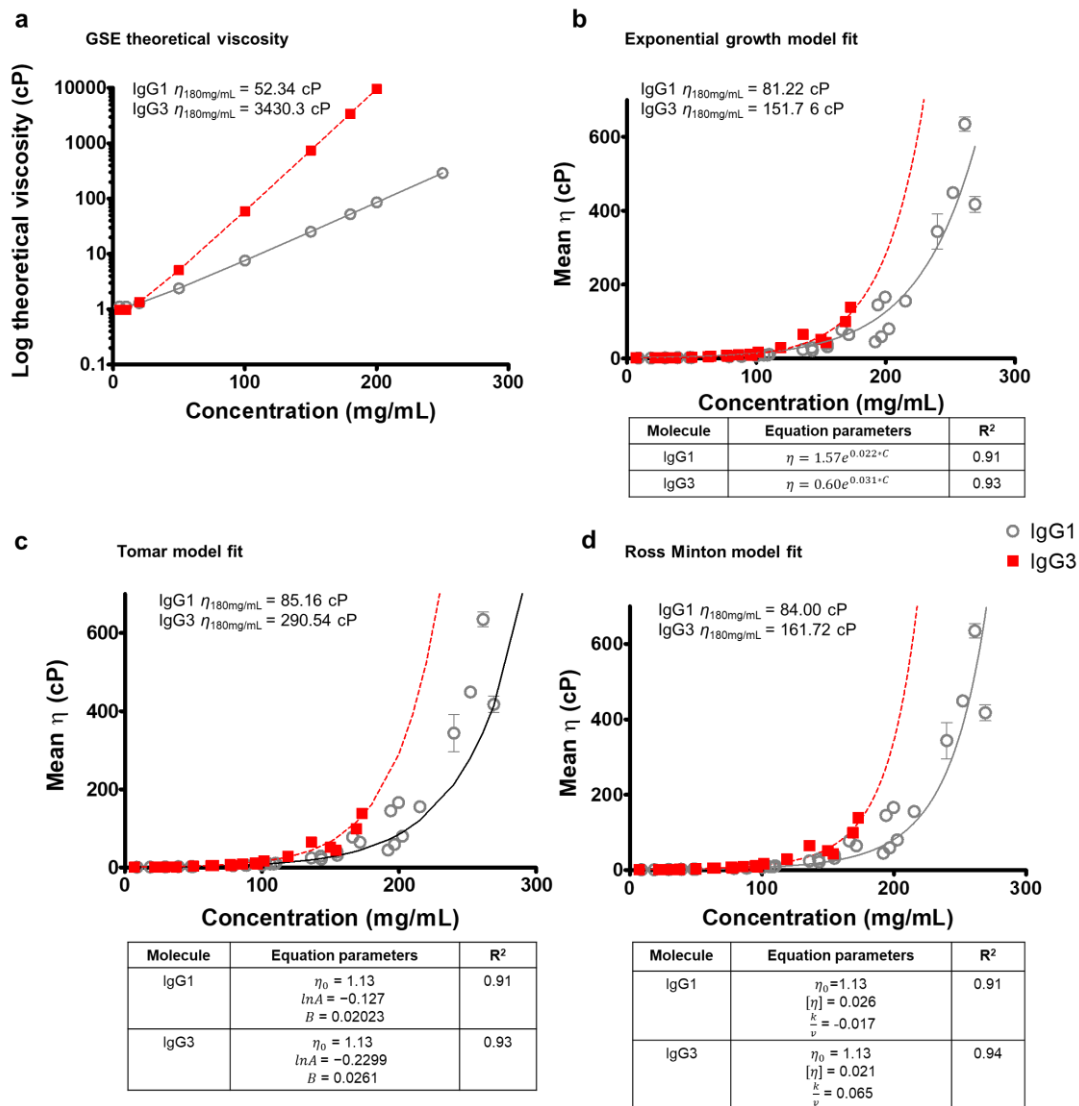


Figure 4.8 IgG3 demonstrated higher apparent viscosity (η) than IgG1 at high concentrations.

a, the Generalised Stokes-Einstein equation was calculated from exponential extrapolation of diffusion coefficients and logarithmic fit of z-average diameters measured in the dilute range (1-20 mg/mL). **b**, the exponential growth model **c**, the modified Ross Minton model, and, **d**, the Tomar fit model. For each model, the predicted viscosity at 180 mg/mL is reported for both IgG1 and IgG3. Error bars represent standard deviation, N=3.

Finally, the individual contributions from each molecule to the solution viscosity was examined by calculating intrinsic viscosity, $[\eta]$, from measurements in the low concentration regime (0-50 mg/mL) (Table 4.2 and Appendix 3 Figure 9.3). Although statistically comparable to IgG1, IgG3 had an increased intrinsic viscosity, correlating with its increased hydrodynamic size. This suggests that the increased size and

effective volume fraction of IgG3 increases the solution's resistance to flow in the dilute regime.

Moreover, the Huggins coefficient (k_H) was computed, describing the changes in rate of viscosity increase from pair-wise interactions. This has been previously equated to 'solvent quality' with values >0.5 suggestive of 'poorer solvents' that have solution viscosities more sensitive to protein-protein interactions (PPIs).³³² Interestingly, IgG3 showed a reduction in k_H compared to IgG1, but both molecules had $k_H >0.5$, indicating poor solvation.

Table 4.2 Intrinsic viscosity and Huggins coefficient for anti-IL-8 IgG1 and IgG3.

Mean \pm standard errors are shown, N=2.

Molecule	Intrinsic viscosity (mL/g)	k_H
IgG1	8.28 (\pm 3.89)	5.30 (\pm 1.2)
IgG3	10.42 (\pm 2.89)	1.27 (\pm 0.8)

4.7. Discussion

The IgG3 mAb subclass possesses a set of unique biological properties, offering significant therapeutic advantages as next-generation therapeutics. For example, the flexibility of the IgG3 hinge region, renders it of interest to targeting epitopes occurring at low abundance and density. Moreover, the Fc portion of the IgG3 molecules results in enhanced engagement with immune effector cell Fc γ Rs with the scope to be harnessed for immunotherapy-based applications. Current literature investigating the developability of IgG3s are broadly limited to assessing conformational flexibility from structural studies,^{333–335} post-translational modifications (primarily glycosylation),³²⁴ and functional activity assessment in the context of immune activation.^{336,337} Therefore, we set to probe the self-association propensity and viscosity-concentration profiles of an anti-IL-8 IgG1 and IgG3 pair using a combination of computational and experimental approaches.

Reduced physical and conformational stability of anti-IL-8 IgG3

Poorer short-term physical and thermal stability was observed for the anti-IL-8 IgG3 compared to IgG1 (**Figure 4.2** and **Figure 4.3**). While there is a lack of any published thermostability data on IgG3 molecules, the anti-IL-8 IgG1 unfolding temperatures are in agreement with IgG1 molecules in previous developability studies.³⁴ The extended

hinge region of IgG3 is proposed to confer reduced *in vivo* stability, increased number of allotypes and reduced half-life.^{329,338–340} Therefore, additional structural analysis of anti-IL-8 IgG3 conformational stability is needed to better understand its role in formulation shelf-life prediction, and pairing these findings with functional stability and immunogenicity assessment. The immunogenicity of IgG3 resulting from concerns on glycosylation propensity has previously been flagged for this subclass,³²⁹ necessitating the monitoring of IgG3 post-translational modifications over time for both batch-to-batch and shelf-life stability.

Predicted charge differences do not translate to differences in isoelectric points

Electrostatic surface potential mapping from homology constructs predicted an increased surface coverage of solvent accessible negatively charged patches for anti-IL-8 IgG3 in comparison to IgG1, suggesting an increased likelihood for electrostatic interactions to occur (**Figure 4.4**). The theoretical isoelectric points (pIs) for IgG3 were predicted to be lower than IgG1 (**Figure 4.5**). However, although slightly lower, the experimental pI for IgG3 was statistically comparable to IgG1. pI_{3D} showed a greater predictive power than pI_{seq} for the anti-IL-8 full IgG models. Thorsteinson *et al.* similarly observed pI_{3D} to have the highest correlations to experimental parameters, but this was based on Fv models only and were statistically comparable to the sequence-based pI method.²⁴² The increased negative patch count and area for IgG3 correlated with a decreased predicted net charge, which has been correlated previously with increased solution viscosity at dose-relevant formulation concentrations.^{161,233,251} Surprisingly, anti-IL-8 IgG3 showed a positive measured zeta potential (ζ) compared to a negative potential for IgG1, which did not align with the *in silico* predictions of zeta potential and isoelectric points. The negative ζ for IgG1 may be accounted for by preferential binding of anions to protein surfaces affecting the pH at which there is zero electrophoretic mobility, which has been reported as at least one pH unit below the pI determined from cIEF.⁷⁴ The possibility of different conformational forms of IgG3 from inferred hinge flexibility with different ionic surface patch exposure may contribute to why a positive ζ was observed for IgG3. Furthermore, ζ is calculated from the electrophoretic mobility of the protein with assumed spherical shape.³⁴¹ It is also dependent on the orientation of the molecule in solution affecting the frequency shift of scattered light which may result in large discrepancies to expected charge.³⁴² Finally, *in silico* ζ predictions do not account for

buffer composition affecting surface bound ions, nor the effect of multiple or alternative species in solution (ζ measured at 5 mg/mL).

Net hydrophobicity of IgG3 does not correlate with predicted hydrophobic potential

Contrary to the predicted increased hydrophobic contributions from the hinge region both on a sequence level (with more cysteine, alanine and proline residues), and on a structure level (with an increased hydrophobic area (**Appendix 3 Table 9.3** and **Table 9.4**)), anti-IL-8 IgG3 showed a shorter retention time on the hydrophobic-interaction chromatography column compared with IgG1 (**Figure 4.6**). The discrepancies between predicted and experimental hydrophobicity are hypothesised to arise from changes in conformational forms of IgG3, varying exposure of the hinge residues and hydrophobic patches on the Fc. Increased net hydrophobicity has previously been correlated with increased solution viscosity occurring *via* cation- π and π - π stacking interactions from aromatic groups of solvent-exposed non-polar amino acid residues.^{232,343} Furthermore, increased hydrophobicity in the constant domain (Fc) of antibodies is widely correlated with a higher aggregation propensity, promoting an elevated mAb solution phase viscosity.^{182,344} In this case, as anti-IL-8 IgG3 showed a decrease in net hydrophobicity, the increased self-association or aggregation propensity could not be attributed to hydrophobic interactions. Currently, there is a significant knowledge gap on drivers of IgG3 hydrophobicity, both measured and predicted, and how this affects the balance of domain-domain stability to unfolding propensity and aggregation.

Increased self-association propensity of anti-IL-8 IgG3 correlates with hydrodynamic size and increased viscosity

The self-interaction parameter, k_D , is widely used for predicting the propensity for protein-protein interactions at the molecular level, which drive elevated solution viscosity at high mAb formulation concentrations. For both molecules the k_D was negative and below the -15 mL/g arbitrary threshold set, suggesting predominant attractive forces. A more negative k_D was observed for anti-IL-8 IgG3 (**Figure 4.7**), indicating more attractive interactions between molecules in the dilute concentration regime compared with IgG1.^{79,83,173,229}

Unexpectedly, the AC-SINS red shift for IgG3, another metric used to experimentally predict mAb self-interaction propensity, showed a comparable absorbance intensity

profile to the anti-IL-8 IgG1. A hypothesis is that an increase in red shift may be masked by the reduced binding of IgG3 to the anti-Fc conjugated gold nanoparticles used during AC-SINS measurements. This may be a result of conformational flexibility provided by the extended IgG3 hinge region, leading to structural blocking of adjacent binding sites on the nanoparticles. Subsequently, this could reduce the number of bound antibodies to engage in self-interactions.

Across all viscosity fitting models applied in this chapter, an increased apparent viscosity was observed for IgG3 in comparison to IgG1, aligning to the decreased predicted net charge, increased negative patch distributions, and increased hydrodynamic self-associations (**Figure 4.8**). The extrapolation of the Generalised Stokes-Einstein (GSE) model (**Figure 4.8a**) shows elevated viscosity, suggesting viscosity-contributing interactions in the dilute regime for anti-IL-8 IgG3. This aligns to the increased intrinsic viscosity for IgG3 (**Table 4.2**), suggesting the increase hydrodynamic radius increases the fluid's resistance to flow. Notably, no increase in the Huggins' coefficient (k_H) was observed for IgG3, which suggests comparable protein-protein pairwise interactions that contribute to IgG1 viscosity, with long-range repulsions prevailing. However, it is worthwhile noting the inaccuracies of the k_H parameter. The error in $[\eta]$, from which the k_H parameter is derived, can arise from the use of simple linear regression of η_{red}/c fits (**Appendix 3 Figure 9.3**) as well as inter-experimental variability in viscosity measurements. Alternate non-linear fits may be able to account for antibody molecules which exceed the hard-sphere limit with regards to effective volume fraction of >2.5 . Another limitation of the Huggins coefficient is that it does not account for solvation effects in dilute antibody solutions.

90,171,251

It is important to note that the homology constructs represent one possible conformation, and particularly with the assumed structure of IgG3, there are risks of under or overestimating the solvent-exposed surface potential. In this chapter, these models were used as guiding tools to better understand mechanistic interactions that lead to molecular biophysical behaviour. There are growing efforts to research different structural modelling tools as well as use of molecular dynamics simulations with coarse grain simulation modelling^{146,345} that could help expand our knowledge of how both sequence and structure dictate interactions that lead to elevated viscosity and stability for IgG3.

4.8. Conclusions

Pre-clinical developability assessment constitutes a prominent area of research for improving the probability of success for early-phase antibody candidates to reach clinical phases. Predictive tools probing the physicochemical and colloidal stability, affinity and viscosity of antibodies in their formulation are being developed in combination with experimental assay pipelines as well as machine-learning algorithms. Various immunoglobulin subclasses (IgG1, IgG2, and IgG4) with differing therapeutic pharmacokinetic profiles have previously been evaluated for their developability characteristics. IgG1 and IgG3 antibodies are known to differ in their sequence, structure and biophysical properties, including their propensity for self-association and elevated solution viscosity at dose-relevant formulation mAb concentrations.

In this chapter, I provide the first insights into the biophysical behaviour a recombinant anti-IL-8 IgG3, comparing its computationally predicted molecular descriptors and experimentally-determined parameters to that of a paired IgG1 with the same variable region sequence. The goal was primarily to assess the differences in physical stability and solution-phase viscosity-concentration profiles for these anti-IL-8 paired isotypes as well as charge, hydrophobic and colloidal parameters. It is recognised that elevated solution viscosity of mAbs is driven by their self-association propensity. Hence, I used a combined *in silico* and comprehensive experimental pipeline to profile any viscosity differences between anti-IL-8 IgG1 and IgG3 molecules. The predicted computational descriptors derived from the *in silico* homology model, including the sequence and structure-based molecular descriptors determined for each anti-IL-8 molecule were reconciled with their measured biophysical properties.

The constant domain of anti-IL-8 IgG3 was found to significantly influence its biophysical profile. IgG3 showed increased charge heterogeneity and self-association propensity, correlating with predicted increased ionic surface potential from *in silico* homology modelling. This, alongside, decreased physical and conformational stability, aligns with the elevated solution viscosity observed for IgG3 compared with IgG1. The increased hydrodynamic size of IgG3 correlated with increased intrinsic viscosity, supporting increased thermodynamic as well as hydrodynamic contributions to solution viscosity.

This work uniquely defines the bounds of manufacturability in the context of biophysical behaviour of an IgG3 molecule. This chapter unearths the potential to further investigate the developability of the IgG3 subclass with formulation optimisations and/or *in silico* directed sequence-engineering. These investigations should be paired with functional assays in the future to support the use of this subclass which holds distinct therapeutic potential.

5. Reconciling predicted and measured viscosity parameters for high concentration monoclonal antibody formulations

The contents of this chapter has been pre-printed as a working paper; Armstrong G.B, Roche A., Lewis W., Rattray Z. “Reconciling Predicted and Measured Viscosity Parameters in High Concentration Antibody Solutions.” *ChemRxiv*, (2024). <https://doi.org/10.26434/chemrxiv-2024-vk935>.

GB Armstrong- author of this thesis- performed all experimental and *in silico* modelling on the reported mAb panel.

5.1. Abstract

In this chapter, a comparison was performed of viscosity prediction and fitting models at different mAb test concentration regimes for measuring viscosity-concentration profiles, using the anti-IL-8 mutant panel and wild-type IgG1 from chapter 2. For viscosity profile fitting, the modified Ross-Minton and exponential growth equations show the highest goodness of fit, but extrapolation from low concentration measurements is cautioned against. Moreover, use of low concentration measurements or descriptors are neither generalisable nor predictive of ultra-high concentration viscosity. This chapter highlights the importance of both analyte concentration range selection, and bespoke viscosity model prediction for antibody series with the same target antigen.

5.2. Introduction

Monoclonal antibodies (mAbs) represent an important therapeutic class, with the growing implementation of autoinjectors in the clinical domain for patient and carer self-administration in the home setting. Administration *via* the subcutaneous route, necessitates the formulation of mAbs at high solution concentrations (> 100 mg/mL) and low dose volumes to achieve target therapeutic effects.³⁴⁶

High-concentration mAbs face significant challenges resulting from molecular crowding at ultra-high mAb concentrations, and the conformational flexibility of mAbs lead to increased intermolecular interactions resulting in elevated opalescence, higher protein aggregation risk, phase separation, and elevated solution viscosity.²⁵¹

Viscosity, a fluid's resistance to flow or rate of deformation, is mechanistically characterized by examining electroviscous effects, mAb molecular size, and surface potential distributions, with these factors determining the likelihood of protein-protein interactions (PPIs).^{163,251}

Developed from colloidal principles, where the protein is assumed to be a charged hard-sphere, the primary electroviscous effect describes the distortion of electrical double-layer thickness in the ultra-dilute regime with varying ionic strength. Changes in counterions and the hydration shell surrounding the mAb molecule will affect the overall molecular hydrodynamic volume and Brownian motion.^{91,347} With the increasing drive for ultra-high concentration mAb formulations, intermolecular excluded volume effects (*i.e.*, secondary electroviscous effect) can reduce mAb solubility and increase solution viscosity.^{168,251} The increased molecular crowding and reduced inter-'particle' distance increase the pair interaction potential.³⁴⁸ The average interaction potential is quantified by the second virial coefficient (B_{22}) or diffusion interaction parameter (k_D) that are correlated with solution-phase viscosity.^{144,349} However, the B_{22} and k_D parameters do not adequately reflect anisotropic interactions arising from differences in surface potential distributions. Derived from the Huggins Equation, used to calculate intrinsic viscosity, the Huggins coefficient (k_H) describes the rate of change in viscosity from pairwise interactions, for instances where strong correlations between k_H and viscosity at low mAb concentrations exist.⁹⁰

Beyond pair-wise interactions, cluster formation from soluble mAb oligomerisation plays a critical role in the viscosity of high concentration mAb solutions. Small-angle x-ray scattering experiments and coarse-grain computational simulations have been used to elucidate mechanisms of mAb self-assembly and microstructure formation, with direct correlations to viscosity.^{64,345,350}

The complexity of viscosity-contributing interactions, and manufacturability and injectability risks arising from high viscosity have led to the development of numerous *in silico* sequence and structure-based models. Numerous regression and clustering models^{161,174,237,238,242} have resulted from identifying correlations between molecular descriptors derived from three-dimensional homology constructs and high concentration viscosity of mAb datasets. To reduce risks associated with the overfitting of small and non-diverse datasets, machine learning classification tools have been deployed to categorise mAb viscosity risks.^{147,153,240,345}

There is a knowledge gap in the appropriateness of different viscosity prediction models for mitigating high mAb solution viscosity, with no previous reports performing a direct cross-comparison of viscosity prediction and fitting models in the ultra-high mAb concentration regime. In this chapter, a comprehensive assessment of viscosity fit and prediction models in a panel of nine anti-IL-8 mAbs is presented, in the context of fitting viscosity profiles and interrogating viscosity-related molecular parameters at high- and ultra-high mAb concentration regimes. A combined computational and experimental approach was used to viscosity analysis and prediction, comparing their utility as tools for triaging mAb developability. This work demonstrates the criticality of obtaining viscosity measurements that extend into the dose relevant, ultra-high concentration regime, and the limitations on the predictive power of model-fit equations, low concentration hydrodynamic properties and *in silico* molecular descriptors.

5.3. Aims

This chapter aims to explore the influence of model fit equation and concentration range examined on the interpretation of viscosity profiles of the anti-IL-8 mAb mutant panel and wild-type. Moreover, low-concentration hydrodynamic parameters are examined to understand their predictive power to ultra-high concentration mAb viscosity. Finally, current regression and machine learning derived viscosity predictive models are tested with the anti-IL-8 mAb panel to investigate their predictive power.

5.4. Materials

Materials for mAb expression, purification and analysis are detailed in **Chapter 2, Table 2.1**.

5.5. Methods

5.5.1 Computational methods

In silico structural modelling and generation of molecular descriptors was performed in Molecular Operating Environment (MOE) software, version 2020.0901 (Chemical Computing Group, Montreal, Canada) (also see chapter 2).

Homology constructs of anti-IL-8 variant Fv structures.

Homology models were constructed as described in chapter 2 for nine anti-IL-8 antibody variable fragment (Fv) regions, eight of which were single-point mutants.

The anti-IL-8 IgG1 wild-type molecule Fab domain crystal structure was previously published as PDB: 505B. Briefly, the *Antibody modeller* feature (version 2020.0901) in MOE was used with default refinement and forcefield settings. Homology constructs of mutant candidates from patch analysis and molecular descriptor generation were then modelled after using the *Residue Scan* feature to introduce single point mutations. The same methods were followed to construct homology constructs of four in-house mAbs.

In silico molecular descriptors

Sequence and structure based physicochemical descriptors were computed using the *Protein Properties* tool and *Descriptors* Feature in *BioMOE* (version 2021-11-18, Chemical Computing Group, Montreal, Canada). Descriptors relevant to viscosity predictive models are reported in **Appendix 4, Table 10.1**.

Aggregation propensity tools: TANGO <http://tango.crg.es/tango.jsp> and **WALTZ** <https://waltz.switchlab.org/>.

The TANGO^{185,351} and WALTZ^{352,184} sequence-based aggregation propensity tools were used to predict cross beta-sheet formation in all anti-IL-8 IgGs examined.

DeepSCM (<https://github.com/Lailabcode/DeepSCM>). A convolutional neural network was used to assess charge distributions of the assumed Fv structure over molecular dynamic simulations.^{239,240} All anti-IL-8 sequences variable heavy and variable light chain sequences were inputted separated as FASTA files and the code was ran in the terminal on a Linux system.

Viscosity prediction from Fv construct molecular descriptors. Three empirical models derived from the regression of viscosity data and molecular descriptors were used to directly predict viscosity at either 150 mg/mL (*Li viscosity model*) or 180 mg/mL (*Sharma and Tomar viscosity models*).

The *viscosity model* by Li *et al.* uses the structure-based isoelectric point and WALTZ aggregation propensity score, normalised by the number of amino acid residues to generate relative viscosity predictions.¹⁶¹

$$\frac{\ln(\eta_{rel})}{Nres_{Fv}} = 0.022182 - 0.55131 * \left(\frac{pI_{3D}}{Nres_{Fv}} \right) + 0.00087416 * \left(\frac{P_{aggWALTZFv}}{Nres_{Fv}} \right)$$

5.1

Where η_{rel} is the relative viscosity (cP), $Nres_{Fv}$ the number of residues in the Fv (N=227 in the anti-IL-8 mutant panel), pI_{3D} (the structure-based isoelectric point, computed from homology constructs in MOE), and $P_{aggWALTZFv}$ the WALTZ aggregation propensity score for the Fv construct.

The *Sharma viscosity model* incorporated a hydrophobic index score (*HI*) and the Fv charge symmetry (F_{vCSP}) to account for non-polar attractive interactions, and repulsive interactions arising from net charge.²³⁷

$$\eta = 10^{((0.15+1.26(0.6))HI-0.043F_vcharge-0.02(0.015)F_{vCSP})}$$

5.2

$$HI = -(\sum niEi/\sum njEj)$$

5.3

Where η is the dynamic viscosity (cP), FvCSP the Fv charge symmetry, and HI the hydrophobic index, calculated using Equation 3B. ni represents the number of hydrophobic amino acids (*i.e.*, A, C, F, I, L, P, V, G, W, and Y), and nj the hydrophilic amino acids (*i.e.*, D, E, H, K, M, N, Q, R, S, and T). E is the Eisenberg hydrophobicity score for each residue.³⁵³

Tomar *et al.* developed an empirical viscosity prediction model from the regression of molecular descriptors for 16 mAbs.²³⁸ To use this model for our anti-IL-8 molecules viscosity predictions at 180 mg/mL, we used pI_{3D} and average intercept and slope values from the original study for the parameter B equation:

$$\ln \frac{\eta}{\eta_0} = -0.58 + Bc$$

5.4

$$B = -0.0044 * pI_{3D} + 0.056$$

5.5

Where η is the dynamic viscosity and η_0 the buffer viscosity. -0.58 is used as the average value of intercept of the slope (B) when $\ln \frac{\eta}{\eta_0}$ is plotted against antibody concentration (c) which is 180 mg/mL in the original study.²³⁸

The *Tomar* model **Equation 5.4** can be additionally used to fit concentration-viscosity profiles, using parameterisation with experimental viscosity measurements to interpolate/extrapolate viscosity at different concentrations ().

5.5.2 Protein expression and purification.

An anti-IL-8 IgG panel was generated in a Chinese Hamster Ovary glutamine-synthetase-knockout cell line as described in chapter 2. Cation exchange polishing followed before diafiltration by small scale tangential flow filtration and concentration of the molecules to ≥ 150 mg/mL in formulation buffer (pH 6.0). Identity and purity was confirmed for each panel molecule as described in chapter 2.

5.5.3 Viscosity measurement.

A VROC Initium (Rheosense, United States) was used to measure mAb viscosity in an optimised protocol to measure sample viscosity using the 'Auto' shear rate function and at fixed shear rates of 100-2000 s^{-1}). Newtonian behaviour was observed across all anti-IL-8 panel mAbs, with consistent viscosities recorded across all shear rates tested. Sample viscosity was measured over a concentration range (up to 260 mg/mL) to derive viscosity-concentration profiles for the anti-IL-8 panel. Viscosity data was segmented into two concentration regimes: high (up to 120 mg/mL) and ultra-high (up to 260 mg/mL, inclusive of high concentration data). Resultant data were subjected to the following criteria; exclusion of priming segments, the percent full scale was in the 5-95% range, the R^2 fit of the pressure sensor position was ≥ 0.998 , and transient curves reached steady plateaus with no drift.

Viscosity parameter fitting.

An exponential growth, a simplified three-parameter exponential, a modified Ross-Minton and Tomar viscosity models were used to fit viscosity-concentration data for the mAb panel to determine the optimal model. Corresponding equations for each model are described in **Table 5.1.**:

Table 5.1 Viscosity model equations used in this work.

η is the dynamic viscosity (cP), and c the concentration (mg/mL). For the exponential growth equation, Y_0 the intercept (cP), k the rate constant (mL/mg). For the three-parameter exponential equation, α_2 the slope for concentration versus $\ln(\eta)$ and α_3 the slope for 1/temperature (K^{-1}) versus $\ln(\eta)$, and α_1 the intercept (cP). For the modified Ross-Minton model, η_0 represents the buffer viscosity (cP) set at 1.13, $[\eta]$ the intrinsic viscosity, k the crowding factor, v the Simha shape parameter. $[\eta]$, k and v were estimated using the Generalised Reduced Gradient non-linear solver function to find the local optimum value to reduce the sum of squared errors. Finally, for the Tomar model $\ln A$ is the intercept of the slope B , when $\ln \frac{\eta}{\eta_0}$ is plotted against concentration. To find the knee of each exponential model, each equation was solved with the first derivative ($f'(x)$) set to 1. For the Ross Minton model, this required solving for c numerically, using the Generalised Reduced Gradient non-linear solver function with the objective of $f'(x)=1$.

Model name	Exponential growth	Three-parameter exponential	Modified Ross-Minton ²⁵¹	Tomar ^{144,238}
Equation	$\eta = Y_0 e^{kC}$	$\eta = e^{(\alpha_1 + \alpha_2 * c + \frac{\alpha_3}{T})}$	$\eta = \eta_0 \exp \left[\frac{[\eta]c}{1 - (k/v)[[\eta]c]} \right]$	$\ln \frac{\eta}{\eta_0} = \ln A + Bc$
References	Simple formula to describe concentration-dependent viscosity ^{75,269} The exponential coefficient, k , can be used to simplify correlations to other hydrodynamic/biophysical parameters. Used for viscosity prediction in neural networks ¹⁴⁷	In-house model developed from simplification of an empirical model ¹⁴⁸	A widely used formula, derived from Mooney's semi-empirical equation relating effective volume fraction to intrinsic viscosity. ¹⁴² Used in fitting viscosity curves ^{145,233} as well as deriving viscosity and hydrodynamic parameters. ^{145,89,347}	Linearized exponential derived from prediction of viscosity curves on a dataset of 16 mAbs. ²³⁸ Based off viscosity concentration fits used by Li <i>et al.</i> ¹⁶¹ and Nichols <i>et al.</i> ¹⁷⁸
Knee of curve equation	$c = \frac{\ln \left(\frac{1}{Y_0 k} \right)}{k}$	$c = \frac{\left(\ln \left(\frac{1}{\alpha_2} \right) \right) - \alpha_1 - \alpha_3}{\alpha_2}$	$f'(x) = 1 = \eta * [\eta] / \left(1 - \left(\frac{k}{v} \right) * [\eta] * c \right)^2$	$c = \frac{\left(\ln \left(\frac{1}{B \eta_0 A} \right) \right)}{B}$

Intrinsic viscosity calculation. For intrinsic viscosity $[\eta]$ measurements multiple priming segments were set up, followed by 10 replicates at the maximum shear rate of $23,080 \text{ s}^{-1}$. Formulation buffer and anti-IL-8 mAbs formulated in the 5-50 mg/mL concentration range were measured to determine the relative viscosities (η_{rel}) (**Equation 5.6**), from which the specific (η_{sp}) (**Equation 5.7**) and reduced viscosities (η_{red}) (**Equation 5.8**) could be calculated.

$$\eta_{rel} = \frac{\eta}{\eta_0}$$

5.6

Where the relative viscosity (η_{rel}), (cP), is the apparent dynamic viscosity of the sample η (cP), divided by the apparent dynamic viscosity of the formulation buffer only, η_0 (cP).

$$\eta_{sp} = \eta_{rel} - 1$$

5.7

Where the specific viscosity (η_{sp}) (cP), that can be used to calculate the reduced viscosity (η_{red}), (cP):

$$\eta_{red} = \frac{\eta_{sp}}{c}$$

5.8

Where c is the mAb solution concentration (mg/mL).

The Huggins equation describes the concentration-dependence of η_{red} in the dilute concentration linear region:

$$\eta_{red} = [\eta] + k_H[\eta]^2c$$

5.9

Where $[\eta]$ is the intrinsic viscosity (mL/g), k_H is the Huggins coefficient.

Slopes and intercept values from the linear regression of η_{red} versus the mAb concentration range tested were used to compute the Huggins coefficient (k_H):

$$k_H = \frac{\text{slope } f(c)}{[\eta]_H^2}$$

5.10

The intrinsic viscosity $[\eta]_H$ was determined from the intercept.

The Kraemer coefficient was also calculated, computing intrinsic viscosity from the linear regression of $\ln \eta_{rel}/c$ over the sample concentration range tested:

$$k_K = \frac{\text{slope } f(c)}{[\eta]_K^2}$$

5.11

Where k_K is the Kraemer Coefficient, and the slope is derived from $\frac{\ln \eta_{rel}}{c}$ versus concentration, where $\ln(\eta_{rel})$ is the natural logarithm of relative viscosity (η_{rel}). Intrinsic viscosity $[\eta]_K$ is determined from the intercept.

The uncertainty of k_H and k_K was calculated from the propagation of error equation:

$$k * \sqrt{\left(\frac{\sigma x}{x}\right)^2 + \left(\frac{(\sigma[\eta]^2)}{([\eta]^2)}\right)^2 - 2 \frac{(\sigma[\eta]^2) * (\sigma x)}{([\eta]^2) * x}}$$

5.12

Where k is the Huggins or Kraemer coefficient, $[\eta]^2$ the squared intrinsic viscosity from either respective linear regression, $\sigma[\eta]^2$ the error of squared intrinsic viscosity, calculated as $\sigma[\eta]^2 = [\eta]^2 * \sqrt{2 * \left(\frac{\sigma[\eta]}{[\eta]}\right)^2}$, x the slope determined from linear regression, and σx error of the slope.

The mean intrinsic viscosity ($[\eta]_{avg}$) was calculated from the intrinsic viscosity, which was determined from the reduced viscosity, $[\eta]_H$, and intrinsic viscosity from the natural logarithm of relative viscosity over concentration, $[\eta]_K$. $[\eta]_{avg}$ error was calculated as follows:

$$\sigma[\eta]_{avg} = \sqrt{(\sigma[\eta]_H)^2 + (\sigma[\eta]_K)^2}$$

5.13

An exponential coefficient (k_{exp}) for relative viscosity was calculated from fitting η_{rel} to **Equation 5.14** with the Generalised Reduced gradient least squares solver function. This empirical model has previously been applied to systems in which an exponential relationship exists between viscosity and concentration.^{75,90}

$$\eta_{rel} = e^{k_{exp} * c}$$

Theoretical viscosities. The Generalised Stokes-Einstein equation (**Equation 5.15**) was used to calculate theoretical viscosities extrapolated from logarithmic fits of z-average values and exponential fits of diffusion coefficients measured in the dilute anti-IL-8 test concentration range (1-20 mg/mL).

$$\eta = \frac{k_B T}{3d_H D \pi}$$

Where k_B is the Boltzmann constant at 298 K, d_H the hydrodynamic diameter (m) measured by dynamic light scattering, and D the diffusion coefficient (m²/s).

Theoretical hydrodynamic properties. Hydrodynamic volume fraction and predicted intrinsic viscosities were computed for each anti-IL-8 molecule. The volume fraction (ϕ) per mutant was computed as follows;

$$r_h = \left(\frac{3[\eta]M_w}{10\pi N_A} \right)^{\frac{1}{3}}$$

$$\phi = \left(\frac{cN_A}{M_w} \right) \frac{4\pi r_h^3}{3}$$

Where r_h is the hydrodynamic radius determined from $[\eta]$, M_w is molecular weight, and N_A is the Avogadro constant. This was used to calculate ϕ (the volume fraction), at a certain c (concentration).

Hydrodynamic properties predictions. The HYDROPRO program (version 10, <https://leonardo.inf.um.es/macromol/programs/hydropro/hydropro.htm>)³⁵⁴ was used to predict hydrodynamic properties for each anti-IL-8 molecule. Full IgG homology constructs of each molecule were exported in pdb format for input into the program and both the residue-level shell and bead calculation modes were selected with partial specific volumes set to 0.75 mL. Respective molecular weights were extracted from peptide mapping liquid-chromatography mass-spectrometry experiments.

Shape factor estimation. The shape factor, v , for each molecule was calculated by computing the solvent-accessible surface area (SASA) and Protein Volume (water

probe) of full IgG homology constructs generated in MOE (Chemical Computing Group, Montreal, Canada)³⁵⁵:

$$\Psi = \frac{SASA}{v^{2/3}}$$

5.18

$$\Psi = 1.454v + 7.085$$

5.19

Where Ψ is the geometric shape coefficient and v the shape factor.

Biophysical analysis of anti-IL-8 molecules.

Assessment of colloidal parameters. Dynamic light scattering was used to measure diffusion coefficients in the 1-20 mg/mL concentration range for the anti-IL-8 molecules as outlined in chapter 2. A Stunner instrument (Unchained Labs, CA, USA) was used to perform five measurements at 25 °C with 10-second acquisition times. A 1% extinction coefficient of 1.55 AUL/(gcm) was applied for all anti-IL-8 IgG molecules. All samples were prepared in formulation buffer (pH 6.0) and the data analysed using the Lunatic & Stunner software (Unchained Labs, CA, US, version 8.1.0.244). The self-interaction parameter, k_D , was obtained from the linear fit of concentration-dependent diffusion coefficient behaviour:

$$D_{app} = D_0(1 + k_D c)$$

5.20

Where D_{app} is the apparent diffusion coefficient, D_0 the self-diffusion coefficient at infinite dilution, and k_D the interaction parameter. This equation assumes linearity of diffusion coefficients over a concentration range, which is usually valid for antibody solutions at <10 mg/mL concentrations.

Measurement of isoelectric point. Capillary isoelectric focussing (cIEF) was used to assess the charge heterogeneity and isoelectric point of the anti-IL-8 panel, using the previously described method from chapter 2. The Empower 3 software (v4, Waters, US) was used for data processing, isoform assignment and analysis.

Electrophoretic light scattering. The zeta potential of all molecules was determined at 5 mg/mL in formulation buffer (pH 6.0) using a Zetasizer Nano ZS (Malvern

Panalytical, Malvern, UK), with each measurement set at 120s equilibration, automatic attenuation and capped at 10 minimum, 100 maximum measurements.

Statistical approaches and predictive modelling. GraphPad Prism (version 5.04) was used for data visualisation. JMP Pro (version 17.0.0, 2022) was used for correlation analysis between computational and experimental data as well as predictive modelling. For partial least squares modelling (PLS), a non-linear iterative PLS algorithm was selected with leave one-out cross-validation. The model chosen was based on the lowest mean root predicted residual error sum of squares (PRESS) and the best Q^2 (*i.e.* $1 - \text{PRESS}/\text{sum of squared deviation from mean}$). The training data include all anti-IL-8 panel molecules, and the test data consisted of four in-house early-stage molecules.

5.6. Results

In this chapter, different viscosity modelling approaches were used for the prediction and fitting of the concentration-dependent viscosity profiles of a panel of nine anti-IL-8 IgG1 molecules formulated in the same buffer. Eight of these molecules carry single-point mutations, designed to disrupt negative (D17N, D70N, D28N, D56N), hydrophobic (V5Q, W32Q) or positive patches (K42E, R53G) and the computational and experimental molecular descriptors for this IgG molecule panel are described in chapter 2. Generally, mAb solutions >100 mg/mL are classed as high concentrations, with >150 mg/mL as ultra-high concentrations.³⁴⁶ In this chapter, the high concentration regime for solution viscosity was set at up to 120 mg/mL (as set out in chapter 2) and the ultra-high at >120 mg/mL. The comparability of viscosity-concentration profile fits was assessed across both regimes.

5.6.1 Viscosity profile fitting for the anti-IL-8 mAb mutant panel

Viscosity-concentration data are often used to fit models, which are then used to extrapolate to higher concentrations or interpolate between data points. Table 5.2 compares four fit models for viscosity-concentration profiles across two concentration regimes; <120 mg/mL (high-concentration) and ≥ 120 mg/mL (ultra-high concentration) (**Figure 5.1** and **Figure 5.2**) formulated in the same buffer (pH 6.0). While D70N and W32Q mutants exhibited viscosity reduction relative to the wild-type (WT), at the high-concentration regime (**Figure 5.1a** and **Figure 5.2a**) no mutants exhibited reduced viscosity at ultra-high mAb concentrations.

A key feature of viscosity-concentration curves is the critical concentration where the curvature changes to pseudo-exponential growth. The knee of the curve was used here to define this critical concentration and to use this value to compare four model fits of the same viscosity-concentration data in two concentration regimes for all nine molecules. Significant shifts in the knee of viscosity-concentration curves were observed with each viscosity model, altering the conclusions that may be drawn from the viscosity altering effects of single point mutations (**Table 5.1**). For example, D70N showed consistent viscosity reduction relative to WT, with all viscosity fitting in the lower concentration regime (**Figure 5.1a**). Expanding the analyses to include ultra-high concentration data show no overall viscosity reduction, except for a small reduction observed with the exponential growth fit (**Figure 5.1b**). These findings demonstrate the importance of obtaining full viscosity-concentration profiles rather than reporting interpolated or extrapolated data, which may vary considerably between different viscosity models across different concentration regimes.

Derived model parameters are all reported in **Appendix 4 Table 10.2**. The Ross-Minton model describes the self-crowding parameter, k , and Simha shape parameter, v . Previous work has reported non self-associating mAbs to have a k/v value of 0.38.¹⁴⁵ In this study, much lower k/v values were observed, indicating an increase in molecular packing resulting from increased attractive forces, particularly at the high concentration (>120 mg/mL) regime viscosity profiles.

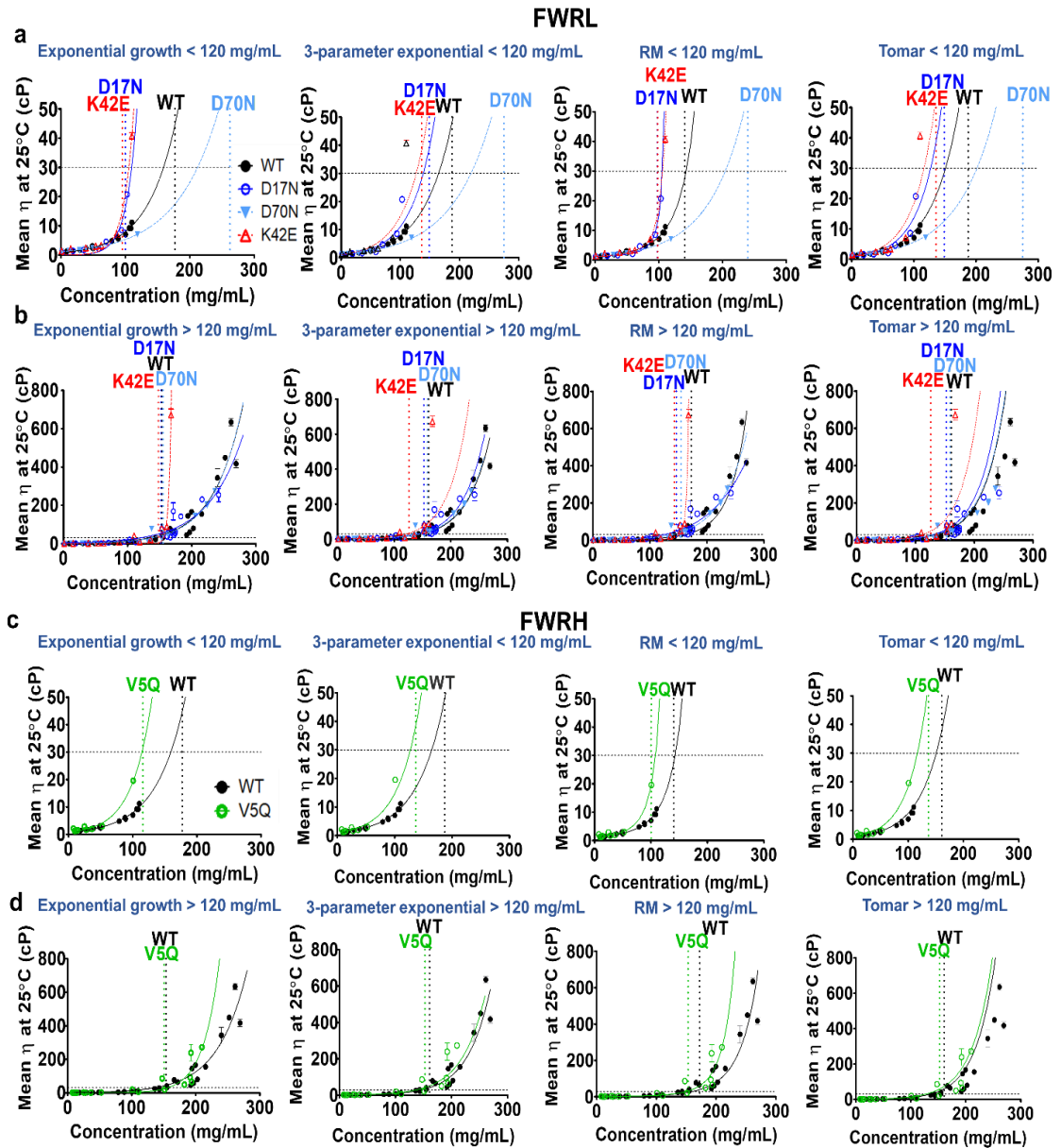


Figure 5.1 Anti-IL-8 IgG framework mutant concentration-viscosity profiles fitted with four models.

An exponential growth equation, a three-parameter exponential model, a modified Ross-Minton (RM) model and the Tomar model (left to right). A horizontal dotted line at 30 cP is the threshold for 'acceptable' viscosity. Vertical dotted lines for each molecule mark the 'knee' of each viscosity-concentration curve. FWRL (a-b) and FWRH (c-d) mutants viscosity data in two concentration regimes are shown; ≤ 120 mg/mL (top row) and > 120 mg/mL (bottom row). Error bars represent standard deviation (N=2). Abbreviations: FWRL= light chain framework region, FWRH= heavy chain framework region, RM= Ross-Minton model.

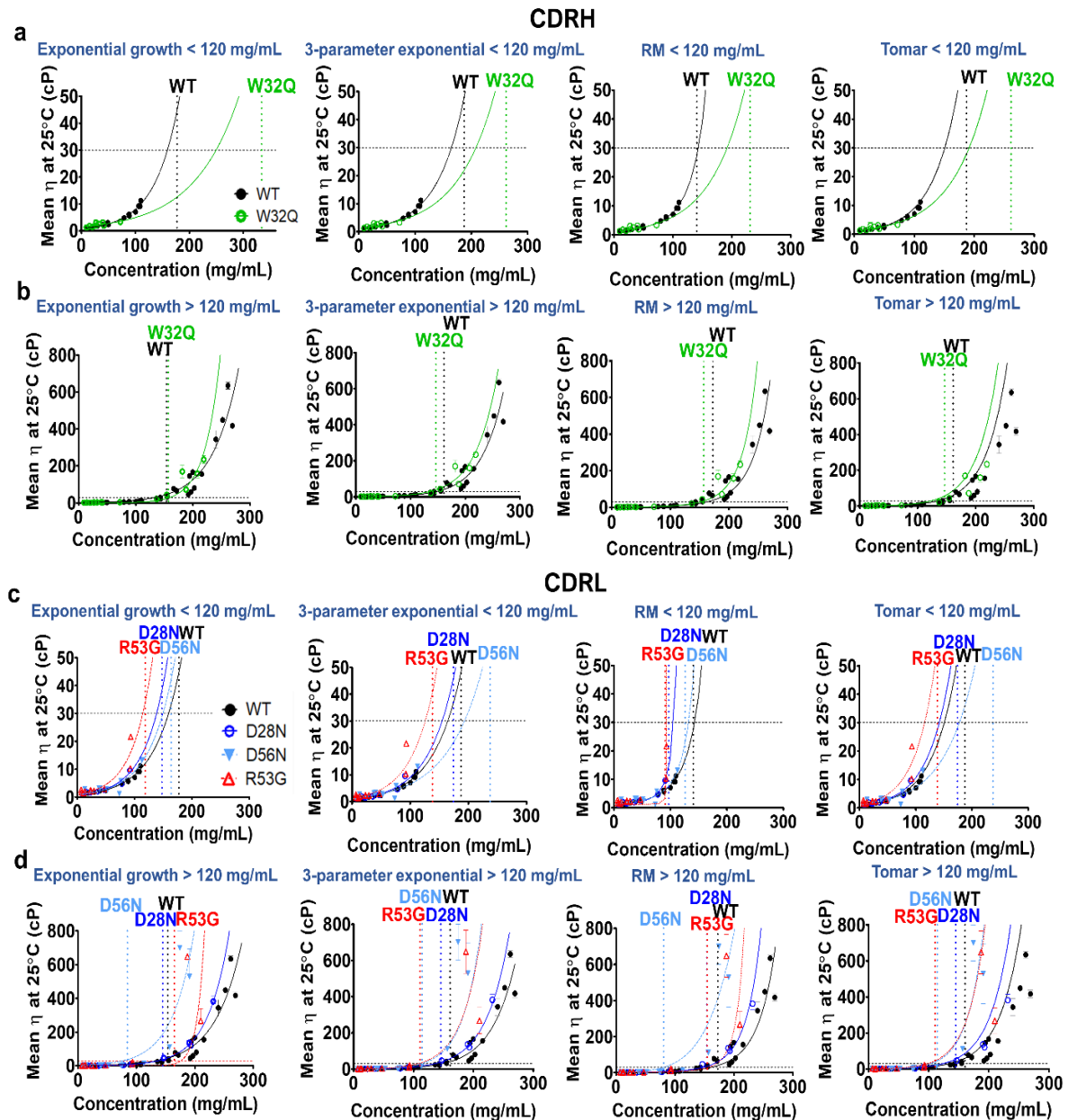


Figure 5.2 Anti-IL-8 CDR mutant concentration-viscosity profiles were fitted with four models.

An exponential growth equation, a three-parameter exponential model, a modified Ross-Minton (RM) model and the Tomar model (left to right). A horizontal dotted line at 30 cP is the threshold for 'acceptable' viscosity. Vertical dotted lines for each molecule mark the 'knee' of each viscosity-concentration curve. CDRH (a-b) and CDRL (c-d) mutants viscosity data in two concentration regimes are shown; up to 120 mg/mL (top row) and over 120 mg/mL (bottom row). Error bars show standard deviations per viscosity measurement (N=2). *Abbreviations: CDRL= light chain complementarity determining region, CDRH= heavy complementarity determining region, RM= Ross-Minton model*

Goodness of fit assessment (average R^2 values) for the growth-exponential or modified Ross-Minton models across both concentration regimes, were determined as 0.89 and 0.91 for high- and ultra-high- concentration range data, respectively. However, both the growth-exponential and Ross-Minton equations significantly overestimated predicted viscosity with the high-concentration range viscosity-concentration data (**Table 5.2**).

For all fit models explored, large discrepancies in predicted viscosity were observed between the two concentration regimes (% differences -186% to +177%), highlighting the lack of predictive power from dose-relevant ultra-high concentrations based on viscosity data obtained for the high- concentration regime. Predictions based on the high-concentration regime viscosity measurements may not accurately account for the complex anisotropic interactions occurring at ultra-high mAb concentrations with increased molecular crowding, including the formation of clusters or transient networks.^{350,356}

Table 5.2 Interpolated/extrapolated viscosity values at 180 mg/mL.

Coefficient of determination and goodness of fit (R² parameter). *Predicted viscosity is >20,000 cP or has reached model failure (~0 cP). Percentage differences between viscosity predictions at 180 mg/mL from ultra-high-concentration versus high- concentration data were calculated with:

$$\frac{c_{HIGH} - c_{MID}}{\frac{c_{HIGH} + c_{MID}}{2}} * 100.$$

Viscosity predictions from the high-concentration data that exceeded predictions from the ultra-high-concentration data (negative

% differences) are highlighted in red.

Molecule	Concentration range of experimental data	N data points	Exponential growth				3-parameter exponential				Modified Ross-Minton				Tomar				Average knee
			Viscosity prediction (cP) at 180 mg/mL	% difference in η between concentration regimes	R ²	Knee of curve	Viscosity prediction (cP) at 180 mg/mL	% difference in η between concentration regimes	R ²	Knee of curve	Viscosity prediction (cP) at 180 mg/mL	% difference in η between concentration regimes	R ²	Knee of curve	Viscosity prediction (cP) at 180 mg/mL	% difference in η between concentration regimes	R ²	Knee of curve	
WT	<120 mg/mL	14	47.69	52%	0.975	177.09	41.23	45%	0.974	187.33	154.59	-106%	0.982	140.61	59.4	53%	0.977	187.33	173.09
	>120 mg/mL	32	81.24		0.91	153.66	65.29		0.905	160.83	47.63		0.865	172.46	102.5		0.892	160.83	161.95
D17N (FWRL)	<120 mg/mL	7	2,442.88	-186%	0.936	99.76	86.43	-9%	0.848	148.93	Too high*	-	0.991	97.38	139.72	-10%	0.866	148.93	123.75
	>120 mg/mL	21	90.89		0.815	152.19	79.34		0.767	152.49	94.22		0.826	146.32	126.74		0.733	152.49	150.87
D70N (FWRL)	<120 mg/mL	6	18.26	124%	0.998	262.53	16.8	122%	0.997	275.31	19.76	119%	0.999	239.56	20.97	135%	0.999	275.31	263.18
	>120 mg/mL	16	77.52		0.973	155.26	69.24		0.972	158.75	77.88		0.973	154.61	107.72		0.967	158.75	156.84
K42E (FWRL)	<120 mg/mL	7	4,228.50	120%	0.984	95.09	121.63	31%	0.862	135.82	Too high*	-	0.999	98.1	199.84	38%	0.887	135.82	116.21
	>120 mg/mL	13	17,023.12		0.978	147.88	166.9		0.496	125.94	Too high*		0.99	142.94	294.29		0.524	125.94	135.68
V5Q (FWRH)	<120 mg/mL	9	245.03	-101%	0.984	115.6	44.54	57%	0.974	136.72	Too high*	-	0.588	100.39	193.43	-43%	0.981	136.72	122.36
	>120 mg/mL	17	80.76		0.787	150.69	80.42		0.754	152.64	79.76		0.795	153.07	124.59		0.766	152.64	152.26
W32Q (CDRH)	<120 mg/mL	10	13.02	132%	0.551	334.17	19.62	130%	0.538	261.53	24.49	96%	0.638	230.96	24.67	143%	0.528	261.53	272.05
	>120 mg/mL	17	63.16		0.985	157.02	92.87		0.947	146.22	70.02		0.989	156.86	148.81		0.967	146.22	151.58
D28N (CDRL)	<120 mg/mL	11	89.38	7%	0.939	147.52	51.77	59%	0.927	174.33	Too high*	-	0.991	97.12	76.42	67%	0.937	174.33	148.33
	>120 mg/mL	15	95.98		0.997	144.75	94.77		0.997	145.33	76.21		0.982	154.06	153.64		0.996	145.33	147.37
D56N (CDRL)	<120 mg/mL	12	62.2	154%	0.835	163.47	24.08	167%	0.791	237.42	892.43	-58%	0.878	126.5	31.2	177%	0.807	237.42	191.20
	>120 mg/mL	15	481.55		0.813	84.48	263.87		0.802	114.26	491.72		0.824	80.58	503.71		0.787	114.26	98.40
R53G (CDRL)	<120 mg/mL	10	208.26	-134%	0.824	118.45	113.15	82%	0.819	138.39	Too high*	-	0.978	90.61	178.38	93%	0.823	138.39	121.46
	>120 mg/mL	13	41.26		0.916	165.11	269.73		0.84	110.8	79.43		0.93	154.62	486.36		0.857	110.8	135.33

5.6.2 Intrinsic viscosity, pair-wise interactions and hydrodynamic properties of the anti-IL-8 mAb mutant panel

One method of assessing anti-IL-8 mAb contribution to solution viscosity, is to determine the intrinsic viscosity ($[\eta]$) (**Appendix 4 Table 10.3**). Apparent dynamic viscosity was calculated in the dilute concentration regime (0-50 mg/mL), and reduced viscosities (η_{red}) and $\ln(\eta_{rel})/c$ plotted against mAb concentration (**Appendix 4 Figure 10.1 and Figure 10.2**). The intercept of each plot was reported as intrinsic viscosity, $[\eta]_H$ and $[\eta]_K$, which were averaged to determine $[\eta]_{avg}$. Most anti-IL-8 mAb mutants had similar $[\eta]_{avg}$ values- except for R53G- which had a higher intrinsic viscosity indicating an increased excluded volume effect.

The Huggins coefficient (k_H) quantifies solution viscosity increases arising from pair-wise interactions. In polymer science, a solution with k_H of ~ 0.7 is categorised as a good solvent where inter-polymer repulsions are strong. Lower k_H values indicate decreased attractive forces and reduced solvation ability. The Kraemer coefficient (k_K) has been used in conjunction with k_H to quantify thermodynamically good solvents, which result in $k_K \sim -0.16$.³⁵⁷ Interestingly, we observed a negative logarithmic relationship between both k_H and k_K and $[\eta]_{avg}$ (**Figure 5.3**). W32Q and R53G had the lowest k_H and k_K coefficients, suggesting weaker pair-wise interactions in dilute solutions.

To account for any curvature in reduced viscosities over concentration plots, a second order polynomial fit was applied to the η_{rel} profiles of each anti-IL-8 mAb (**Appendix 4 Figure 10.4**), with the assumed approximation that intrinsic viscosity ($[\eta]_v$)= k_1 in the equation $\eta_{rel} = 1 + k_1c + k_2c^2$.⁷⁴ The $[\eta]_v$ values aligned with linear derived intrinsic viscosities ($[\eta]_{avg}$) ($R^2=0.73$) (**Appendix 4 Figure 10.5**), but showed increased variation amongst the anti-IL-8 panel.

The HYDROPRO tool³⁵⁸ was used to compute intrinsic viscosity ($[\eta]_{HYD}$) and radius of gyration (R_g) estimations for anti-IL-8 mutants (**Appendix 4 Table 10.3**). These were computed at residue-levels in both shell and bead mode. Though no strong correlations were found with $[\eta]_{HYD}$ to experimental $[\eta]$ ($<0.7 R^2$) in either mode, the residue-shell mode better aligned to experimental intrinsic viscosity ($[\eta]_{avg}$) ($R^2 = 0.56$) than the residue-bead mode ($R^2 = 0.27$) (**Appendix 4 Table 10.6**).

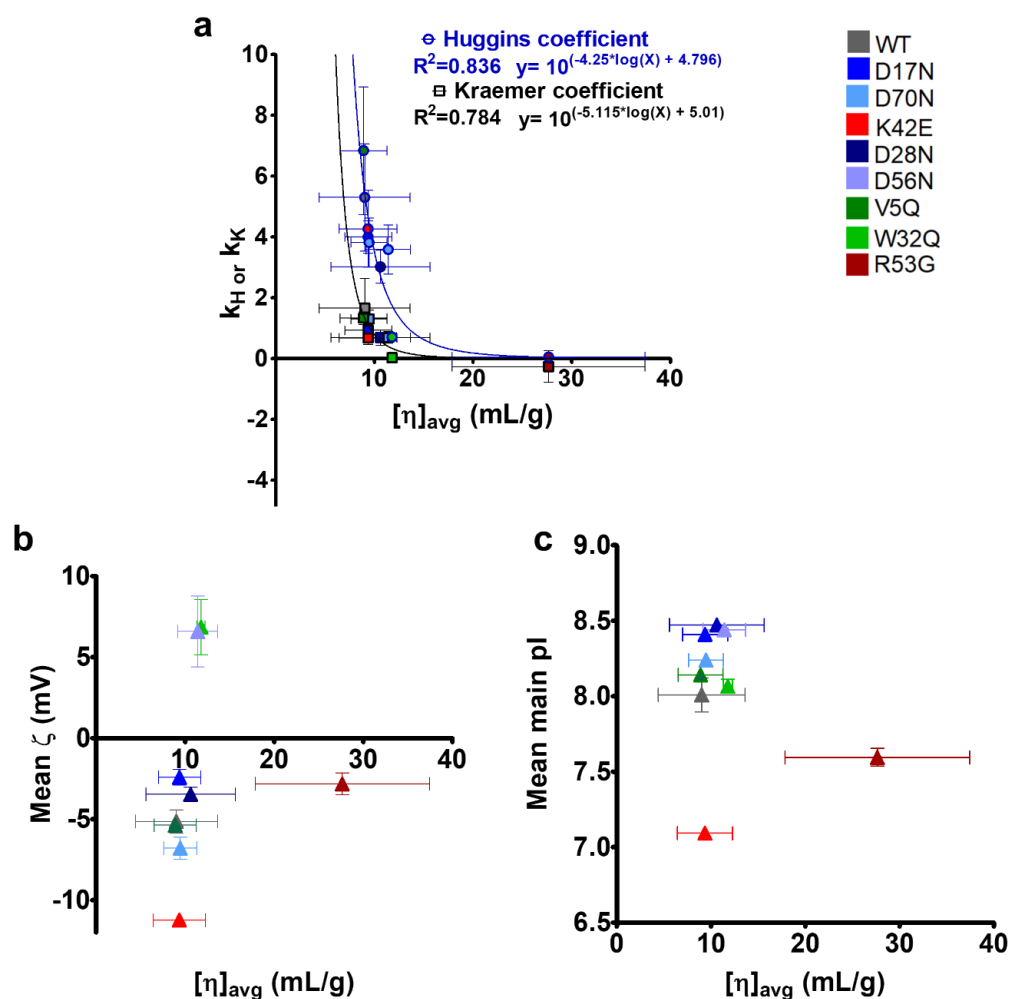


Figure 5.3 Negative correlation between average intrinsic viscosity and Huggins and Kraemer coefficients, but no correlation with anti-IL-8 mAb charge.

Huggins (k_H) (blue line) and Kraemer (k_K) (black line) coefficients (y-axis) exhibited a negative logarithmic relationship to the average intrinsic viscosity ($[\eta]_{avg}$) (a). No strong correlations were observed between $[\eta]_{avg}$ and charge parameters, zeta potential (ζ) (b) or mean isoelectric point (pI) (c). Vertical error bars represent standard errors of k_H and k_K , and standard deviations for ζ and pI. Horizontal error bars represent the standard error of $[\eta]_{avg}$. Logarithmic equations shown for k_H/k_K over $[\eta]_{avg}$ plot.

Intrinsic viscosity can also be derived from the Ross-Minton model (**Table 5.1**). Here, the Ross-Minton derived viscosities poorly correlated with $[\eta]_{avg}$ in both concentration regimes (**Appendix 4 Figure 10.7**). This demonstrates how the ultra-high-concentration data, from which the Ross-Minton viscosity is derived, skew $[\eta]$ to no

longer be representative of molecular size and molecular diffusivity in the ultra-dilute regime.

Next, the linear correlations of hydrodynamic radius (r_h) measurements derived from the linear intrinsic viscosity ($[\eta]_{\text{avg}}$) and polynomial intrinsic viscosity ($[\eta]_v$) to the DLS-derived hydrodynamic radius ($r_{h\text{DLS}}$) were compared (**Figure 5.4**). R53G, which had the highest r_h from intrinsic viscosity, did not exhibit an increase in hydrodynamic size measured by DLS, resulting in poor correlation with intrinsic viscosity-derived r_h (**Figure 5.4a**). Removal of the R53G molecule improved the correlation to $R^2= 0.559$ (**Figure 5.4b**), suggesting R53G is an outlier. However, the use of $[\eta]_v$ to derive r_h ($r_{h[\eta]_v}$) resulted in no correlation to $r_{h\text{DLS}}$ (**Figure 5.4c**). This indicates potential inaccuracies in Z-ave DLS measurements at 1 mg/mL or misrepresentation of intrinsic viscosity from using the polynomial function on η_{rel} , where we are accounting for higher order interactions. Effective volume fraction (ϕ) was computed < 100 mg/mL from $[\eta]_{\text{avg}}$ according to **Equation 5.6 (Figure 5.4d)**. R53G exhibited a significantly higher hydrodynamic volume across the whole concentration range.

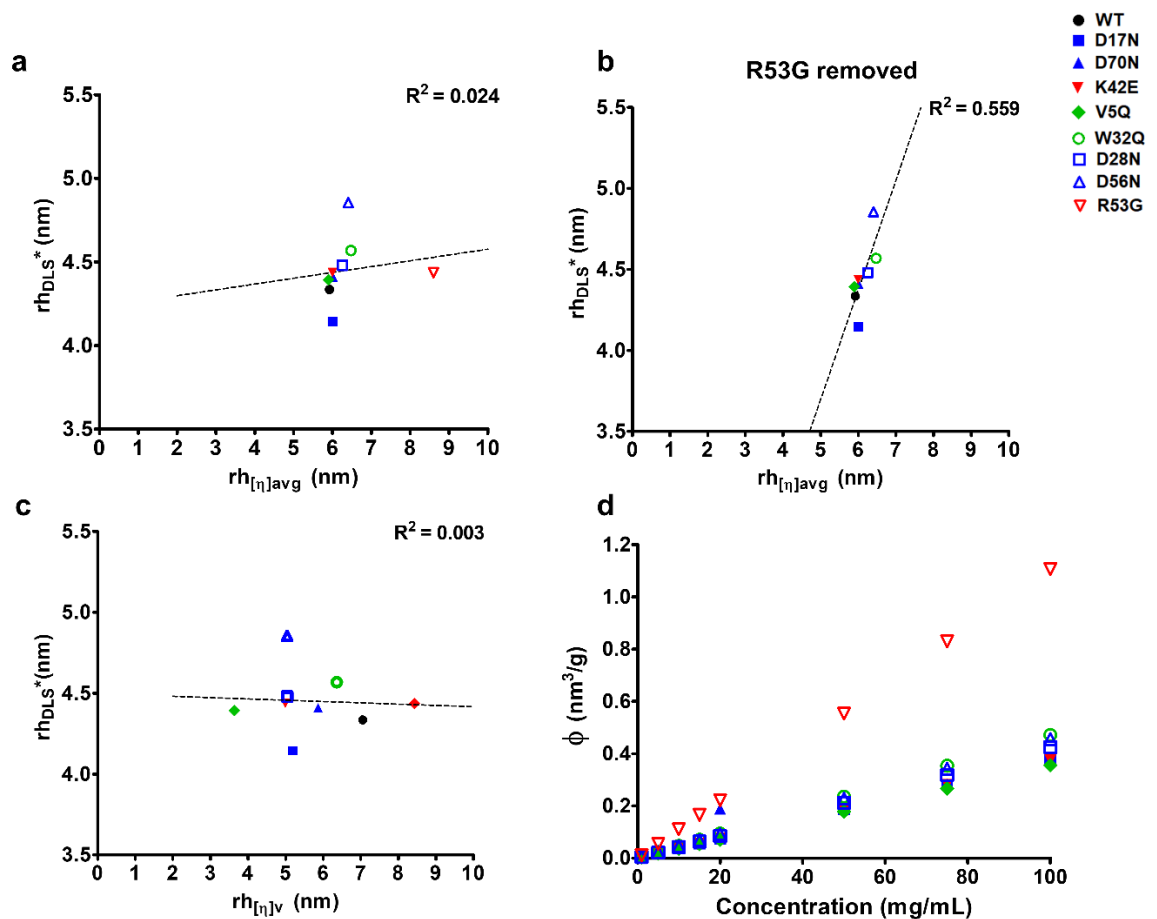


Figure 5.4 Hydrodynamic diameter from intrinsic viscosity versus dynamic light scattering and effective volume fraction of anti-IL-8 molecules.

a, DLS-derived r_h values poorly correlated to r_h values from either the r_h derived from average intrinsic viscosity ($r_{h[\eta]_{avg}}$), **b**, with the R53G molecule removed, **c**, or from polynomial intrinsic viscosity ($r_{h[\eta]_v}$). R_h $[\eta]_{avg}$ was used to compute the theoretical effective volume fraction (ϕ) for each molecule up to 100 mg/mL(**d**) using Equation 5.6.

Two methods were used to generate shape information for each anti-IL-8 molecule (**Appendix 4 Figure 10.8**). The HYDROPRO program was used in shell mode to predict the radius of gyration (R_g) and its ratio to r_h (the shape ratio (ρ)) was computed for each molecule (**Appendix 4 Figure 10.8a**). The r_h values from both intrinsic viscosity (linear ($[\eta]_{avg}$) and polynomial ($[\eta]_v$) and DLS were used. The shape ratio determined for each molecule was ~ 0.775 , which was attributed to spherical, globular proteins.^{359–361} Interestingly, R53G showed the lowest ratios $R_g/r_{h[\eta]_{avg}}$ and $R_g/r_{h[\eta]_v}$ demonstrating a deviation in shape.^{362,363} Use of DLS r_h values showed comparable ratios for all anti-IL-8 molecules.

Subsequently, shape coefficients (Ψ) and shape factors (ν) were calculated from computed solvent-accessible surface areas (SASA) and protein volumes of IgG homology constructs of the anti-IL-8 panel (**Appendix 4 Figure 10.8b**). Since the same IgG1 scaffold was used with single amino acid substitutions for the anti-IL-8 panel, SASA and protein volumes were comparable and therefore no distinguishable differences in shape factors were observed.

The Generalised Stokes-Einstein equation (**Equation 5.15**) was used to compute the theoretical viscosities of all anti-IL-8 molecules (**Figure 5.5**). Extrapolation of dynamic light scattering Z-ave values and diffusion coefficients resulted in a lower predicted theoretical viscosity for D70N, K42E and D28N compared to the WT. Hydrophobic patch-disrupting mutant, W32Q, had the lowest theoretical viscosity (25.5 cP versus 88.4 cP at 200 mg/mL for W32Q and WT, respectively), aligning to the lower experimental viscosity observed in the high-concentration regime (**Figure 5.2a** and **Table 5.2**). Positive patch-disrupting mutant, R53G had a large increase in theoretical viscosity compared to WT (222 cP, 200 mg/mL), which was also in agreement with experimental viscosities (**Figure 5.2c, d** and **Table 5.2**) as well as increased intrinsic viscosity (**Appendix 4 Table 10.3**). Overall, the generalised Stokes-Einstein equation consistently underestimated the experimental viscosities, not accounting for higher order interactions as the concentration increases.

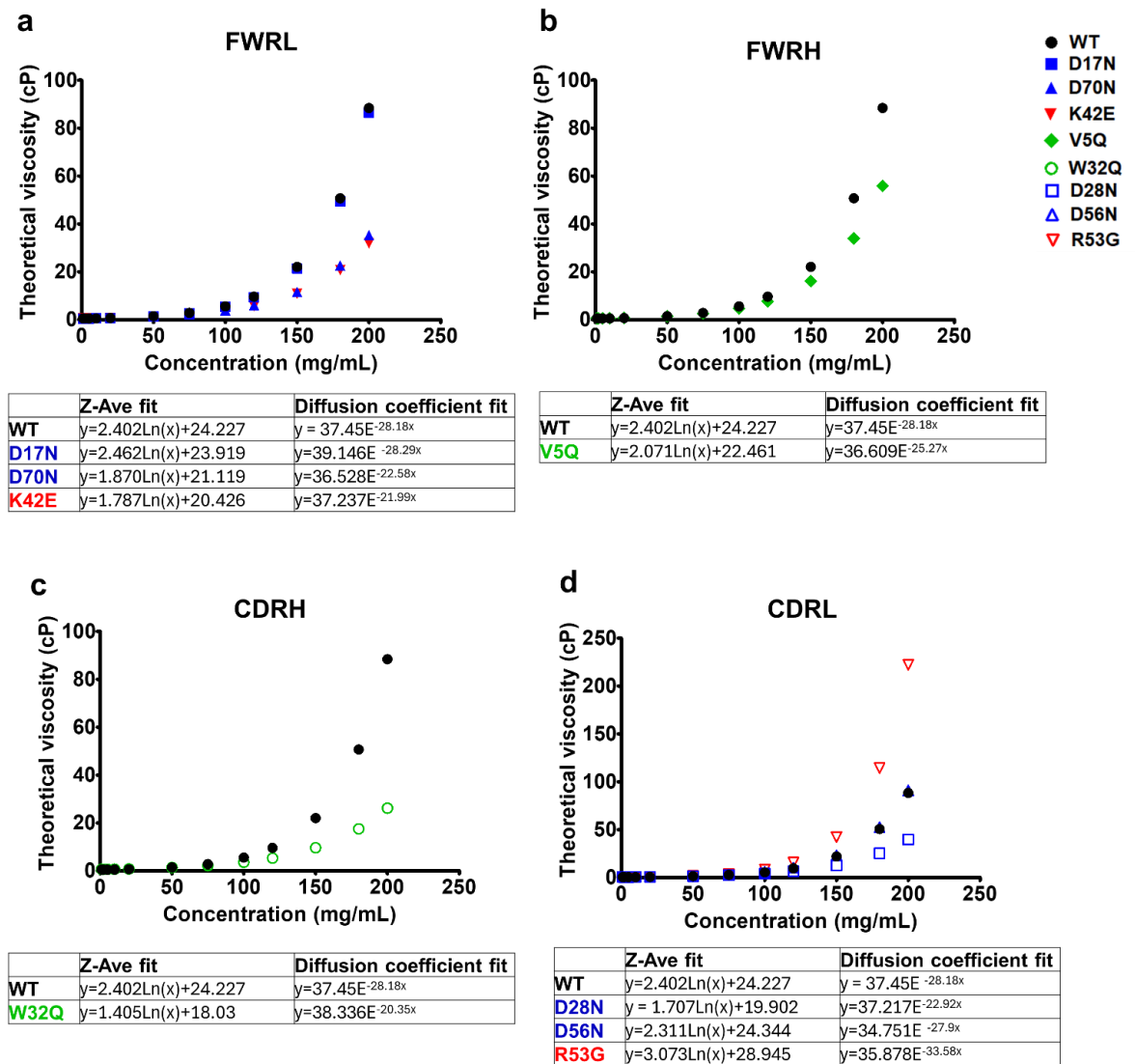


Figure 5.5 Theoretical viscosities for anti-IL-8 molecules derived from Generalised Stokes Einstein equation.

Negative patch disrupting mutants (blue), positive patch disrupting mutants (red) and hydrophobic patch disrupting mutants (green) are divided into location **a**, FWRL, **b**, FWRH, **c**, CDRH and **d**, CDRL.

5.6.3 Computational viscosity predictions of the anti-IL-8 mAb mutant panel

Numerous empirical viscosity prediction models from small datasets of proprietary development phase mAbs have been developed to-date. Li *et al.* studied the relationship of 18 different molecular descriptors on 11 Fv constructs to viscosity data of these mAbs at 150 mg/mL.¹⁶¹ The best regression model for viscosity prediction

was found to include isoelectric point and aggregation propensity predictions (**Equation 5.1**). A similar regression model on 14 IgG1 mAbs viscosity data at 180 mg/mL was developed by Sharma *et al.*, drawing a relationship between viscosity and Fv charge, charge symmetry and hydrophobic index (**Equation 5.2**).²³⁷ Finally, Tomar *et al.* found that pI correlated with parameter B in the logarithmic fitting of 16 development phase mAb viscosity profiles at concentrations up to 180 mg/mL (**Equation 5.4**).²³⁸ Here, these approaches were used to derive viscosity prediction scores for an anti-IL-8 mAb panel (**Figure 5.6**). With all models, negative patch disrupting mutants were predicted to have lower viscosity compared to the wild-type, with ≤ 30 cP predicted for mutants (180 mg/mL) using the Sharma scores. Positive patch disrupting mutants were predicted to increase viscosity compared to wild-type IgG, with viscosities >30 cP with both Sharma and Tomar scores at 180 mg/mL. Hydrophobic patch disrupting mutants showed similar predicted viscosities to wild-type as these models primarily use charge-based descriptors. With regards to model performance, the Li viscosity model significantly underestimates viscosities at 150 mg/mL when comparing to all experimental model fits (**Figure 5.6b**). For viscosity predictions at 180 mg/mL, the true experimental viscosity appears to lie in between the Sharma and Tomar viscosity scores (**Figure 5.6e**), with Sharma scores underpredicting and Tomar scores overpredicting viscosities. Since inaccuracies from quantitative predictions from the Li, Sharma and Tomar scores were observed, qualitative prediction was assessed to identify if molecule rankings are correct (**Appendix 4, Table 10.5**). None of the predictions directly matched the experimental viscosity ranking of the anti-IL-8 panel.

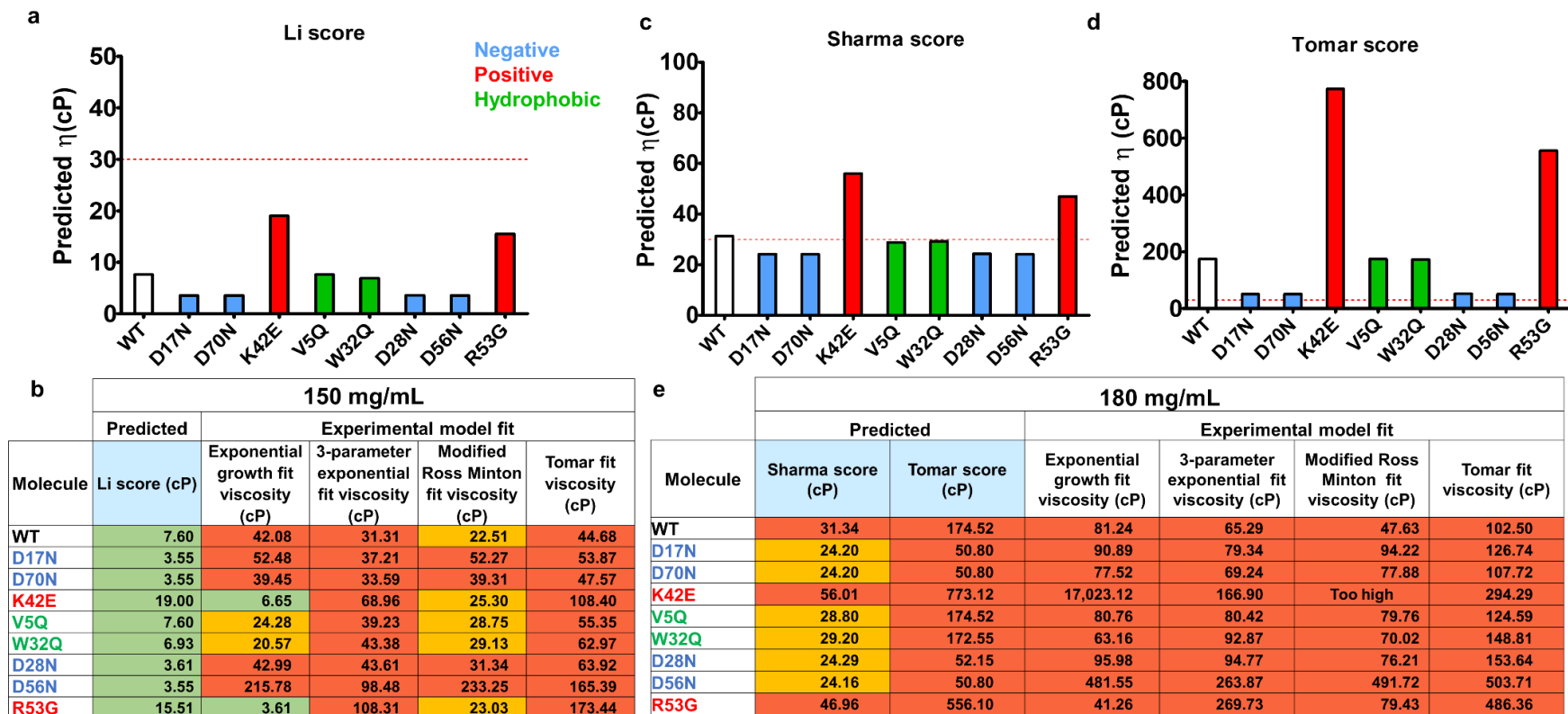


Figure 5.6 Predicted viscosity (η) scores from three regression models.

a, Li model (predicted η at 150 mg/mL) and **c**, Sharma and **d**, Tomar (both predicted η at 180 mg/mL) for anti-IL-8 mutants and wild-type (WT). Comparisons to experimental data at **b**, 150 mg/mL and **e**, 180 mg/mL with all model fits reported. Red dotted line represents an 'acceptable' viscosity threshold of 30 cP. For predicted versus experimental viscosity data, the following thresholds were set: ≤ 20 cP (green), $20\text{cP} \leq \geq 30$ cP (amber) and ≥ 30 cP (red).

A previous study examined a larger dataset (N=59), including approved 'developable' mAbs to better identify non-redundant *in silico* descriptors and experimental parameters, that result in improved developability characteristics (viscosity and opalescence).¹⁷⁴ Clustering analysis showed distinct correlations between mAbs with favourable developability characteristics and k_D , measured pI and the effective charge. They also assessed sequence-based molecular descriptors (hydrophobic index and charge symmetry), finding that such singular descriptors did not have the same discrimination level as the experimental parameters.

In this chapter, the same parameters and thresholds were used to test these trends to viscosity, using both high and ultra-high concentration data (**Figure 5.7a** and **b** respectively). Here, low or high viscosity molecules at either concentration regime examined could not be distinguished with the use of either experimental parameters (k_D , pI or zeta potential) or molecular descriptors.

The structure-based ensemble charge (ens_charge) descriptor has previously been shown to correlate with viscosity; molecules with ens_charge values of $\geq +2$ C were correlated with reduced viscosity.²⁴² Here, only positive patch disrupting mutants had an ens_charge of $< +2$ (**Appendix 4, Table 10.1**). At 120 mg/mL, these mutants had high viscosities (>30 cP), but three highly viscous molecules had ens_charge values $> +2$ (false positives) when examining the high concentration data (67% accuracy) (**Appendix 4, Table 10.7**), suggesting limitations in the use of this singular descriptor for predicting viscosity. Interpolations from ultra-high concentration data for viscosity at 120 mg/mL resulted in 55% accuracy, with both false negatives and false positives present.

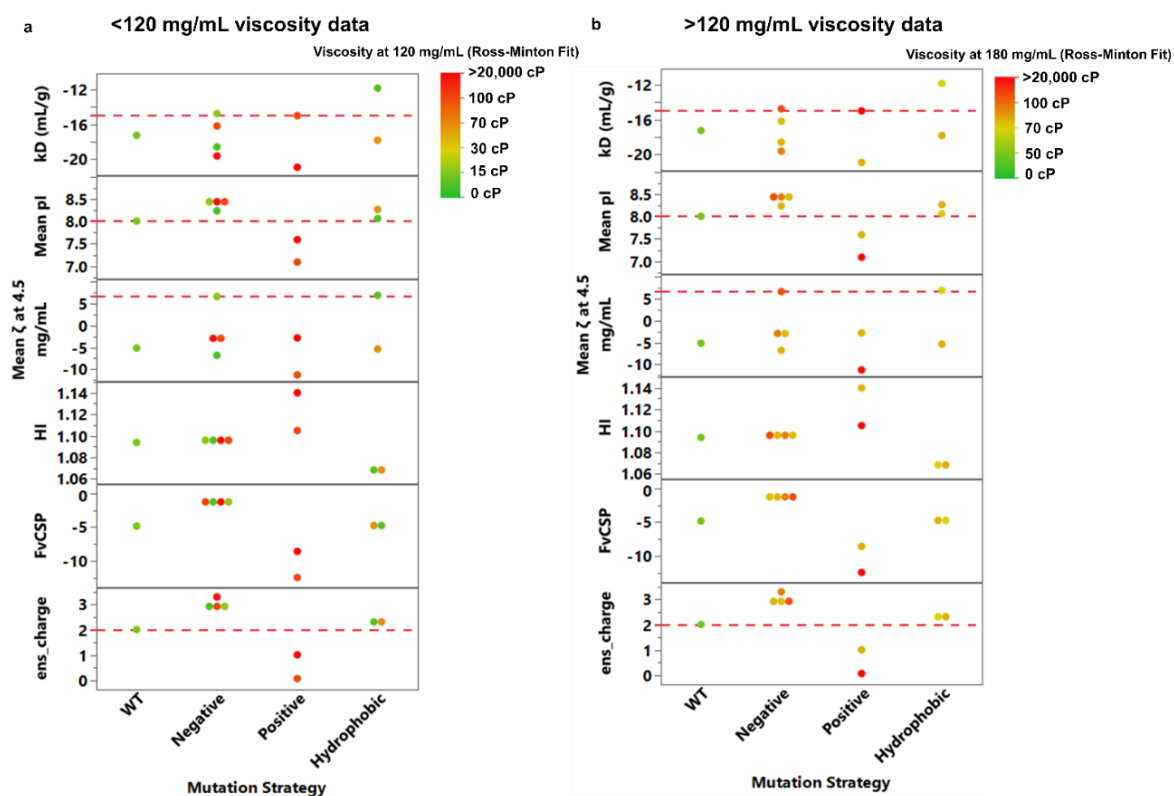


Figure 5.7 Experimental parameters and sequence-based molecular descriptors, categorised according to Kingsbury *et al.*¹⁷⁴ for anti-IL-8 IgGs, categorised by mutation strategy.

Comparisons used viscosity data from two concentration regimes; across **a**, the high concentration (< 120 mg/mL) viscosity data and, **b**, ultra-high concentration (≥ 120 mg/mL) viscosity data. Ross-Minton model fitted experimental viscosities were used to grade each molecule from low viscosity to high viscosity (green to red) (**Appendix 4 Table 10.6**). Experimental parameters were the self-interaction parameter, k_D , mean measured isoelectric point (pI) and mean zeta potential (ζ) at 5 mg/mL. Computed molecular descriptors were hydrophobic index (HI) and Fv charge symmetry (FvCSP), and ensemble charge. Red dotted lines represent thresholds determined from clustering analysis from original studies where correlations with viscosity were found.

5.6.4 Machine learning for viscosity prediction

Interpretable learning models are a trending approach to predict the viscosity of biologics, incorporating expansive datasets of both computational and experimental biophysical descriptors on a diverse range of molecules. Lai *et al.* used classification models of 27 approved mAbs to generate a decision tree for categorising viscosity risk at 150 mg/mL based on computed net charge and the number of hydrophilic and hydrophobic residues in the Fv.¹⁵¹ In this chapter, all molecules were classed with high viscosity risks (≥ 30 cP) using the same thresholds (**Figure 5.8**). This agrees with experimental viscosities of the anti-IL-8 mAb panel, which were >30 cP with the three-parameter exponential and Tomar model fits at 150 mg/mL, using the high concentration data (100% true negatives using either a 20 cP or 30 cP cut-off, **Appendix 4 Table 10.8**).

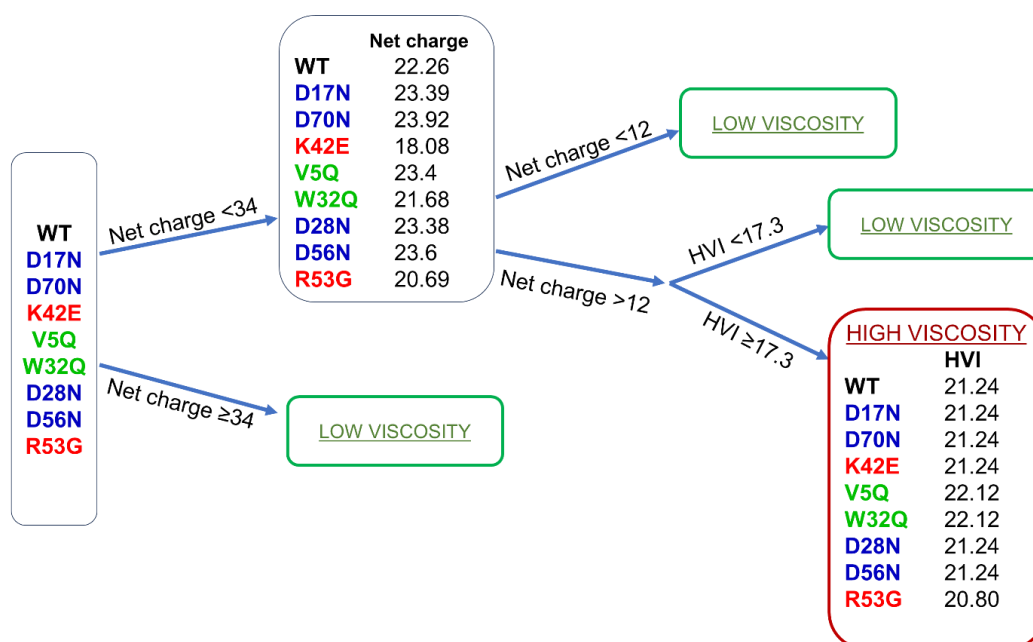


Figure 5.8 Lai¹⁵¹ decision tree classed all anti-IL-8 mAb molecules to have high viscosity at 150 mg/mL.

Net charge of full IgG homology constructs and hydrophobic (A, F, I, L, M, P, V, W) and hydrophilic (S, T, N, Q, Y, K, R, H, D, E) residue counts in the Fv were obtained to generate the High Viscosity Index (HVI) with the equation $(N_{hyph} - N_{hyd})/N_{res} * 100$.²⁶⁹ Thresholds from original model development for low viscosity (<30 cP at 150 mg/mL) were <34 C net charge and <17.3 HVI if the net charge >12 C.

Recently, Makowski *et al.* developed an alternative decision tree for viscosity classification using three molecular properties from 79 proprietary and 94 clinical

stage mAbs.¹⁵³ Structure-based isoelectric point (pI_{3D}), largest hydrophobic patch and number of negative patches from Fv homology models were strongly correlated features used for the classifier algorithm. In our study, we saw that only negative-patch targeting mutants (DàN) reached the pI threshold of ≥ 6.3 , classifying these molecules with low viscosity predictions ($<20\text{cP}$ at $>100\text{ mg/mL}$) (**Figure 5.9**). Although all molecules had ‘acceptable’ values for the largest hydrophobic area and number of negative patches, WT, hydrophobic patch targeting and positive patch targeting molecules were classed to have high viscosity due to lower pI values. This classification had lower prediction accuracy to experimental compared to the Lai *et al.* triaging tool, with 56% true negatives and 44% false positives for the three-parameter exponential and Tomar fitted viscosities (**Appendix 4 Table 10.9**).

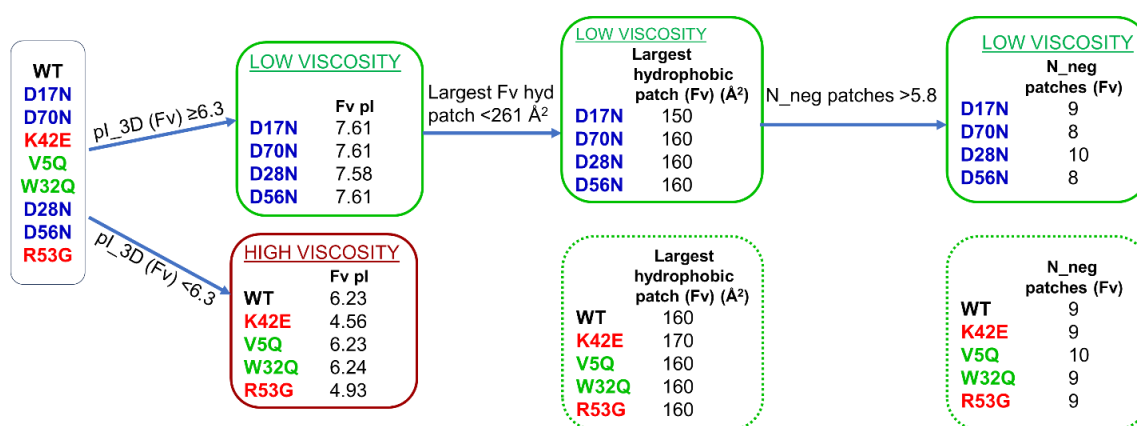


Figure 5.9 Negative patch targeting mutants predicted to have lower viscosity using the Makowski decision tree.¹⁵³

Fv homology constructs were used to derive isoelectric points (pI_{3D}), largest hydrophobic patch area (\AA^2) and number of negative patches. Cut-offs from original model development were pI_{3D} ≥ 6.3 , largest hyd patch $< 261 \text{ \AA}^2$ and N_neg patches > 5.8 . Only DàN mutants passed the pI criteria.

5.6.5 Predictive modelling of the anti-IL-8 molecule panel

I next sought to develop and assess a simple regression model to predict the viscosity of the anti-IL-8 panel (**Figure 5.10**). Here, the ‘knee’ found for each model-fitted viscosity profile was averaged and assessed correlations with computational molecular descriptors (**Appendix 4 Figure 10.9**). Five of the highest correlating variables (Pearson correlation coefficient $R > 0.5$) were used in partial least squared (PLS) regression, resulting in a final equation (**Figure 5.10b**) with an R^2 value of 0.76

(Figure 5.10d). Model performance was tested with a set of four in-house molecules (Ab1-4), which saw a reduction in R^2 to 0.31 **(Figure 5.10e)**. The regression model underpredicted the viscosity knee values for the test molecules, which were significantly higher than the training anti-IL-8 panel, demonstrating the need for a case-by-case approach when predicting viscosity, particularly with small datasets.

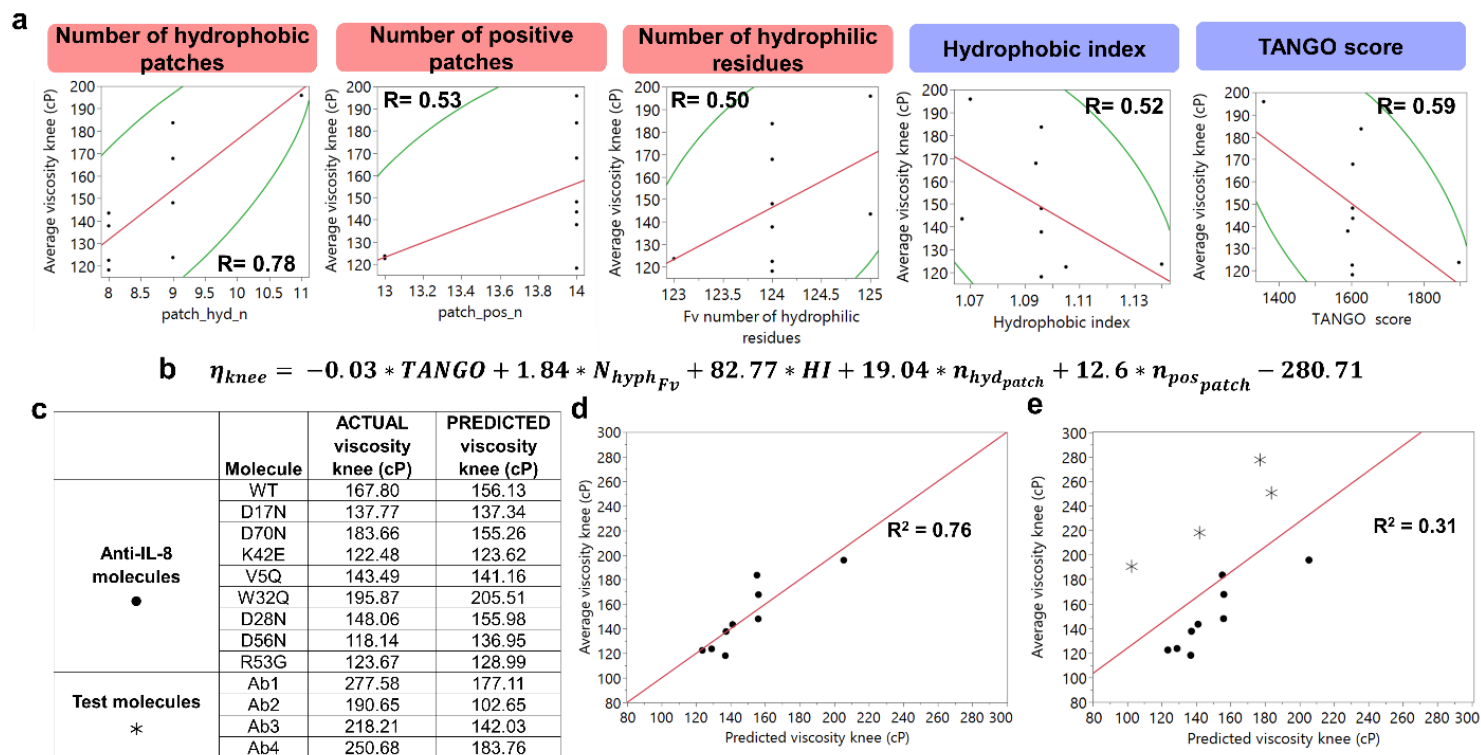


Figure 5.10 Viscosity regression model from an anti-IL-8 mAb panel lacked predictive ability with in-house test molecules.

a, Five molecular descriptor variables were selected for modelling to predict the averaged knee for each viscosity profile per molecule. The respective scatter plots with Pearson correlation coefficients (R) per variable are reported. **b**, The resulting equation was generated through non-linear iterative partial least square (NIPLS) regression with leave-one-out cross validation. **c**, Predicted viscosity knee values were lower for the more viscous anti-IL-8 molecules compared to the less viscous test molecules. **d**, The model predicted the anti-IL-8 viscosity knee values well ($R^2=0.76$, $RMSE=12.7$, $R=0.87$) but, **e**, underpredicted for the test set ($R^2=0.31$, $RMSE=43.8$, $R=0.56$).

5.7. Discussion

Mitigating for high solution viscosity in high concentration mAb formulations, is a key goal of mAb drug development efforts, which can be achieved through sequence-based^{229,232,233} and formulation strategies.^{266,364,365} The ability to predict sequences giving rise to elevated solution viscosity at high mAb formulation concentrations can aid the triaging and developability risk assessment of early-stage mAb candidates.

In this chapter, I used structure- and sequence-based molecular descriptors, performing parallel assessment of findings from predictions with experimentally derived viscosity parameters across different concentration regimes. The goal was to compare differences in viscosity predictions from viscosity model fits, from hydrodynamic properties, as well as from empirical and machine-learning derived models for a panel of anti-IL-8 IgG molecules. These molecules were designed previously in chapter 2 with single-point mutations targeting computed electrostatic or hydrophobic surface patches, which had significant effects on viscosity.

Interpretation of viscosity data dependent on concentration regime and model fit

Volume-limiting routes of administration (*i.e.*, subcutaneous), necessitate high (>100 mg/mL) or ultra-high (>150 mg/mL) mAb concentrations to achieve therapeutically-relevant doses. The mechanisms governing high solution viscosity of mAb formulations are not only molecule-dependent, with intrinsic differences in hydrodynamic size and anisotropic surface charges and hydrophobicity^{144,332,270,232}, but also concentration-dependent. Contributions to viscosity present in infinitely dilute systems are typically characterised with light scattering techniques to derive the self-interaction parameter, k_D , or the second osmotic virial coefficient, B_{22} . Pairwise and higher-order associations in more concentrated solutions with increased complexities of interactions, however, are not as simply defined and remain challenging to model.

Here, viscosity profiles of an anti-IL-8 mutant panel in two concentration regimes (high and ultra-high) was evaluated (**Figure 5.1** and **Figure 5.2**). Whilst two mutants (D70N and W32Q) showed reduction in viscosity relative to the wild-type (WT) molecule in the lower concentration regime, expanding the dataset to include ultra-high concentration measurements resulted in all mutants having higher viscosities relative to WT. Therefore, all anti-IL-8 molecules were categorised as ‘high risk’ in terms of their developability at dose-relevant concentrations.

This is the first study that directly compares multiple models to fit viscosity profiles and the impact of these on the interpretation of viscosity data. Four prominent models that are routinely used when examining viscosity curves were selected (**Table 5.1**). The growth exponential or modified Ross Minton equations were found to be optimum models with highest R^2 values, but the lower concentration data could not be used to accurately predict viscosity at higher concentrations with increased complexities of higher order interactions (**Table 5.2**). Furthermore, the 'knee' of each curve was introduced to standardise where the viscosity starts to increase exponentially and aid model-to-model comparisons. The significant differences in modelled viscosities at the same concentrations emphasises the importance of examining full concentration-viscosity profiles, and not interpolated or extrapolated results.

Parameters derived from the modified Ross-Minton model fit, such as the k/v crowding factor and intrinsic viscosity ($[\eta]_{RM}$) were also assessed. I observed increased molecular packing and attractive forces particularly in the ultra-high concentration regime, represented with lower k/v values (**Appendix 4 Table 10.2**). However, $[\eta]_{RM}$ did not align with experimental $[\eta]$ values (**Appendix 4 Figure 10.7**), suggesting overfitting of high concentration viscosity data using the generalised reduced gradient algorithm, and highlighting the lack of translatability between concentration regimes (experimental $[\eta]$ measured in 0-50 mg/mL range).

Viscosity predictions and deeper mechanistic understanding from hydrodynamic parameters

Traditionally, the hydrodynamic behaviour of proteins has been modelled from colloidal principles (charged hard-sphere models) and expanded with the integration of polymer science to account for shape anisotropy.⁶⁷ In this chapter, I assessed the anti-IL-8 molecule panel with an extensive range of hydrodynamic parameters, such as intrinsic viscosity ($[\eta]$), the Huggins (k_H) coefficient, shape descriptors and volume fraction. I aimed to identify correlations with high concentration viscosities and other biophysical parameters we previously examined.

For most mutants, comparable $[\eta]$ values were observed with WT molecule (**Appendix 4 Table 10.3** and **Figure 5.3**), indicating comparable contributions from their respective hydrodynamic sizes, exemplified by computed volume fraction occupied (ϕ) (**Figure 5.4**). The positive-patch disrupting mutant, R53G, showed an increased $[\eta]$ and inferred size, although this was not reflected in DLS measurements

at 1 mg/mL, reducing the correlation observed between hydrodynamic radius (r_h) derived from $[\eta]$ to r_h derived from DLS (**Figure 5.4a,b**). Pair-wise interaction quantification from k_H and k_K values demonstrated comparable results for all molecules, except from W32Q and, interestingly, R53G, which both had lower inferred pair-wise contributions (**Appendix 4 Table 10.3**). These findings align with the viscosity profiles of W32Q (hydrophobic patch-disrupting mutant) in the lower concentration regime (**Figure 5.2a**), but contrast against the higher viscosity and increased $[\eta]$ observed for R53G (**Figure 5.2c,d**). Furthermore, unlike other mutants, R53G η_{red} does not scale linearly with concentration (**Appendix 4 Figure 10.1**). I hypothesise that this mutant is clustering at concentrations from 1 mg/mL upwards, hence no detected differences in r_{hDLS} . When interacting in small clusters, the short-ranged attractive interactions apply only to the near neighbours of the molecules interacting in the cluster. However, long-range repulsive interactions are additive and apply in an isotropic range from the cluster.^{90,366} This could result in an effect where the cluster stabilises at a critical cluster number, as the attractive forces remain in play due to the reduced distance between the molecules but the combined repulsion repels any new entrants to the cluster. When measuring interactions based on bulk solution flow properties, the base unit being measured would be the cluster as the constituent proteins move as one entity within the flow. The cluster has a larger hydrodynamic radius than the underlying mAb leading to the observed increased intrinsic viscosity, however the clusters do not interact strongly with one another due resulting in the low observed k_H . The base unit being measured in DLS is the protein, even when clustering is occurring, demonstrated by the more negative k_D for R53G observed in the 1-30 mg/mL range, stemming from the reduced molecular diffusivity and increased self-association of the protein when entrained in a cluster. Conversely, W32Q had a less negative k_D , aligning with reduced k_H .

It is worthwhile to note that the variability in both concentration and viscosity measurements results in large measurement errors for intrinsic viscosity. Furthermore, the derivation of intrinsic viscosity from linear regression of solutions exceeding the infinitely dilute regime and containing higher order interactions, results in the misrepresentation of pair-wise contributions. Previous work demonstrated minimum and maximum concentration limits for protein solutions, around 2-40 mg/mL, observing a three-state power law model for $\log(\eta)$ versus $\log(c)$.⁷⁴ To reduce the curvature of our data, we excluded the highest concentration data points for each

molecule in the η_{red}/c plots. Overall, this approach did not significantly reduce $[\eta]$ error, and in most cases the linear fit was dependent on only three data points (**Appendix 4 Figure 10.3**). I therefore chose to include the polynomial fitting of η_{rel} over concentration to derive $[\eta]_v$, previously proposed by Yadav and coworkers³³², but this similarly showed high error (**Appendix 4 Figure 10.4**).

The correlations of multiple biophysical parameters to the hydrodynamic properties and viscosity of the anti-IL-8 molecule panel were examined (**Appendix 4 Table 10.3**). According to the primary electroviscous effect, the higher the net charge of a molecule, the greater the distortion of the electrical double-layer (EDL) surrounding the molecule, increasing drag force in solution and $[\eta]$.³⁶⁷ Here, I saw no correlation in surface zeta potential (ζ) nor isoelectric point to $[\eta]$ for the anti-IL-8 molecules (**Figure 5.3**). This lack of correlation has been observed previously^{74,332} and suggests that ζ measurements at 5 mg/mL (where different molecular weight species may be present) are not representative of the expected molecular surface charge at infinite dilution. The exponential constant, k_{exp} , derived from η_{rel}/c exponential modelling, strongly correlated with k_D , aligning to the use of k_D in predicting viscosity in the low concentration regime.^{91,144,349} However, these correlations were reduced significantly when comparing to high concentration data, suggesting limits to predicting viscosity at dose-relevant concentrations.

Beyond size, pair interactions and charge, the shape factor (R_g/r_h) and computed shape coefficients were used to gauge morphological differences of the anti-IL-8 molecule panel (**Appendix 4 Figure 10.8**). No strong correlations were observed between these shape parameters, and $[\eta]$ or high concentration viscosity. Both methods derived molecular volume information from homology constructs, which did not account for environmental differences (buffer components, surface counterions) nor the effect of neighbouring molecules on molecular conformations.

The limitations in scaling viscosity predictions from hydrodynamic and colloidal parameters in low concentration regimes to viscosities in the dose-relevant concentration regime was exemplified by assessing theoretical viscosities from the Generalised Stokes-Einstein (GSE) equation (**Figure 5.5**). These GSE-derived viscosities correlated with the lower concentration regime viscosity data (**Figure 5.2a,c**). However, as these predictions are from extrapolations of the Z-ave and

diffusion coefficient data in the dilute range (1-30 mg/mL), these poorly correlated with high concentration viscosity data.

Limited predictive power of viscosity models

The development of models using sequence-based and structure-based molecular descriptors to predict and mitigate viscosity risks is an ever-growing field of research. I iterated through testing simple regression models developed from mAb molecular descriptors of small datasets. Li¹⁶¹ and Sharma²³⁷ models underpredicted the viscosities of the anti-IL-8 molecule panel, whilst the Tomar²³⁸ model was over-predictive (**Figure 5.6**), suggesting overfitting.

Furthermore, clustering according to the five descriptors identified by Kingsbury *et al.*¹⁷⁴ did not show specific trends that would categorise viscosity risks for the anti-IL-8 molecules at either the high or ultra-high concentration regime (**Figure 5.7**). Classification according to the ensemble charge parameter only had an accuracy of 55-66% according to concentration regime used to interpolate/extrapolate viscosity values at 120 mg/mL (**Appendix 4 Table 10.6 and Table 10.7**).

Generally, there is a consensus amongst these models that both electrostatic and hydrophobic parameters play a role in predicting viscosity, but the accuracy of these models rely heavily on the diversity and size of their datasets. Therefore, machine learning approaches are increasingly popular, with use of all potential molecular descriptors and larger datasets, which typically are limited to clinical-phase mAbs for data accessibility purposes. I tested two classification decision trees recently published^{153,269} to assess their predictive ability with the anti-IL-8 molecules, which have poor developability with high viscosity flags (all >20 cP at 150 mg/mL). Whilst the Lai decision tree¹⁵¹ (**Figure 5.8**), which introduced a 'high viscosity index' (HVI) showed accurate classification of all mutants as highly viscous, the Makowski decision tree¹⁵³ (**Figure 5.9**) classed negative-patch disrupting mutants (*i.e.* DàN) with low viscosity determined from the predicted isoelectric point threshold. It is worthwhile noting that the prediction accuracy of classification models is dependent on which model used for fitting and interpolating concentration-dependent viscosities, the concentration range is examined, and cut-off points used to define viscosity risk thresholds. There is general consensus that a low viscosity threshold is 20-30 cP, but some studies have proposed as low as 15 cP.³⁶⁸ The confusion matrices to test Lai and Makowski decision trees (**Appendix 4 Table 10.8 and Table 10.9**) demonstrated

how the proportion of true positives/negatives versus false positive/negative results are significantly impacted between models, concentration and cut-off points used.

Finally, I aimed to identify which computational parameters would accurately predict the knee of viscosity curves for the anti-IL-8 molecule panel. Significant correlations were seen with the TANGO score, number of hydrophilic residues, hydrophobic index, number of hydrophobic patches and number of positive patches, incorporating both electrostatic and hydrophobic profiling (**Appendix 4 Figure 10.9**). I developed a model from partial least-squared regression and leave-one-out cross validation (**Figure 5.10**). This regression model demonstrated 0.76 R^2 accuracy (RMSE= 12.7, Pearson's $R = 0.87$), proposing that key parameters can be defined for viscosity predictions in early phase screening on a per-project basis. The introduction of a test set of proprietary in-house molecules showed this model to be overfitted to the mutant panel, similarly to previously assessed regression models, highlighting how low-information models with few parameters miss out on some factors affecting viscosity. Reduction of terms from step-wise regression resulted in a significant reduction in R^2 , suggesting a larger dataset is required with the incorporation of other scaffolds as well as mAb molecules with a range of viscosities to generate a robust predictive model.

5.8. Conclusion

Knowledge of the factors governing elevated mAb solution viscosity at high formulation concentrations is critical in developing new mAbs for self-administration. Early measurements of solution viscosity are hindered by significant material-associated cost burdens. Therefore, a combination of predictive and experimental frameworks for solution viscosity prediction are required.

In this chapter, I address the question of which predictive and viscosity fitting models are optimal for viscosity prediction, using an anti-IL-8 IgG panel. I saw that the selection of model to fit concentration-viscosity profiles plays a critical role in the interpretation of viscosity results and the use of interpolated or extrapolated results carries significant variability risk. I found the extrapolation of viscosity measurements in a high (≤ 120 mg/mL) concentration regime are not predictive of viscosities in the ultra-high (up to 260 mg/mL) concentration regime, suggesting different concentration-dependent mechanisms governing self-interaction, assembly, and aggregation. The use of hydrodynamic and colloidal parameters for elucidating

drivers of viscosity in low concentration regimes was highlighted, but these did not correlate to ultra-high concentration viscosities.

Predictive regression models from small datasets, including the one developed in this work, tend to be overfitted and lack generalisability. I demonstrate the limitations of current machine learning models that use global parameters which are insensitive to residue-level differences which can impact viscosity. I propose that the future of viscosity predictive models relies on machine learning but with the incorporation of both amino acid sequences as well as structure based descriptors and/or dilute solution data to improve the probability of identifying sequence motifs governing molecular properties which give rise to viscosity. I also suggest the use of 'non-developable' molecules in training and testing datasets to better calibrate biophysical risks in early-phase development.

6. General discussion, conclusions and future work

The progression of a therapeutic mAb from early phase discovery through to clinical trials hinges on its developability profile, assessing conformational, colloidal and chemical stability, immunogenicity, biological activity, manufacturability and viscosity. The high viscosity of high concentration mAb formulations present a large problem with regards to issues of stability, filterability, filling and injectability in subcutaneous autoinjector devices. Mitigation strategies for high viscosity mAbs span from formulation development to molecular design with directed engineering to disrupt intermolecular interactions contributing to viscosity.

This chapter summarises the key findings of this thesis, discussing 1) the developability of an anti-IL8 mAb mutant panel designed from *in silico* molecular descriptors, 2) the manufacturability of the anti-IL8 mutant panel with regards to process observations and process-related impurity abundance, 3) the developability of an IgG3 anti-IL8 molecule against its IgG1 ortholog and 4) the limitations of viscosity model fitting, the concentration dependence of viscosity and the generalisability of viscosity predictive models.

6.1. Thesis summary

In **Chapter 2**, the rational design of 24 anti-IL8 IgG1 variants was performed with single-point mutations disrupting either hydrophobic, negative or positive surface patches mapped onto homology Fv constructs. Triaging of mutants was achieved by scoring in accordance with *in silico* molecular descriptors, previous correlated with viscosity. A systematic framework for comprehensive biophysical characterisation of mAbs was developed to assess charge, hydrophobicity, colloidal properties, and viscosity alongside computed molecular descriptors. Experimental observations using between the wild-type anti-IL-8 mAb and eight engineered mutant variants revealed that viscosity reduction is influenced by the location of hydrophobic interactions, supported by correlations between reduced hydrophobic interaction chromatography retention times to decreased viscosity and self-association propensity. Meanwhile, targeting positively charged patches significantly increased viscosity in comparison to wild-type anti-IL-8 mAb, as hypothesised from increasing the net negative charge. Interestingly the disruption of negative patches and increase in isoelectric point did not result in viscosity reduction. Moreover, poor correlations were seen between experimental high concentration viscosity of the mAb panel (up

to 120 mg/mL) and *in silico* physicochemical properties, demonstrating that no single computed descriptor can predict viscosity.

In **Chapter 3**, the same engineered anti-IL-8 mAb panel was evaluated in the context of manufacturability. Here, the implications of single-point mutations on the upstream process and downstream process were evaluated. Reduced cell growth, viability and mAb expression was observed with increased proportional expression of free light chain for heavy chain mutants in either framework or complementarity determining regions. This was hypothesised to be from either reduced transfection efficiency, or from reduced conformational stability and misfolding. Furthermore, the reduced charge of mutants that targeted positive surface patches required a lower cation exchange buffer pH for separation of free light chain compared to negative or hydrophobic patch disrupting mutants. Gelation points derived from flux extrapolations in the tangential flow filtration processing step poorly correlated to viscosities of the anti-IL-8 mutant panel (up to 120 mg/mL). Moreover, inconsistencies between phase behaviour and colloidal parameters and viscosity were observed. Finally, *in silico* post-translational modification screening was capable of flagging potential liabilities to aid explanations of changes in biophysical behaviour of mAbs.

Chapter 4 describes the application of the same biophysical characterisation framework developed in chapter 2 on an anti-IL-8 IgG3 molecule to give a first time insight into the developability of this unique subclass compared with an IgG1 ortholog. Overall, IgG3 presented with reduced conformational and colloidal stability, aligning with increased viscosity compared with IgG1. Since IgG3 had reduced net hydrophobicity, the increase self-association could not be attributed to increased hydrophobic interactions. Instead, increased hydrodynamic size (increased excluded volume) as well as anisotropic electrostatic attractions from predicted surface charge heterogeneity were postulated to increase self-association propensity. The latter however was not reflected by changes in measured effective surface charge. Moreover, conformational flexibility from the extended hinge region invoking different conformational forms of IgG3 was indicated by 1) intrinsic fluorescence scattering fluctuations, 2) increased peak hydrophobic interaction chromatography peak width, and 3) a hypothesised masked red shift in affinity chromatography self-interaction nano-spectroscopy.

Viscosity profiles of the anti-IL8 mutant panel in the ultra-high concentration regime (> 150 mg/mL) were evaluated in **chapter 5**. Whilst mutants with net reduced hydrophobicity showed the reduction in viscosity in the high concentration regime assessed in chapter 2, no mutants had enhanced viscosity in the ultra-high concentration, dose-relevant regime. As well as concentration dependence, the choice of viscosity fit equation had a large impact on viscosity values, cautioning against use of interpolated or extrapolated viscosity profile data where possible. This chapter also explored the use of hydrodynamic parameters which were briefly introduced in the assessment of IgG3 in chapter 4. Low concentration parameters such as intrinsic viscosity, volume fraction, theoretical Stokes-Einstein viscosities and shape factor showed some correlations to self-association propensity but limited predictive power of viscosity, particularly in ultra-high concentrations where higher order interactions and clustering effects prevail.

6.2. Future work

Increasing the dataset size and diversity

This thesis described the developability screening of ten molecules; an anti-IL-8 IgG1 wild-type, from which eight single-point Fv-mutant molecules were engineered as well as the developability of an Fv-matched IgG3 molecule. One of the evident limitations to the assessment of correlations and predictive power of *in silico* molecular descriptors to high concentration viscosity is the small dataset size and lack of domain diversity. All anti-IL-8 molecules showed suboptimal developability baselines and it would be prudent to include more developable mAbs into this dataset to increase confidence in trends. Investigation of whether reducing hydrophobicity similarly affects the viscosity of mAbs with alternative scaffolds (different CDRs/epitope targets/subclasses) would provide more information on the applicability of learnings from the anti-IL-8 model and the necessity for case-by-case evaluation of mAb viscosity. Moreover, sequence engineering to improve the developability of the IgG3 molecule could promote further research on its therapeutic potential.

Combining mutations for enhanced viscosity profiles

A key objective of this thesis was to design single-point mutations to enhance the viscosity profiles of an anti-IL-8 mAb model. Whilst mutants with significant reductions in hydrophobicity (D70N and W32Q) showed reduced viscosity at high concentrations, none of the mutants had improved viscosity in the ultra-high

concentration regime (>150 mg/mL) which is more dose relevant. D70N could be used as a scaffold for a future mutation round to combine mutations and explore additive effects that have previously been reported.^{227,233,235}

Decoupling interaction types and domain contributions

Understanding what type of interactions govern viscosity disruption was another objective of this thesis. It is clear from the literature that there is no consensus on the importance of hydrophobic *versus* electrostatic potential in dictating self-association nor viscosity. Therefore, the three strategies of disrupting either hydrophobic, negative or positive patches were explored. The reduced hydrophobicity aligning to decreased high-concentration viscosity in the case of the anti-IL8 IgG1 model with no viscosity improvements from mutants with increased net charge indicated hydrophobic interactions play the predominant role in governing viscosity. This aligns with some literature^{231,232,369,235} but is contrary to other studies where electrostatic disruptions are more influential^{223,178,229,233,98}. Confirmation of hydrophobicity-driven self-association could also be achieved by assessing if there are any decreases in viscosity with the addition of salt into the formulation buffer which would disrupt electrostatic interactions.²³⁵

Additionally, a deeper understanding of domain contributions could be achieved by individual preparation of scFvs and Fab fragments of the anti-IL8 mutant panel to identify the presence of Fab-Fab clustering.^{227,229,235}

The elevated viscosity of IgG3 in chapter 4, indicates the significant role of the increased surface potential from the Fc region on self-association. Some studies have shown reduction in viscosity independent of any Fc contributions,²³⁵ whilst others have reasoned that Fab-Fc interactions are pivotal in self-association.^{370,371,236} Therefore, the design Fc mutations, such as half-life extending combinations (*e.g.* YTE), could be explored. These could offer reduced potential impact on affinity compared with Fv variants but necessitate bioassays to assess if effector functions are impacted.

Alternative rational design of mutants; molecular dynamics and machine-learning directed mutagenesis

A caveat to the computational pipeline for the generation of molecular descriptors is the reliance on single homology models with no dynamic conformational sampling. Assumed structures carry the risks mispositioning of side-chains affecting the solvent

exposure and surface patch contributions. Furthermore, fragment and aggregate species as well as formulation components are not modelled in this thesis due to computational expense. The emergence of molecular dynamics and coarse-grained modelling for understanding mAb interactions, ligand docking and solubility screening, is an alternate method for mutant design.^{345,66,146,369} Therefore, in a similar manner to Tilegenova *et al.*²³² a molecular dynamics simulation was set up (**Appendix 1 section 7.3**) to assess the contact number of residues to free solvated arginine. Those residues with significant (>2 standard deviations) contact numbers to arginine are listed in **Table 6.1**. Unlike Tilegenova and coworkers, no residues with aromatic rings or charged residues were flagged from this simulation, suggesting interactions are distance based/dipole-like with the anti-IL8 IgG1 scaffold.

Table 6.1 Alternative residues to mutate proposed from molecular dynamics of anti-IL8 IgG1 wild-type.

Polar aliphatic residues are in purple and non-polar aliphatic residues are in green.

Residue of anti-IL8 IgG1
S14 (VL FWR)
V15 (VL FWR)
G15 (VL FWR)
L54 (CDRL2)
Q3 (VH FWR)

Finally future directed mutagenesis could be guided by predictive machine learning (ML) tools such as those mentioned in chapter 5 but an increased dataset size and diversity is required.^{151,153} Currently, there is a lack of accessible data sets on early-phase pre-clinical mAbs with disclosure limitations for in-house proprietary assets, restricting the development of ML tools that have generalisability to molecules with suboptimal developability profiles, such as the anti-IL8 model used in this thesis.

6.3. Conclusion

This thesis presents the impact of single-point mutations and subclass on the developability of an anti-IL8 IgG1 model, focussing on enhancing viscosity profiles. A computational and experimental biophysical screening framework was developed to assess of viscosity alterations from surface-patch targeting Fv mutants and provide a first time insight into the developability of Fv-matched IgG3 molecule. This thesis contributes to the expanding research into directed mutagenesis to improve the viscosity of high concentration mAb formulations, reducing manufacturability risks and injectability risks in self-administered subcutaneous devices.

7. Appendix 1

7.1. Computational design of anti-IL8 mutants

Patch analysis of candidate mutants

Table 7.1 Top-scoring residues contributing to hydrophobic (res_hyd), positive (res_pos) and negative (res_neg) patches.

Residues close to interactions with the GroBeta ligand are marked with an asterisk.

res_hyd score (Å ²)	Residue	Position	Mutant variant
61.4	F83	Framework L	F83Q
57.1	Y55*	CDRH2	Y55L
46.9	L110	Framework H	L110Q
44.7	F57*	CDRH2	F57L
40	Y99	CDRH3	Y99L
33	V11	Framework H	V11Q
32.9	V5	Framework H	V5Q
28	W32	CDRH2	W32Q
res_pos score (Å ²)	Residue	Position	Mutant variant
52.9	R53	CRDL2	R53G
44.6	K42	Framework L	K42E
41.8	K23	Framework H	K23E
35.3	K63	CDRH2	K63E
31.8	R18	Framework L	R18G
31.3	K13	Framework H	K13E
26.3	R85	Framework H	R85G
24.8	R70	Framework H	R70G
res_neg score (Å ²)	Residue	Position	Mutant variant
70.5	E30A*	CDRL1	E30AQ
38.9	D56	CDRL2	D56N

27.1	Q27	CDRL1	Q27N
24.2	D70	Framework L	D70N
23.6	D28	CDRL1	D28N
20.3	E10	Framework H	E10Q
20.3	E87	Framework H	E97Q
18.1	D17	Framework L	D17N

Patch numbers and corresponding surface area for anti-IL-8 WT and the generated mutants

Table 7.2 Patch numbers and corresponding area coverage for candidate mutant Fv homology constructs.

Ordered by mutation location, colour coded by mutation strategy; hydrophobic (green), positive (red) or negative (blue) patch targeting.

Mutation position	Molecule	patch_hyd (Å ²)	patch_hyd_n	patch_hyd %	patch_ion (Å ²)	patch_ion_n	patch_pos (Å ²)	patch_pos_n	patch_pos %	patch_neg (Å ²)	patch_neg_n	patch_neg %	patch_cdr_pos (Å ²)	patch_cdr_pos_n	patch_cdr_neg (Å ²)	patch_cdr_neg_n	patch_cdr_hyd (Å ²)	patch_cdr_hyd_n	Res_AS A (Å ²)	BSA_LC_HC
-	WT	680	9	38%	1100	23	690	14	39%	410	9	23%	380	6	280	5	280	2	10078.9	681.10
FWR L	D17N	620	8	34%	1190	23	760	14	42%	430	9	24%	380	6	300	5	260	2	10109.3	681.19
FWR L	D70N	660	9	38%	1071	22	690	14	40%	380	8	22%	380	6	250	4	260	2	10051.4	681.19
FWR L	F83Q	540	8	31%	1190	24	740	14	43%	450	10	26%	430	6	290	5	260	2	10080.5	681.19
FWR L	R18G	660	9	38%	1080	22	660	13	38%	420	9	24%	380	6	290	5	260	2	10036.4	681.19
FWR L	K42E	640	8	38%	1060	22	640	13	38%	420	9	25%	380	6	290	5	260	2	10016	683.39
FWR H	V5Q	620	8	35%	1170	24	700	14	39%	470	10	26%	380	6	290	5	260	2	10060.9	680.64
FWR H	E10Q	660	9	37%	1140	23	740	15	41%	400	8	22%	380	6	300	5	260	2	10069.2	681.19
FWR H	E87Q	660	9	37%	1130	22	740	14	41%	390	8	22%	380	6	290	5	260	2	10075.7	681.19
FWR H	L110Q	590	8	35%	1110	23	690	14	41%	420	9	25%	380	6	290	5	260	2	10058.1	681.14
FWR H	V11Q	620	8	36%	1120	23	690	14	40%	430	9	25%	380	6	300	5	260	2	10073.1	681.19
FWR H	R85G	660	9	38%	1070	21	650	13	38%	420	8	24%	380	6	290	5	260	2	10086.4	681.19
FWR H	R70G	630	8	37%	1080	22	650	13	38%	430	9	25%	340	5	290	5	260	2	10136.5	681.19

FWR H	K23E	620	8	35%	1140	23	640	13	36%	500	10	28%	380	6	290	5	260	2	10090	681.19
FWR H	K13E	660	9	36%	1160	22	660	13	36%	500	9	27%	380	6	290	5	260	2	10096.7	681.19
CRDL2	R53G	710	9	41%	1030	22	630	13	36%	400	9	23%	320	5	270	5	310	2	10057.6	661.34
CDRL2	D56N	640	8	36%	1120	22	740	14	42%	380	8	22%	350	5	250	4	270	2	10032.1	702.68
CDRL1	D28N	700	9	40%	1040	24	690	14	40%	350	10	20%	380	6	220	6	300	2	10050.4	681.19
CDRL1	E30aQ	700	9	39%	1090	24	690	14	39%	400	10	22%	380	6	270	6	300	2	10038.9	684.97
CDRL1	Q27N	660	9	36%	1170	22	680	14	37%	490	8	27%	370	6	360	4	260	2	10055.5	681.19
CDRH3	W105Q	630	8	35%	1170	24	720	14	40%	450	10	25%	340	5	320	6	260	2	10096.4	682.89
CDRH3	Y99L	670	9	37%	1130	23	700	14	39%	430	9	24%	390	6	300	5	270	2	10072.1	661.51
CDRH3	W102bQ	670	9	38%	1110	24	680	14	38%	430	10	24%	370	6	300	6	270	2	10064.5	608.28
CDRH2	W32Q	610	11	35%	1120	23	700	14	40%	420	9	24%	390	6	290	5	180	3	9997.4	688.06
CDRH2	F57L	660	9	38%	1090	23	670	14	38%	420	9	24%	360	6	290	5	260	2	9999.2	697.78
CDRH2	Y55L	660	9	38%	1060	22	640	13	37%	420	9	23%	330	5	290	5	260	2	10036.7	678.32
CDRH2	K63E	660	9	36%	1160	23	640	13	35%	520	10	28%	340	5	390	6	260	2	10105.9	684.52

Physicochemical molecular descriptors

Table 7.3 Physicochemical descriptors computed for WT and mutant homology models that have been used in previous studies to predict viscosity.

Name	Description	Correlation to viscosity
patch_hyd	Summed area of hydrophobic patches (\AA^2). ³⁷²	Increased accessible hydrophobic patches correlated to increased viscosity. ^{230,235}
patch_hyd_n	Summed number of hydrophobic patches. ³⁷²	
asa_hyd \AA^2	Solvent-accessible surface area of hydrophobic atoms of a protein (\AA^2). ³⁷²	
Res_hyd	The summed hydrophobic contribution from each residue to hydrophobic patch area in \AA^2 . This was calculated through the Protein Properties tool in MOE 2020 and manually summed subsequently. The target pH was set to 6, temperature set to 300K and salt concentration to 0.1M. ³⁷²	
patch_pos \AA^2	Summed area of positive patches (\AA^2). ³⁷²	Prevalence of positively charged residues in Fab correlated with increased viscosity. ^{229,231}
patch_pos_n	Summed number of positive patches.	
patch_neg \AA^2	Summed area of negative patches (\AA^2). ³⁷²	Increased net negative charge correlated with increased viscosity. ²³³
patch_neg_n	Summed number of negative patches. ³⁷²	
patch_ion	Summed area of ionic (positive and negative) patches (\AA^2). ³⁷²	Electrostatically driven attractions contributing to viscosity have been primarily attributed to CDRs. ^{147,223}
patch_ion_n	Summed number of charged (positive and negative) patches. ³⁷²	
patch_cdr_hyd	Summed area of hydrophobic patches near the CDRs (\AA^2). ³⁷²	Hydrophobicity in CDRs correlated with increased aggregation propensity. ²⁴¹
patch_cdr_hyd_n	Summed number of hydrophobic patches near the CDRs. ³⁷²	
patch_cdr_pos	Summed area of positive patches near the CDRs (\AA^2). ³⁷²	Increased positive patches in CDRs correlated with reduced developability. ²⁴¹
patch_cdr_pos_n	Summed number of positive patches near the CDRs. ³⁷²	
patch_cdr_neg	Summed area of negative patches near the CDRs (\AA^2). ³⁷²	Increased negative patches in CDRs correlated with reduced developability. ²⁴¹
patch_cdr_neg_n	Summed number of negative patches near the CDRs. ³⁷²	
Hydrophobic Imbalance	A vector that describes the displacement of the superficial geometric centre of the protein when the respective ASA values of each amino acid is considered. ³⁷³ This was calculated through the descriptors function in the BioMOE module in MOE 2020. Default parameters were used with no sampling. This was calculated off the Fv model at default values of pH 7.4, temperature of 300K and a salt concentration of 0.1M. ³⁷⁴	Increased hydrophobic anisotropy correlated with poor solution behaviour. ²⁴³
Fv_chml	The Fv heavy chain (V_H) charge – Fv light chain (V_L) charge. This was calculated through the descriptors function in the BioMOE module in MOE 2020. Default parameters were used with no sampling. This was calculated from the Fv model at default values of pH 7.4, temperature of 300K and a salt concentration of 0.1M. ³⁷⁴	<4 or >4 Fv_chml values correlated with increased viscosity. ²⁴²
Pro_Fv_net_charge	The protein net charge on Fv only. This was calculated through the descriptors function in the BioMOE module in MOE 2020. Default	Net negative/ decreased charge correlated with

	parameters were used with no sampling. This was calculated off the Fv model at default values of pH 7.4, temperature of 300K and a salt concentration of 0.1M. ³⁷⁴	increased viscosity. ^{161,237,233}
Pro_net_charge	The protein net charge. This was calculated through the descriptors function in the BioMOE module in MOE 2020. Default parameters were used with no sampling. This was calculated off the Fv model at default values of pH 7.4, temperature of 300K and a salt concentration of 0.1M. ³⁷⁴	
Net_charge	The formal protein net charge at a given pH. This was calculated through the Protein Properties tool in MOE 2020. The target pH was set to 6, temperature set to 300K and salt concentration to 0.1M. ³⁷²	
Dipole_moment	Dipole calculated across the protein from uneven distribution of charges. This was calculated through the Protein Properties tool in MOE 2020. The target pH was set to 6, temperature set to 300K and salt concentration to 0.1M. ³⁷²	Increased dipole moment correlated with increased viscosity. ^{178,223,226,249}
Hyd_moment	Hydrophobicity moment where each residue side chain hydrophobicity is calculated from the Kyte-Doolittle scale across the length of the protein. ³⁷⁵ This was calculated through the Protein Properties tool in MOE 2020. The target pH was set to 6, temperature set to 300K and salt concentration to 0.1M. ³⁷²	Increased hydrophobic moment correlated with increased viscosity. ¹⁶¹
Pro_hyd_moment	Hydrophobicity moment where each residue side chain hydrophobicity is calculated from the Kyte-Doolittle scale across the length of the protein. ³⁷⁵ This was calculated through the descriptors function in the BioMOE module in MOE 2020. Default parameters were used with no sampling. This was calculated off the Fv model at default values of pH 7.4, temperature of 300K and a salt concentration of 0.1M. ³⁷⁴	
Hydrophobicity Index	The summation of hydrophobic residues' Eisenberg scores over the summation of hydrophilic residues' Eisenberg scores. Sharma <i>et al.</i> correlated Lower Eisenberg scores with lower viscosity. ²³⁷	Increased hydrophobic index correlated with increased viscosity. ²³⁷
Zeta	Zeta potential is the electrical potential observed at the slipping plane. ³⁷⁶ This was calculated through the Protein Properties tool in MOE 2020. The target pH was set to 6, temperature set to 300K and salt concentration to 0.1M. ³⁷²	Negative zeta potential correlated with increased viscosity. ¹⁶¹
pI_seq	The isoelectric point of a protein calculated from amino acid composition. ³⁷⁷ This was calculated through the Protein Properties tool in MOE 2020. The target pH was set to 6, temperature set to 300K and salt concentration to 0.1M. ³⁷²	Higher predicted pI_seq // further distanced from solution pH correlated with increased viscosity. ²⁴²
BSA_LC_HC	The buried surface area (BSA) between the heavy and light chains in Å ² . This was calculated through the descriptors function in the BioMOE module in MOE 2020. Default parameters were used with no sampling. This was calculated off This was calculated off the Fv model at default values of pH 7.4, temperature of 300K and a salt concentration of 0.1M. ³⁷⁴	Decreased BSA between heavy and light chain correlated with decreased conformational stability. ²⁴³

Ens_charge	The ensemble average charge of the full molecule. This was calculated through the Protein Properties tool in MOE 2020. The target pH was set to 6, temperature set to 300K and salt concentration to 0.1M. ³⁷²	An ens_charge of <+2 correlated with increased viscosity. ²⁴²
pl_3D	The isoelectric point of the molecule calculated through a modified version of Sillero's model. The PROPKA algorithm is used. This was calculated through the Protein Properties tool in MOE 2020. The target pH was set to 6, temperature set to 300K and salt concentration to 0.1M. ³⁷²	Strongly correlated with viscosity of Tomar dataset. ²³⁸
Fv charge symmetry (FvSCP)	Charge symmetry of the Fv was calculated with charge of the light chain multiplied by the net charge of the heavy chain. ²³⁷	Decreased symmetry correlated with increased viscosity. ²³⁷
Res_ASA	The summed contribution from each residue to the accessible surface area in Å ² . This was calculated through the Protein Properties tool in MOE 2020 and manually summed subsequently. The target pH was set to 6, temperature set to 300K and salt concentration to 0.1M. ³⁷²	Increased surface exposure correlated with increased viscosity. ²³⁵
Dipole moment/hydrophobic moment ratio (RM)	The ratio of Fv dipole moment over the Fv hydrophobic moment to describe the balance of polar versus nonpolar distributions per molecule. This was previously identified as an intrinsic non-redundant descriptor for a dataset of commercial mAbs. ²⁴³	Ahmed <i>et al.</i> found RM ~1.1 for 'developable' marketed mAbs. ²⁴³
Ionic/hydrophobic patch area ratio (RP)	The ratio of Fv ionic patch area to hydrophobic patch area. This was previously identified as an intrinsic non-redundant descriptor for a dataset of commercial mAbs. ²⁴³	Ahmed <i>et al.</i> found RP ~1.8 for 'developable' marketed mAbs. ²⁴³

Physicochemical descriptor results of mutant variants.

Table 7.4 Charge-based physicochemical descriptors computed for each anti-IL-8 mutant Fv homology construct.

Ordered by mutation location, colour coded by mutation strategy; hydrophobic (green), positive (red) or negative (blue) patch targeting.

Position of mutation	Molecule	Fv_chml	pro_Fv_net_charge	pro_net_charge	net_charge	dipole_moment	Predicted zeta at Deybe length (mV)	pI_seq	ens_charge	pI_3D	VL net charge	VH net charge	Fv charge symmetry	Deep SCM
-	WT	3	3.0	-0.41	0.05	554.21	0.19	6.42	2.01	6.23	-1.23	3.93	-4.83	1197.42
FWR L	D17N	2	4.0	0.17	0.62	578.20	1.79	6.68	3.30	7.61	-0.32	3.93	-1.26	1164.43
FWR L	D70N	2	4.0	0.17	0.63	466.75	1.58	6.68	2.90	7.61	-0.32	3.93	-1.26	1136.54
FWR L	F83Q	3	3.0	-0.40	0.05	554.97	0.19	6.42	2.10	6.23	-1.23	3.93	-4.83	1203.71
FWR L	R18G	4	2.0	-1.29	-0.84	602.97	-2.18	6.07	1.31	4.92	-2.18	3.91	-8.52	1224.63
FWR L	K42E	5	1.0	-2.27	-1.81	482.48	-4.14	5.62	0.07	4.56	-3.16	3.93	-12.42	1253.89
FWR H	V5Q	3	3.0	-0.41	0.05	561.51	0.19	6.42	2.25	6.23	-1.23	3.83	-4.71	1194.19
FWR H	E10Q	4	4.0	0.17	0.62	614.54	1.64	6.68	3.00	7.61	-1.23	4.83	-5.94	1162.09
FWR H	E87Q	4	4.0	0.17	0.63	528.25	1.54	6.68	3.25	7.61	-1.23	4.88	-6.00	1178.73
FWR H	L110Q	3	3.0	-0.41	0.05	555.58	0.19	6.42	1.96	6.23	-1.23	3.91	-4.81	1197.28
FWR H	V11Q	3	3.0	-0.41	0.05	557.56	0.19	6.42	2.10	6.23	-1.23	3.92	-4.82	1206.02
FWR H	R85G	2	2.0	-1.30	-0.84	587.77	-1.98	6.07	0.98	4.92	-1.23	2.93	-3.60	1217.96

FWR H	R70G	2	2.0	-1.29	-0.83	565.14	-1.99	6.07	0.94	4.94	-1.23	2.93	-3.60	1261.49
FWR H	K23E	1	1.0	-2.21	-1.72	390.65	-4.03	5.62	0.11	4.68	-1.23	0.95	-1.17	1317.79
FWR H	K13E	1	1.0	-2.21	-1.73	578.86	-4.40	5.62	0.25	4.64	-1.23	0.94	-1.16	1290.93
CDRL2	R53G	4	2.0	-1.29	-0.83	576.62	-1.96	6.07	1.01	4.93	-2.18	3.93	-8.57	1256.43
CDRL2	D56N	2	4.0	0.17	0.63	598.31	1.51	6.68	3.00	7.61	-0.32	3.82	-1.22	1136.34
CDRL1	D28N	2	4.0	0.16	0.62	484.86	1.46	6.68	2.88	7.58	-0.34	3.93	-1.34	1062.51
CDRL1	E30aQ	2	4.0	0.00	0.71	511.01	1.67	6.68	2.96	7.40	-0.35	3.93	-1.38	1104.96
CDRL1	Q27N	3	3.0	-0.47	0.05	557.86	0.20	6.42	2.11	6.23	-1.23	3.93	-4.83	1194.81
CDRH3	W105Q	3	3.0	-0.41	0.06	547.28	0.21	6.42	2.62	6.25	-1.23	3.94	-4.85	1188.64
CDRH3	Y99L	3	3.0	-0.40	0.05	551.36	0.19	6.42	1.92	6.23	-1.23	3.9	-4.80	1189.43
CDRH3	W102bQ	3	3.0	-0.41	0.06	552.14	0.20	6.42	2.17	6.24	-1.33	3.87	-5.15	1190.74
CDRH2	W32Q	3	3.0	-0.41	0.05	566.44	0.21	6.42	2.38	6.24	-1.22	3.92	-4.78	1213.87
CDRH2	F57L	3	3.0	-0.45	0.05	555.44	0.19	6.42	2.07	6.21	-1.23	3.93	-4.83	1199.18
CDRH2	Y55L	3	3.0	-0.41	0.05	555.09	0.19	6.42	2.11	6.23	-1.23	3.93	-4.83	1200.79
CDRH2	K63E	1	1.0	-2.19	-1.71	655.50	-4.03	5.62	0.13	4.65	-1.23	0.94	-1.16	1279.49

Table 7.5 Hydrophobicity-based physicochemical molecular descriptors and TANGO aggregation propensity scores of anti-IL-8 mutant variants. Dipole and ionic to hydrophobicity ratios are also reported.

Ordered by mutation location, colour coded by mutation strategy; hydrophobic (green), positive (red) or negative (blue) patch targeting.

Position of mutation	Molecule	Hydrophobic imbalance	hyd_moment	pro_hyd_moment	Hydrophobic index	Normalised hydrophobicity score (%)	ASA_hyd Å ²	Res-Hyd Å ²	Dipole moment/hyd patch area	Ionic/hydrophobic patch area ratio	TANGO Aggregation propensity
-	WT	1.08	396.57	396.57	1.094	5.14	5647.53	518.50	1.07	1.62	1603.94
FWR L	D17N	1.14	395.70	395.70	1.096	4.91	5581.12	496	1.20	1.92	1590.12
FWR L	D70N	1.09	397.58	397.58	1.096	4.96	5648.77	498.3	0.95	1.62	1627.07
FWR L	F83Q	1.22	334.44	334.44	1.065	4.05	5575.46	408.2	1.39	2.20	1577.65
FWR L	R18G	1.03	432.39	432.39	1.140	4.96	5639.26	498.1	1.23	1.64	1589.75
FWR L	K42E	1.13	400.56	400.56	1.105	5.06	5574.70	507.3	0.96	1.66	1602.38
FWR H	V5Q	0.80	325.88	325.88	1.067	4.96	5599.16	498.8	1.15	1.89	1603.94
FWR H	E10Q	1.08	396.95	396.95	1.092	4.96	5662.86	499.1	1.25	1.73	1602.71
FWR H	E87Q	1.09	396.28	396.28	1.092	4.94	5664.91	498	1.08	1.71	1632.24
FWR H	L110Q	1.03	355.72	355.72	1.067	4.22	5604.93	424.2	1.32	1.88	1530.25
FWR H	V11Q	1.08	378.72	378.72	1.067	4.95	5598.55	498.6	1.14	1.81	1603.94
FWR H	R85G	1.07	394.59	394.59	1.140	4.94	5647.25	498.4	1.20	1.62	1603.62

FWR H	R70G	1.12	401.40	401.40	1.140	4.92	5666.67	498.8	1.15	1.71	1603.94
FWR H	K23E	1.08	399.60	399.60	1.105	4.95	5557.77	499.4	0.80	1.84	1624.98
FWR H	K13E	1.08	396.35	396.35	1.105	4.94	5627.99	499.1	1.16	1.76	1605.15
CDRL2	R53G	1.08	401.05	401.05	1.140	5.40	5691.33	542.8	1.07	1.45	1897.13
CDRL2	D56N	1.11	397.34	397.34	1.096	5.02	5649.88	503.3	1.20	1.75	1602.95
CDRL1	D28N	1.05	396.57	396.57	1.096	5.32	5652.63	535	0.91	1.49	1603.43
CDRL1	E30aQ	1.06	397.01	397.01	1.092	5.37	5655.14	538.6	0.96	1.56	1638
CDRL1	Q27N	1.10	396.47	396.47	1.095	4.98	5618.84	500.3	1.12	1.77	1603.79
CDRH3	W105Q	1.03	380.86	380.86	1.070	4.94	5599.76	498.6	1.09	1.86	1603.88
CDRH3	Y99L	1.09	393.52	393.52	1.105	5.11	5675.74	514.2	1.08	1.69	1603.96
CDRH3	W102bQ	1.04	402.35	402.35	1.070	4.97	5598.06	500.3	1.10	1.66	1604.05
CDRH2	W32Q	1.11	408.27	408.27	1.070	3.44	5597.72	343.7	1.67	1.84	1357.71
CDRH2	F57L	1.13	387.53	387.53	1.092	4.91	5663.06	491.3	1.13	1.65	1602.02
CDRH2	Y55L	1.11	353.42	353.42	1.105	4.98	5664.70	500.3	1.13	1.61	1605.53
CDRH2	K63E	1.08	392.53	392.53	1.105	4.93	5608.40	498.3	1.34	1.76	1605.17

Therapeutic antibody profiler (TAP) scores for anti-IL-8 mutant variants

Therapeutic Antibody Profiler (<https://opig.stats.ox.ac.uk/webapps/sabdab-sabpred/sabpred/tap>). The therapeutic antibody profiler (TAP) is a developability ranking tool that incorporates CDR length, hydrophobicity, positive and negative charges of CDR patches and Fv charge symmetry of homology structures.^{241,260} The web application was used to submit heavy and light chain sequences of the wild-type and mutant panel.

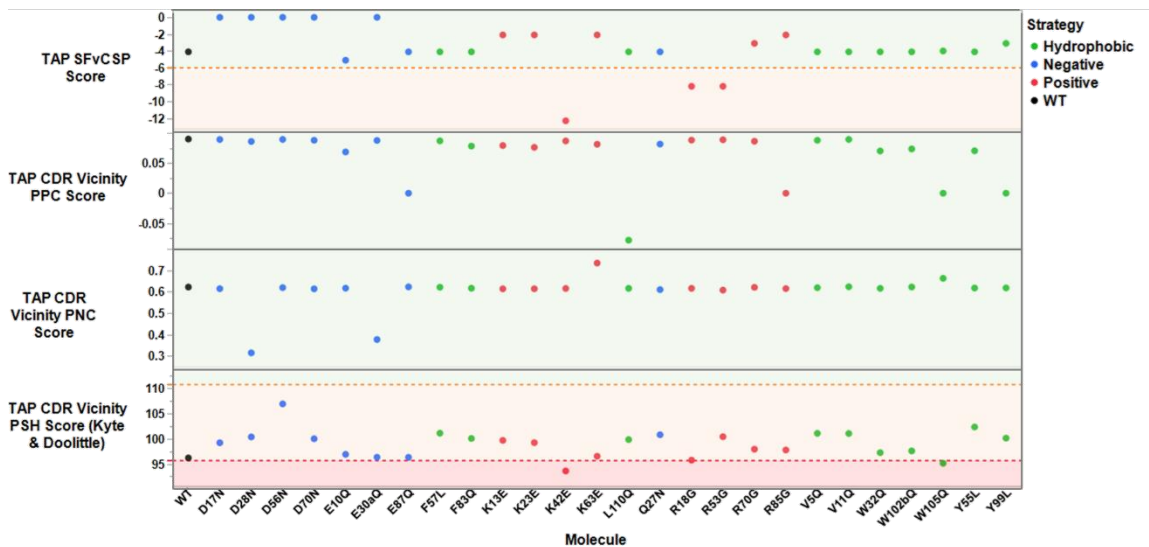


Figure 7.1 The Therapeutic Antibody Profiler (TAP) tool computed four structural attributes for anti-IL-8 candidate mutants.

This tool used the heavy and light chain sequences of the variable regions for each molecule and the ABodyBuilder2 tool was used to construct homology models. The red-amber-green thresholds were set from previous work analysing 137 clinical stage antibodies. For all mutants the CDR length was 46 residues which was within the green threshold. Structural Fv Charge Symmetry Parameter (SFvCSP) showed three positive-patch disrupting mutants with amber flags (K42E, R18G and R53G). The patches of positive charge (PPC) metric and the patches of negative charge (PNC) metric across the CDR vicinity showed no flags for all mutants. However, all mutants had at least an amber flag for the patches of Surface Hydrophobicity (PSH) metric across the CDR vicinity, with two red flags for K42E and W105Q.

Modified Fv patch areas of expressed mutants

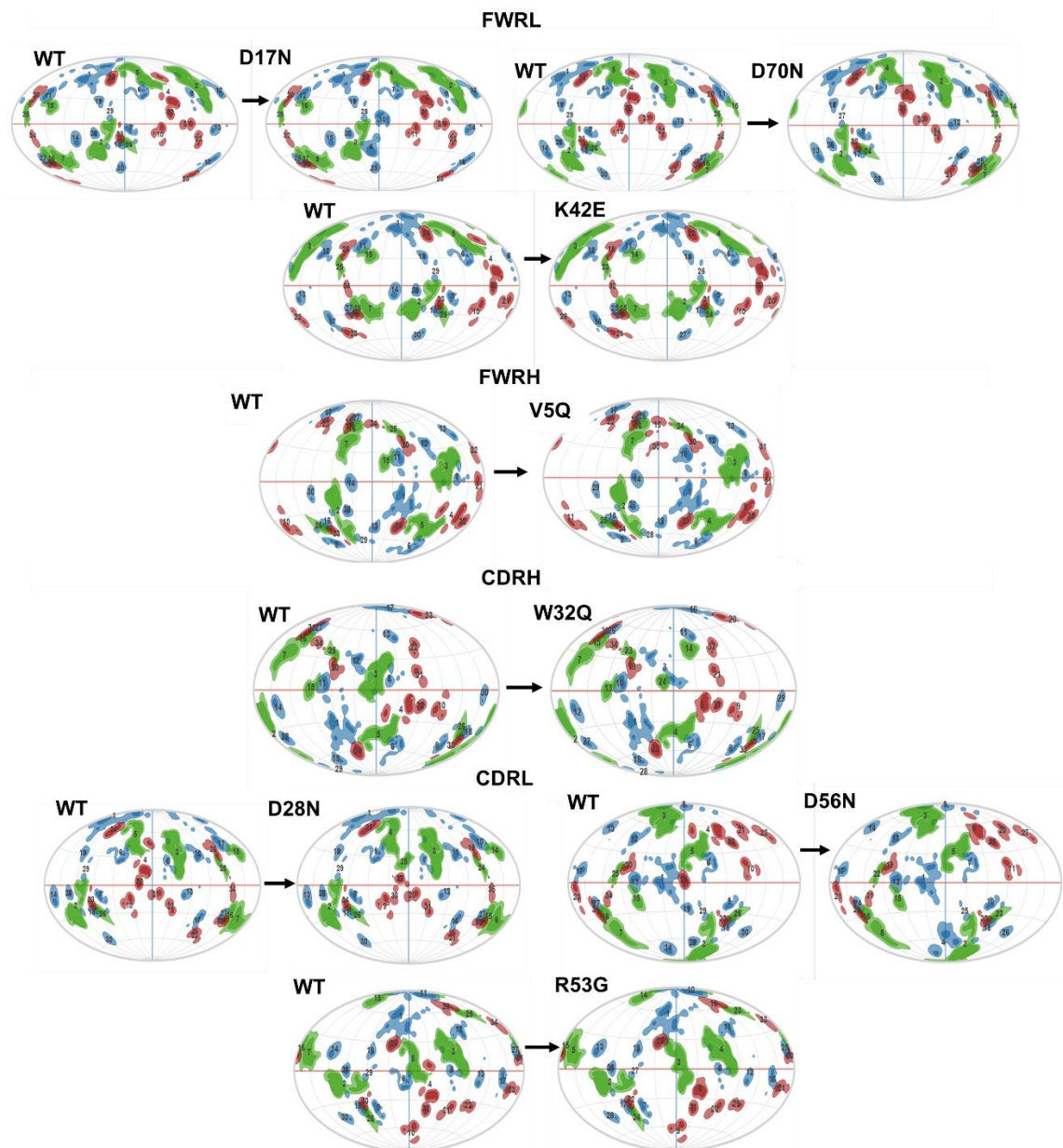


Figure 7.2 Two-dimensional patch maps of expressed mutants Fv homology constructs.

Hydrophobic (green), positive (blue) and negative (red) patches were analysed for the area and energy changes for each expressed anti-IL-8 mutant. The field of view is rotated for each WT and expressed mutant pair to have the site of mutation at the centre.

Table 7.6 Quantitation of specific modified patch areas and energy changes for expressed mutants Fv homology constructs.

Molecule	WT 2D Map Number	Patch Type	Patch Area (Å ²)		Average energy per Å ² (kcal/mol)		Other significant residues
			WT	Mutant	WT	Mutant	
D17N	33	neg	30	Removed	-49.42	Removed	S14, G16
	26	hyd	30	Removed	-0.11	Removed	P8, L11, A13, V19
D70N	10	neg	60	Removed	-49.72	Removed	Q24, Q69
K42E	14	pos	50	Removed	-54.26	Removed	P40, G41
	28	pos	30	Removed	-51.72	Removed	K39, P40, E81, F83
W32Q	3	hyd	150	30	-0.16	-0.13	Y51C
	8	pos	70	130	-41.71	-48.24	H91, E93, S93A, P95
V5Q	15	hyd	40	Removed	-0.14	Removed	K23
	11	pos	50	60	-61.18	-61.1	K23 T74 S75
D28N	32	neg	30	30	-55.96	-43.85	E30, G68
	N/A	hyd	30	Addition	-0.15	Addition	E30A, Y32
D56N	24	neg	40	Removed	-69.48	Removed	N/A
	19	pos	40	Removed	-45.54	Removed	K45, G57, V58, P59
R53G	6	pos	80	Removed	-53.93	Removed	Y50 T52 L54
	5	hyd	110	150	-0.15	-0.16	Y32, Y49, Y50

Triage of candidate mutants

Table 7.7 Top and bottom scoring anti-IL-8 mutants progressed to experimental characterisation based on min-max normalisation.

Scoring was based on hydrophobic index, zeta potential, BSA_{LC}_HC, ens_charge, normalised hydrophobicity, and TANGO aggregation propensity. Each descriptor value was weighted evenly and normalised to ensure that the lower the score, the increased likelihood of reduced hypothesised viscosity.

Molecule	Mutation	Summed normalised score
WT (-)	-	3.28
W32Q (CDRH2)	Hydrophobic	1.76
D56N (CDRL2)	Negative	2.13
D17N (FWL)	Negative	2.21
D70N (FWL)	Negative	2.35
V5Q (FWH)	Hydrophobic	2.37
D28N (CDRL1)	Negative	2.42
R53G (CDRL2)	Positive	5.83
K42E (FWL)	Positive	6.22

7.2. Biophysical Characterisation of anti-IL8 mutant panel

Analysis of identity by mass spectrometry

Table 7.8 Verification of anti-IL-8 WT and mutant variant identity by peptide fragmentations.

Trypsin or chymotrypsin digest of this peptide following the same methodology showed coverage of this missing peptide, ensuring full identity verification. For post-translational modifications (PTMs), the % detection was relative to only peptides with expected full enzyme cleavage. PTMs with relative detection were noted. *Abbreviations HC: Heavy chain; LC: Light chain; mwt: molecular weight; PTM: post-translational modification*

Molecule	LC coverage (%)	HC coverage (%)	LC mwt (Da)	HC mwt (Da)	LC PTMs	HC PTMs
WT	97.66	96.66	23433.83	49204.09	M4 oxidation (0.4%)	M81 oxidation (0.2%), N317 deamidation (0.6%), M254 oxidation (4.2%), N363 deamidation (0.4%), M430 oxidation (1.8%)
D17N	97.66	97.44	23432.85	49204.09	M4 oxidation (0.3%)	M81 oxidation (0.2%), M254 oxidation (4.5%), N317 deamidation (0.1%), N363 deamidation (0.4%), M430 oxidation (2.1%)
D70N	99.07	98.22	23432.85	49204.09	M4 oxidation (0.3%), possible N70 modification but not confirmed due to poor fragmentation (see map coverage below Figure 7.3)	M81 oxidation (0.2%), M254 oxidation (4.8%), N288 deamidation (0.1%), N317 deamidation (0.3%), N363 deamidation (0.2%), N436 deamidation (1.42%)
K42E	97.66	98.22	23434.77	49204.09	M4 oxidation (0.3%)	M81 oxidation (1.12%), N317 deamidation (0.4%), M430 oxidation (1.9%), N436 deamidation (3.3%)
V5Q	97.66	98.22	23433.83	49233.09	None	N363 deamidation (0.2%)
W32Q	97.66	79.73*	23433.83	49146.01	None	S methylation (100%), N317 deamidation (2.5%)

D28N	97.66	98.22	23432.85	49204.09	N28 deamidation (12.3%)	N317 deamidation (0.4%), N363 deamidation (0.2%), N436 deamidation (1%)
D56N	97.66	98.22	23432.85	49204.09	N56 deamidation (1.85%)	N436 deamidation (0.8%)
R53G	97.66	98.22	23334.7	49204.09	M4 oxidation (1%)	M430 oxidation (1.6%)

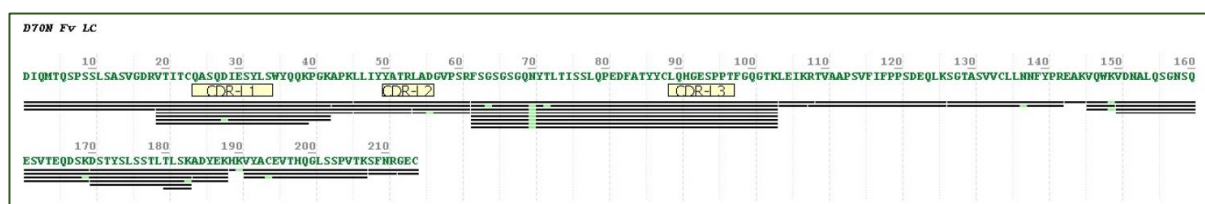


Figure 7.3 Peptide map coverage for D70N light chain. Possible modification site at N70 flagged (light green).

Analysis of Monomeric Purity by Analytical Size Exclusion Chromatography (aSEC)

Samples were injected onto a TSKgel Super SW3000, 4.6 x 300 mm (TOSOH Bioscience, United States) column on an Agilent 1260 series HPLC, with 0.1M sodium phosphate containing 400 mM NaCl (pH 6.8) as the mobile phase. All samples were analysed at 5 mg/mL at a 0.2 mL/min flow rate, and detected at 280 nm. The OpenLab CDS Data Analysis software (version 2.6, Agilent, California, US) was used to process and integrate the chromatograms. Areas under the chromatographic peaks were integrated to quantify the monomeric mAb, and high and low molecular weight species. The target monomeric purity of $\geq 95\%$ was met by all anti-IL-8 molecules and aSEC was used to monitor physicochemical stability, by monitoring changes in chromatogram peak retention times and profiles for each molecule throughout processing. Analysis of the expressed anti-IL-8 mutants showed retention times comparable to the anti-IL-8 WT IgG1 (~27.5 minutes), except for the D70N mutant, which had a consistent reduced retention time of ~26.6 minutes suggesting a slight increase in molecular size.

Table 7.9 Monomeric purity of all anti-IL-8 molecules (N=3).

Mab	RT (min)	Peak Width (min)	%HMW species	%Monomer	% LMW species
WT	27.5 (± 0.5)	0.53 (± 0.05)	1.3 (± 0.2)	97.1 (± 0.5)	1.6 (± 0.5)
D17N (FWL)	27.4 (± 0.3)	0.51 (± 0.05)	1.2 (± 0.1)	98.0 (± 0.5)	0.9 (± 0.5)

D70N (FWL)	26.6 (± 0.3)	0.75 (± 0.03)	1.5 (± 0.2)	98.0 (± 0.4)	0.6 (± 0.3)
K42E (FWL)	27.3 (± 0.3)	0.51 (± 0.05)	1.4 (± 0.2)	97.2 (± 0.6)	1.4 (± 0.5)
V5Q (FWH)	27.5 (± 0.5)	0.53 (± 0.06)	1.2 (± 0.3)	97.4 (± 0.7)	1.4 (± 0.5)
W32Q (CDRH2)	27.5 (± 0.6)	0.51 (± 0.05)	2.1 (± 0.6)	96.8 (± 1.1)	1.1 (± 0.5)
D28N (CDRL1)	27.6 (± 0.5)	0.55 (± 0.1)	1.8 (± 0.3)	96.5 (± 0.8)	1.7 (± 0.8)
D56N (CDRL2)	27.5 (± 0.5)	0.53 (± 0.05)	1.4 (± 0.6)	97.0 (± 1.1)	1.7 (± 0.5)
R53G (CDRL1)	27.5 (± 0.5)	0.53 (± 0.05)	1.5 (± 0.4)	97.2 (± 0.7)	1.2 (± 0.4)

Hydrophobic interaction chromatography

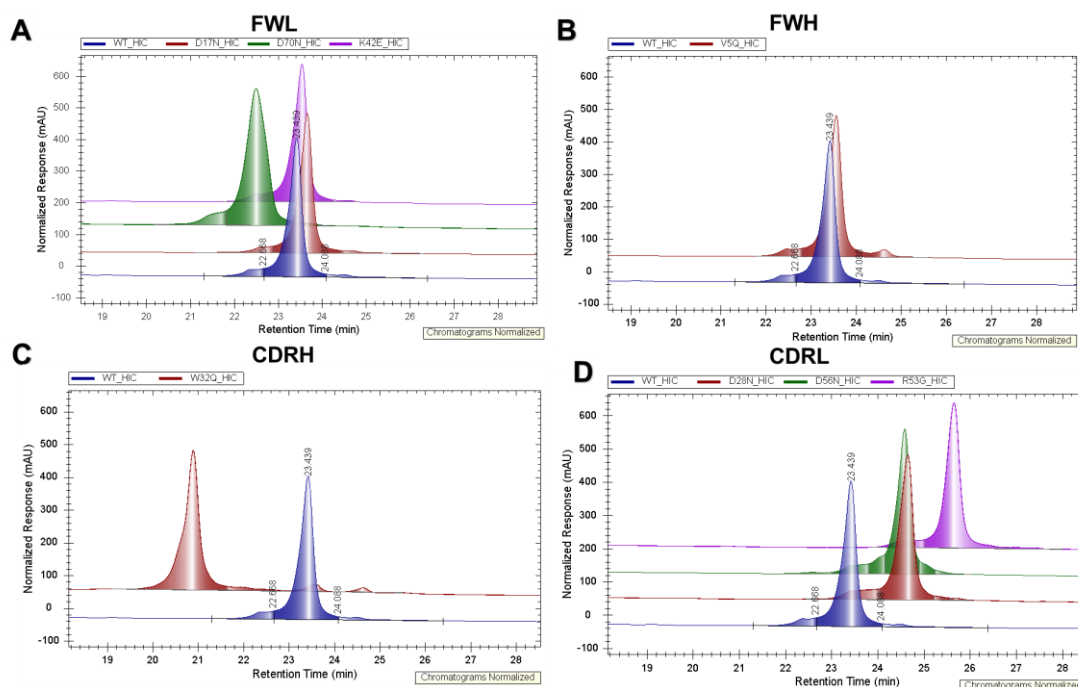


Figure 7.4 Hydrophobic interaction chromatography chromatograms for anti-IL-8 mutants.

For all chromatograms, the WT (blue) retention time was observed at ~23.5 minutes. For FWL mutants (**A**), only D70N (green) had a shift in retention time and an increase in peak breadth. A slight increase in retention time was seen for FWH (**B**) V5Q mutant (red), and a large reduction in retention time for the CDRH (**C**) W32Q mutant (red). For all CDRL mutants (**D**), an increased retention time was observed relative to WT, particularly for R53G (pink).

Binding analysis

The impact of introducing single-point mutations on the ligand binding affinity of anti-IL-8 mutant variants was measured by SPR. The mean binding affinity across all mutant variants was equivalent to the anti-IL-8 WT (3.92 nM), except for the W32Q mutant (CDRH), which had no binding for the target antigen (*i.e.* no association) (Table 7.10).

Table 7.10 Biacore analysis of binding kinetics. Wild-type and mutant anti-IL-8 binding to an IL-8 antigen was assessed with SPR.

Data in the table (all from 2 replicates) includes the binding on-rate (k_a), the binding off-rate (k_d) and the equilibrium dissociation constant (K_D), as well as the maximum response (R_{max}) and goodness of fit (Chi-squared) of the 1:1 binding model. All framework mutants and CDRL mutants showed no significant change in affinity relative to the anti-IL-8 WT. The WàQ single point mutation in the CDRH2 domain knocked out all binding affinity to IL8 antigen (K_D appears to be higher due to lack of dissociation from little association).

Abbreviations: *FWL*: light chain framework region; *FWH*: heavy chain framework region; *CDRH2*: heavy chain complementarity-determining region 2; *CDRL1*: light chain complementarity-determining region 1; *CDRL2*: light chain complementarity-determining region 2 ($N=2$).

Molecule	1:1 binding kinetics				Kinetics (χ^2)
	$k_a \times 10^5$ ($M^{-1}s^{-1}$)	$k_d \times 10^{-4}$ (s^{-1})	K_D (nM)	R_{max} (RU)	
WT	2.53 (± 0.13)	9.90 (± 0.04)	3.92 (± 0.18)	23.35 (± 0.78)	0.94 (± 0.01)
D17N (FWL)	2.89 (± 0.01)	9.78 (± 0.03)	3.39 (± 0.01)	27.75 (± 0.07)	1.48 (± 0.07)
D70N (FWL)	2.57 (± 0.13)	0.102 (± 0.14)	3.98 (± 0.26)	20.9 (± 0.71)	0.038 (± 0.04)
K42E (FWL)	2.49 (± 0.04)	9.54 (± 0.06)	3.84 (± 0.08)	19.65 (± 0.07)	0.72 (± 0.01)
V5Q (FWH)	2.13 (± 0.01)	9.82 (± 0.03)	4.62 (± 0.03)	24.55 (± 0.07)	2.01 (± 0.08)
W32Q (CDRH2)	28.6 (± 6.01)	0.37 (± 0.05)	0.01 (± 0.02)	0.45 (± 0.07)	0.06 (± 0.00)
D28N (CDRL1)	2.60 (± 0.01)	11.00 (± 0.01)	4.24 (± 0.06)	26.1 (± 0.14)	1.19 (± 0.07)
D56N (CDRL2)	3.12 (± 0.01)	10.5 (± 0.01)	3.38 (± 0.11)	29.1 (± 0.42)	1.74 (± 0.04)
R53G (CDRL2)	3.07 (± 0.01)	11.5 (± 1.63)	4.17 (± 0.16)	13.5 (± 0.28)	1.96 (± 0.04)

Differential Scanning Fluorimetry (DSF)

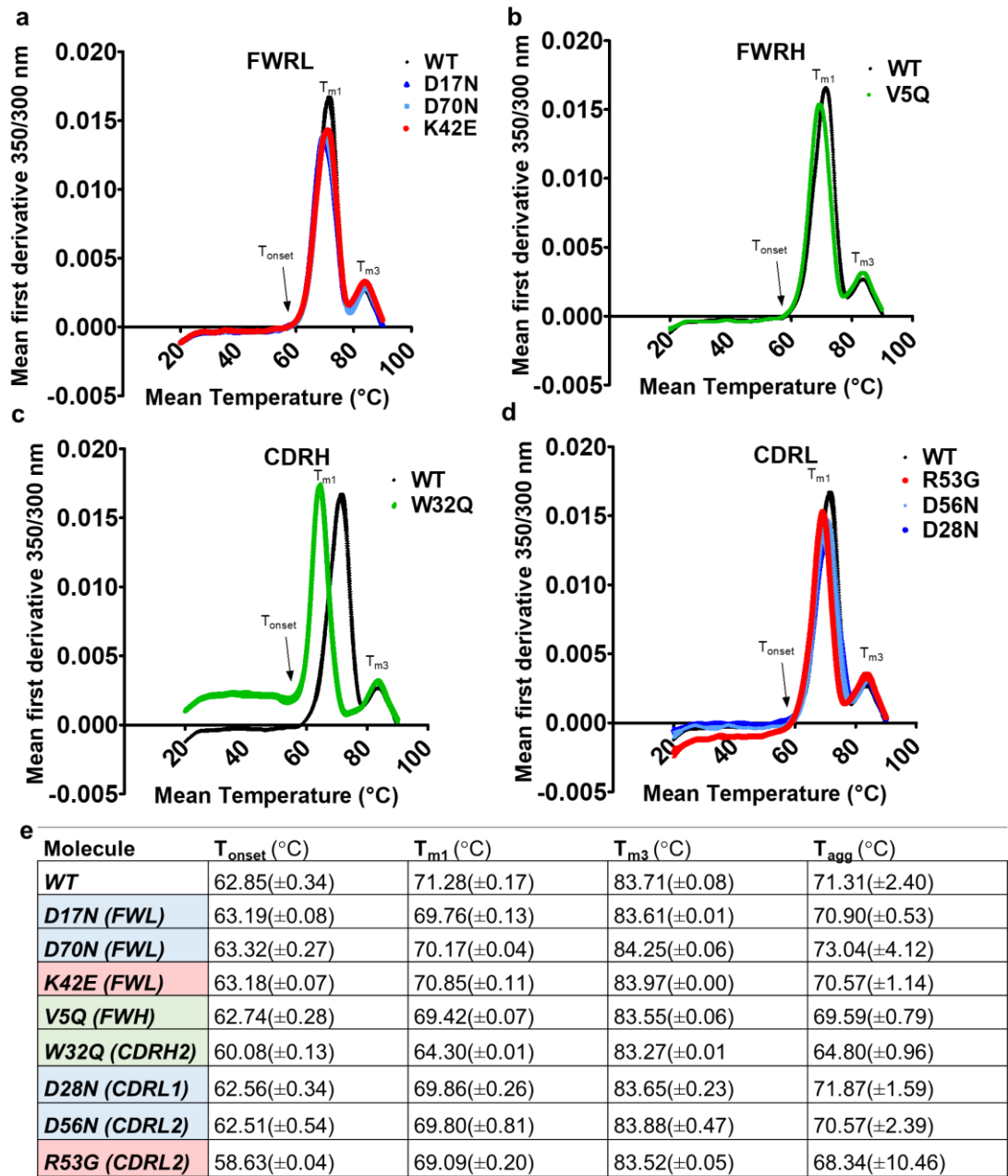


Figure 7.5 Thermal unfolding profiles for all anti-IL-8 mutant panel and wild-type.

a-d, The first derivative of 350nm/330nm ratio was used to identify melting temperature peaks. The onset of unfolding (T_{onset}) was identified at the inflection point of the first peak.

Only T_{m1} and T_{m3} peaks were detected for all molecules. **e**, Summary table of unfolding temperatures. T_{agg} (onset of aggregation) was calculated from the first derivative of scattering intensity profiles. ± standard deviation shown, N=2

Dynamic light scattering (DLS)

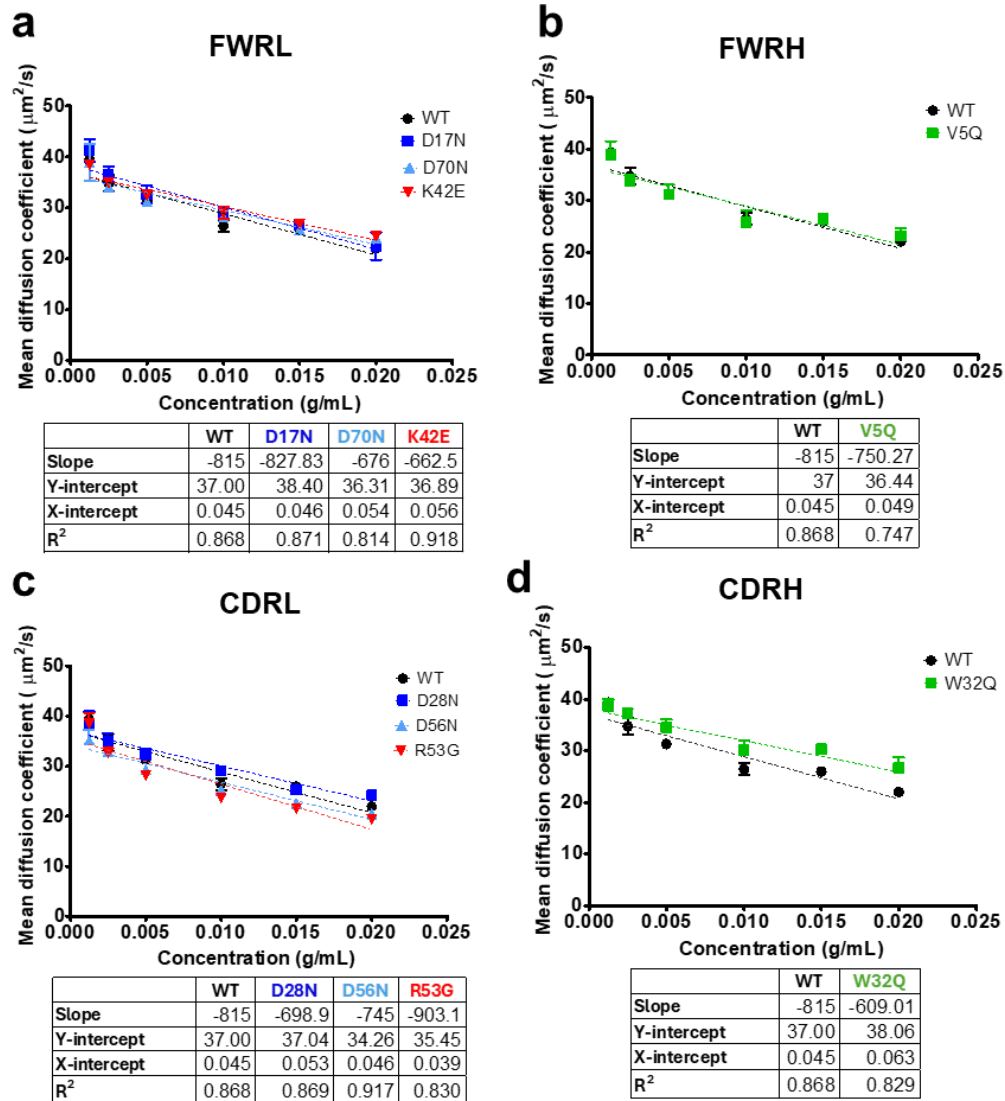


Figure 7.6 Diffusion coefficients for each expressed anti-IL-8 mutant and WT over a dilute concentration range (1-20 mg/mL), fitted with linear regression.

Goodness of fit R-squared values are reported along with linear equations used to calculate self-interaction K_D values by dividing the slope over the Y intercept. Error bars for each measurement represent standard deviation.

7.3. Molecular dynamics- an alternative mutagenesis strategy

The homology model of the full IgG1 structure was solvated in a periodic box of water with no counter-ions in MOE (version 2020.0901, CCG, Canada). A custom arginine solvent was added at a concentration of 0.5M using the BioMoe module (version 2020.0901, CCG, Canada). Then, the system was solvated with sodium chloride to neutralise the environment. Molecular dynamics simulations were performed using the NAMD program, available through the MOE software. The Amber10:EHT (combination of Amber10³⁷⁸ and EHT³⁷⁹ provided in MOE) forcefield was used to define the equations for bonding and non-bonding interactions, angles, dihedrals and impropers. The simulation had a time step of 0.002ps, was sampled every 10ps and a checkpoint at every 500ps.

Table 7.11 Details for segments specified in molecular dynamics simulation set-up.

Segment	Time (picoseconds)	Temperature (Kelvin)	System pressure (kPa)	Tether Restraint (Å)
Minimisation	10	0	-	-
Heat	100	10, 300	-	0.5, 100
Production simulation	1000	300	100	-

A bash shell script was generated to analyse the number and residues of IgG1 in contact with the free Arginine through the resulting trajectory. Contact was defined as being at least within 5 Å of the structure.

Tilegenova *et al.*²³² used molecular dynamics to identify the residues of their IgG structures that come into contact (within 5 Å) of solvated free arginine. Here, the same approach was employed to see which residues have the most contacts (**Figure 7.7**), but also analysed the average strength of these interactions (**Figure 7.8** and **Figure 7.9**).

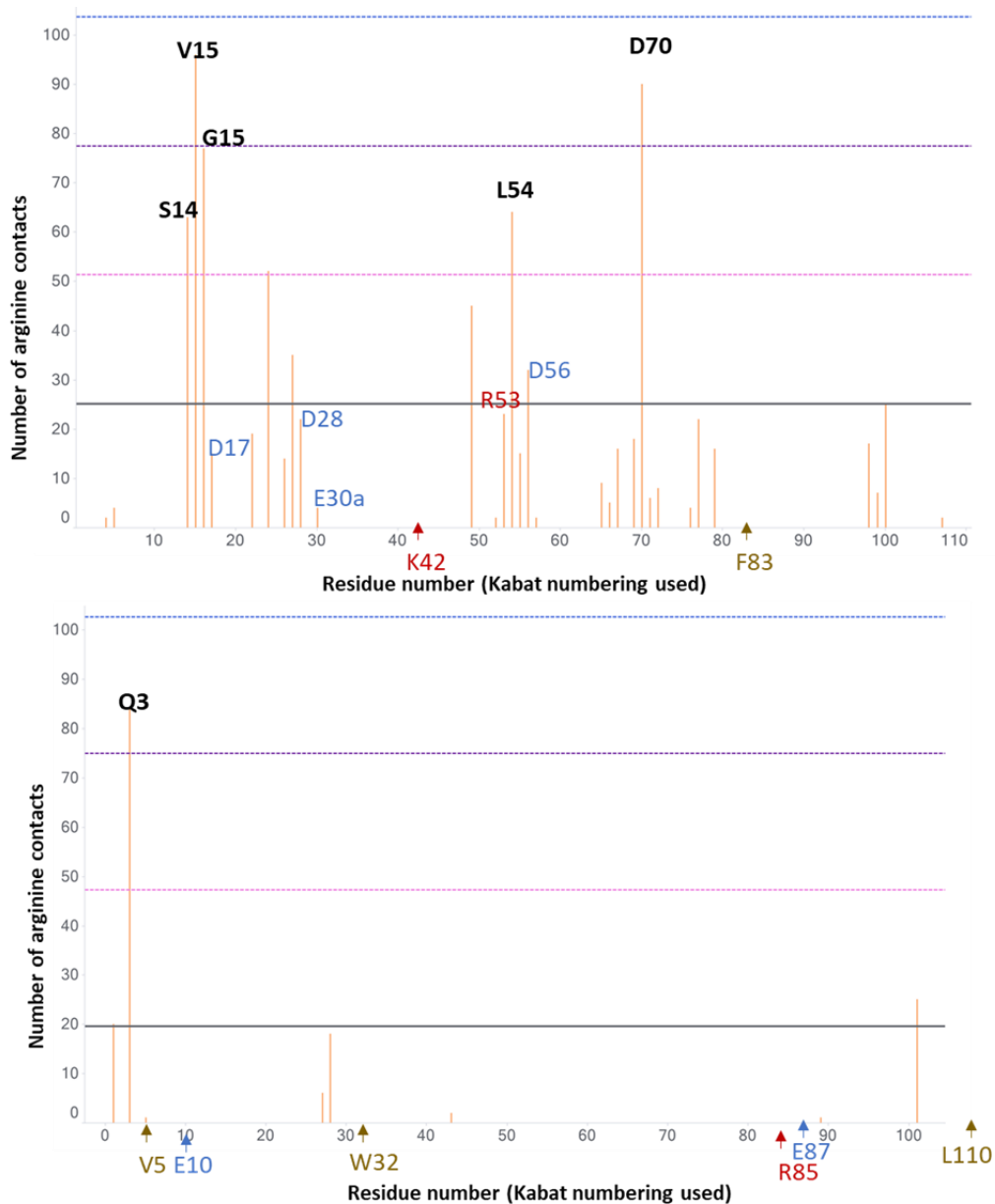


Figure 7.7 Number of arginine contacts summed per residue for the light chain Fv (A) and heavy chain Fv (B), ordered by residue number.

The average (dark grey horizontal line), +1 SD (pink dotted horizontal line), +2 SD (purple dotted horizontal line) and +3 SD (blue dotted horizontal line) are depicted. Residues with > 1 SD are labelled in black font. Residues selected in chapter 2 from previous *in silico* work to be mutated are also labelled with hydrophobic residues (orange), the positive residues (red) and negative residues (blue).

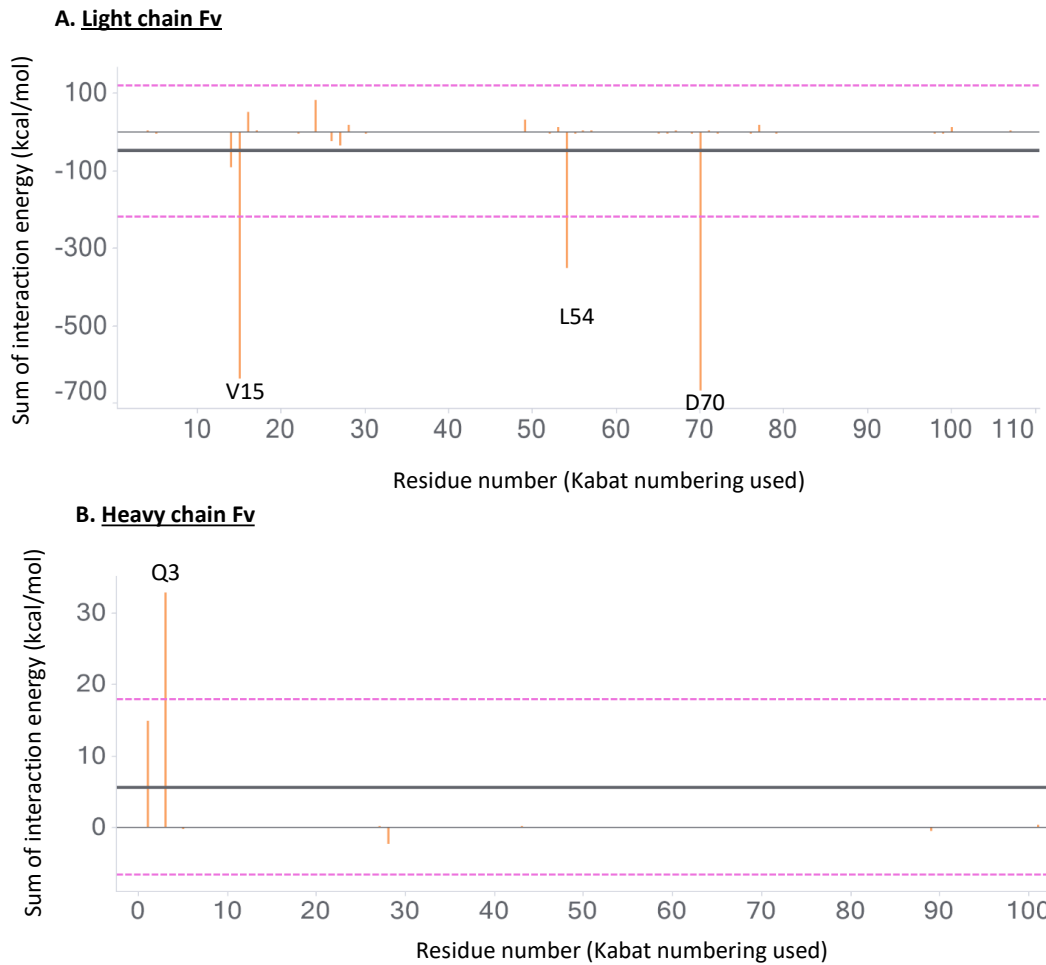


Figure 7.8 Summed interaction energies for each residue of the light chain Fv (A) and heavy chain Fv (B).

This is indicative of the strength of interaction to arginine molecules. The average (dark grey horizontal line) and ± 1 SD (pink dotted horizontal line) are shown. Residues with $> \pm 1$ SD are labelled. In the light chain, V15, L54 and D70 were detected to have the strongest negative interaction energies that surpassed the standard deviation. In the heavy chain, only Q3 had an interaction energy that was greater than 1SD.

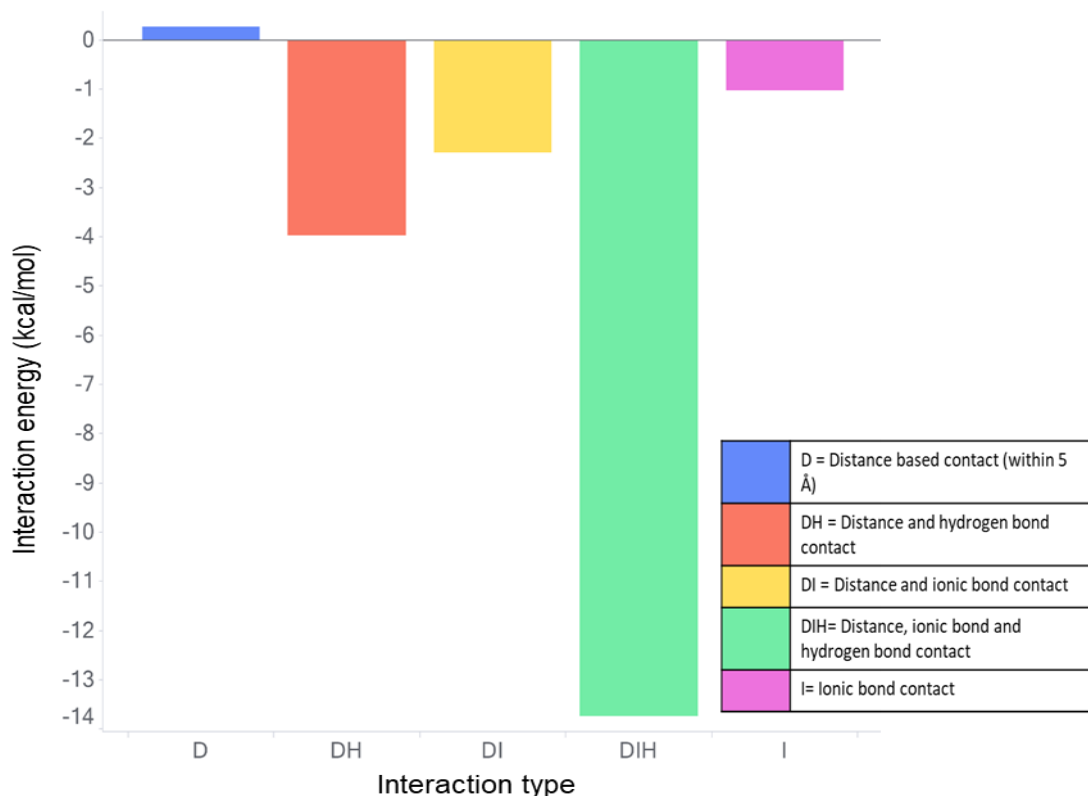


Figure 7.9 Average interaction energies per interaction type for all contacts assessed in the trajectory (variable and constant regions considered).

Interactions that are a combination of distance-based, hydrogen bonding and ionic bonding are seen to have the average most negative interaction energy. Those which are just distance-based interactions have a slightly positive interaction energy.

In the light chain Fv, S14, V15, G16, L54 and D70 had the most interactions with the solvated arginine. In the heavy chain, just Q3 had an above average contact count with solvated arginine. Considering interaction energies, V15, L54 and D70 had the strongest interactions in the light chain. This is due to increased hydrogen bonding with all residues and ionic bonding detected for D70 with arginine. Some hydrogen bonding was also detected with the Q3 residue in the heavy chain and arginine. The more negative the interaction energy, the more indicative of hydrogen bonding interactions and ionic interactions. This is due to the decrease in potential energy upon bond formation. **Figure 7.9** demonstrates the average interaction energies per type of interaction detected in this simulation. Q3 had a positive interaction energy from the high frequency of just distance based interactions.

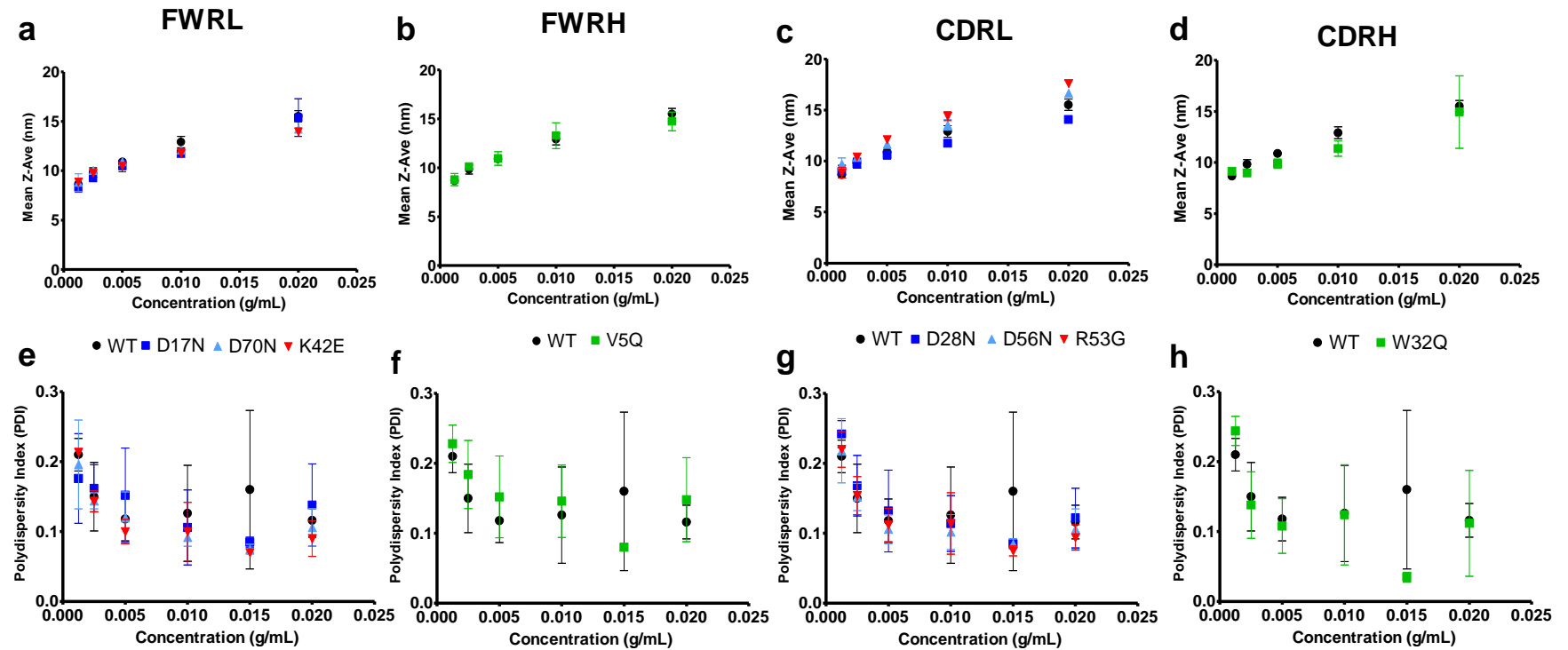


Figure 7.10 Mean hydrodynamic diameters (Z-ave) and polydispersity indices for anti-IL-8 WT and mutant panel.

These were measured over a dilute concentration range (1-20 mg/mL), derived from dynamic light scattering measurements. Error bars represent standard deviations, N=3.

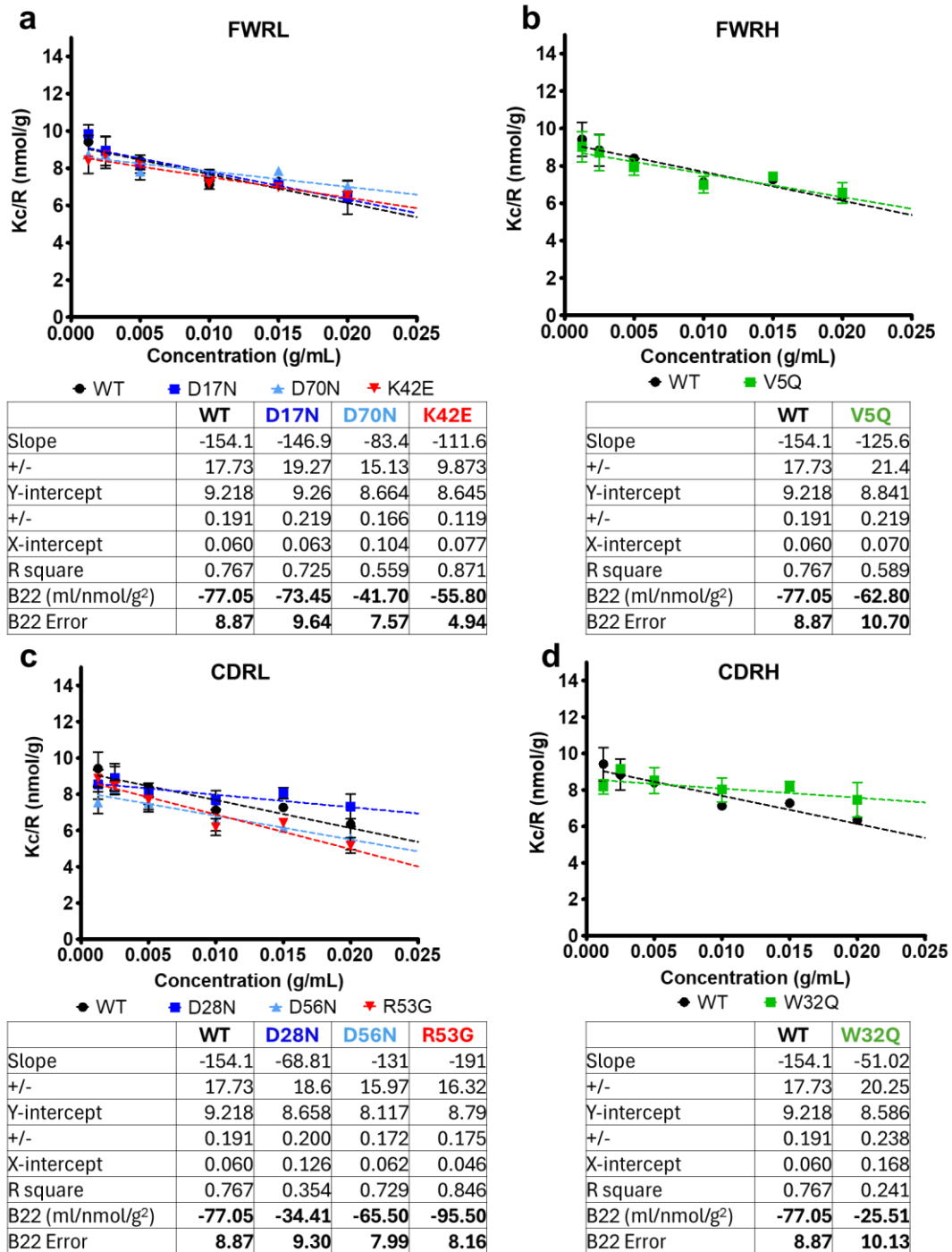


Figure 7.11 The second virial coefficient, B_{22} (mL/nmol/g²) for anti-IL-8 molecules.

B_{22} was derived from dynamic light scattering using the slope of Kc/R over the 1-20 mg/mL concentration range, where K is the optical constant, c is the concentration (g/mL), and R is the Rayleigh ratio. Error bars represent standard deviations of measurements ($N=3$). Linear fits are plotted, with the equation parameters as well as R^2 goodness-of-fit values.

8. Appendix 2

8.1. Free kappa light chain abundance

Protein L chromatography with Capto L affinity resin (Cytiva, Danaher, USA) was used as a capture step for all anti-IL-8 molecules. Due to exclusive light chain affinity, a high abundance of free kappa light chain fragment was observed in Protein L eluate which was confirmed and quantified by sodium dodecyl sulfate-polyacrylamide gel electrophoresis (SDS-PAGE) and analytical size-exclusion chromatography (aSEC). Wild-type molecule protein L eluate composition is seen in Figure 8.1 alongside eluate derived from a small-scale protein A chromatography run (MabSelect Prisma resin, Cytiva, Danaher, USA) as well as a NIST mAb (humanised IgG1k) standard (reference material 8671, National Institute of Standards and Technology, MD, USA).

For SDS-PAGE analysis, samples were diluted to 1mg/mL in phosphate buffered saline containing 0.05% Tween 20 (PBS-T). 4X NuPAGE™ LDS sample buffer (Invitrogen, MA, USA) was pre-heated to 70 °C. 12µL of each sample was added to a master mix of either 15µL pre-heated sample buffer with 3µL water (non-reducing), or 15µL pre-heated sample buffer with 3µL 10X Novex NuPAGE™ reducing agent (Invitrogen, MA, USA) (reducing). Samples were then heated to 70 °C for 10 minutes before centrifuging at 10,000 rpm for 90 s. 25µL of each sample was pipetted into respective lanes of a NuPAGE Bis-Tris Gel (Invitrogen, MA, USA) which was inserted into a XCell SureLock tank (Invitrogen, MA, USA). A Precision Plus Protein™ pre-stained molecular weight ladder (Bio-Rad, CA, USA) bracketed sample lanes. 1X SDS running buffer was prepared from NuPAGE™ MOPS SDS Running Buffer (20X) (Invitrogen, MA, USA) and filled the tank before running the electrophoresis for 1 hour at a constant voltage 150 V at 200 mA. Finally, SimplyBlue™ SafeStain (Invitrogen, MA, USA) was used to incubate the gel overnight, before de-staining with water and band analysis using Image Lab software (version 6.1, Bio-Rad, CA, USA).

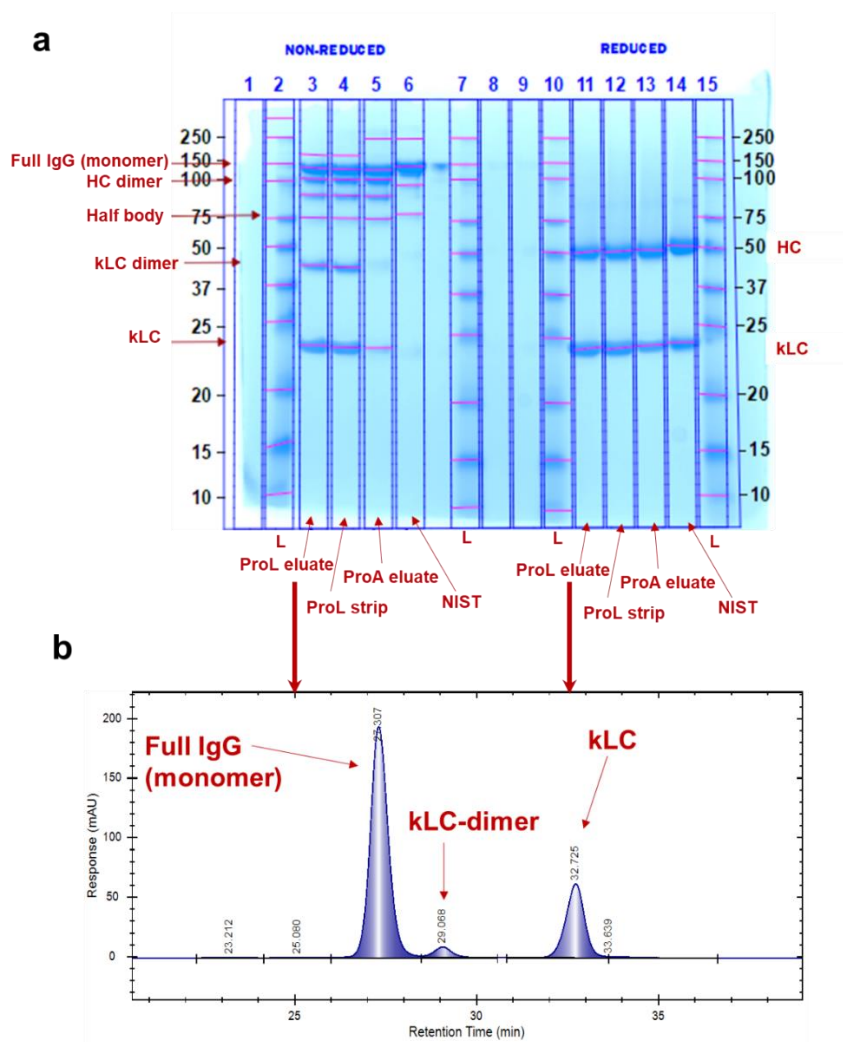


Figure 8.1 A high abundance of free kappa light chain (kLC) was observed in the Protein L eluates of anti-IL-8 molecules.

a, SDS-PAGE of WT molecule eluates in non-reducing (left) and reducing (right) conditions. The presence of kLC was confirmed in the protein L eluate of WT molecule with a large band ~22 kDa (lane 3). A low pH strip step after elution saw a similar kLC abundance (lane 4). Protein A chromatography was also performed and free kLC in the culture was not co-eluted due to Fc capture (lane 5). NIST mAb standards were used (lanes 6 and 14). Ladders in lanes 2, 7, 10 and 15 mark molecular weights (kDa). b, analytical size-exclusion chromatography chromatogram for WT protein L eluate shows presence of low molecular weight species which can be attributed to kLC dimer (29 min retention time) and kLC (32.7 min retention time). Abbreviations: *L*: molecular weight ladder, *ProL*: Protein L, *ProA*: Protein A, *kLC*: kappa light chain, *HC*: heavy chain

8.2. Clearance of free kappa light chain via cation exchange chromatography

Table 8.1 Cation exchange chromatography in bind-elute mode was deployed, screening at multiple pH conditions, for clearance of free kappa light chain (kLC).

Analytical size-exclusion chromatography (aSEC) was used to characterise high molecular weight species (HMwS), low molecular weight species (LMwS) and monomeric purity of pooled flow-through and eluate. Eluate yields and the proportional monomer yields were reported. 4.67 mL columns were used for initial screenings and then scaled up to either 123 or 287 mL columns for bulk processing. In some instances, pH selected from small-scale screening did not translate to sufficient kLC clearance or had monomer loss in the flow through upon scale-up. Therefore, flow-through material was reprocessed at a lower pH. Charge predictions are shown per operation pH, computed from kLC, Fv and full IgG homology constructs. Finally the difference between full IgG net charge and kLC charge was computed.

Molecule	pH	ProL Eluate			Flow-through			Eluate			Eluate % Yield	Mon %Yield	Column volume (mL)	kLC predictions			Fv predictions			Full IgG predictions			Δ charge full IgG-kLC
		% HMwS	% Mon	% LMwS	% HMwS	% Mon	% LMwS	% HMwS	% Mon	% LMwS				net charge	pl_seq	pl_3D	net charge	pl_seq	pl_3D	net charge	pl_seq	pl_3D	
WT	5	0	63.68	36.32	0	5.63	94.37	0.43	99.04	0.54	40.32	37.10	4.67	-0.53			0.76			31.03			31.56
	6	0	63.34	36.66	0	42.18	57.82	0	58.65	41.35	47.25	25.90	4.67	-0.93	4.8	4.6	0.25	6.4	6.2	26.12	6.8	8	27.05
	7	0	63.24	36.76	0	50.03	49.97	0	83.16	16.84	29.59	23.00	4.67	-1.66			-0.05			18.35			20.01
D17N	6	0.18	67.17	32.65	0	5.7	93.9	0.23	99.13	0.65	50.00	49.60	4.67	0.01	5.6	5.5	0.82	7.9	7.6	26.07	6.8	8.3	26.06
	6	0.538	67.04	32.42	0	7.73	92.27	0.36	99.2	0.44	27.40	27.20	4.67	0.41			0.62			23.39			22.98
D70N	6	0.617	87.7	11.69	0	6	94.1	0.38	99.62	0	69.10	68.90	4.67	0	5.6	5.5	0.82	6.7	7.6	26.44	6.8	8.2	26.44
	6	0.507	87.66	11.83	0.21	81.22	18.57	0.11	99.88	0.01	17.30	17.30	4.67	-0.32			0.63			23.92			24.24
K42E	6	0.082	76.11	23.81	0.1	50.6	49.4	0.27	98.98	0.75	35.70	35.30	4.67	-2.83	4.3	3.9	-1.61	5.6	4.6	20.99	6.7	7.8	23.82
	6	0.191	76.05	23.76	0.22	54.59	45.2	0.01	99.54	0.45	7.40	7.40	4.67	-3.16			-1.81			18.08			21.24
V5Q	6	0.221	52.07	47.71	0	1.88	98.12	0.65	98.29	1.06	32.40	31.90	4.67	-1.23	4.84	4.6	0.05	5.42	6.2	23.4	6.79	8.18	24.63

W32Q	6	0.671	53.26	46.07	0	3.81	96.39	5.1	94.9	0	30.80	29.30	4.67	-1.22	4.84	4.6	0.05	6.42	6.2	21.68	6.79	8.15	22.9
D28N	6	0	62.38	37.62	0	12.75	87.25	0.88	98.13	0.99	30.00	29.40	4.67	-0.34	5.58	5.35	0.62	6.68	7.6	23.38	6.84	8.21	23.72
D56N	6	0	61.32	38.69	0	0	100.01	0.34	95.92	3.74	34.60	33.20	4.67	-0.32	5.58	5.5	0.63	6.68	7.6	23.6	6.84	8.24	23.92
R53G	5	0	60.68	39.32	0	7.49	92.51	1.49	97.43	1.08	45.50	44.30	4.67	-1.45	4.5	4.2	-0.11	6.1	4.9	28.57	6.7	7.9	30.02
	6	0.572	66.35	33.08	0	29	71	0.18	98.85	0.97	39.80	39.30	4.67	-1.85			-0.63			24.18			26.03
	6	0.178	66.75	33.07	0.27	54.45	45.27	0.2	99.13	0.68	6.60	6.50	4.67	-2.18			-0.83			20.69			22.87
WT	5	0	63.68	36.32	0	7.4	92.6	0.66	98.71	0.64	37.20	36.70	287	-0.53	4.84	4.64	0.76	6.42	6.2	31.03	6.79	7.96	31.56
D17N	6	0.085	68.07	31.85	0	7.22	92.78	0.25	99.75	0	60.00	59.90	287	0.01	5.58	5.52	0.82	7.9	7.6	26.07	6.84	8.27	26.06
D70N	6	0.354	84.67	14.08	0	5.84	94.16	2.54	96.45	1.01	74.90	72.20	123	0	5.58	5.5	0.82	6.68	7.6	26.44	6.84	8.22	26.44
K42E	5	0.077	76.24	23.68	0	2.45	97.54	1.75	94.71	3.55	44.20	41.80	287	-2.41	4.32	3.88	-1.09	5.62	4.6	25.17	6.68	7.75	27.58
V5Q	6	0.381	63.31	36.31	0	43.71	56.29	0.74	99.18	0.08	28.70	28.50	287	-1.23	4.8	4.6	4.6	5.4	6.2	23.4	6.8	8.2	24.63
	5	0.093	49.42	50.49	0	11.44	88.56	0.11	99.8	0.08	20.30	20.20	287	-0.5			0.76		6.2	30.31			30.81
W32Q	6	0.919	50.61	48.48	0.03	31.92	68.05	1.43	83.23	15.35	24.40	20.30	287	-1.22	4.8	4.6	0.05	6.4	6.2	21.68	6.8	8.2	22.9
	5	0.14	39.09	60.77	0	7.3	92.7	1.46	98.48	0.07	26.60	26.20	287	-0.49			0.79		6.2	28.12			28.61
D28N	6	0.215	58.19	51.6	0	38.2	61.8	0.64	99.2	0.16	25.80	25.60	287	-0.34	5.6	5.4	0.62	6.7	7.6	23.38	6.8	8.2	23.72
	5	0.045	52.12	47.83	0	7.41	92.59	0.43	99.5	0.07	43.00	42.80	287	0.18			1.12		7.6	29.7			29.52
D56N	6	0.591	57.44	41.97	0	7.81	92.19	0.45	99.26	0.29	32.10	31.90	287	-0.32	5.58	5.5	0.63	6.68	7.6	23.6	6.84	8.24	23.92
R53G	5	0.364	66.73	32.91	0	4.51	95.49	0.6	98.13	1.27	34.40	33.80	287	-1.45	4.48	4.15	-0.11	6.07	4.9	28.57	6.73	7.94	30.02

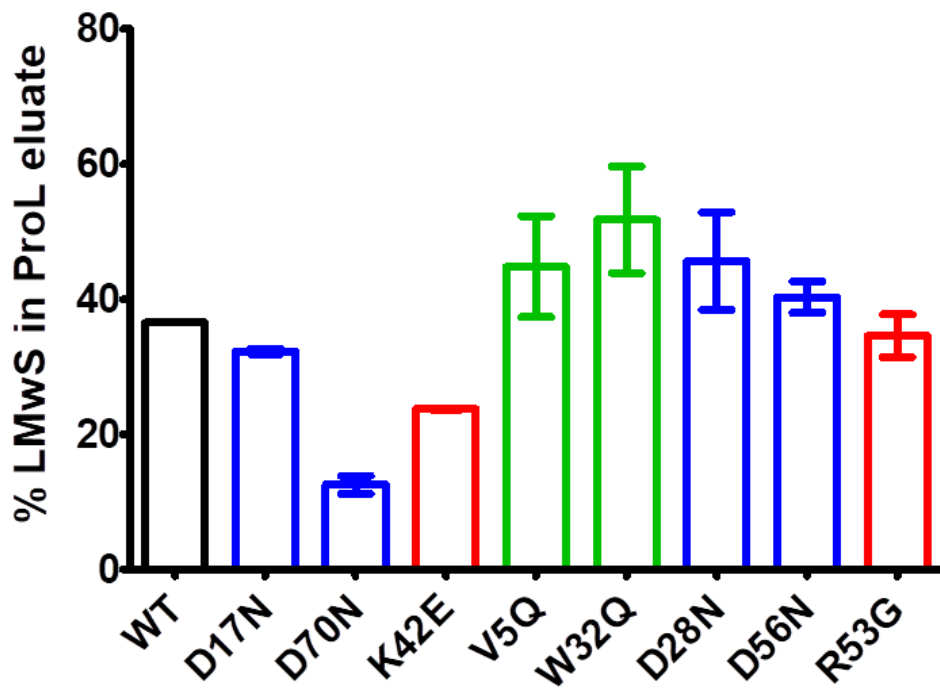


Figure 8.2: Mean % low molecular weight species from protein L eluates per anti-IL8 IgG1 molecule.

Error bars represent standard deviation, N=2.

8.3. Gel point calculation for anti-IL-8 molecule panel

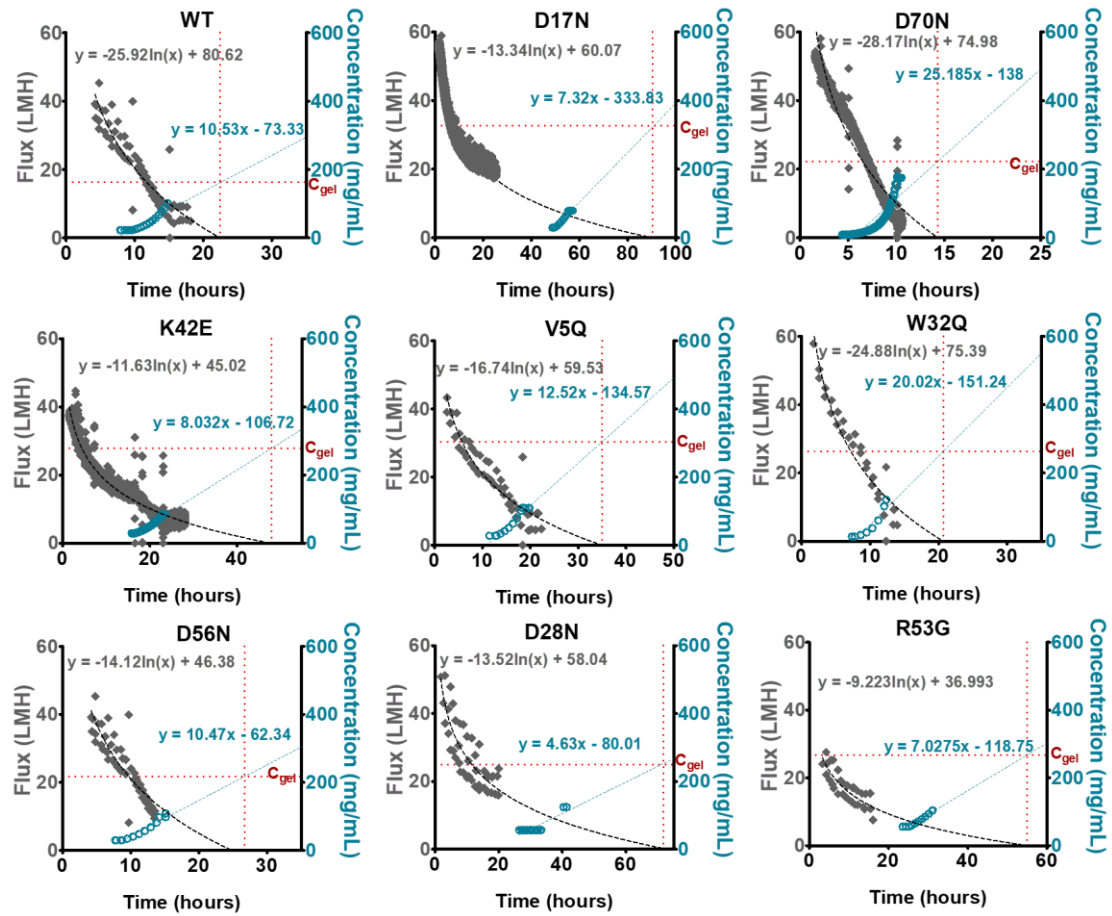


Figure 8.3 Gel points for anti-IL-8 mAb molecules were calculated from logarithmic extrapolation of flux during the first concentration phase (UF1) in small-scale TFF. Retentate concentrations were estimated from retentate vessel weight changes during UF1. Linear extrapolation of concentrations were used to calculate the concentration at which the flux reached zero.

8.4. Opacity/turbidity observed during concentration of anti-IL-8 molecules

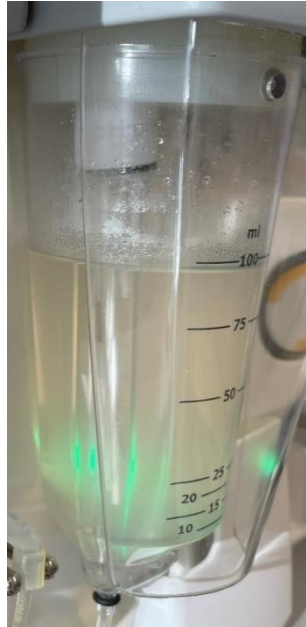


Figure 8.4: Opacity observed during TFF for all anti-IL-8 molecules.

Here, D28N retentate was showed high turbidity during UF1 stage concentration.

9. Appendix 3

9.1. Homology modelling of IgG3

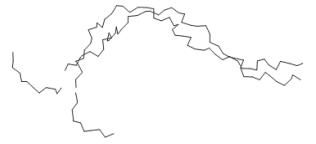
Table 9.1 IgG3 hinge was designed based off copied sequence of mouse IgG2A hinge (pdb 1IGT).

Residue sequence of 1IGT was used to aid construction of the IgG3 hinge. Cysteines are in highlighted in bold. The first 6 residues (yellow) contain two of the cysteines used to construct the IgG3 hinge in positions 2 and 5. To align the third cysteine for the anti-IL-8 IgG3 hinge (position 11), the full 1IGT sequence was copied after the 6 residues (blue). This module was copied three more times to generate the four modules of the IgG3 hinge.

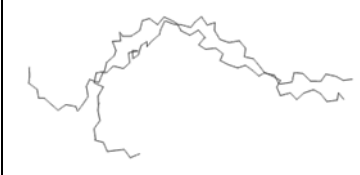
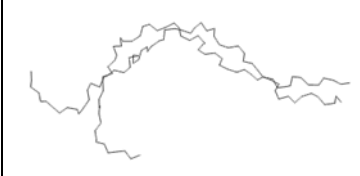
1IGT	1	2	3	4	5	6	7	8	9						
	P	C	P	P	C	K	C	P	A						
anti-IL-8 IgG3	1	2	3	4	5	6	7	8	9	10	11	12	13	14	15
hinge module 1	P	C	P	P	C	K	P	C	P	P	C	K	C	P	A

Table 9.2 Hinge homology models for anti-IL-8 IgG3.

10 models were generated from the homology modeller tool in MOE (version 2020.0901) using the modified 1IGT hinge template (Table 9.1). Normalisation was performed for each quality parameter; normalisations to 1 used the minimum scores for RMSDs, minimum contact energy, highest packing score, minimum GB/VI interaction energies, minimum total potential energy (U), minimum solvation, electrostatic and van der Waal energies and minimum clashes and outliers. Model #2 was selected due to the lowest RMSD to Mean. This model also had the best (lowest) total normalised score. RMSD to mean: heavy atom root mean square deviation to the average position of intermediate models, CA: alpha-carbon, GB/VI: Coulomb and Generalized Born interaction energies, U: total potential energy, E sol: solvation energy of the model, E ele: electrostatic energy of the model, E vdW: van der Waals energy of the model, BB; backbone

Model #	RMSD to Mean	CA RMSD to Mean	Contact Energy	Packing Score	GB/VI	U	E sol	E ele	E vdW	E bond	Atom Clashes	BB Bond Outliers	BB Angle Outliers	BB Torsion Outliers	Rotamer Outliers	Hinge model	Total Normalised Score
1	0.63	0.47	-21.97	1.98	-4358.36	-619.12	-1458.85	-2062.63	-89.76	1533.2	93	10	21	20	1		7.91
2	0.58	0.42	-22.82	2.12	-4047.83	686.84	-2291.7	-1042.57	-36.16	1765.6	7	9	14	33	0		5.48

3	0.65	0.47	-25.34	2.09	-4039.06	731.05	-2192.11	-1018.76	-14.76	1764.6	6	11	19	40	0		8.80
4	0.59	0.42	-21.46	2.16	-4036.56	688.62	-2246.02	-1036.27	-36.85	1761.7	7	7	17	27	0		5.56
5	0.619	0.47	-20.32	2.11	-4033.33	805.83	-2405.26	-931.9	-42.82	1780.6	7	11	16	29	0		7.87
6	0.6	0.44	-24.28	2.05	-4032.27	796.83	-2184.16	-1008.91	1.019	1804.7	11	14	19	28	0		7.99
7	0.58	0.42	-26.8	2.1	-4004.76	1058.4 6	-2466.78	-864.31	29.79	1893.0	10	12	20	32	0		7.50

8	0.63	0.43	-23.3	2.01	-3993.05	871.17	-2396.08	-889.87	-13.97	1775.0	9	10	14	33	0		7.48
9	0.58	0.42	-25.07	2.18	-3977.17	1012.47	-2545.39	-802.08	-14.35	1828.9	14	9	14	31	0		5.56
10	0.616	0.45	-20.77	2.16	-3967.21	1061.24	-2467.2	-815.9	58.66	1818.5	10	10	15	39	0		8.61

Additional patch analysis and physicochemical descriptors

Table 9.3 Additional patch and physicochemical descriptors applied to anti-IL-8 IgG1 and IgG3 homology constructs.

Hinge_res_ASA	The summed contribution from each residue in the hinge region to the accessible surface area in Å ² . This was calculated from manually summing Res_ASA scores from residues in the hinge region.
Hinge_res_hyd	The summed hydrophobic contribution from each residue in the hinge to hydrophobic patch area in Å ² . This was calculated from manually summing Res_hyd scores from residues in the hinge region.
Hinge_res_pos	The summed positive charge contribution from each residue in the hinge to positive patch area in Å ² . This was calculated from manually summing Res_pos scores from residues in the hinge region.
Hinge_res_neg	The summed negative charge contribution from each residue in the hinge to negative patch area in Å ² . This was calculated from manually summing Res_neg scores from residues in the hinge region.
Hinge_res_ASA contribution (%) to res_ASA	$\frac{\text{Hinge_res_ASA}}{\text{Res_ASA}} * 100$
Hinge_res_hyd contribution (%) to res_hyd	$\frac{\text{Hinge_res_hyd}}{\text{Res_hyd}} * 100$
Hinge_res_pos contribution (%) to res_pos	$\frac{\text{Hinge_res_pos}}{\text{Res_pos}} * 100$
Hinge_res_neg contribution (%) to res_neg	$\frac{\text{Hinge_res_neg}}{\text{Res_neg}} * 100$
BSA	The buried surface area (BSA) of all chains in Å ² . This was calculated through the descriptors function in the BioMOE module in MOE 2020. Default parameters were used with no sampling. This was calculated off This was calculated at default values of pH 7.4, temperature of 300K and a salt concentration of 0.1M. ³⁷⁴
BSA_HC	The buried surface area (BSA) between the heavy and light chains in Å ² . This was calculated through the descriptors function in the BioMOE module in MOE 2020. Default parameters were used with no sampling. This was calculated off This was calculated at default values of pH 7.4, temperature of 300K and a salt concentration of 0.1M. ³⁷⁴

Patch analysis of mAb 1 IgG1 and IgG3

Table 9.4 Analysis of positive, negative and hydrophobic surface patches for anti-IL-8 IgG1 and IgG3 homology constructs.

Molecule	patch_hyd (Å ²)	patch_hyd %	patch_hyd_n	patch_pos %	patch_pos (Å ²)	patch_pos_n	patch_neg %	patch_neg (Å ²)	patch_neg_n	patch_ion (Å ²)	patch_ion_n	patch_cdr_hyd (Å ²)	patch_cdr_hyd_n	patch_cdr_pos (Å ²)	patch_cdr_pos_n	patch_cdr_neg (Å ²)	patch_cdr_neg_n	patch_cdr_ion (Å ²)	patch_cdr_ion_n	Asa_hyd (Å ²)	Res_ASA (Å ²)	Res_hyd (Å ²)	Res_pos (Å ²)	Res_neg (Å ²)
IgG1	3790	42%	65	33%	2940	65	25%	2250	40	5190	105	540	4	500	13	570	8	1070	21	33365.7	3747	57905	2924	2188
IgG3	5140	37%	82	31%	4240	81	32%	4450	72	8690	153	560	4	460	12	530	9	990	21	40569.1	4450	70184	4232	4434

Table 9.5 Analysis of positive, negative and hydrophobic surface patches for the hinge regions of anti-IL-8 IgG1 and IgG3 homology constructs.

Molecule	Hinge_res_ASA (Å ²)	Hinge_res_hyd (Å ²)	Hinge_res_pos (Å ²)	Hinge_res_neg (Å ²)	Hinge_res_ASA contribution to res_ASA	Hinge_res_hyd contribution to res_hyd	Hinge_res_pos contribution to res_pos	Hinge_res_neg contribution to res_neg
IgG1	958	50	35	77	2%	1%	1%	4%
IgG3	5902	456	375	493	8%	9%	9%	11%

Physicochemical descriptors for anti-IL-8 IgG1 and IgG3

Table 9.6 Sequence and structure based descriptors computed for anti-IL-8 IgG1 and IgG3 homology constructs.

Molecule	pI_seq	pI_3 D	Net Charge	Dipole Moment	Hydrop hobicity Moment	Zeta Potentia I	Hydrop hobic imbalan ce	Hydrop hobic index	Dipole moment / hyd moment ratio	Ionic/ hyd patch area ratio	BSA	BSA_H C	BSA_LC _HC
IgG1	6.67	7.97	22.68	704.98	4353.5	15.26	0.71	1.00	0.16	1.37	5160.49	1636.04	3473.99
IgG3	6.54	7.84	21	2788.2	7340.2	6.21	1.08	0.94	0.38	1.69	5744.45	2030.33	3714.12
IgG3 Fab	6.58	8.06	5.96	724.71	918.1	9.01	-	1.08	0.79	1.38	1728.93	-	1728.93
IgG3 hinge	6.55	7.34	1.35	482.48	344.4	2.12	-	0.35	1.40	2.02	1090.92	-	-
IgG3 Fc	6.57	7.28	5.82	578.76	1146.12	7.11	-	0.92	0.50	1.97	932.22	932.22	-

9.2. Biophysical Characterisation

9.2.1 Analysis of identity by mass spectrometry

Table 9.7 Verification of anti-IL-8 IgG1 and IgG3 identity by peptide fragmentations.

Trypsin digest of this peptide following the same methodology showed coverage of this missing peptide, ensuring full identity verification. For post-translational modifications (PTMs), the % detection was relative to only peptides with expected full enzyme cleavage. PTMs with relative detection were noted. HC: Heavy chain; LC: Light chain; mwt: molecular weight; PTM: post-translational modification

Molecule	LC coverage (%)	HC coverage (%)	LC mwt (Da)	HC mwt (Da)	LC PTMs	HC PTMs
IgG1	97.66	96.66	23433.83	49204.09	M4 oxidation (0.4%)	M81 oxidation (0.2%), N317 deamidation (0.6%), M254 oxidation (4.2%), N363 deamidation (0.4%), M430 oxidation (1.8%)
IgG3	97.66	98.79	23433.83	54375.06	M4 oxidation (0.6%), Q147 pyroglutamate (29.6%)	M81 oxidation (0.6%), M301 oxidation (6.9%), N263 deamidation (0.5%), N410 deamidation (0.5%), M446 oxidation (1.4%), N470 deamidation (0.2%), S473 methylation (1.7%), M477 oxidation (2.9%)

9.2.2 Scattering intensity profiles from nano-differential scanning fluorimetry (nano-DSF) of anti-IL-8 IgG1 and IgG3

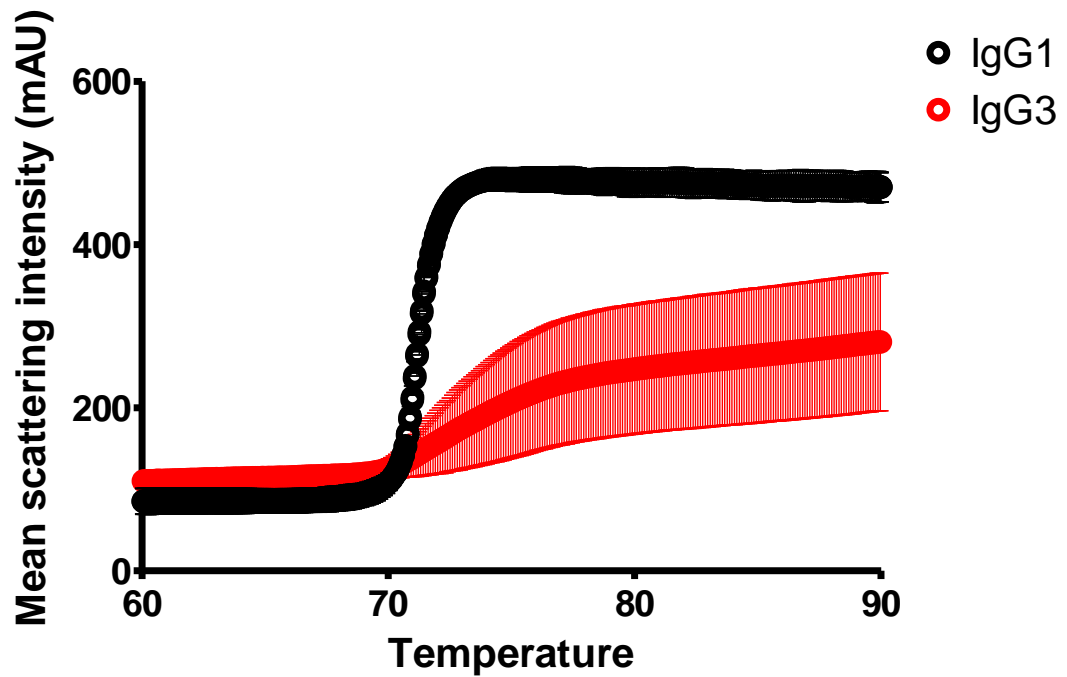


Figure 9.1 Mean scattering intensity for anti-IL-8 IgG1 (black) and IgG3 (red) differential scanning fluorimetry experiments.

IgG1 N=2, IgG3 N=3. Standard deviation error bars are shown.

9.2.3 Diffusion coefficients from dynamic light scattering (DLS) for anti-IL-8 IgG1 and IgG3

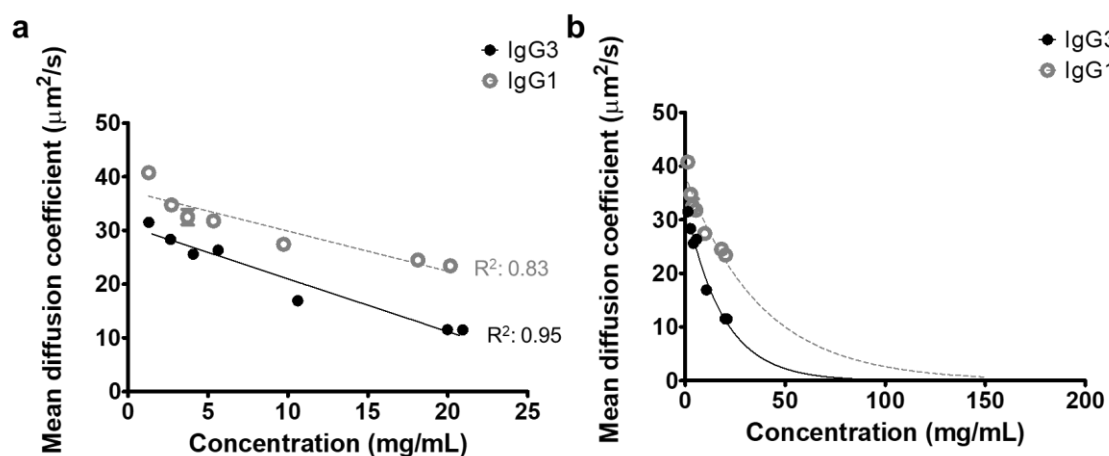


Figure 9.2 Diffusion coefficients measured from dynamic light scattering (DLS) experiments.

a, linear regression of anti-IL-8 IgG1 and IgG3 diffusion coefficients for self-interaction parameter, k_D , calculation. IgG1 linear equation: $y = -746.89x + 37.36$, IgG3 linear equation: $y = -983.83x + 30.848$. **b**, exponential growth fit of diffusion coefficients to extrapolate to 200mg/mL for theoretical viscosity calculations (Generalised Stokes Einstein equation). IgG1 exponential equation: $y = 37.65e^{-0.025x}$, IgG3 exponential equation: $y = 32.704e^{-0.052x}$.

9.2.4 Intrinsic viscosity and the Huggins coefficient for anti-IL-8 IgG1 and IgG3

To determine the intrinsic viscosity, $[\eta]$, and subsequently the Huggins coefficients for anti-IL-8 IgG1 and IgG3 molecules, the relative viscosity, η_{rel} , was calculated **Equation 9.1**.

$$\eta_{rel} = \eta/\eta_0$$

9.1

Where the solution viscosity is η_0

Subsequently, the reduced viscosity, η_{red} , was calculated **Equation 9.2** and the intercept from the linear regression of η_{red} over concentration (g/mL) determined $[\eta]$. The Huggins coefficient was computed as described in **Equation 4.7**.

$$\eta_{red} = ((\eta_{rel} - 1)/c) \times 1000$$

9.2

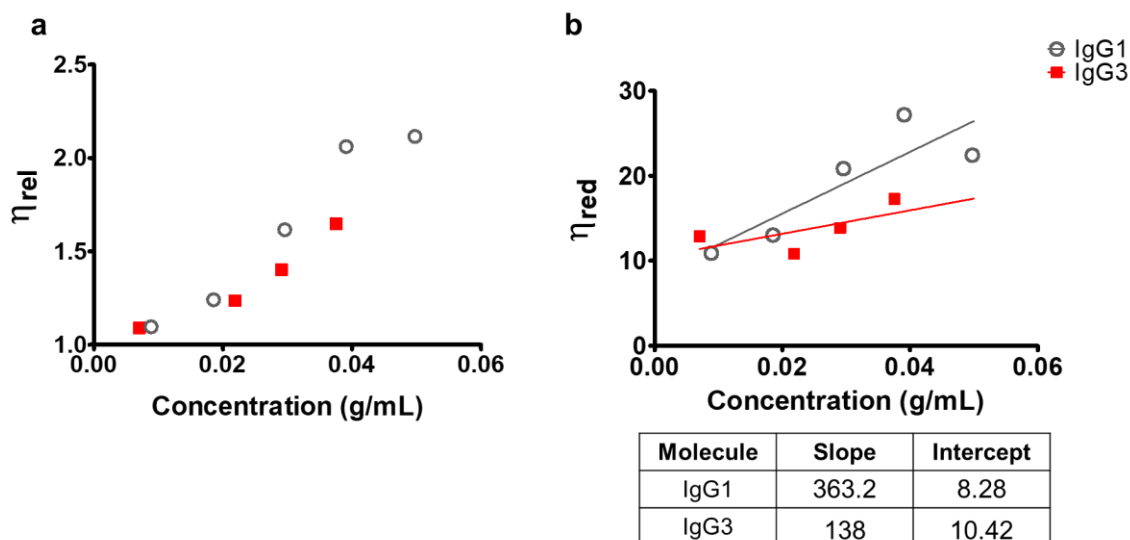


Figure 9.3 a, Relative (η_{rel}) and b, reduced (η_{red}) viscosity for anti-IL-8 IgG1 (grey) and IgG3 (red) over concentration (g/mL) in the dilute regime.

Linear regression for reduced viscosity over concentration determined the intrinsic viscosity (intercept).

10. Appendix 4

10.1. Molecular descriptors relevant to viscosity modelling

Table 10.1 *In silico* molecular descriptors for anti-IL-8 molecules computed from Fv homology constructs.

Molecule	net_charge	Predicted ζ at Deybe length (mV)	ens_charge	pI_seq	pI_3D	VL net charge	VH net charge	FvCSP	Hydrophobic index	TANGO score	WALTZ score	Deep SCM
WT	0.05	0.19	2.01	6.42	6.23	-1.23	3.93	-4.83	1.094	1603.94	486.574	1197.42
D17N (FWRL)	0.62	1.79	3.30	6.68	7.61	-0.32	3.93	-1.26	1.096	1590.12	486.574	1164.43
D70N (FWRL)	0.63	1.58	2.90	6.68	7.61	-0.32	3.93	-1.26	1.096	1627.07	486.574	1136.54
K42E (FWRL)	-1.81	-4.14	0.07	5.62	4.56	-3.16	3.93	-12.42	1.105	1602.38	486.574	1253.89
V5Q (FWRH)	0.05	0.19	2.25	6.42	6.23	-1.23	3.83	-4.71	1.067	1603.94	486.574	1194.19
W32Q (CDRH)	0.05	0.21	2.38	6.42	6.24	-1.22	3.92	-4.78	1.070	1357.71	389.25	1213.87
D28N (CDRH)	0.62	1.46	2.88	6.68	7.58	-0.34	3.93	-1.34	1.096	1603.43	486.574	1062.51
D56N (CDRH)	0.63	1.51	3.00	6.68	7.61	-0.32	3.82	-1.22	1.096	1602.95	486.574	1136.34
R53G (CDRH)	-0.83	-1.96	1.01	6.07	4.93	-2.18	3.93	-8.57	1.140	1897.13	486.574	1256.43

10.2. Viscosity model fit parameters

Table 10.2 Parameters derived from four viscosity model fits applied to concentration-viscosity profiles for mutant variants and WT molecule.

Molecule	Concentration regime (mg/mL)	Exponential growth			3-parameter exponential			Modified Ross Minton		Tomar		
		Y0	k	Tau (1/k)	Slope A3 (K ⁻¹)	Slope A2	A1 (cP)	k/v	[η] mL/g	η ₀	B	LnA
WT	<120	0.848	0.022	44.675	0.000	0.021	-0.02879	0.190	14.131	1.13	0.02082	-0.15101
	>120	1.568	0.022	45.598	0.000	0.024	-0.23068	0.068	16.588	1.13	0.02449	-0.3529
D17N	<120	0.031	0.063	15.947	0.000	0.026	-0.17547	1.086	6.785	1.13	0.02574	-0.29769
	>120	3.368	0.018	54.621	0.000	0.025	-0.16936	-0.052	31.986	1.13	0.02523	-0.29158
D70N	<120	1.145	0.015	64.995	0.000	0.015	0.17827	0.025	14.824	1.13	0.01468	0.05606
	>120	1.347	0.023	44.412	0.000	0.024	-0.10261	-0.009	24.418	1.13	0.02411	-0.22483
K42E	<120	0.027	0.066	15.062	0.000	0.026	0.04139	0.666	9.623	1.13	0.02644	-0.08083
	>120	0.000	0.262	3.823	0.000	0.029	-0.18578	1.247	4.251	1.13	0.02946	-0.308
V5Q	<120	0.779	0.032	31.297	0.000	0.026	0.07214	0.297	15.342	1.13	0.02613	-0.05008
	>120	0.060	0.040	24.959	0.000	0.024	0.07958	0.135	15.003	1.13	0.02393	-0.04264
W32Q	<120	1.494	0.012	83.143	0.000	0.015	0.27649	0.000	17.090	1.13	0.01500	0.15428
	>120	0.075	0.037	26.748	0.000	0.025	-0.03551	0.085	16.992	1.13	0.02537	-0.15773
D28N	<120	0.797	0.026	38.135	0.000	0.022	0.01149	0.696	9.420	1.13	0.02186	-0.11073
	>120	0.775	0.027	37.353	0.000	0.026	-0.1051	0.080	17.500	1.13	0.02587	-0.22732
D56N	<120	0.852	0.024	41.947	0.000	0.016	0.24863	0.283	12.832	1.13	0.01629	0.12642
	>120	3.898	0.027	37.371	0.000	0.033	-0.33795	-0.049	48.246	1.13	0.03285	-0.46016
R53G	<120	1.031	0.029	33.907	0.000	0.025	0.28738	18.269	0.577	1.13	0.02467	0.16516
	>120	0.000	0.081	12.317	0.000	0.030	0.12262	0.248	11.507	1.13	0.03042	0.00041

10.3. Determination of the Huggins and Kraemer Parameters

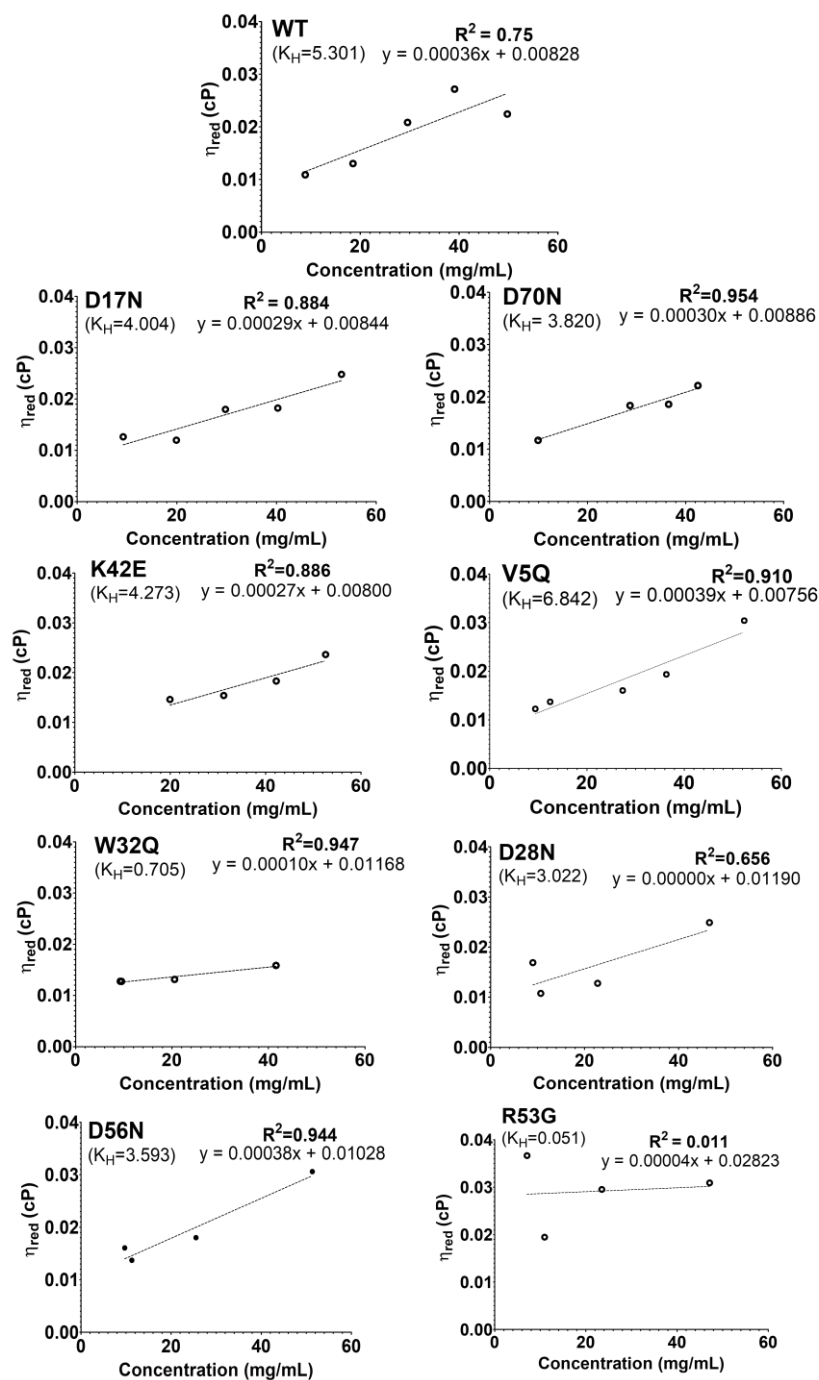


Figure 10.1 Individual linear regression plots of reduced viscosity (η_{sp}/c) versus concentration profiles used to derive the Huggins coefficient for the anti-IL-8 panel.

The Huggins coefficient (K_H) was determined from the intrinsic viscosity (intercept) and slope of the plot. R^2 values are reported to show goodness of fit to linear regression model.

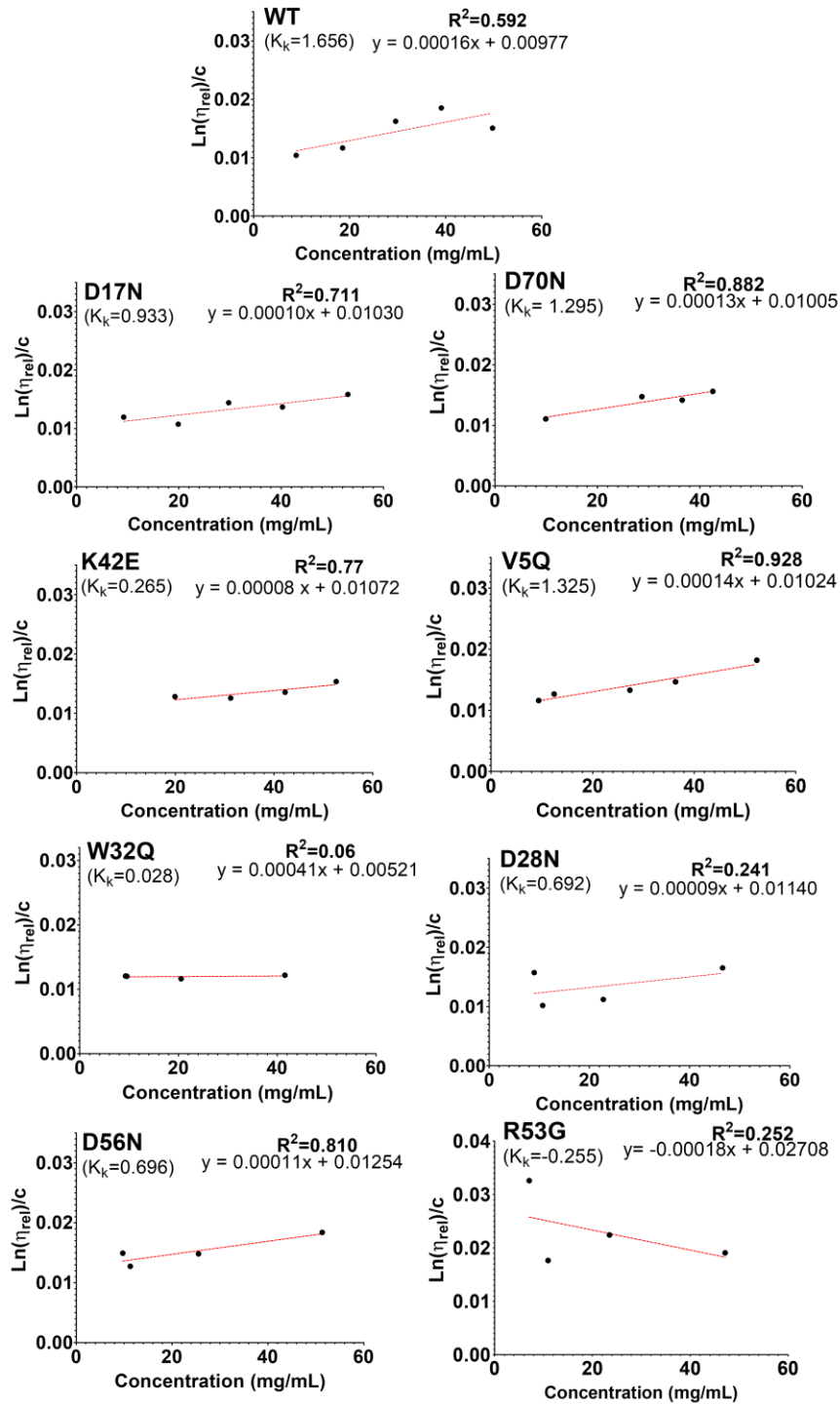


Figure 10.2 Individual linear regression plots of natural log of relative viscosity (η_{rel}/C) versus concentration profiles used to derive the Kraemer coefficient for the anti-IL-8 panel.

The Kraemer coefficient (K_k) was determined from the intrinsic viscosity (intercept) and slope of the plot. R^2 values are reported to show goodness of fit to linear regression model.

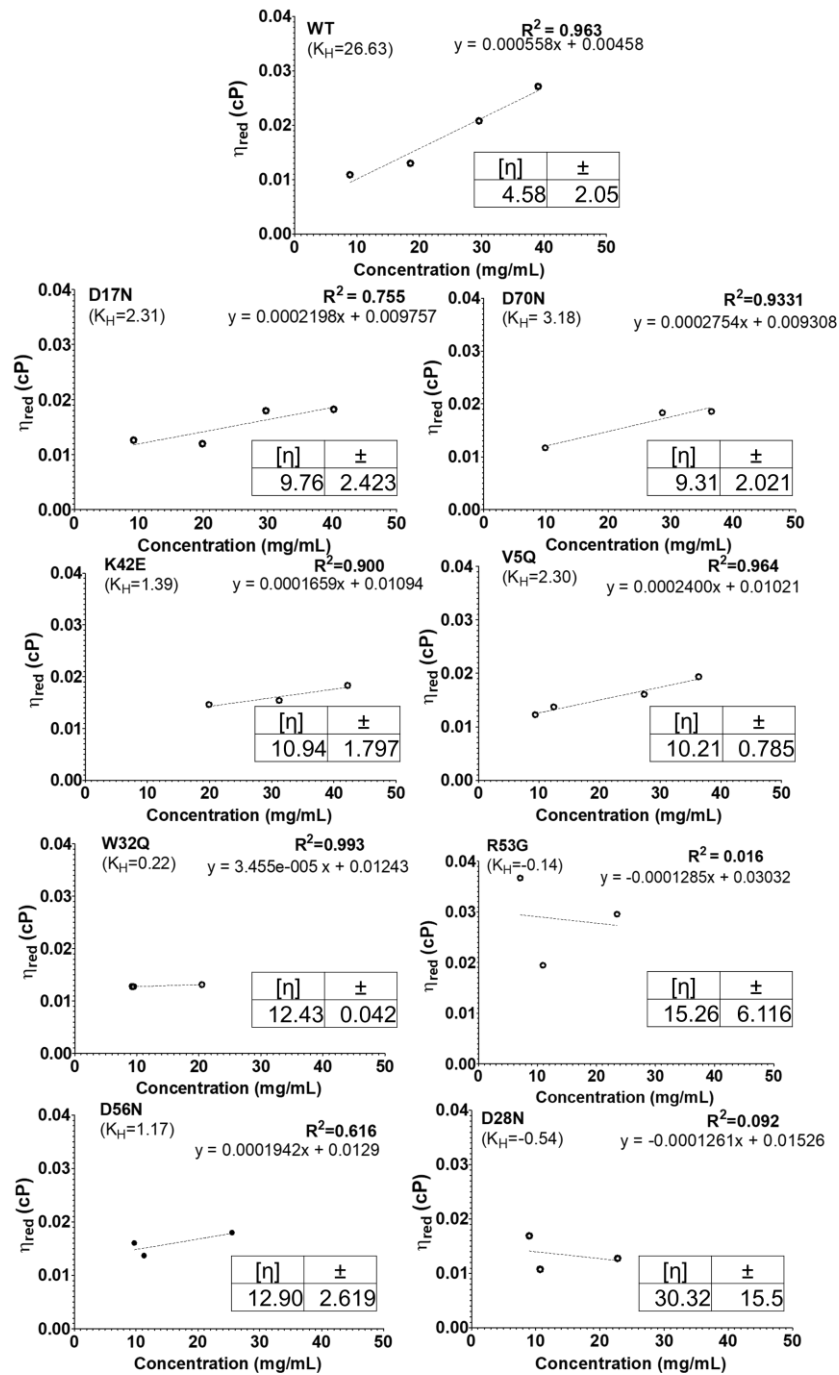


Figure 10.3 Reduced viscosity (η_{red}) (cP) over concentration (mg/mL) plots for anti-IL-8 mutants with highest concentration data points removed.

Intrinsic viscosities ($[\eta]$) were derived from the intercept of the linear regression and used with the slope to derive Huggins coefficients (K_H). R^2 goodness fits to the linear regression model are shown.

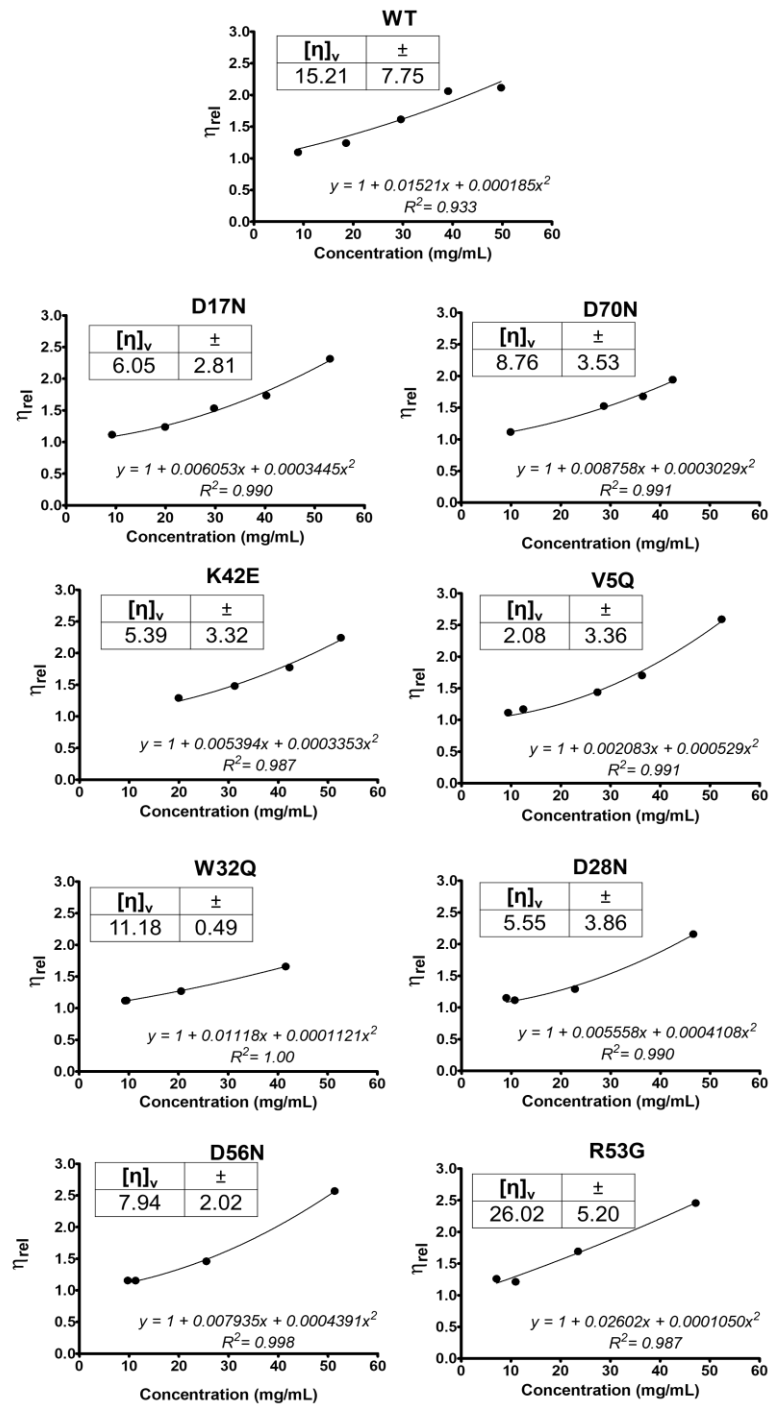


Figure 10.4 Individual second order polynomial (quadratic) plots of relative viscosity versus concentration profiles used to derive $[\eta]_v$ for the anti-IL-8 mutant panel.

K1 was constrained to 1 so $[\eta]_v$ could not be negative.

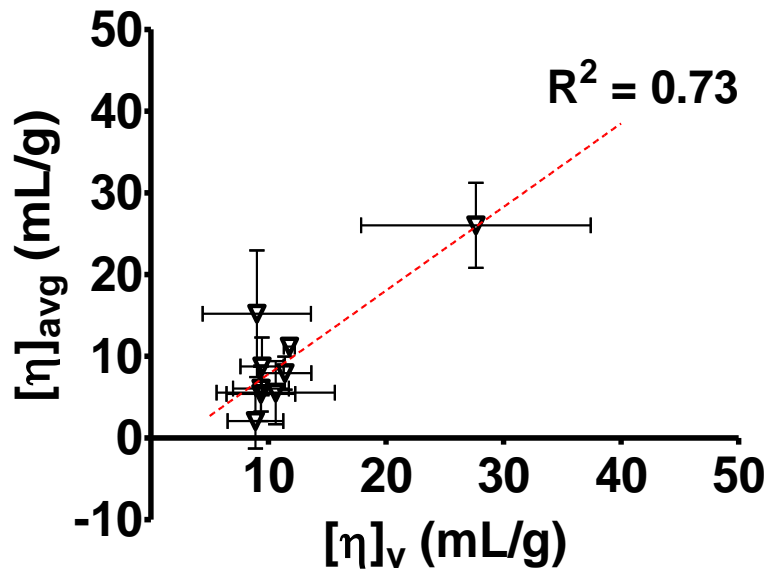


Figure 10.5 Correlation between intrinsic viscosities derived from linear regression ($[\eta]_{avg}$) and polynomial non-linear fitting ($[\eta]_v$).

Error bars represent mean standard error of intercepts from each respective model fit.

Goodness of fit R^2 reported.

Table 10.3 Mean intrinsic viscosity, $[\eta]_{\text{avg}}$, k_{exp} , Huggins and Kraemer coefficients determined for anti-IL-8 mAbs.

Linear regression of the reduced viscosity-concentration was performed to determine the Huggins intrinsic viscosity, $[\eta]_{\text{H}}$, and Huggins coefficient, k_{H} . Linear regression from the natural logarithm of relative viscosity/concentration over concentration was performed to determine Kraemer intrinsic viscosity, $[\eta]_{\text{K}}$, and Kraemer coefficient, k_{K} . Second-order polynomial fitting of relative viscosities was used to obtain alternate intrinsic viscosities ($[\eta]_{\text{v}}$). The exponential constant, k_{exp} , is shown from fitting relative viscosity (η_{rel}) data. Molecular weights are from mass spectrometry peptide mapping experiments and were used in the HYDROPRO program for $[\eta]$ and radius of gyration (R_{g}) predictions. Values are represented as mean (\pm standard deviation), $N=4$.

Molecule	$[\eta]_{\text{H}}$ (mL/g)	$[\eta]_{\text{K}}$ (mL/g)	$[\eta]_{\text{avg}}$ (mL/g)	$[\eta]_{\text{v}}$ (mL/g)	k_{exp}	Huggins coefficient, k_{H}	Kraemer coefficient, k_{K}	Molecular weight (Da)	HYDROPRO Residue-shell mode		HYDROPRO Residue-bead mode	
									$[\eta]$ (mL/g)	R_{g} (nm)	$[\eta]$ (mL/g)	R_{g} (nm)
WT	8.28 (± 3.89)	9.77 (± 2.47)	9.02 (± 4.61)	15.21 (± 7.75)	15.78	5.30(± 1.77)	1.66(± 0.97)	145276	7.426	5.32	7.165	5.102
D17N (FWL)	8.44 (± 2.03)	10.30 (± 1.24)	9.37 (± 2.38)	6.05 (± 2.81)	14.39	4.00(± 0.53)	0.93(± 0.18)	145274	7.426	5.253	7.09	5.045
D70N (FWL)	8.86 (± 1.49)	10.05 (± 1.08)	9.46 (± 1.84)	8.76 (± 3.53)	14.71	3.82(± 0.80)	1.30(± 0.29)	145274	7.43	5.279	7.079	5.057
K42E (FWL)	8.00 (± 2.67)	10.72 (± 1.18)	9.36 (± 2.92)	5.39 (± 3.32)	14.09	4.27(± 1.27)	0.68(± 0.21)	145278	7.424	5.259	7.144	5.092
V5Q (FWH)	7.56 (± 2.26)	10.24 (± 0.71)	8.90 (± 2.37)	2.08 (± 3.36)	15.95	6.84(± 2.1)	1.33(± 0.21)	145334	7.281	5.27	7.047	5.069
W32Q (CDRH2)	11.68 (± 0.39)	11.90 (± 0.26)	11.79 (± 0.47)	11.18 (± 0.49)	12.04	0.71(± 0.11)	0.03(± 0.07)	145160	7.436	5.259	7.097	5.062
D28N (CDRL1)	9.83 (± 4.02)	11.40 (± 3.03)	10.62 (± 5.03)	5.55 (± 3.86)	14.86	3.02(± 0.54)	0.69(± 0.25)	145274	7.44	5.272	7.111	5.102
D56N (CDRL2)	10.28 (± 1.95)	12.54 (± 1.11)	11.41 (± 2.24)	7.94 (± 2.02)	17.06	3.59(± 0.81)	0.70(± 0.19)	145274	7.361	5.243	7.062	5.068
R53G (CDRL1)	28.23 (± 7.56)	27.08 (± 6.19)	27.65 (± 9.77)	26.02 (± 5.20)	20.32	0.05 (± 0.09)	-0.26(± 0.52)	145078	7.571	5.3	7.174	5.108

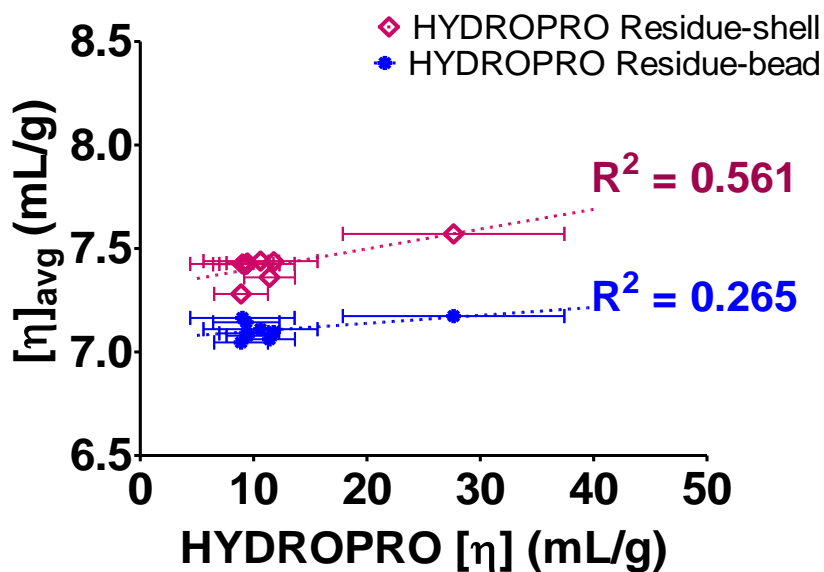


Figure 10.6 Correlations of intrinsic viscosity from HYDROPRO program to experimental intrinsic viscosity ($[\eta]_{avg}$).

Both residue-level modes were selected, and the residue-shell predictions had a stronger correlation to $[\eta]_{avg}$. Linear goodness of fit R^2 reported. Error bars represent standard error of $[\eta]_{avg}$.

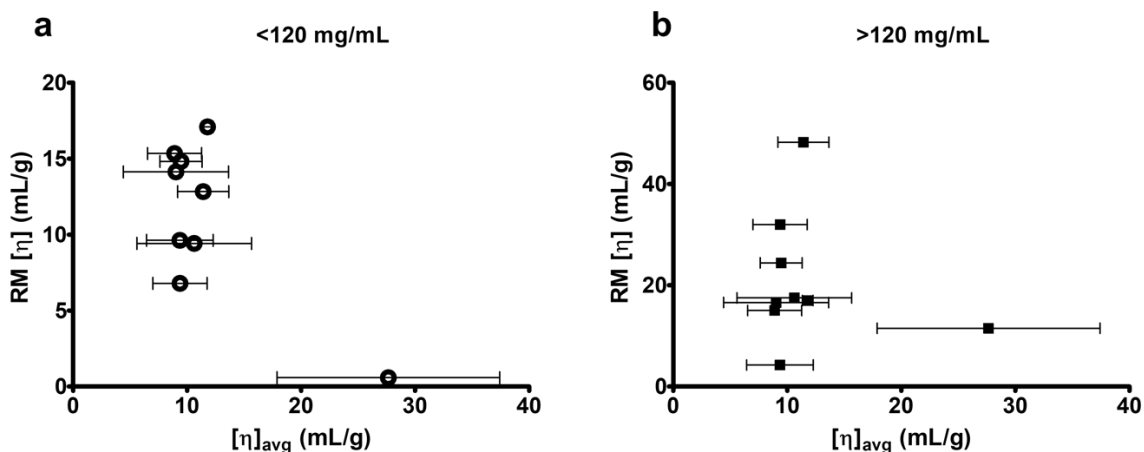


Figure 10.7 Poor correlations were observed between the Ross-Minton fit derived intrinsic viscosity versus the average intrinsic viscosity ($[\eta]_{avg}$).

This was examined with a, mid-concentration and, b, high concentration viscosity profiles. Error bars represent standard error $[\eta]_{avg}$ values.

10.4. Shape factors of anti-IL-8 molecule panel

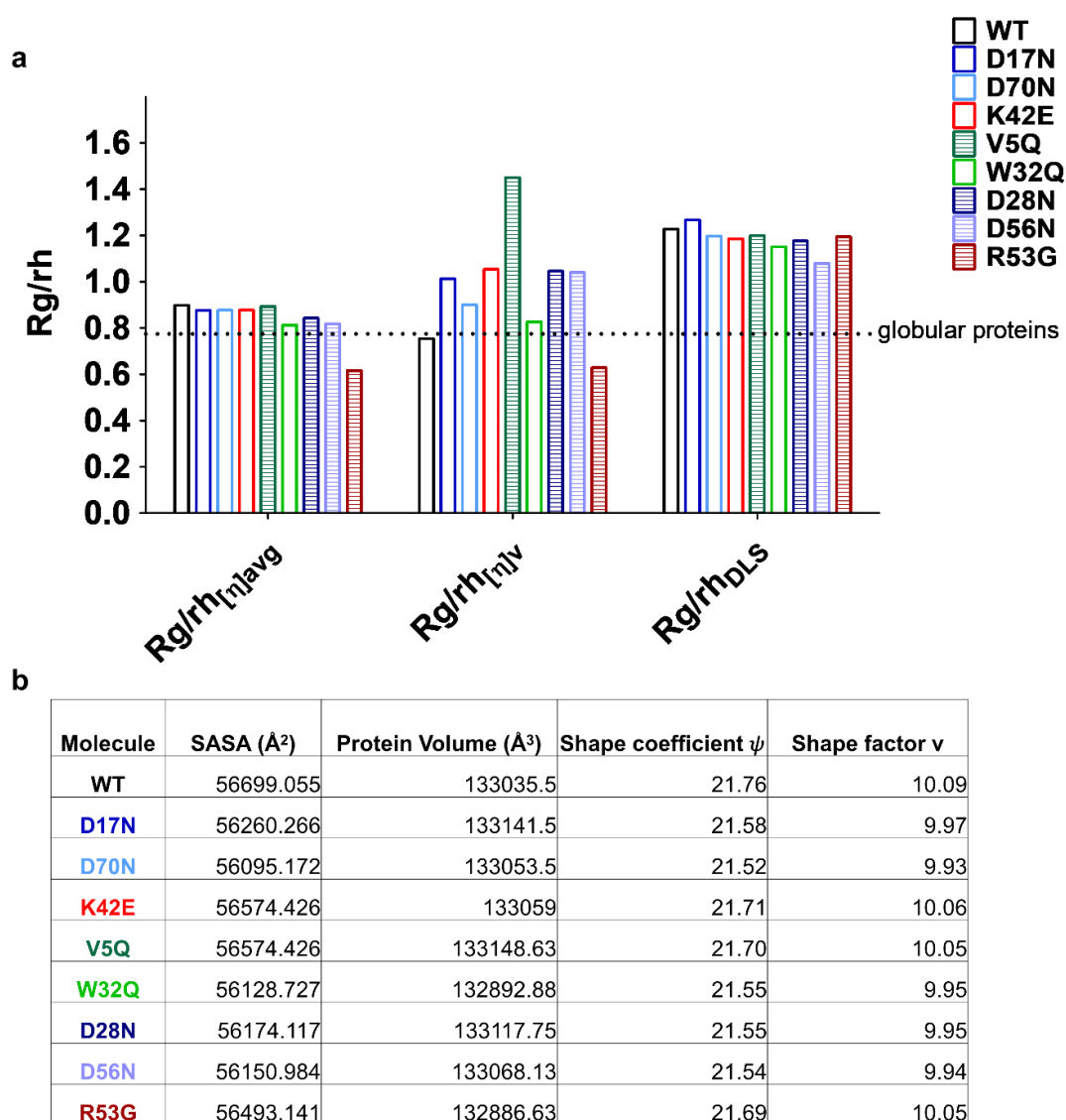


Figure 10.8 Shape factors of the anti-IL-8 mAb panel.

a, Radius of gyration (R_g) from the HYDROPRO program (shell mode) and three hydrodynamic radii (r_h) were used as denominators; derived either from the linear average intrinsic viscosity $[\eta]_{avg}$, the polynomial intrinsic viscosity $[\eta]_v$ or DLS (**a**). A dotted line at 0.775 represents the expected ratio value for a spherical globular protein.³⁶⁰ **b**, Alternatively, computational solvent accessible surface area (SASA) and protein volumes were calculated from IgG homology constructs, and Equations 5.18 and 5.19 were used to compute shape coefficients and factors (ν).

10.5. Cross-correlating hydrodynamic parameters to experimental viscosity

Table 10.4 Cross-correlation matrix for hydrodynamic parameters and high concentration viscosity (η) for anti-IL-8 mAb panel.

Pearson correlation coefficients (R) values are reported, and colour graded with positive correlations in blue and negative correlations in red.

Correlations where $R > 0.8$ are in white font.

	Intrinsic viscosity, Huggins coefficient, hydrodynamic radii, volume fraction													Measured size and charge					Shape descriptors					High conc η		
	$[\eta]_H$ (mL/g)	$[\eta]_K$ (mL/g)	$[\eta]_{avg}$ (mL/g)	$[\eta]_V$ (mL/g)	k_H	k_K	k_{exp}	$rh_{[\eta]_{avg}}$ at 1mg/mL	$rh_{[\eta]_V}$ at 1mg/mL	rh_{DLS} at 1mg/mL	V_h (nm ³)	ϕ (nm ³ /g) at 1 mg/mL ($[\eta]_{avg}$)	ϕ (nm ³ /g) at 1 mg/mL ($[\eta]_V$)	ϕ (nm ³ /g) at 1 mg/mL ($[\eta]_{DLS}$)	Z-ave at 1mg/mL	k_D (mL/g)	B_{22} (ml/nmol/g ²)	ζ at 5mg/mL (mV)	Main peak isoelectric point	SASA (Å ²)	Protein Volume (Å ³)	ψ	ν	HYDROPRO R _g (Bead)	HYDROPRO R _g (Shell)	Average viscosity knee (cP)
$[\eta]_H$ (mL/g)	1.00	0.99	1.00	0.87	-0.75	-0.74	0.73	1.00	0.76	0.09	1.00	1.00	0.86	0.08	0.09	-0.64	-0.50	0.16	-0.31	0.09	-0.71	0.14	0.17	0.45	0.35	-0.26
V_h (nm ³)	1.00	0.99	1.00	0.87	-0.75	-0.75	0.72	1.00	0.76	0.10	1.00	1.00	0.86	0.09	0.10	-0.64	-0.49	0.16	-0.31	0.08	-0.72	0.14	0.17	0.45	0.35	-0.26
ϕ (nm ³ /g) at 1 mg/mL ($[\eta]_{avg}$)	1.00	1.00	1.00	0.85	-0.72	-0.74	0.75	1.00	0.73	0.10	1.00	1.00	0.84	0.09	0.10	-0.66	-0.52	0.14	-0.32	0.11	-0.69	0.16	0.19	0.46	0.34	-0.31
$[\eta]_{avg}$ (mL/g)	1.00	1.00	1.00	0.85	-0.72	-0.74	0.75	1.00	0.73	0.10	1.00	1.00	0.84	0.09	0.10	-0.66	-0.52	0.14	-0.32	0.11	-0.69	0.16	0.19	0.46	0.34	-0.31
$rh_{[\eta]_{avg}}$ at 1mg/mL	1.00	0.99	1.00	0.85	-0.76	-0.77	0.73	1.00	0.73	0.16	1.00	1.00	0.83	0.15	0.16	-0.63	-0.48	0.20	-0.30	0.05	-0.71	0.11	0.14	0.45	0.30	-0.30
$[\eta]_K$ (mL/g)	0.99	1.00	1.00	0.83	-0.69	-0.73	0.78	0.99	0.70	0.11	0.99	1.00	0.82	0.10	0.11	-0.68	-0.55	0.12	-0.34	0.13	-0.65	0.19	0.21	0.47	0.32	-0.37
$[\eta]_V$ (mL/g)	0.87	0.83	0.85	1.00	-0.66	-0.50	0.63	0.85	0.97	0.01	0.87	0.85	0.99	0.00	0.01	-0.63	-0.54	0.13	-0.31	0.22	-0.80	0.28	0.30	0.51	0.64	-0.01
ϕ (nm ³ /g) at 1 mg/mL ($[\eta]_V$)	0.86	0.82	0.84	0.99	-0.65	-0.48	0.59	0.83	0.97	-0.08	0.86	0.84	1.00	-0.09	-0.08	-0.60	-0.52	0.07	-0.34	0.25	-0.80	0.32	0.34	0.52	0.68	0.03
$rh_{[\eta]_V}$ at 1mg/mL	0.76	0.70	0.73	0.97	-0.69	-0.45	0.43	0.73	1.00	-0.06	0.76	0.73	0.97	-0.07	-0.06	-0.48	-0.39	0.12	-0.29	0.13	-0.82	0.20	0.22	0.45	0.65	0.16
k_{exp}	0.73	0.78	0.75	0.63	-0.17	-0.21	1.00	0.73	0.43	0.13	0.72	0.75	0.59	0.14	0.13	-0.91	-0.80	-0.05	-0.13	0.34	-0.19	0.34	0.35	0.49	0.41	-0.60
HYDROPRO R _g (Bead)	0.45	0.47	0.46	0.51	-0.18	-0.19	0.49	0.45	0.45	0.08	0.45	0.46	0.52	0.05	0.08	-0.32	-0.30	-0.32	-0.47	0.55	-0.29	0.58	0.59	1.00	0.63	-0.28
HYDROPRO R _g (Shell)	0.35	0.32	0.34	0.64	0.00	0.22	0.41	0.30	0.65	-0.36	0.35	0.34	0.68	-0.39	-0.36	-0.44	-0.41	-0.38	-0.22	0.58	-0.31	0.60	0.61	0.63	1.00	0.24
ν	0.17	0.21	0.19	0.30	0.31	0.18	0.35	0.14	0.22	-0.36	0.17	0.19	0.34	-0.38	-0.36	-0.41	-0.61	-0.54	-0.66	0.99	-0.08	1.00	1.00	0.59	0.61	-0.29
ζ at 5mg/mL (mV)	0.16	0.12	0.14	0.13	-0.46	-0.43	-0.05	0.20	0.12	0.61	0.16	0.14	0.07	0.63	0.61	-0.01	0.19	1.00	0.51	-0.56	-0.36	-0.53	-0.54	-0.32	-0.38	0.16
Shape coefficient ψ	0.14	0.19	0.16	0.28	0.34	0.21	0.34	0.11	0.20	-0.35	0.14	0.16	0.32	-0.37	-0.35	-0.40	-0.60	-0.53	-0.64	1.00	-0.05	1.00	1.00	0.58	0.60	-0.28
Z-ave at 1mg/mL	0.09	0.11	0.10	0.01	-0.26	-0.33	0.13	0.16	-0.06	1.00	0.10	0.10	-0.08	1.00	1.00	0.11	0.25	0.61	0.11	-0.37	-0.26	-0.35	-0.36	0.08	-0.36	-0.14
rh_{DLS} at 1mg/mL	0.09	0.11	0.10	0.01	-0.26	-0.33	0.13	0.16	-0.06	1.00	0.10	0.10	-0.08	1.00	1.00	0.11	0.25	0.61	0.11	-0.37	-0.26	-0.35	-0.36	0.08	-0.36	-0.14
SASA (Å ²)	0.09	0.13	0.11	0.22	0.41	0.27	0.34	0.05	0.13	-0.37	0.08	0.11	0.25	-0.39	-0.37	-0.40	-0.61	-0.56	-0.61	1.00	0.03	1.00	0.99	0.55	0.58	-0.31
ϕ (nm ³ /g) at 1 mg/mL ($[\eta]_{DLS}$)	0.08	0.10	0.09	0.00	-0.25	-0.32	0.14	0.15	-0.07	1.00	0.09	0.09	-0.09	1.00	1.00	0.09	0.23	0.63	0.13	-0.39	-0.24	-0.37	-0.38	0.05	-0.39	-0.17
Average viscosity knee (cP)	-0.26	-0.37	-0.31	-0.01	-0.10	0.19	-0.60	-0.30	0.16	-0.14	-0.26	-0.31	0.03	-0.17	-0.14	0.54	0.61	0.16	0.26	-0.31	-0.27	-0.28	-0.29	-0.28	0.24	1.00
Main peak isoelectric point	-0.31	-0.34	-0.32	-0.31	0.14	0.29	-0.13	-0.30	-0.29	0.11	-0.31	-0.32	-0.34	0.13	0.11	0.02	0.25	0.51	1.00	-0.61	0.41	-0.64	-0.66	-0.47	-0.22	0.26
B_{22} (ml/nmol/g ²)	-0.50	-0.55	-0.52	-0.54	-0.07	0.00	-0.80	-0.48	-0.39	0.25	-0.49	-0.52	-0.52	0.23	0.25	0.94	1.00	0.19	0.25	-0.61	0.05	-0.60	-0.61	-0.30	-0.41	0.61
k_D (mL/g)	-0.64	-0.68	-0.66	-0.63	0.10	0.11	-0.91	-0.63	-0.48	0.11	-0.64	-0.66	-0.60	0.09	0.11	1.00	0.94	-0.01	0.02	-0.40	0.13	-0.40	-0.41	-0.32	-0.44	0.54
Protein Volume (Å ³)	-0.71	-0.65	-0.69	-0.80	0.82	0.71	-0.19	-0.71	-0.82	-0.26	-0.72	-0.69	-0.80	-0.24	-0.26	0.13	0.05	-0.36	0.41	0.03	1.00	-0.05	-0.08	-0.29	-0.31	-0.27
k_K	-0.74	-0.73	-0.74	-0.50	0.90	1.00	-0.21	-0.77	-0.45	-0.33	-0.75	-0.74	-0.48	-0.32	-0.33	0.11	0.00	-0.43	0.29	0.27	0.71	0.21	0.18	-0.19	0.22	0.19
k_H	-0.75	-0.69	-0.72	-0.66	1.00	0.90	-0.17	-0.76	-0.69	-0.26	-0.75	-0.72	-0.65	-0.25	-0.26	0.10	-0.07	-0.46	0.14	0.41	0.82	0.34	0.31	-0.18	0.00	-0.10

10.6. Predicting viscosity from molecular descriptors

Table 10.5 Ranking of anti-IL-8 molecules, in increasing viscosity order, according to Li, Sharma and Tomar predictions against experimental viscosity fitted across four models at 150 and 180 mg/mL.

	150 mg/mL					180 mg/mL						
	Li score (cP)	Exponential growth fit viscosity (cP)	3-parameter exponential fit viscosity (cP)	Modified Ross Minton fit viscosity (cP)	Tomar fit viscosity (cP)	Sharma score (cP)	Tomar score (cP)	Exponential growth fit viscosity (cP)	3-parameter exponential fit viscosity (cP)	Modified Ross Minton fit viscosity (cP)	Tomar fit viscosity (cP)	Average knee (cP)
β Increasing predicted viscosity	D17N	R53G	WT	WT	WT	D56N	D56N	R53G	WT	WT	WT	WT
	D70N	K42E	D70N	R53G	D70N	D70N	D70N	W32Q	D70N	W32Q	D70N	D70N
	D56N	W32Q	D17N	K42E	D17N	D17N	D17N	D70N	D17N	D28N	V5Q	V5Q
	D28N	V5Q	V5Q	V5Q	V5Q	D28N	D28N	V5Q	V5Q	D70N	D17N	W32Q
	W32Q	D70N	W32Q	W32Q	W32Q	V5Q	W32Q	WT	W32Q	R53G	W32Q	D17N
	WT	WT	D28N	D28N	D28N	W32Q	V5Q	D17N	D28N	V5Q	D28N	D28N
	V5Q	D28N	K42E	D70N	K42E	WT	WT	D28N	K42E	D17N	K42E	K42E
	R53G	D17N	D56N	D17N	D56N	R53G	R53G	D56N	D56N	D56N	R53G	R53G
	K42E	D56N	R53G	D56N	R53G	K42E	K42E	K42E	R53G	K42E	D56N	D56N

Table 10.6 Viscosity values from Ross-Minton fitting at 120 , 150 and 180 mg/mL with high-concentration and ultra-high-concentration data.

Viscosity values >30cP are shaded in red and <30cP are shaded in green. All molecules at 180 mg/mL had over the 30cP threshold when interpolating from ultra-high concentration regime data.

Concentration regime used:	High (<120 mg/mL)	Ultra-high (>120 mg/mL)	High (<120 mg/mL)	Ultra-high (>120 mg/mL)	High (<120 mg/mL)	Ultra-high (>120 mg/mL)
Molecule	Ross-Minton fitted viscosity at 120 mg/mL (cP)		Ross-Minton fitted viscosity at 150 mg/mL (cP)		Ross-Minton fitted viscosity at 180 mg/mL (cP)	
WT	13.78	11.27	39.21	22.51	154.59	47.63
D17N	1302.84	27.61	Too high	52.27	Too high	94.22
D70N	7.28	19.68	11.92	39.31	19.76	77.88
K42E	166.68	4.59	Too high	25.30	Too high	Too high
V5Q	65.14	12.22	1584.29	28.75	Too high	79.76
W32Q	8.78	13.28	14.67	29.13	24.49	70.02
D28N	225.76	14.10	Too high	31.34	Too high	76.21
D56N	17.32	101.84	77.56	233.25	892.44	491.72
R53G	>20,000	9.21	Too high	23.03	Too high	79.43

Table 10.7 Confusion matrix demonstrating number of molecules with predicted low or high viscosity from use of ensemble charge (ens_charge).

Using the high concentration regime data, three out of the nine molecules would be classified as low viscosity despite >30cP experimental viscosities at 120 mg/mL. Using the ultra-high concentration regime data, two molecules would be classified as low viscosity despite >30cP experimental viscosity reported/ at 120 mg/mL.

High (<120 mg/mL) concentration regime		
<i>No. molecules</i>	Low viscosity (<30 cP) at 120 mg/mL	High viscosity (>30 cP) at 120 mg/mL
Predicted low viscosity (ens_charge >+2)	4	3
Predicted high viscosity (ens_charge <+2)	0	2
Ultra-high (>120 mg/mL) concentration regime		
<i>No. molecules</i>	Low viscosity (<30 cP) at 120 mg/mL	High viscosity (>30 cP) at 120 mg/mL
Predicted low viscosity (ens_charge >+2)	5	2
Predicted high viscosity (ens_charge <+2)	2	0

Table 10.8 Confusion matrices of viscosity classification of anti-IL-8 molecules from Lai *et al.* decision tree¹⁵¹ versus experimental viscosity data.

The experimental data used are the interpolated viscosities at 120 mg/mL and 150 mg/mL from all fitting models used (modified Ross-Minton, growth exponential, 3- parameter exponential and Tomar models). Two cut-off points were used (20 or 30 cP) as the ‘low viscosity’ threshold. Top left quadrant of each matrix represents true positives, bottom left quadrant represents false negatives, top right quadrant represents false positives and bottom right quadrant represents true negatives. True positive or negative values are in green font and false positive or negatives are in red font.

		Viscosity classification at 120 mg/mL				Viscosity classification at 150 mg/mL			
		20cP cut off		30 cP cut off		20cP cut off		30 cP cut off	
Modified Ross-Minton fitted viscosities									
<i>No. molecules</i>	Low viscosity (<20 cP) at 120 mg/mL	High viscosity (>20 cP) at 120 mg/mL	Low viscosity (<30 cP) at 120 mg/mL	High viscosity (>30 cP) at 120 mg/mL	<i>No. molecules</i>	Low viscosity (<20 cP) at 150 mg/mL	High viscosity (>20 cP) at 150 mg/mL	Low viscosity (<30 cP) at 150 mg/mL	High viscosity (>30 cP) at 150 mg/mL
Predicted low viscosity	0	0	0	0	Predicted low viscosity	0	0	0	0
Predicted high viscosity	7	2	8	1	Predicted high viscosity	0	9	5	4
Growth exponential fitted viscosities									
Predicted low viscosity	0	0	0	0	Predicted low viscosity	0	0	0	0
Predicted high viscosity	6	3	7	2	Predicted high viscosity	2	7	4	5
3-parameter exponential fitted viscosities									
Predicted low viscosity	0	0	0	0	Predicted low viscosity	0	0	0	0

Predicted high viscosity	4	5	7	2	Predicted high viscosity	0	9	0	9
Tomar fitted viscosities									
Predicted low viscosity	0	0	0	0	Predicted low viscosity	0	0	0	0
Predicted high viscosity	1	8	6	3	Predicted high viscosity	0	9	0	9

Table 10.9 Confusion matrix of viscosity classification of anti-IL-8 molecules from Makowski *et al.* decision tree¹⁵³ versus experimental viscosity data.

The experimental data used are the interpolated viscosities at 120 mg/mL and 150 mg/mL from all fitting models used (modified Ross-Minton, growth exponential, 3- parameter exponential and Tomar models). Two cut-off points were used (20 or 30 cP) as the ‘low viscosity’ threshold. Top left quadrant of each matrix represents true positives, bottom left quadrant represents false negatives, top right quadrant represents false positives and bottom right quadrant represents true negatives. True positive or negative values are in green font and false positive or negatives are in red font.

		Viscosity classification at 120 mg/mL				Viscosity classification at 150 mg/mL					
		20cP cut off		30 cP cut off		20cP cut off		30 cP cut off			
Modified Ross-Minton fitted viscosities											
<i>No. molecules</i>		Low viscosity (<20 cP) at 120 mg/mL	High viscosity (>20 cP) at 120 mg/mL	Low viscosity (<30 cP) at 120 mg/mL	High viscosity (>30 cP) at 120 mg/mL	<i>No. molecules</i>		Low viscosity (<20 cP) at 150 mg/mL	High viscosity (>20 cP) at 150 mg/mL	Low viscosity (<30 cP) at 150 mg/mL	High viscosity (>30 cP) at 150 mg/mL
Predicted low viscosity		2	2	3	1	Predicted low viscosity		0	4	0	4
Predicted high viscosity		5	0	5	0	Predicted high viscosity		0	5	5	0
Growth exponential fitted viscosities											
Predicted low viscosity		2	2	2	2	Predicted low viscosity		0	4	0	4
Predicted high viscosity		5	1	5	0	Predicted high viscosity		0	5	1	1
3-parameter exponential fitted viscosities											
Predicted low viscosity		3	1	3	1	Predicted low viscosity		0	4	0	4
Predicted high viscosity		2	3	3	1	Predicted high viscosity		0	5	0	5

		Tomar fitted viscosities								
Predicted low viscosity		0	4	3	1	Predicted low viscosity	0	4	0	4
Predicted high viscosity		1	4	3	2	Predicted high viscosity	0	5	0	5

Figure 10.9 a, Correlations and b, variable importance plot (VIP) of averaged knee of viscosity profiles for anti-IL-8 panel to computational molecular descriptors.

Highest correlated descriptors ($R \geq 0.5$) which are marked with red arrows on the VIP were used in partial least squares regression for predictive modelling. Partial least squared modelling was used to generate the VIP and a threshold of 1.7 (red dotted line) was set.

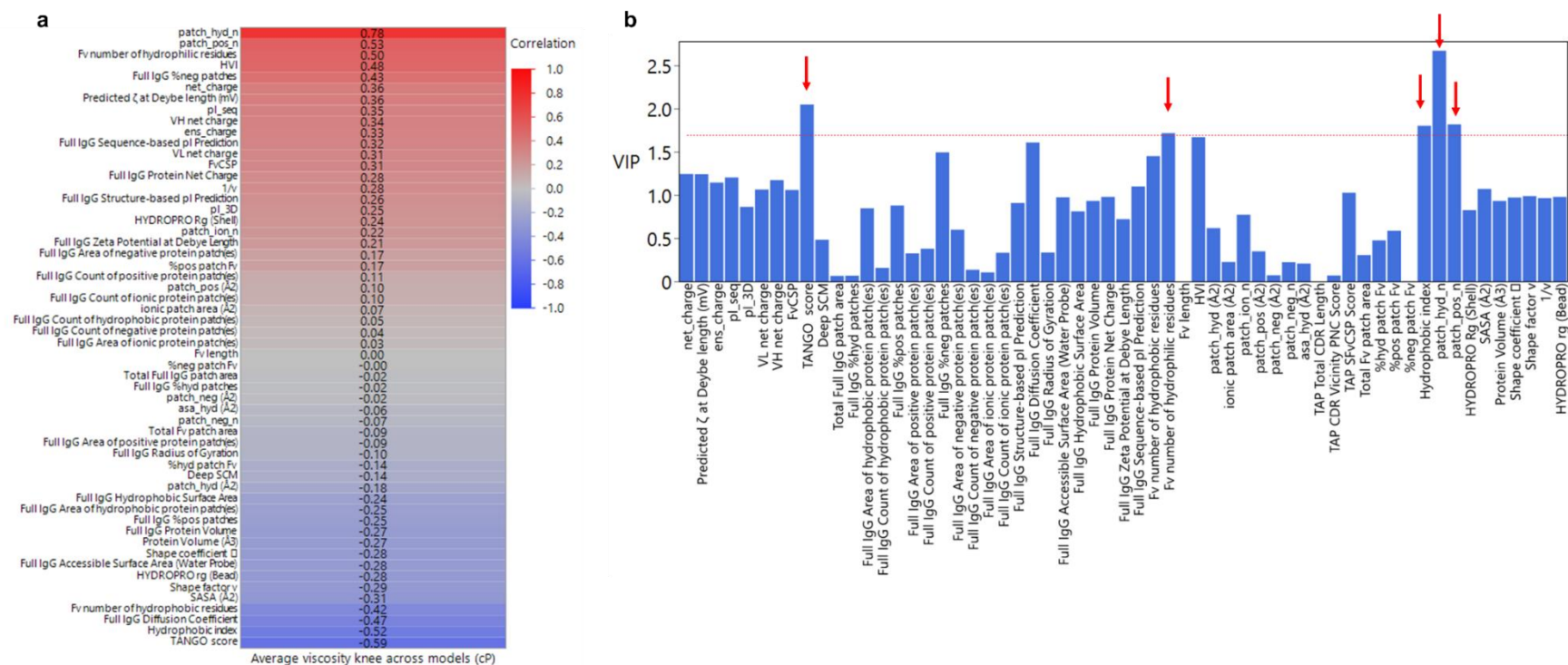


Table 10.10 Molecular descriptors from four in-house proprietary mAbs were used to test regression model developed from anti-IL-8 panel.

Molecule	Hydrophobic index	TANGO	Fv number of hydrophilic residues	Fv number of hydrophobic residues	HVI	Full IgG %neg patches	Full IgG diffusion coefficient	Count of hydrophobic protein patch(es)	Count of positive protein patch(es)
Ab1	1.048	683.77	118	84	14.72	21.07%	4.70E-07	11	11
Ab2	1.087	863.13	120	81	16.81	27.55%	4.70E-07	10	7
Ab3	1.124	384.17	125	85	16.81	22.88%	4.70E-07	9	10
Ab4	1.069	770.32	124	80	18.88	23.82%	4.80E-07	11	11

Bibliography

1. Scott, C. mAb Development: Trends and Technologies. *BioProcess International* <https://bioprocessintl.com/manufacturing/monoclonal-antibodies/mab-development-bioprocess-advancements-challenge-platform-assumptions/> (2020).
2. The Antibody Society. Antibody therapeutics approved or in regulatory review in the EU or US. <https://www.antibodysociety.org/resources/approved-antibodies/>.
3. Kelley, B., De Moor, P., Douglas, K., Renshaw, T. & Traviglia, S. Monoclonal antibody therapies for COVID-19: lessons learned and implications for the development of future products. *Curr. Opin. Biotechnol.* **78**, 102798 (2022).
4. Lu, R.-M. *et al.* Development of therapeutic antibodies for the treatment of diseases. *J. Biomed. Sci.* **27**, 1 (2020).
5. Bazan, J., Całkosinski, I. & Gamian, A. Phage display—A powerful technique for immunotherapy. *Hum. Vaccines Immunother.* **8**, 1817–1828 (2012).
6. Teymennet-Ramírez, K. V., Martínez-Morales, F. & Trejo-Hernández, M. R. Yeast Surface Display System: Strategies for Improvement and Biotechnological Applications. *Front. Bioeng. Biotechnol.* **9**, 794742 (2022).
7. Boder, E. T., Raeeszadeh-Sarmazdeh, M. & Price, J. V. Engineering antibodies by yeast display. *Arch. Biochem. Biophys.* **526**, 99–106 (2012).
8. Pedrioli, A. & Oxenius, A. Single B cell technologies for monoclonal antibody discovery. *Trends Immunol.* **42**, 1143–1158 (2021).
9. Sino Biological. Generation of Functional Monoclonal Antibodies by Single B Cell Cloning. <https://www.sinobiological.com/news/single-b-cell-cloning> (2021).

10. Mahdavi, S. Z. B. *et al.* An overview on display systems (phage, bacterial, and yeast display) for production of anticancer antibodies; advantages and disadvantages. *Int. J. Biol. Macromol.* **208**, 421–442 (2022).
11. Doria-Rose, N. A. & Joyce, M. G. Strategies to guide the antibody affinity maturation process. *Curr. Opin. Virol.* **11**, 137–147 (2015).
12. Burkovitz, A. & Ofra, Y. Understanding differences between synthetic and natural antibodies can help improve antibody engineering. *mAbs* (2016).
13. Zhang, Y. Evolution of phage display libraries for therapeutic antibody discovery. *mAbs* (2023).
14. Li, J. *et al.* Affinity maturation of antibody fragments: A review encompassing the development from random approaches to computational rational optimization. *Int. J. Biol. Macromol.* **247**, 125733 (2023).
15. Lim, Y. W., Adler, A. S. & Johnson, D. S. Predicting antibody binders and generating synthetic antibodies using deep learning. *mAbs* (2022).
16. Ho, M. & Pastan, I. Mammalian cell display for antibody engineering. *Methods Mol. Biol. Clifton NJ* **525**, 337–352, xiv (2009).
17. Li, W. *et al.* Structural Elucidation of Chemical and Post-translational Modifications of Monoclonal Antibodies. *NIST* 119–183 (2015).
18. O’Flaherty, R. *et al.* Mammalian cell culture for production of recombinant proteins: A review of the critical steps in their biomanufacturing. *Biotechnol. Adv.* **43**, 107552 (2020).
19. Velugula-Yellela, S. R. *et al.* Use of High-Throughput Automated Microbioreactor System for Production of Model IgG1 in CHO Cells. *J. Vis. Exp. JoVE* 58231 (2018).

20. Matte, A. Recent Advances and Future Directions in Downstream Processing of Therapeutic Antibodies. *Int. J. Mol. Sci.* **23**, 8663 (2022).
21. Łacki, K. M. & Riske, F. J. Affinity Chromatography: An Enabling Technology for Large-Scale Bioprocessing. *Biotechnol. J.* **15**, e1800397 (2020).
22. Li, Y. Viral removal by column chromatography in downstream processing of monoclonal antibodies. *Protein Expr. Purif.* **198**, 106131 (2022).
23. Ichihara, T., Ito, T. & Gillespie, C. Polishing approach with fully connected flow-through purification for therapeutic monoclonal antibody. *Eng. Life Sci.* **19**, 31–36 (2019).
24. Rathore, A. S., Kumar, D. & Kateja, N. Recent developments in chromatographic purification of biopharmaceuticals. *Biotechnol. Lett.* **40**, 895–905 (2018).
25. Suh, D., Kim, M., Lee, C. & Baek, Y. Virus filtration in biopharmaceutical downstream processes: key factors and current limitations. *Sep. Purif. Rev.* **53**, 26–39 (2024).
26. Shukla, A., Hubbard, B., Tressel, T., Guhan, S. & Low, D. Downstream processing of monoclonal antibodies—Application of Platform Approaches. *J. Chromatogr. B Analyt. Technol. Biomed. Life. Sci.* **848**, 28–39 (2007).
27. Singh, S. M. *et al.* Size exclusion chromatography for the characterization and quality control of biologics. *J. Liq. Chromatogr. Relat. Technol.* **44**, 265–278 (2021).
28. Murisier, A. *et al.* Direct coupling of size exclusion chromatography and mass spectrometry for the characterization of complex monoclonal antibody products. *J. Sep. Sci.* **45**, 1997–2007 (2022).
29. Pilely, K. *et al.* A novel approach to evaluate ELISA antibody coverage of host cell proteins—combining ELISA-based immunocapture and mass spectrometry. *Biotechnol. Prog.* **36**, e2983 (2020).

30. Van Manen-Brush, K. *et al.* Improving Chinese hamster ovary host cell protein ELISA using Ella®: an automated microfluidic platform. *BioTechniques* **69**, 186–192 (2020).
31. Liu, X., Susic, Z. & Krull, I. S. Capillary isoelectric focusing as a tool in the examination of antibodies, peptides and proteins of pharmaceutical interest. *J. Chromatogr. A* **735**, 165–190 (1996).
32. Chen, G., Tao, L. & Li, Z. Recent advancements in mass spectrometry for higher order structure characterization of protein therapeutics. *Drug Discov. Today* **27**, 196–206 (2022).
33. Forest-Nault, C., Gaudreault, J., Henry, O., Durocher, Y. & De Crescenzo, G. On the Use of Surface Plasmon Resonance Biosensing to Understand IgG-FcγR Interactions. *Int. J. Mol. Sci.* **22**, 6616 (2021).
34. Bailly, M. *et al.* Predicting Antibody Developability Profiles Through Early Stage Discovery Screening. *mAbs* **12**, 1743053 (2020).
35. Mieczkowski, C. *et al.* Blueprint for antibody biologics developability. *mAbs* **15**, 2185924 (2023).
36. Alberts, B. *et al.* The Adaptive Immune System. in *Molecular Biology of the Cell. 4th edition* (Garland Science, 2002).
37. In brief: The innate and adaptive immune systems. in *InformedHealth.org [Internet]* (Institute for Quality and Efficiency in Health Care (IQWiG), 2023).
38. Chiu, M. L., Goulet, D. R., Teplyakov, A. & Gilliland, G. L. Antibody Structure and Function: The Basis for Engineering Therapeutics. *Antibodies* **8**, 55 (2019).
39. Mills, B. J., Moussa, E. M. & Jameel, F. Chapter 1: Monoclonal Antibodies: Structure, Physicochemical Stability, and Protein Engineering. in *Development of Biopharmaceutical*

- Drug-Device Products* (eds. Jameel, F., Skoug, J. W. & Nesbitt, R. R.) 3–26 (Springer International Publishing, Cham, 2020). doi:10.1007/978-3-030-31415-6_1.
40. Charles A Janeway, J., Travers, P., Walport, M. & Shlomchik, M. J. Structural variation in immunoglobulin constant regions. in *Immunobiology: The Immune System in Health and Disease. 5th edition* (Garland Science, 2001).
41. Nimmerjahn, F. & Ravetch, J. V. Four keys to unlock IgG. *J. Exp. Med.* **218**, e20201753 (2021).
42. Vidarsson, G., Dekkers, G. & Rispen, T. IgG Subclasses and Allotypes: From Structure to Effector Functions. *Front. Immunol.* **5**, (2014).
43. Castelli, M. S., McGonigle, P. & Hornby, P. J. The pharmacology and therapeutic applications of monoclonal antibodies. *Pharmacol. Res. Perspect.* **7**, e00535 (2019).
44. Le Basle, Y., Chennell, P., Tokhadze, N., Astier, A. & Sautou, V. Physicochemical Stability of Monoclonal Antibodies: A Review. *J. Pharm. Sci.* **109**, 169–190 (2020).
45. Temel, D. B., Landsman, P. & Brader, M. L. Chapter Fourteen - Orthogonal Methods for Characterizing the Unfolding of Therapeutic Monoclonal Antibodies: Differential Scanning Calorimetry, Isothermal Chemical Denaturation, and Intrinsic Fluorescence with Concomitant Static Light Scattering. in *Methods in Enzymology* (ed. Feig, A. L.) vol. 567 359–389 (Academic Press, 2016).
46. Gooran, N. & Kopra, K. Fluorescence-Based Protein Stability Monitoring—A Review. *Int. J. Mol. Sci.* **25**, 1764 (2024).
47. Bai, N., Roder, H., Dickson, A. & Karanicolas, J. Isothermal Analysis of ThermoFluor Data can readily provide Quantitative Binding Affinities. *Sci. Rep.* **9**, 2650 (2019).

48. Durowoju, I. B., Bhandal, K. S., Hu, J., Carpick, B. & Kirkitadze, M. Differential Scanning Calorimetry — A Method for Assessing the Thermal Stability and Conformation of Protein Antigen. *J. Vis. Exp. JoVE* 55262 (2017) doi:10.3791/55262.
49. Kunz, P. *et al.* The structural basis of nanobody unfolding reversibility and thermoresistance. *Sci. Rep.* **8**, 7934 (2018).
50. Manning, M. C. *et al.* Stability of Protein Pharmaceuticals: Recent Advances. *Pharm. Res.* **41**, 1301–1367 (2024).
51. Kunz, P. *et al.* Understanding opalescence measurements of biologics – A comparison study of methods, standards, and molecules. *Int. J. Pharm.* **628**, 122321 (2022).
52. Raut, A. S. & Kalonia, D. S. Opalescence in Monoclonal Antibody Solutions and Its Correlation with Intermolecular Interactions in Dilute and Concentrated Solutions. *J. Pharm. Sci.* **104**, 1263–1274 (2015).
53. Kingsbury, J. S., Lantz, M. M., Saini, A., Wang, M. Z. & Gokarn, Y. R. Characterization of Opalescence in low Volume Monoclonal Antibody Solutions Enabled by Microscale Nephelometry. *J. Pharm. Sci.* **110**, 3176–3182 (2021).
54. Trabjerg, E., Nazari, Z. E. & Rand, K. D. Conformational analysis of complex protein states by hydrogen/deuterium exchange mass spectrometry (HDX-MS): Challenges and emerging solutions. *TrAC Trends Anal. Chem.* **106**, 125–138 (2018).
55. Narang, D., Lento, C. & J Wilson, D. HDX-MS: An Analytical Tool to Capture Protein Motion in Action. *Biomedicines* **8**, 224 (2020).
56. Lengyel, J., Hnath, E., Storms, M. & Wohlfarth, T. Towards an integrative structural biology approach: combining Cryo-TEM, X-ray crystallography, and NMR. *J. Struct. Funct. Genomics* **15**, 117–124 (2014).

57. Tokunaga, Y. & Takeuchi, K. Role of NMR in High Ordered Structure Characterization of Monoclonal Antibodies. *Int. J. Mol. Sci.* **22**, 46 (2020).
58. Song, Y., Yu, D., Mayani, M., Mussa, N. & Li, Z. J. Monoclonal antibody higher order structure analysis by high throughput protein conformational array. *mAbs* **10**, 397–405 (2018).
59. Kuzman, D. *et al.* Long-term stability predictions of therapeutic monoclonal antibodies in solution using Arrhenius-based kinetics. *Sci. Rep.* **11**, 20534 (2021).
60. Bunc, M., Hadži, S., Graf, C., Bončina, M. & Lah, J. Aggregation Time Machine: A Platform for the Prediction and Optimization of Long-Term Antibody Stability Using Short-Term Kinetic Analysis. *J. Med. Chem.* **65**, 2623–2632 (2022).
61. Huelsmeyer, M. *et al.* A universal tool for stability predictions of biotherapeutics, vaccines and in vitro diagnostic products. *Sci. Rep.* **13**, 10077 (2023).
62. Izadi, S., Patapoff, T. W. & Walters, B. T. Multiscale Coarse-Grained Approach to Investigate Self-Association of Antibodies. *Biophys. J.* **118**, 2741–2754 (2020).
63. Mahmoud, A. H., Masters, M., Lee, S. J. & Lill, M. A. Accurate Sampling of Macromolecular Conformations Using Adaptive Deep Learning and Coarse-Grained Representation. *J. Chem. Inf. Model.* **62**, 1602–1617 (2022).
64. Chowdhury, A. *et al.* Coarse-Grained Molecular Dynamics Simulations for Understanding the Impact of Short-Range Anisotropic Attractions on Structure and Viscosity of Concentrated Monoclonal Antibody Solutions. *Mol. Pharm.* (2020) doi:10.1021/acs.molpharmaceut.9b00960.
65. Nissley, D. Coarse-grained models of antibody solutions | Oxford Protein Informatics Group. <https://www.blopig.com/blog/2022/11/coarse-grained-models-of-antibody-solutions/> (2022).

66. Kanada, R., Terayama, K., Tokuhisa, A., Matsumoto, S. & Okuno, Y. Enhanced Conformational Sampling with an Adaptive Coarse-Grained Elastic Network Model Using Short-Time All-Atom Molecular Dynamics. *J. Chem. Theory Comput.* **18**, 2062–2074 (2022).
67. Stradner, A. & Schurtenberger, P. Potential and limits of a colloid approach to protein solutions. *Soft Matter* **16**, 307–323 (2020).
68. Agmo Hernández, V. An overview of surface forces and the DLVO theory. *ChemTexts* **9**, 10 (2023).
69. Wu, J. Understanding the Electric Double-Layer Structure, Capacitance, and Charging Dynamics. *Chem. Rev.* **122**, 10821–10859 (2022).
70. Kamble, S. *et al.* Revisiting Zeta Potential, the Key Feature of Interfacial Phenomena, with Applications and Recent Advancements. *ChemistrySelect* **7**, e202103084 (2022).
71. Schermeyer, M.-T., Wöll, A. K., Kokke, B., Eppink, M. & Hubbuch, J. Characterization of highly concentrated antibody solution - A toolbox for the description of protein long-term solution stability. *mAbs* (2017).
72. Zeta Potential Analysis (2:5). *Chemistry LibreTexts*
[https://chem.libretexts.org/Bookshelves/Analytical_Chemistry/Physical_Methods_in_Chemistry_and_Nano_Science_\(Barron\)/02%3A_Physical_and_Thermal_Analysis/2.05%3A_Zeta_Potential_Analysis](https://chem.libretexts.org/Bookshelves/Analytical_Chemistry/Physical_Methods_in_Chemistry_and_Nano_Science_(Barron)/02%3A_Physical_and_Thermal_Analysis/2.05%3A_Zeta_Potential_Analysis) (2016).
73. Mohammadi-Jam, S., Waters, K. E. & Greenwood, R. W. A review of zeta potential measurements using electroacoustics. *Adv. Colloid Interface Sci.* **309**, 102778 (2022).
74. Roche, A. Intermolecular interactions and rheological properties in monoclonal antibody solutions. (University of Manchester, 2021).

75. Connolly, B. D. *et al.* Weak Interactions Govern the Viscosity of Concentrated Antibody Solutions: High-Throughput Analysis Using the Diffusion Interaction Parameter. *Biophys. J.* **103**, 69–78 (2012).
76. Bansal, R., Gupta, S. & Rathore, A. S. Analytical Platform for Monitoring Aggregation of Monoclonal Antibody Therapeutics. *Pharm. Res.* **36**, 1–11 (2019).
77. Geersing, T. H. *et al.* Aggregate Formation and Antibody Stability in Infusion Bags: The Impact of Manual and Robotic Compounding of Monoclonal Antibodies. *J. Pharm. Sci.* **113**, 1029–1037 (2024).
78. Lavoisier, A. & Schlaeppi, J.-M. Early developability screen of therapeutic antibody candidates using Taylor dispersion analysis and UV area imaging detection. *mAbs* **7**, 77–83 (2014).
79. Stetefeld, J., McKenna, S. A. & Patel, T. R. Dynamic light scattering: a practical guide and applications in biomedical sciences. *Biophys. Rev.* **8**, 409–427 (2016).
80. Malvern Instruments Limited. *Understanding the Colloidal Stability of Protein Therapeutics Using Dynamic Light Scattering.* <https://cdn.technologynetworks.com/TN/Resources/PDF/Whitepaper%20BP%20SP%201.pdf> (2014).
81. Bajaj, H., Sharma, V. K. & Kalonia, D. S. Determination of Second Virial Coefficient of Proteins Using a Dual-Detector Cell for Simultaneous Measurement of Scattered Light Intensity and Concentration in SEC-HPLC. *Biophys. J.* **87**, 4048–4055 (2004).
82. How to perform kD measurements. *NanoTemper Technologies* <https://support.nanotempertech.com/hc/en-us/articles/19261806416017-How-to-perform-kD-measurements>.

83. Dingfelder, F., Henriksen, A., Wahlund, P.-O., Arosio, P. & Lorenzen, N. Measuring Self-Association of Antibody Lead Candidates with Dynamic Light Scattering (DLS). *Ther. Antibodies Methods Protoc.* 241–258 (2022).
84. Ma, Y. *et al.* Determination of the second virial coefficient of bovine serum albumin under varying pH and ionic strength by composition-gradient multi-angle static light scattering. *J. Biol. Phys.* **41**, 85–97 (2015).
85. Rakel, N., Bauer, K. C., Galm, L. & Hubbuch, J. From osmotic second virial coefficient (B₂₂) to phase behavior of a monoclonal antibody. *Biotechnol. Prog.* **31**, 438–451 (2015).
86. Razinkov, V. I., Treuheit, M. J. & Becker, G. W. Accelerated Formulation Development of Monoclonal Antibodies (mAbs) and mAb-Based Modalities: Review of Methods and Tools. *J. Biomol. Screen.* **20**, 468–483 (2015).
87. Chaturvedi, S. K. *et al.* Measuring aggregates, self-association, and weak interactions in concentrated therapeutic antibody solutions. *mAbs* (2020).
88. Dear, B. J., Hung, J. J., Truskett, T. M. & Johnston, K. P. Contrasting the Influence of Cationic Amino Acids on the Viscosity and Stability of a Highly Concentrated Monoclonal Antibody. *Pharm. Res.* **34**, 193–207 (2017).
89. Wang, W., Lilyestrom, W. G., Hu, Z. Y. & Scherer, T. M. Cluster Size and Quinary Structure Determine the Rheological Effects of Antibody Self-Association at High Concentrations. *J. Phys. Chem. B* **122**, 2138–2154 (2018).
90. Roche, A. *et al.* Towards an improved prediction of concentrated antibody solution viscosity using the Huggins coefficient. *J. Colloid Interface Sci.* **607**, 1813–1824 (2022).

91. Yadav, S., Shire, S. J. & Kalonia, D. S. Viscosity Behavior of High-Concentration Monoclonal Antibody Solutions: Correlation with Interaction Parameter and Electroviscous Effects. *J. Pharm. Sci.* **101**, 998–1011 (2012).
92. Shi, S., Uchida, M., Cheung, J., Antochshuk, V. & Shameem, M. Method qualification and application of diffusion interaction parameter and virial coefficient. *Int. J. Biol. Macromol.* **62**, 487–493 (2013).
93. Thiagarajan, G., Semple, A., James, J. K., Cheung, J. K. & Shameem, M. A comparison of biophysical characterization techniques in predicting monoclonal antibody stability. *mAbs* (2016).
94. Austin, J., Fernandes, D., Ruzsala, M. J. A., Hill, N. & Corbett, J. Routine, ensemble characterisation of electrophoretic mobility in high and saturated ionic dispersions. *Sci. Rep.* **10**, 4628 (2020).
95. Oyama, H. *et al.* Relation of Colloidal and Conformational Stabilities to Aggregate Formation in a Monoclonal Antibody. *J. Pharm. Sci.* **109**, 308–315 (2020).
96. Sorret, L. L., DeWinter, M. A., Schwartz, D. K. & Randolph, T. W. Challenges in Predicting Protein-Protein Interactions from Measurements of Molecular Diffusivity. *Biophys. J.* **111**, 1831–1842 (2016).
97. Liu, Y. *et al.* High-throughput screening for developability during early-stage antibody discovery using self-interaction nanoparticle spectroscopy. *mAbs* (2014) doi:10.4161/mabs.27431.
98. Improving antibody drug development using bionanotechnology. *Curr. Opin. Biotechnol.* **74**, 137–145 (2022).
99. Janke, J. J. *et al.* Computational Screening for mAb Colloidal Stability with Coarse-Grained, Molecular-Scale Simulations. *J. Phys. Chem. B* **128**, 1515–1526 (2024).

100. Ramazi, S. & Zahiri, J. Post-translational modifications in proteins: resources, tools and prediction methods. *Database J. Biol. Databases Curation* **2021**, baab012 (2021).
101. Mimura, Y., Saldova, R., Mimura-Kimura, Y., Rudd, P. M. & Jefferis, R. Micro-Heterogeneity of Antibody Molecules. in *Antibody Glycosylation* 1–26 (Springer, Cham, 2021). doi:10.1007/978-3-030-76912-3_1.
102. Boune, S., Hu, P., Epstein, A. L. & Khawli, L. A. Principles of N-Linked Glycosylation Variations of IgG-Based Therapeutics: Pharmacokinetic and Functional Considerations. *Antibodies* **9**, 22 (2020).
103. Nguyen, N. T. B. *et al.* Optimizing effector functions of monoclonal antibodies via tailored N-glycan engineering using a dual landing pad CHO targeted integration platform. *Sci. Rep.* **13**, 15620 (2023).
104. N-glycosylation heterogeneity and the influence on structure, function and pharmacokinetics of monoclonal antibodies and Fc fusion proteins. *Eur. J. Pharm. Biopharm.* **100**, 94–100 (2016).
105. Structural Analysis of Human IgG-Fc Glycoforms Reveals a Correlation Between Glycosylation and Structural Integrity. *J. Mol. Biol.* **325**, 979–989 (2003).
106. Kaur, H. Characterization of glycosylation in monoclonal antibodies and its importance in therapeutic antibody development. *Crit. Rev. Biotechnol.* (2021).
107. Geng, S.-L. *et al.* Recombinant therapeutic proteins degradation and overcoming strategies in CHO cells. *Appl. Microbiol. Biotechnol.* **108**, 182 (2024).
108. Dunphy, K., Dowling, P., Bazou, D. & O’Gorman, P. Current Methods of Post-Translational Modification Analysis and Their Applications in Blood Cancers. *Cancers* **13**, 1930 (2021).

109. Chen, X., Shi, S.-P., Xu, H.-D., Suo, S.-B. & Qiu, J.-D. A homology-based pipeline for global prediction of post-translational modification sites. *Sci. Rep.* **6**, 25801 (2016).
110. H. Li, G. X., Vogel, C. & Choi, H. PTMscape: an open source tool to predict generic post-translational modifications and map modification crosstalk in protein domains and biological processes. *Mol. Omics* **14**, 197–209 (2018).
111. Yan, Y. *et al.* MIND-S is a deep-learning prediction model for elucidating protein post-translational modifications in human diseases. *Cell Rep. Methods* **3**, (2023).
112. Wang, D. *et al.* MusiteDeep: a deep-learning based webserver for protein post-translational modification site prediction and visualization. *Nucleic Acids Res.* **48**, W140–W146 (2020).
113. Satława, T. *et al.* LAP: Liability Antibody Profiler by sequence & structural mapping of natural and therapeutic antibodies. *PLOS Comput. Biol.* **20**, e1011881 (2024).
114. Ito, T. *et al.* Host cell proteins in monoclonal antibody processing: Control, detection, and removal. *Biotechnol. Prog.* **n/a**, e3448.
115. Jones, M. *et al.* “High-risk” host cell proteins (HCPs): A multi-company collaborative view. *Biotechnol. Bioeng.* **118**, 2870–2885 (2021).
116. Pham, N. B. & Meng, W. S. Protein aggregation and immunogenicity of biotherapeutics. *Int. J. Pharm.* **585**, 119523 (2020).
117. Loisel, S. *et al.* Relevance, advantages and limitations of animal models used in the development of monoclonal antibodies for cancer treatment. *Crit. Rev. Oncol. Hematol.* **62**, 34–42 (2007).
118. From cell line development to the formulated drug product: The art of manufacturing therapeutic monoclonal antibodies. *Int. J. Pharm.* **594**, 120164 (2021).

119. Wohlenberg, O. J. *et al.* Optimization of a mAb production process with regard to robustness and product quality using quality by design principles. *Eng. Life Sci.* **22**, 484–494 (2022).
120. Clarke, H. *et al.* When will we have a clone? An industry perspective on the typical CLD timeline. *Biotechnol. Prog.* **n/a**, e3449.
121. Deorkar, N., Oh, J. & Vengsarkar, P. *Maximising-mAbs-Purification-Efficiency_Focus-Areas-for-Reducing-Bottlenecks-in-Downstream-Processing.Pdf*. https://international-biopharma.com/wp-content/uploads/2021/12/Maximising-mAbs-Purification-Efficiency_Focus-Areas-for-Reducing-Bottlenecks-in-Downstream-Processing.pdf (2021).
122. Joshi, V., Shivach, T., Kumar, V., Yadav, N. & Rathore, A. Avoiding antibody aggregation during processing: Establishing hold times. *Biotechnol. J.* **9**, 1195–1205 (2014).
123. Kannan, A., Shieh, I. C., Negulescu, P. G., Chandran Suja, V. & Fuller, G. G. Adsorption and Aggregation of Monoclonal Antibodies at Silicone Oil–Water Interfaces. *Mol. Pharm.* **18**, 1656–1665 (2021).
124. Kanthe, A. D. *et al.* Armoring the Interface with Surfactants to Prevent the Adsorption of Monoclonal Antibodies. *ACS Appl. Mater. Interfaces* **12**, 9977–9988 (2020).
125. Shen, K. *et al.* Competitive Adsorption of a Monoclonal Antibody and Nonionic Surfactant at the PDMS/Water Interface. *Mol. Pharm.* **20**, 2502–2512 (2023).
126. Saurabh, S. *et al.* Mechanistic Insights into the Adsorption of Monoclonal Antibodies at the Water/Vapor Interface. *Mol. Pharm.* **21**, 704–717 (2024).

127. Das, T. K. *et al.* Stress Factors in mAb Drug Substance Production Processes: Critical Assessment of Impact on Product Quality and Control Strategy. *J. Pharm. Sci.* **109**, 116–133 (2020).
128. Fernandez-Cerezo, L. *et al.* An ultra scale-down method to investigate monoclonal antibody processing during tangential flow filtration using ultrafiltration membranes. *Biotechnol. Bioeng.* **116**, 581–590 (2019).
129. Kollár, É., Balázs, B., Tari, T. & Siro, I. Development challenges of high concentration monoclonal antibody formulations. *Drug Discov. Today Technol.* (2020).
130. Yang, Y., Velayudhan, A., Thornhill, N. F. & Farid, S. S. Multi-criteria manufacturability indices for ranking high-concentration monoclonal antibody formulations. *Biotechnol. Bioeng.* **114**, 2043–2056 (2017).
131. Lenk, R. S. The Characterisation of Viscous Flow. Viscosity, Shear Rate and Shear Stress. in *Polymer Rheology* (ed. Lenk, R. S.) 1–14 (Springer Netherlands, Dordrecht, 1978). doi:10.1007/978-94-010-9666-9_1.
132. Bair, S. Shear Dependence of Viscosity. in *Encyclopedia of Tribology* (eds. Wang, Q. J. & Chung, Y.-W.) 3074–3078 (Springer US, Boston, MA, 2013). doi:10.1007/978-0-387-92897-5_598.
133. Basics of rheology | Anton Paar Wiki. *Anton Paar* <https://wiki.anton-paar.com/en/basics-of-rheology/>.
134. Chapter 9: Fluids - Microfluidics: Modeling, Mechanics and Mathematics [Book]. <https://www.oreilly.com/library/view/microfluidics-modeling-mechanics/9781455731510/B9781455731411500095.xhtml>.
135. Einstein, A. Eine neue Bestimmung der Moleküldimensionen. *Ann. Phys.* **324**, 289–306 (1906).

136. Jeffery, G. B. & Filon, L. N. G. The motion of ellipsoidal particles immersed in a viscous fluid. *Proc. R. Soc. Lond. Ser. Contain. Pap. Math. Phys. Character* **102**, 161–179 (1997).
137. Smoluchowski, M. v. Theoretische Bemerkungen über die Viskosität der Kolloide. *Kolloid-Z.* **18**, 190–195 (1916).
138. Booth, F. & Mott, N. F. The electroviscous effect for suspensions of solid spherical particles. *Proc. R. Soc. Lond. Ser. Math. Phys. Sci.* **203**, 533–551 (1997).
139. Mooney, M. The viscosity of a concentrated suspension of spherical particles. *J. Colloid Sci.* **6**, 162–170 (1951).
140. PAL, R. Evaluation of the mooney viscosity/concentration equation for liquid-liquid emulsions. *Chem. Eng. Commun.* (1990) doi:10.1080/00986449008940571.
141. Krieger, I. M. & Dougherty, T. J. A Mechanism for Non-Newtonian Flow in Suspensions of Rigid Spheres. *Trans. Soc. Rheol.* **3**, 137–152 (1959).
142. Ross, P. D. & Minton, A. P. Hard quasispherical model for the viscosity of hemoglobin solutions. *Biochem. Biophys. Res. Commun.* **76**, 971–976 (1977).
143. Sarangapani, P. S., Hudson, S. D., Migler, K. B. & Pathak, J. A. The limitations of an exclusively colloidal view of protein solution hydrodynamics and rheology. *Biophys. J.* **105**, 2418–2426 (2013).
144. Tomar, D. S., Kumar, S., Singh, S. K., Goswami, S. & Li, L. Molecular basis of high viscosity in concentrated antibody solutions: Strategies for high concentration drug product development. *mAbs* **8**, 216–228 (2016).
145. Kanai, S., Liu, J., Patapoff, T. W. & Shire, S. J. Reversible Self-Association of a Concentrated Monoclonal Antibody Solution Mediated by Fab–Fab Interaction That Impacts Solution Viscosity. *J. Pharm. Sci.* **97**, 4219–4227 (2008).

146. Prass, T. M., Garidel, P., Blech, M. & Schäfer, L. V. Viscosity Prediction of High-Concentration Antibody Solutions with Atomistic Simulations. *J. Chem. Inf. Model.* **63**, 6129–6140 (2023).
147. Schmitt, J., Razvi, A. & Grapentin, C. Predictive modeling of concentration-dependent viscosity behavior of monoclonal antibody solutions using artificial neural networks. *mAbs* **15**, 2169440 (2023).
148. Schwenger, W., Pellet, C., Attonaty, D. & Authelin, J.-R. An Empirical Quantitative Model Describing Simultaneously Temperature and Concentration Effects on Protein Solution Viscosity. *J. Pharm. Sci.* **109**, 1281–1287 (2020).
149. Schmit, J. D. *et al.* Entanglement Model of Antibody Viscosity. *J. Phys. Chem. B* **118**, 5044–5049 (2014).
150. Ramallo, N., Paudel, S. & Schmit, J. Cluster Formation and Entanglement in the Rheology of Antibody Solutions. *J. Phys. Chem. B* **123**, 3916–3923 (2019).
151. Lai, P.-K. *et al.* Machine Learning Applied to Determine the Molecular Descriptors Responsible for the Viscosity Behavior of Concentrated Therapeutic Antibodies. *Mol. Pharm.* (2021) doi:10.1021/acs.molpharmaceut.0c01073.
152. Ertelt, M. *et al.* Combining machine learning with structure-based protein design to predict and engineer post-translational modifications of proteins. *PLOS Comput. Biol.* **20**, e1011939 (2024).
153. Makowski, E. K. *et al.* Reduction of monoclonal antibody viscosity using interpretable machine learning. *mAbs* **16**, 2303781 (2024).
154. Pathak, J. A., Sologuren, R. R. & Narwal, R. Do clustering monoclonal antibody solutions really have a concentration dependence of viscosity? *Biophys. J.* **104**, 913–923 (2013).

155. Wang, W., Alphonse Ignatius, A., Ohtake, S. & Yang, T.-C. Introduction to High-Concentration Proteins. in *Challenges in Protein Product Development* (eds. Warne, N. W. & Mahler, H.-C.) 99–123 (Springer International Publishing, Cham, 2018). doi:10.1007/978-3-319-90603-4_4.
156. George, H. F. & Qureshi, F. Newton's Law of Viscosity, Newtonian and Non-Newtonian Fluids. in *Encyclopedia of Tribology* (eds. Wang, Q. J. & Chung, Y.-W.) 2416–2420 (Springer US, Boston, MA, 2013). doi:10.1007/978-0-387-92897-5_143.
157. Castellanos, M. M., Pathak, J. A., Leach, W., Bishop, S. M. & Colby, R. H. Explaining the Non-Newtonian Character of Aggregating Monoclonal Antibody Solutions Using Small-Angle Neutron Scattering. *Biophys. J.* **107**, 469–476 (2014).
158. Woldeyes, M. A., Qi, W., Razinkov, V. I., Furst, E. M. & Roberts, C. J. Temperature Dependence of Protein Solution Viscosity and Protein–Protein Interactions: Insights into the Origins of High-Viscosity Protein Solutions. *Mol. Pharm.* **17**, 4473–4482 (2020).
159. Difference Between Shear & Extensional Viscosity. <https://blog.rheosense.com/difference-between-shear-extensional-viscosity>.
160. James, D. F. Extensional Viscosity, An Elusive Property of Mobile Liquids. in *Third European Rheology Conference and Golden Jubilee Meeting of the British Society of Rheology* (ed. Oliver, D. R.) 241–243 (Springer Netherlands, Dordrecht, 1990). doi:10.1007/978-94-009-0781-2_86.
161. Li, L. *et al.* Concentration Dependent Viscosity of Monoclonal Antibody Solutions: Explaining Experimental Behavior in Terms of Molecular Properties. *Pharm. Res.* **31**, 3161–3178 (2014).
162. How to measure viscosity | Anton Paar Wiki. *Anton Paar* <https://wiki.anton-paar.com/en/how-to-measure-viscosity/>.

163. Bhattad, A. Review on viscosity measurement: devices, methods and models. *J. Therm. Anal. Calorim.* **148**, 6527–6543 (2023).
164. Xia, Q., Xiao, H., Pan, Y. & Wang, L. Microrheology, advances in methods and insights. *Adv. Colloid Interface Sci.* **257**, 71–85 (2018).
165. Escobar, E. L. N., Vaclaw, M. C., Lozenski, J. T. & Dhar, P. Using Passive Microrheology to Measure the Evolution of the Rheological Properties of NIST mAb Formulations during Adsorption to the Air–Water Interface. *Langmuir* **40**, 4789–4800 (2024).
166. Lewis, C. M. *et al.* The viscoelasticity of high concentration monoclonal antibodies using particle tracking microrheology. *APL Bioeng.* **8**, 026105 (2024).
167. Pindrus, M. A., Shire, S. J., Yadav, S. & Kalonia, D. S. Challenges in Determining Intrinsic Viscosity Under Low Ionic Strength Solution Conditions. *Pharm. Res.* **34**, 836–846 (2017).
168. Li, J., Cheng, Y., Chen, X. & Zheng, S. Impact of electroviscous effect on viscosity in developing highly concentrated protein formulations: Lessons from non-protein charged colloids. *Int. J. Pharm. X* **1**, 100002 (2019).
169. Mcdonogh, R. W. & Hunter, R. J. The Primary Electroviscous Effect. *J. Rheol.* **27**, 189–199 (1983).
170. Huisman, I. H., Prádanos, P. & Hernández, A. Electrokinetic characterisation of ultrafiltration membranes by streaming potential, electroviscous effect, and salt retention. *J. Membr. Sci.* **178**, 55–64 (2000).
171. Pathak, J. A. *et al.* Comparison of Huggins Coefficients and Osmotic Second Virial Coefficients of Buffered Solutions of Monoclonal Antibodies. *Polymers* **13**, 601 (2021).

172. Laue, T. Proximity energies: a framework for understanding concentrated solutions. *J. Mol. Recognit.* **25**, 165–173 (2012).
173. Lai, P.-K., Austin Gallegos, Mody, N., Sathish, H. A. & Trout, B. L. Machine learning prediction of antibody aggregation and viscosity for high concentration formulation development of protein therapeutics. *mAbs* **14**, (2022).
174. Kingsbury, J. S. *et al.* A single molecular descriptor to predict solution behavior of therapeutic antibodies. *Sci. Adv.* **6**, eabb0372 (2020).
175. Mieczkowski, C. *et al.* Characterization and Modeling of Reversible Antibody Self-Association Provide Insights into Behavior, Prediction, and Correction. *Antibodies* **10**, 8 (2021).
176. Esfandiary, R., Parupudi, A., Casas-Finet, J., Gadre, D. & Sathish, H. Mechanism of Reversible Self-Association of a Monoclonal Antibody: Role of Electrostatic and Hydrophobic Interactions. *J. Pharm. Sci.* **104**, 577–586 (2015).
177. Xu, X. *et al.* Deciphering the High Viscosity of a Therapeutic Monoclonal Antibody in High Concentration Formulations by Microdialysis-Hydrogen/Deuterium Exchange Mass Spectrometry. *J. Pharm. Sci.* **111**, 1335–1345 (2022).
178. Nichols, P. *et al.* Rational design of viscosity reducing mutants of a monoclonal antibody: Hydrophobic versus electrostatic inter-molecular interactions. *mAbs* **7**, 212–230 (2015).
179. Sormanni, P. & Vendruscolo, M. Protein Solubility Predictions Using the CamSol Method in the Study of Protein Homeostasis. *Cold Spring Harb. Perspect. Biol.* **11**, a033845 (2019).
180. Understanding and controlling the molecular mechanisms of protein aggregation in mAb therapeutics. *Biotechnol. Adv.* **67**, 108192 (2023).

181. Roberts, C. J. Therapeutic protein aggregation: mechanisms, design, and control. *Trends Biotechnol.* **32**, 372–380 (2014).
182. Heads, J. T., Kelm, S., Tyson, K. & Lawson, A. D. G. A computational method for predicting the aggregation propensity of IgG1 and IgG4(P) mAbs in common storage buffers. *mAbs* **14**, 2138092 (2022).
183. Conchillo-Solé, O. *et al.* AGGRESKAN: a server for the prediction and evaluation of ‘hot spots’ of aggregation in polypeptides. *BMC Bioinformatics* **8**, 65 (2007).
184. Oliveberg, M. Waltz, an exciting new move in amyloid prediction. *Nat. Methods* **7**, 187–188 (2010).
185. Fernandez-Escamilla, A.-M., Rousseau, F., Schymkowitz, J. & Serrano, L. Prediction of sequence-dependent and mutational effects on the aggregation of peptides and proteins. *Nat. Biotechnol.* **22**, 1302–1306 (2004).
186. Sankar, K., Krystek, S. R., Carl, S. M., Day, T. & Maier, J. K. X. AggScore: Prediction of aggregation-prone regions in proteins based on the distribution of surface patches. *Proteins* **86**, 1147–1156 (2018).
187. Voynov, V., Chennamsetty, N., Kayser, V., Helk, B. & Trout, B. L. Predictive tools for stabilization of therapeutic proteins. *mAbs* **1**, 580–582 (2009).
188. Sormanni, P., Aprile, F. A. & Vendruscolo, M. The CamSol Method of Rational Design of Protein Mutants with Enhanced Solubility. *J. Mol. Biol.* **427**, 478–490 (2015).
189. Nicoud, L., Lattuada, M., Yates, A. & Morbidelli, M. Impact of aggregate formation on the viscosity of protein solutions. *Soft Matter* **11**, 5513–5522 (2015).
190. Sleutel, M. *et al.* Does Solution Viscosity Scale the Rate of Aggregation of Folded Proteins? *J. Phys. Chem. Lett.* **3**, 1258–1263 (2012).

191. Elkordy, A. A., Parveen, A. & Haj-Ahmad, R. Chapter Four - Route of monoclonal antibodies administration. in *Formulation of Monoclonal Antibody Therapies* (ed. Elkordy, A. A.) 209–258 (Academic Press, 2023). doi:10.1016/B978-0-12-823365-8.00005-0.
192. Jin, J.-F. *et al.* The optimal choice of medication administration route regarding intravenous, intramuscular, and subcutaneous injection. *Patient Prefer. Adherence* **9**, 923–942 (2015).
193. Luo, S. *et al.* Defining the right diluent for intravenous infusion of therapeutic antibodies. *mAbs* **12**, 1685814 (2019).
194. Collins, D. S. *et al.* Optimizing the Bioavailability of Subcutaneously Administered Biotherapeutics Through Mechanochemical Drivers. *Pharm. Res.* **34**, 2000–2011 (2017).
195. Sánchez-Félix, M., Burke, M., Chen, H. H., Patterson, C. & Mittal, S. Predicting bioavailability of monoclonal antibodies after subcutaneous administration: Open innovation challenge. *Adv. Drug Deliv. Rev.* **167**, 66–77 (2020).
196. Bittner, B. & Schmidt, J. Advancing Subcutaneous Dosing Regimens for Biotherapeutics: Clinical Strategies for Expedited Market Access. *BioDrugs* **38**, 23–46 (2024).
197. Sree, V., Zhong, X., Billionis, I., Ardekani, A. & Tepole, A. B. Optimizing autoinjector devices using physics-based simulations and Gaussian processes. *J. Mech. Behav. Biomed. Mater.* **140**, 105695 (2023).
198. Waller, C. F., Möbius, J. & Fuentes-Albuero, A. Intravenous and subcutaneous formulations of trastuzumab, and trastuzumab biosimilars: implications for clinical practice. *Br. J. Cancer* **124**, 1346–1352 (2021).

199. Wang, H. *et al.* Comparison of Subcutaneous Injection Versus Intravenous Infusion of Cytarabine for Induction Therapy in Young Adult Acute Myeloid Leukemia: Results of a Prospective, Multicenter, Noninferiority, Randomized Trial. *Blood* **136**, 4 (2020).
200. Abad-Sazatornil, M. R. *et al.* Impact of the subcutaneous formulations of trastuzumab and rituximab on efficiency and resource optimization in Spanish hospitals: H-Excelencia study. *BMC Health Serv. Res.* **21**, 320 (2021).
201. Mao, C.-P. *et al.* Subcutaneous versus intravenous administration of rituximab: pharmacokinetics, CD20 target coverage and B-cell depletion in cynomolgus monkeys. *PloS One* **8**, e80533 (2013).
202. Viola, M. *et al.* Subcutaneous delivery of monoclonal antibodies: How do we get there? *J. Control. Release Off. J. Control. Release Soc.* **286**, 301–314 (2018).
203. Ryman, J. T. & Meibohm, B. Pharmacokinetics of Monoclonal Antibodies. *CPT Pharmacomet. Syst. Pharmacol.* **6**, 576–588 (2017).
204. Richter, W. F. & Jacobsen, B. Subcutaneous absorption of biotherapeutics: knowns and unknowns. *Drug Metab. Dispos. Biol. Fate Chem.* **42**, 1881–1889 (2014).
205. Desai, M., Kundu, A., Hageman, M., Lou, H. & Boisvert, D. Monoclonal antibody and protein therapeutic formulations for subcutaneous delivery: high-concentration, low-volume vs. low-concentration, high-volume. *mAbs* **15**, 2285277 (2023).
206. SHL Medical. How autoinjector devices breathe new life into injectable medicines. *Pharmaceutical Technology* <https://www.pharmaceutical-technology.com/sponsored/how-autoinjector-devices-breathe-new-life-into-injectable-medicines/> (2021).
207. Mathaes, R., Koulov, A., Joerg, S. & Mahler, H.-C. Subcutaneous Injection Volume of Biopharmaceuticals-Pushing the Boundaries. *J. Pharm. Sci.* **105**, 2255–2259 (2016).

208. Eakins, M. N. Plastic Pre-fillable Syringes and Vials: Progress Towards a Wider Acceptance. <https://www.americanpharmaceuticalreview.com/Featured-Articles/116942-Plastic-Pre-fillable-Syringes-and-Vials-Progress-Towards-a-Wider-Acceptance/> (2010).
209. Laurusonis, L., Cleathero, I. & Jensen, H. J. Chapter 33: Design and Development Considerations for Autoinjector Delivery Systems: Technology Developer and Industry Perspectives. in *Development of Biopharmaceutical Drug-Device Products* (eds. Jameel, F., Skoug, J. W. & Nesbitt, R. R.) vol. 35 791–811 (Springer International Publishing, Cham, 2020).
210. Fry, A. Injecting Highly Viscous Drugs. *Pharm. Technol.* **38**, (2014).
211. Schneider, A., Jost, R., Jordi, C. & Lange, J. Autoinjectors for large-volume subcutaneous drug delivery: a review of current research and future directions. *Expert Opin. Drug Deliv.* **20**, 815–830 (2023).
212. Dou, Z. *et al.* Performance characterization of spring actuated autoinjector devices for Emgality and Aimovig. *Curr. Med. Res. Opin.* **36**, 1343–1354 (2020).
213. Zhong, X. *et al.* The role of liquid rheological properties on the injection process of a spring-driven autoinjector. *Int. J. Pharm.* **628**, 122296 (2022).
214. Zhong, X., Billionis, I. & Ardekani, A. M. A framework to optimize spring-driven autoinjectors. *Int. J. Pharm.* **617**, 121588 (2022).
215. Jiskoot, W., Hawe, A., Menzen, T., Volkin, D. B. & Crommelin, D. J. A. Ongoing Challenges to Develop High Concentration Monoclonal Antibody-based Formulations for Subcutaneous Administration: Quo Vadis? *J. Pharm. Sci.* **111**, 861–867 (2022).
216. Sarin, D., Krishna, K., Nejadnik, M. R., Suryanarayanan, R. & Rathore, A. S. Impact of Excipient Extraction and Buffer Exchange on Recombinant Monoclonal Antibody Stability. *Mol. Pharm.* **21**, 1872–1883 (2024).

217. Saurabh, S. *et al.* Understanding the Stabilizing Effect of Histidine on mAb Aggregation: A Molecular Dynamics Study. *Mol. Pharm.* **19**, 3288–3303 (2022).
218. Ren, S. Effects of arginine in therapeutic protein formulations: a decade review and perspectives. *Antib. Ther.* **6**, 265–276 (2023).
219. Inoue, N., Takai, E., Arakawa, T. & Shiraki, K. Specific Decrease in Solution Viscosity of Antibodies by Arginine for Therapeutic Formulations. *Mol. Pharm.* **11**, 1889–1896 (2014).
220. He, F. *et al.* Effect of Sugar Molecules on the Viscosity of High Concentration Monoclonal Antibody Solutions. *Pharm. Res.* **28**, 1552–1560 (2011).
221. Sudrik, C., Cloutier, T., Pham, P., Samra, H. S. & Trout, B. L. Preferential interactions of trehalose, L-arginine.HCl and sodium chloride with therapeutically relevant IgG1 monoclonal antibodies. *mAbs* **9**, 1155–1168 (2017).
222. Zidar, M., Rozman, P., Belko-Parkel, K. & Ravnik, M. Control of viscosity in biopharmaceutical protein formulations. *J. Colloid Interface Sci.* **580**, 308–317 (2020).
223. Yadav, S. *et al.* Establishing a link between amino acid sequences and self-associating and viscoelastic behavior of two closely related monoclonal antibodies. *Pharm. Res.* **28**, 1750–1764 (2011).
224. Liu, J., Nguyen, M. D. H., Andya, J. D. & Shire, S. J. Reversible self-association increases the viscosity of a concentrated monoclonal antibody in aqueous solution. *J. Pharm. Sci.* **94**, 1928–1940 (2005).
225. Yadav, S., Liu, J., Shire, S. J. & Kalonia, D. S. Specific interactions in high concentration antibody solutions resulting in high viscosity. *J. Pharm. Sci.* **99**, 1152–1168 (2010).

226. Singh, S. N., Yadav, S., Shire, S. J. & Kalonia, D. S. Dipole-Dipole Interaction in Antibody Solutions: Correlation with Viscosity Behavior at High Concentration. *Pharm. Res.* **31**, 2549–2558 (2014).
227. Bethea, D. *et al.* Mechanisms of self-association of a human monoclonal antibody CNTO607. *Protein Eng. Des. Sel.* **25**, 531–538 (2012).
228. Wu, S.-J. *et al.* Structure-based engineering of a monoclonal antibody for improved solubility. *Protein Eng. Des. Sel.* **23**, 643–651 (2010).
229. Chow, C.-K., Allan, B. W., Chai, Q., Atwell, S. & Lu, J. Therapeutic Antibody Engineering To Improve Viscosity and Phase Separation Guided by Crystal Structure. *Mol. Pharm.* **13**, 915–923 (2016).
230. Geoghegan, J. C. *et al.* Mitigation of reversible self-association and viscosity in a human IgG1 monoclonal antibody by rational, structure-guided Fv engineering. *mAbs* **8**, 941–950 (2016).
231. Shan, L. *et al.* Developability Assessment of Engineered Monoclonal Antibody Variants with a Complex Self-Association Behavior Using Complementary Analytical and in Silico Tools. *Mol. Pharm.* **15**, 5697–5710 (2018).
232. Tilegenova, C. *et al.* Dissecting the molecular basis of high viscosity of monospecific and bispecific IgG antibodies. *mAbs* **12**, 1692764 (2020).
233. Apgar, J. R. *et al.* Modeling and mitigation of high-concentration antibody viscosity through structure-based computer-aided protein design. *PLOS ONE* **15**, e0232713 (2020).
234. Makowski, E. K. *et al.* Reduction of therapeutic antibody self-association using yeast-display selections and machine learning. *mAbs* (2022).
235. Dai, J. *et al.* Variable domain mutational analysis to probe the molecular mechanisms of high viscosity of an IgG1 antibody. *mAbs* **16**, 2304282 (2024).

236. Heisler, J., Kovner, D., Izadi, S., Zarzar, J. & Carter, P. J. Modulation of the high concentration viscosity of IgG1 antibodies using clinically validated Fc mutations. *mAbs* (2024).
237. Sharma, V. K. *et al.* In silico selection of therapeutic antibodies for development: Viscosity, clearance, and chemical stability. *Proc. Natl. Acad. Sci.* **111**, 18601–18606 (2014).
238. Tomar, D. S. *et al.* In-silico prediction of concentration-dependent viscosity curves for monoclonal antibody solutions. *mAbs* **9**, 476–489 (2017).
239. Agrawal, N. J. *et al.* Computational tool for the early screening of monoclonal antibodies for their viscosities. *mAbs* **8**, 43–48 (2016).
240. Lai, P.-K. DeepSCM: An efficient convolutional neural network surrogate model for the screening of therapeutic antibody viscosity. *Comput. Struct. Biotechnol. J.* **20**, 2143–2152 (2022).
241. Raybould, M. I. J. *et al.* Five computational developability guidelines for therapeutic antibody profiling. *Proc. Natl. Acad. Sci.* **116**, 4025–4030 (2019).
242. Thorsteinson, N., Gunn, J. R., Kelly, K., Long, W. & Labute, P. Structure-based charge calculations for predicting isoelectric point, viscosity, clearance, and profiling antibody therapeutics. *mAbs* **13**, 1981805 (2021).
243. Ahmed, L. *et al.* Intrinsic physicochemical profile of marketed antibody-based biotherapeutics. *Proc. Natl. Acad. Sci.* **118**, e2020577118 (2021).
244. Rai, B. K., Apgar, J. R. & Bennett, E. M. Low-data interpretable deep learning prediction of antibody viscosity using a biophysically meaningful representation. *Sci. Rep.* **13**, 2917 (2023).

245. Estes, B. *et al.* Sequence-Based Viscosity Prediction for Rapid Antibody Engineering. *Biomolecules* **14**, 617 (2024).
246. Ghosh, I., Gutka, H., Krause, M. E., Clemens, R. & Kashi, R. S. A systematic review of commercial high concentration antibody drug products approved in the US: formulation composition, dosage form design and primary packaging considerations. *mAbs* **15**, 2205540 (2023).
247. Prašnikar, M. *et al.* The search for novel proline analogs for viscosity reduction and stabilization of highly concentrated monoclonal antibody solutions. *Int. J. Pharm.* **655**, 124055 (2024).
248. Makowski, E. K. *et al.* Reduction of monoclonal antibody viscosity using interpretable machine learning. *mAbs* **16**, 2303781 (2024).
249. Hartl, J. *et al.* Dipolar Interactions and Protein Hydration in Highly Concentrated Antibody Formulations. *Mol. Pharm.* **19**, 494–507 (2022).
250. Chaudhri, A. *et al.* The Role of Amino Acid Sequence in the Self-Association of Therapeutic Monoclonal Antibodies: Insights from Coarse-Grained Modeling. *J. Phys. Chem. B* **117**, 1269–1279 (2013).
251. Yadav, S., Shire, S. J. & Kalonia, D. S. Factors affecting the viscosity in high concentration solutions of different monoclonal antibodies. *J. Pharm. Sci.* **99**, 4812–4829 (2010).
252. Proj, M. *et al.* Discovery of compounds with viscosity-reducing effects on biopharmaceutical formulations with monoclonal antibodies. *Comput. Struct. Biotechnol. J.* **20**, 5420–5429 (2022).

253. Srivastava, A. *et al.* Viscosity Reduction and Stability Enhancement of Monoclonal Antibody Formulations Using Derivatives of Amino Acids. *J. Pharm. Sci.* **111**, 2848–2856 (2022).
254. Wolf Pérez, A.-M., Lorenzen, N., Vendruscolo, M. & Sormanni, P. Assessment of Therapeutic Antibodies Developability by Combinations of In Vitro and In Silico Methods. *Ther. Antibodies Methods Protoc.* 57–113 (2022) doi:10.1007/978-1-0716-1450-1_4.
255. Fernandez-Escamilla, A.-M., Rousseau, F., Schymkowitz, J. & Serrano, L. Prediction of sequence-dependent and mutational effects on the aggregation of peptides and proteins. *Nat. Biotechnol.* **22**, 1302–1306 (2004).
256. Linding, R., Schymkowitz, J., Rousseau, F., Diella, F. & Serrano, L. A comparative study of the relationship between protein structure and beta-aggregation in globular and intrinsically disordered proteins. *J. Mol. Biol.* **342**, 345–353 (2004).
257. Agrawal, N. J. *et al.* Computational tool for the early screening of monoclonal antibodies for their viscosities. *mAbs* **8**, 43–48 (2016).
258. Kim, S. H., Yoo, H. J., Park, E. J. & Na, D. H. Nano Differential Scanning Fluorimetry-Based Thermal Stability Screening and Optimal Buffer Selection for Immunoglobulin G. *Pharm. Basel Switz.* **15**, (2021).
259. Vilar, S., Cozza, G. & Moro, S. Medicinal Chemistry and the Molecular Operating Environment (MOE): Application of QSAR and Molecular Docking to Drug Discovery. *Curr. Top. Med. Chem.* **8**, 1555–1572 (2008).
260. Raybould, M. I. J. & Deane, C. M. The Therapeutic Antibody Profiler for Computational Developability Assessment. *Ther. Antibodies* 115–125 (2022).
261. Wei, Y. *et al.* Improved Diffusion Interaction Parameter Measurement to Predict the Viscosity of Concentrated mAb Solutions. *Mol. Pharm.* **20**, 6420–6428 (2023).

262. Engineering Stability, Viscosity, and Immunogenicity of Antibodies by Computational Design - ScienceDirect.
<https://www.sciencedirect.com/science/article/pii/S0022354920300162?via%3Dihub#sec3>.
263. Protein aggregation and immunogenicity of biotherapeutics - ScienceDirect.
<https://www.sciencedirect.com/science/article/pii/S037851732030507X>.
264. Akbar, R. *et al.* In silico proof of principle of machine learning-based antibody design at unconstrained scale. *mAbs* **14**, 2031482 (2022).
265. Full article: Predicting Antibody Developability Profiles Through Early Stage Discovery Screening.
<https://www.tandfonline.com/doi/full/10.1080/19420862.2020.1743053>.
266. Wang, S. *et al.* Viscosity-Lowering Effect of Amino Acids and Salts on Highly Concentrated Solutions of Two IgG1 Monoclonal Antibodies. *Mol. Pharm.* **12**, 4478–4487 (2015).
267. Xu, A. Y. *et al.* Effects of Monovalent Salt on Protein-Protein Interactions of Dilute and Concentrated Monoclonal Antibody Formulations. *Antibodies* **11**, 24 (2022).
268. Full article: Calculation of therapeutic antibody viscosity with coarse-grained models, hydrodynamic calculations and machine learning-based parameters.
<https://www.tandfonline.com/doi/full/10.1080/19420862.2021.1907882>.
269. Lai, P.-K., Gallegos, A., Mody, N., Sathish, H. A. & Trout, B. L. Machine learning prediction of antibody aggregation and viscosity for high concentration formulation development of protein therapeutics. *mAbs* **14**, 2026208 (2022).

270. Yadav, S., Laue, T. M., Kalonia, D. S., Singh, S. N. & Shire, S. J. The Influence of Charge Distribution on Self-Association and Viscosity Behavior of Monoclonal Antibody Solutions. *Mol. Pharm.* **9**, 791–802 (2012).
271. Shukla, A. A., Wolfe, L. S., Mostafa, S. S. & Norman, C. Evolving trends in mAb production processes. *Bioeng. Transl. Med.* **2**, 58 (2017).
272. Kelley, B. Developing therapeutic monoclonal antibodies at pandemic pace. *Nat. Biotechnol.* **38**, 540–545 (2020).
273. Tihanyi, B. & Nyitray, L. Recent advances in CHO cell line development for recombinant protein production. *Drug Discov. Today Technol.* **38**, 25–34 (2020).
274. Majumdar, S., Desai, R., Hans, A., Dandekar, P. & Jain, R. From Efficiency to Yield: Exploring Recent Advances in CHO Cell Line Development for Monoclonal Antibodies. *Mol. Biotechnol.* 1–24 (2024) doi:10.1007/s12033-024-01060-6.
275. Kumar, D., Gangwar, N., Rathore, A. S. & Ramteke, M. Multi-objective optimization of monoclonal antibody production in bioreactor. *Chem. Eng. Process. - Process Intensif.* **180**, 108720 (2022).
276. Maier, M. *et al.* Tailoring polishing steps for effective removal of polysorbate-degrading host cell proteins in antibody purification. *Biotechnol. Bioeng.* **n/a**,
277. Aoyama, S., Matsumoto, Y., Mori, C. & Sota, K. Application of novel mixed mode chromatography (MMC) resins having a hydrophobic modified polyallylamine ligand for monoclonal antibody purification. *J. Chromatogr. B* **1191**, 123072 (2022).
278. Maruthamuthu, M. K., Rudge, S. R., Ardekani, A. M., Ladisch, M. R. & Verma, M. S. Process Analytical Technologies and Data Analytics for the Manufacture of Monoclonal Antibodies. *Trends Biotechnol.* **38**, 1169–1186 (2020).

279. Alhazmi, H. A. & Albratty, M. Analytical Techniques for the Characterization and Quantification of Monoclonal Antibodies. *Pharmaceuticals* **16**, 291 (2023).
280. Yu, L. X. *et al.* Understanding Pharmaceutical Quality by Design. *AAPS J.* **16**, 771–783 (2014).
281. Luciani, F. *et al.* Implementing quality by design for biotech products: Are regulators on track? *mAbs* **7**, 451–455 (2015).
282. Von Kreudenstein, T. S. *et al.* Improving biophysical properties of a bispecific antibody scaffold to aid developability: Quality by molecular design. *mAbs* **5**, 646–654 (2013).
283. Park, S.-Y., Park, C.-H., Choi, D.-H., Hong, J. K. & Lee, D.-Y. Bioprocess digital twins of mammalian cell culture for advanced biomanufacturing. *Curr. Opin. Chem. Eng.* **33**, 100702 (2021).
284. Tiwari, A., Masampally, V. S., Agarwal, A. & Rathore, A. S. Digital twin of a continuous chromatography process for mAb purification: Design and model-based control. *Biotechnol. Bioeng.* **120**, 748–766 (2023).
285. Kozorog, M. *et al.* Model-based process optimization for mAb chromatography. *Sep. Purif. Technol.* **305**, 122528 (2023).
286. Wahlgreen, M. R. *et al.* Modeling and Simulation of Upstream and Downstream Processes for Monoclonal Antibody Production. *IFAC-Pap.* **55**, 685–690 (2022).
287. Zhang, L., Parasnavis, S., Li, Z., Chen, J. & Cramer, S. Mechanistic modeling based process development for monoclonal antibody monomer-aggregate separations in multimodal cation exchange chromatography. *J. Chromatogr. A* **1602**, 317–325 (2019).
288. Saleh, D. *et al.* Modeling the impact of amino acid substitution in a monoclonal antibody on cation exchange chromatography. *Biotechnol. Bioeng.* **118**, 2923–2933 (2021).

289. Modeling of biopharmaceutical UF/DF from laboratory to manufacturing scale. *Comput. Chem. Eng.* **177**, 108337 (2023).
290. Whitaker, N. *et al.* Developability Assessments of Monoclonal Antibody Candidates to Minimize Aggregation During Large-Scale Ultrafiltration and Diafiltration (UF-DF) Processing. *J. Pharm. Sci.* **111**, 2998–3008 (2022).
291. Ultrafiltration concentration of monoclonal antibody solutions: Development of an optimized method minimizing aggregation. *J. Membr. Sci.* **342**, 50–59 (2009).
292. High concentration tangential flow ultrafiltration of stable monoclonal antibody solutions with low viscosities. *J. Membr. Sci.* **508**, 113–126 (2016).
293. Mohammadzadehmarandi, A. & Zydney, A. L. Buffer effects on protein sieving losses in ultrafiltration and their relationship to biophysical properties. *Biotechnol. Prog.* e3481 (2024) doi:10.1002/btpr.3481.
294. Zheng, K., Bantog, C. & Bayer, R. The impact of glycosylation on monoclonal antibody conformation and stability. *mAbs* **3**, 568–576 (2011).
295. Popovici, S.-T., Kok, W. Th. & Schoenmakers, P. J. Band broadening in size-exclusion chromatography of polydisperse samples. *J. Chromatogr. A* **1060**, 237–252 (2004).
296. Trappe, A. *et al.* Correlative *N*-glycan and charge variant analysis of cetuximab expressed in murine, chinese hamster and human expression systems. *J. Chromatogr. B* **1194**, 123186 (2022).
297. Alt, N. *et al.* Determination of critical quality attributes for monoclonal antibodies using quality by design principles. *Biologicals* **44**, 291–305 (2016).

298. Wang, S. *et al.* Early determination of potential critical quality attributes of therapeutic antibodies in developability studies through surface plasmon resonance-based relative binding activity assessment. *mAbs* (2024).
299. Xu, W.-J., Lin, Y., Mi, C.-L., Pang, J.-Y. & Wang, T.-Y. Progress in fed-batch culture for recombinant protein production in CHO cells. *Appl. Microbiol. Biotechnol.* **107**, 1063–1075 (2023).
300. Donaldson, J. S., Dale, M. P. & Rosser, S. J. Decoupling Growth and Protein Production in CHO Cells: A Targeted Approach. *Front. Bioeng. Biotechnol.* **9**, 658325 (2021).
301. Pereira, S., Kildegaard, H. F. & Andersen, M. R. Impact of CHO Metabolism on Cell Growth and Protein Production: An Overview of Toxic and Inhibiting Metabolites and Nutrients. *Biotechnol. J.* **13**, 1700499 (2018).
302. Ahmadi, S. *et al.* Monoclonal antibodies expression improvement in CHO cells by PiggyBac transposition regarding vectors ratios and design. *PLOS ONE* **12**, e0179902 (2017).
303. Sissolak, B., Lingg, N., Sommeregger, W., Striedner, G. & Vorauer-Uhl, K. Impact of mammalian cell culture conditions on monoclonal antibody charge heterogeneity: an accessory monitoring tool for process development. *J. Ind. Microbiol. Biotechnol.* **46**, 1167–1178 (2019).
304. Weng, Z., Jin, J., Shao, C. & Li, H. Reduction of charge variants by CHO cell culture process optimization. *Cytotechnology* **72**, 259–269 (2020).
305. Roche Diagnostics Gmb. Human IgG Assay for Cedex Bio & Bio HT Analyzers. https://custombiotech.roche.com/content/dam/acadia/brochure/575/17/CustomBiotech_Cedex_IgG_Assay.pdf (2023).

306. Haryadi, R. *et al.* Optimization of Heavy Chain and Light Chain Signal Peptides for High Level Expression of Therapeutic Antibodies in CHO Cells. *PLOS ONE* **10**, e0116878 (2015).
307. Wang, Y. *et al.* An innovative platform to improve asymmetric bispecific antibody assembly, purity, and expression level in stable pool and cell line development. *Biochem. Eng. J.* **188**, 108683 (2022).
308. Antibody sequence-based prediction of pH gradient elution in multimodal chromatography. *J. Chromatogr. A* **1711**, 464437 (2023).
309. Field, R. W. & Wu, J. J. Permeate Flux in Ultrafiltration Processes—Understandings and Misunderstandings. *Membranes* **12**, 187 (2022).
310. Lu, P. J. *et al.* Gelation of particles with short-range attraction. *Nature* **453**, 499–503 (2008).
311. Komarov, P. *et al.* On Molecular Gelation Mechanism of L-Cysteine Based Hydrogel. *Nanosci. Nanoeng. Publ.* **1**, 23–35 (2013).
312. Bonilla, J. C. & Clausen, M. P. Super-resolution microscopy to visualize and quantify protein microstructural organization in food materials and its relation to rheology: Egg white proteins. *Food Hydrocoll.* **124**, 107281 (2022).
313. Salinas, B. A. *et al.* Understanding and Modulating Opalescence and Viscosity in a Monoclonal Antibody Formulation. *J. Pharm. Sci.* **99**, 82–93 (2010).
314. Kheddo, P. *et al.* Investigating Liquid–Liquid Phase Separation of a Monoclonal Antibody Using Solution-State NMR Spectroscopy: Effect of Arg·Glu and Arg·HCl. *Mol. Pharm.* **14**, 2852–2860 (2017).

315. Bramham, J. E., Davies, S. A., Podmore, A. & Golovanov, A. P. Stability of a high-concentration monoclonal antibody solution produced by liquid–liquid phase separation. *mAbs* **13**, 1940666 (2021).
316. Jefferis, R. Posttranslational Modifications and the Immunogenicity of Biotherapeutics. *J. Immunol. Res.* **2016**, 5358272 (2016).
317. Vatsa, S. In silico prediction of post-translational modifications in therapeutic antibodies. *mAbs* (2022).
318. Gritti, F. & Meyyappan, S. Physical origin of the peak tailing of monoclonal antibodies in size-exclusion chromatography using bio-compatible systems and columns. *Anal. Bioanal. Chem.* **416**, 1281–1291 (2024).
319. Cui, X. *et al.* Global characterization of modifications to the charge isomers of IgG antibody. *J. Pharm. Anal.* **12**, 156–163 (2022).
320. Bryan, L., Clynes, M. & Meleady, P. The emerging role of cellular post-translational modifications in modulating growth and productivity of recombinant Chinese hamster ovary cells. *Biotechnol. Adv.* **49**, 107757 (2021).
321. Nigro, C. L. *et al.* NK-mediated antibody-dependent cell-mediated cytotoxicity in solid tumors: biological evidence and clinical perspectives. *Ann. Transl. Med.* **7**, 105–105 (2019).
322. Yu, J., Song, Y. & Tian, W. How to select IgG subclasses in developing anti-tumor therapeutic antibodies. *J. Hematol. Oncol. J Hematol Oncol* **13**, 45 (2020).
323. Cain, P., Huang, L., Tang, Y., Anguiano, V. & Feng, Y. Impact of IgG subclass on monoclonal antibody developability. *mAbs* **15**, 2191302 (2023).
324. Plomp, R. *et al.* Hinge-Region O-Glycosylation of Human Immunoglobulin G3 (IgG3). *Mol. Cell. Proteomics MCP* **14**, 1373–1384 (2015).

325. Bolton, M. J. *et al.* IgG3 subclass antibodies recognize antigenically drifted influenza viruses and SARS-CoV-2 variants through efficient bivalent binding. *Proc. Natl. Acad. Sci.* **120**, e2216521120 (2023).
326. Boero, E. *et al.* Natural Human Immunity Against Staphylococcal Protein A Relies on Effector Functions Triggered by IgG3. *Front. Immunol.* **13**, 834711 (2022).
327. Amaral, J., Inganäs, M., Cabral, J. & Prazeres, D. Study on the scale-up of human IgG3 purification using protein A affinity chromatography. *Bioseparation* **10**, 139–143 (2001).
328. Stapleton, N. M. *et al.* Competition for FcRn-mediated transport gives rise to short half-life of human IgG3 and offers therapeutic potential. *Nat. Commun.* **2**, 599 (2011).
329. Chu, T. H., Patz, E. F. J. & Ackerman, M. E. Coming together at the hinges: Therapeutic prospects of IgG3. *mAbs* **13**, 1882028 (2021).
330. Damelang, T., Rogerson, S. J., Kent, S. J. & Chung, A. W. Role of IgG3 in Infectious Diseases. *Trends Immunol.* **40**, 197–211 (2019).
331. Kim, S. H., Yoo, H. J., Park, E. J. & Na, D. H. Nano Differential Scanning Fluorimetry-Based Thermal Stability Screening and Optimal Buffer Selection for Immunoglobulin G. *Pharmaceuticals* **15**, 29 (2022).
332. Yadav, S., Shire, S. J. & Kalonia, D. S. Factors Affecting the Viscosity in High Concentration Solutions of Different Monoclonal Antibodies. *J. Pharm. Sci.* **99**, 4812–4829 (2010).
333. Ryazantsev, S., Tishchenko, V., Vasiliev, V., Zav'Yalov, V. & Abramov, V. Structure of human myeloma IgG3 K_uc. *Eur. J. Biochem.* **190**, 393–399 (1990).

334. Hansen, K. *et al.* A Mass-Spectrometry-Based Modelling Workflow for Accurate Prediction of IgG Antibody Conformations in the Gas Phase. *Angew. Chem.* **130**, 17440–17445 (2018).
335. Spiteri, V. A. *et al.* Solution structures of human myeloma IgG3 antibody reveal extended Fab and Fc regions relative to the other IgG subclasses. *J. Biol. Chem.* **297**, (2021).
336. Abendstein, L. *et al.* Complement is activated by elevated IgG3 hexameric platforms and deposits C4b onto distinct antibody domains. *Nat. Commun.* **14**, 4027 (2023).
337. Alsaid, H. *et al.* Non invasive imaging assessment of the biodistribution of GSK2849330, an ADCC and CDC optimized anti HER3 mAb, and its role in tumor macrophage recruitment in human tumor-bearing mice. *PLOS ONE* **12**, e0176075 (2017).
338. Irani, V. *et al.* Molecular properties of human IgG subclasses and their implications for designing therapeutic monoclonal antibodies against infectious diseases. *Mol. Immunol.* **67**, 171–182 (2015).
339. Liu, H. & May, K. Disulfide bond structures of IgG molecules: Structural variations, chemical modifications and possible impacts to stability and biological function. *mAbs* **4**, 17–23 (2012).
340. Li, W. *et al.* Antibody Aggregation: Insights from Sequence and Structure. *Antibodies* **5**, 19 (2016).
341. Chun, M.-S. & Lee, I. Rigorous estimation of effective protein charge from experimental electrophoretic mobilities for proteomics analysis using microchip electrophoresis. *Colloids Surf. Physicochem. Eng. Asp.* **318**, 191–198 (2008).
342. Understanding Electrophoretic Light Scattering. *Waters | Wyatt Technology*
<https://www.wyatt.com/library/theory/electrophoretic-light-scattering-theory.html>.

343. Ausserwöger, H. *et al.* Non-specificity as the sticky problem in therapeutic antibody development. *Nat. Rev. Chem.* **6**, 844–861 (2022).
344. Waibl, F. *et al.* Comparison of hydrophobicity scales for predicting biophysical properties of antibodies. *Front. Mol. Biosci.* **9**, (2022).
345. Lai, P.-K., Swan, J. W. & Trout, B. L. Calculation of therapeutic antibody viscosity with coarse-grained models, hydrodynamic calculations and machine learning-based parameters. *mAbs* **13**, 1907882 (2021).
346. Jiskoot, W., Hawe, A., Menzen, T., Volkin, D. B. & Crommelin, D. J. A. Ongoing Challenges to Develop High Concentration Monoclonal Antibody-based Formulations for Subcutaneous Administration: Quo Vadis? *J. Pharm. Sci.* **111**, 861–867 (2022).
347. Prass, T. M., Garidel, P., Blech, M. & Schäfer, L. V. Viscosity Prediction of High-Concentration Antibody Solutions with Atomistic Simulations. *J. Chem. Inf. Model.* **63**, 6129–6140 (2023).
348. Arzenšek, D., Kuzman, D. & Podgornik, R. Colloidal interactions between monoclonal antibodies in aqueous solutions. *J. Colloid Interface Sci.* **384**, 207–216 (2012).
349. Saito, S. *et al.* Behavior of Monoclonal Antibodies: Relation Between the Second Virial Coefficient (B_2) at Low Concentrations and Aggregation Propensity and Viscosity at High Concentrations. *Pharm. Res.* **29**, 397–410 (2012).
350. Skar-Gislinge, N., Camerin, F., Stradner, A., Zaccarelli, E. & Schurtenberger, P. Using Cluster Theory to Calculate the Experimental Structure Factors of Antibody Solutions. *Mol. Pharm.* (2023) doi:10.1021/acs.molpharmaceut.3c00191.
351. Linding, R., Schymkowitz, J., Rousseau, F., Diella, F. & Serrano, L. A Comparative Study of the Relationship Between Protein Structure and β -Aggregation in Globular and Intrinsically Disordered Proteins. *J. Mol. Biol.* **342**, 345–353 (2004).

352. Maurer-Stroh, S. *et al.* Exploring the sequence determinants of amyloid structure using position-specific scoring matrices. *Nat. Methods* **7**, 237–242 (2010).
353. Eisenberg, D., Schwarz, E., Komaromy, M. & Wall, R. Analysis of membrane and surface protein sequences with the hydrophobic moment plot. *J. Mol. Biol.* **179**, 125–142 (1984).
354. Ortega, A., Amorós, D. & García de la Torre, J. Prediction of Hydrodynamic and Other Solution Properties of Rigid Proteins from Atomic- and Residue-Level Models. *Biophys. J.* **101**, 892–898 (2011).
355. Tian, Z., Jiang, X., Chen, Z., Huang, C. & Qian, F. Quantifying Protein Shape to Elucidate Its Influence on Solution Viscosity in High-Concentration Electrolyte Solutions. *Mol. Pharm.* **21**, 1719–1728 (2024).
356. Lilyestrom, W. G., Yadav, S., Shire, S. J. & Scherer, T. M. Monoclonal Antibody Self-Association, Cluster Formation, and Rheology at High Concentrations. *J. Phys. Chem. B* **117**, 6373–6384 (2013).
357. Lu, W. & Mays, J. Chapter 7- Dilute solution viscometry of polymers. in *Molecular Characterization of Polymers* 261–280 (Elsevier, 2021).
358. García De La Torre, J., Huertas, M. L. & Carrasco, B. Calculation of Hydrodynamic Properties of Globular Proteins from Their Atomic-Level Structure. *Biophys. J.* **78**, 719–730 (2000).
359. Marc L. Mansfield, *, Jack F. Douglas, *, Saba Irfan, † and & Kang†, E.-H. Comparison of Approximate Methods for Calculating the Friction Coefficient and Intrinsic Viscosity of Nanoparticles and Macromolecules. *ACS Publications* <https://pubs.acs.org/doi/abs/10.1021/ma061069f> (2007) doi:10.1021/ma061069f.

360. Abdelmohsen, L. K. E. A., Rikken, R. S. M., Christianen, P. C. M., Van Hest, J. C. M. & Wilson, D. A. Shape characterization of polymersome morphologies via light scattering techniques. *Polymer* **107**, 445–449 (2016).
361. Muza, U. L., Williams, C. D. & Lederer, A. Unravelling the thermo-responsive evolution from single-chain to multiple-chain nanoparticles by thermal field-flow fractionation. *Polym. Chem.* **14**, 3302–3308 (2023).
362. Hydrodynamic Radius - Radius of Gyration | Malvern Panalytical. <https://www.malvernpanalytical.com/en/learn/knowledge-center/insights/size-matters-rh-versus-rg>.
363. Chong Meng Kok & Rudin, A. Relationship between the hydrodynamic radius and the radius of gyration of a polymer in solution. *Makromol. Chem., Rapid Commun.* **2**, (1981).
364. Hong, T., Iwashita, K. & Shiraki, K. Viscosity Control of Protein Solution by Small Solutes: A Review. *Curr. Protein Pept. Sci.* **19**, 746–758 (2018).
365. Rodrigues, D. *et al.* Product-Specific Impact of Viscosity Modulating Formulation Excipients During Ultra-High Concentration Biotherapeutics Drug Product Development. *J. Pharm. Sci.* **110**, 1077–1082 (2021).
366. Yearley, E. J. *et al.* Observation of Small Cluster Formation in Concentrated Monoclonal Antibody Solutions and Its Implications to Solution Viscosity. *Biophys. J.* **106**, 1763–1770 (2014).
367. Stone-Masui, J. & Watillon, A. Electroviscous effects in dispersions of monodisperse polystyrene latices. *J. Colloid Interface Sci.* **28**, 187–202 (1968).

368. Mock, M. *et al.* Development of in silico models to predict viscosity and mouse clearance using a comprehensive analytical data set collected on 83 scaffold-consistent monoclonal antibodies. *mAbs* **15**, 2256745 (2023).
369. Chowdhury, A. A. *et al.* Characterizing Protein–Protein Interactions and Viscosity of a Monoclonal Antibody from Low to High Concentration Using Small-Angle X-ray Scattering and Molecular Dynamics Simulations. *Mol. Pharm.* **20**, 5563–5578 (2023).
370. Nishi, H. *et al.* Fc domain mediated self-association of an IgG1 monoclonal antibody under a low ionic strength condition. *J. Biosci. Bioeng.* **112**, 326–332 (2011).
371. Arora, J. *et al.* Charge-mediated Fab-Fc interactions in an IgG1 antibody induce reversible self-association, cluster formation, and elevated viscosity. *mAbs* (2016).
372. Chemical Computing Group ULC. MOE 2020.09: Ensemble Protein Properties. (2021).
373. Salgado, J. C., Rapaport, I. & Asenjo, J. A. Predicting the behaviour of proteins in hydrophobic interaction chromatography: 1: Using the hydrophobic imbalance (HI) to describe their surface amino acid distribution. *J. Chromatogr. A* **1107**, 110–119 (2006).
374. Long, W. Bio-MOE: Custom MOE Biologics Applications. (2021).
375. Kyte, J. & Doolittle, R. F. A simple method for displaying the hydropathic character of a protein. *J. Mol. Biol.* **157**, 105–132 (1982).
376. Tanford, C. Physical chemistry of macromolecules. *J. Pharm. Sci.* **51**, 190–190 (1962).
377. Sillero, A. & Ribeiro, J. M. Isoelectric points of proteins: Theoretical determination. *Anal. Biochem.* **179**, 319–325 (1989).
378. Case, D. *et al.* AMBER 10, University of California, San Francisco. (2008).

379. Gerber, P. R. & Müller, K. MAB, a generally applicable molecular force field for structure modelling in medicinal chemistry. *J. Comput. Aided Mol. Des.* **9**, 251–268 (1995).